

HIGH-DENSITY HIGH-EFFICIENCY
POWER MAGNETICS

by

ZHIGANG DANG

JABER ABU QAHOUC, COMMITTEE CHAIR

TIM A. HASKEW
JEFF JACKSON
SHUHUI LI
BHARAT BALASUBRAMANIAN

A DISSERTATION

Submitted for partial fulfillment of the requirements
for the Degree of Doctor of Philosophy
in the Department of Electrical and Computer Engineering
in the Graduate School of
The University of Alabama

TUSCALOOSA, ALABAMA

2016

ABSTRACT

This dissertation presents several concepts and techniques in order to (1) increase the inductance density and power density of power inductors (PIs) with high power efficiency and (2) achieve magnetically coupled wireless power transfer (WPT) systems with higher efficiency and longer transmission distances under varying conditions.

Chapter 1 provides an overview and introduction on applications of power magnetic devices and systems along with the challenges facing the state-of-the-art PIs and WPT systems.

Chapter 2 develops a concept which results in doubling the saturation current of a high current PI with NdFeB permanent magnet (PMPI). By adding a well-designed small piece of fabricated NdFeB magnet in the air gap of the PI, the saturation current of the PMPI is doubled with the same size and inductance value. Chapter 3 presents a two-phase coupled power inductor (CPI) that utilizes a PM in order to achieve almost doubled saturation current with the same size compared to the CPI and more than 70% core size reduction compared to the single-phase non-coupled PIs. Both the PMPI and PMCI concepts are experimentally verified in DC-DC power converter prototypes.

Chapter 4 and 5 present a two-coil and a four-coil reconfigurable WPT system topology, respectively, in order to optimize transmission efficiency under different distance and misalignment conditions. The two-coil reconfigurable WPT system achieves re-configurability by switching between different values of series and shunt capacitors at Tx side and/or Rx side. The four-coil reconfigurable WPT system achieves re-configurability by switching between

different sizes of drive loops and load loops. Experimental results verified effectiveness of developed reconfiguration methods.

Chapter 6 presents a method to achieve wired power conversion and WPT using a hybrid “Power Converter-WPT system”. By achieving WPT using AC switching ripple of power converter, the system eliminates the need for a transmitter stage of conventional WPT system, which could be beneficial for system size and cost reduction. The method is verified and demonstrated using Buck-WPT system as an example.

The last chapter summarizes this work and provides conclusions before discussing some possible future research directions related to the dissertation work.

LIST OF ABBREVIATIONS AND SYMBOLS

3-D	Three Dimensional
A_c	Cross Section Area of Power Inductor Core
A_e, A_{eff}	Effective Cross Section Area
AC	Alternating Current
ANSYS® HFSS®	A Software Package from ANSYS®
ANSYS®/Maxwell®	A Software Package from ANSYS®
B	Flux Density
B_r	Residual Flux Density
B_{sat}	Saturation Flux Density
$(BH)_{\text{max}}$	Maximum Energy Product
Big-CPI	A CPI with Bigger Core
BPU	Battery Power Unit
C-MRC-WPT	Conventional Magnetic-Resonance Coupled Wireless Power Transfer
C_{in}	Input Capacitor/Capacitance
C_o	Output Capacitor/Capacitance
CPI	Coupled Power Inductor

d_{lc}	Distance Between Loop and Coil
$DIS_{critical}$	Critical Transmission Distance
DC	Direct Current
DCR	DC Resistance
DIS	Distance
DL_i	i -th Drive Loop
E_{core}	Maximum Magnetic Energy Stored in Magnetic Core
E_{PM}	Maximum Magnetic Energy Stored in a PM
EMI	Electromagnetic Interference
EV	Electric Vehicle
FEA	Finite Element Analysis
FET	Field Effect Transistors
F_{PM}	Magnetomotive Force Generated by PM
H	Applied Magnetic Field
H_{ci}	Intrinsic Coercivity
HEV	Hybrid Electric Vehicle
H_{knee}	The H value at “knee” point
H_{sat}	Magnetic Field When Magnetic Core Gets to B_{sat}
i	Current

I_{driver}	Current of Driver
I_{Lmax}	Maximum Inductor Current
I_{Lmin}	Minimum Inductor Current
I_o	Output Current
I_{sat}	Saturation Current
I_{sat_PMTPI}	Saturation Current of PMTPI
I_{sat_TPI}	Saturation Current of TPI
I_{sat_CPI}	Saturation Current of CPI
I_{sat_PMCI}	Saturation Current of PMCI
IPT	Inductive Wireless Power Transfer
$k_c / k_{critical}$	Critical Coupling Factor
k_{c_i}	Critical Coupling Factor for Configuration- i
k_{lc}	Coupling Factor Between Loop and Coil
k_{DT}	Coupling Factor Between Drive Loop and Tx Coil
k_{TR}	Coupling Factor Between Tx and Rx
k_{RL}	Coupling Factor Between Load Loop and Rx Coil
k_{TR-2}	Coupling Factor Between Tx and Rx of Two-Coil WPT System
KVL	Kirchhoff's Voltage Law
LED	Light-Emitting Diode

L	Inductance
L_{SS}	Steady State Inductance
L_{tr}	Equivalent Transient Inductance
L_{max}	Maximum Inductance
l_{PM}	Length of PM
LF	Low Frequency
l_e, l_{eff}	Effective Length of Magnetic Path
l_m	Length of Magnetic Path
LCR	Inductor-Capacitor-Resistor
LL_ i	i th Load Loop
L_{loop_i}	Inductance of i th Loop
M/ M_{xy}	Mutual Inductance
M_{lc}	Mutual Inductance Between Loop and Coil
MIS	Misalignment
MMF	Magnetomotive Force
MOSFET	Metal-Oxide-Semiconductor Field-Effect Transistors
MRC	Magnetic Resonance Coupled/Coupling
MRC-WPT	Magnetic-Resonance Coupled Wireless Power Transfer
N	Number of Turns

NdFeB	Neodymium-Iron-Boron
NdFeB-N35EH	One Type of NdFeB Magnet
P_{AC}	AC Power Loss
P_{DC}	DC Power Loss
P_{driver}	Power Loss of Driver
P_A	Maximum Available Power at Drive-loop
P_L	Load Power
P_t	Total Power Inductor Losses
P_{t_PMTPI}	P_t of PMTPI
P_{t_TPI}	P_t of TPI
PI	Power Inductor
PM	Permanent Magnet
PMCI	Permanent Magnet Coupled Power Inductor
PMPI	Permanent Magnet Power Inductor
PMTPI	Permanent Magnet Toroid Power Inductor
PPMS	Physical Property Measurement System
PP	Parallel-Parallel
PS	Parallel-Series
Q	Quality Factor

Q_{coil}	Quality Factor of Coil
Q_{loop_i}	Quality Factor of i th Loop
R_c	Reluctance of the Ferrite Core
R_{eq}	Equivalent Reluctance
R_g	Reluctance of the Airgap
R_{gl}	Reluctance of Airgap of the PMTPI
r_i	Radius of i th Loop
R-MRC-WPT	Reconfigurable Magnetic Resonance Coupled Wireless Power Transfer
R_{opt}	Optimum Resistance
R_{PM}	Reluctance of the PM
R_s	Source Impedance
R_L	Load Impedance
R_{s-2}	Source Impedance of the Two-Coil WPT System
R_{L-2}	Load Impedance of the Two-Coil WPT System
R_{lp}	Parasitic Resistor
Rx	Receiver
RF	Radio Frequency
RFID	Radio-Frequency Identification
SmCo	Samarium–Cobalt Magnet

S_{21}	S_{21} Parameter
$ S_{21} _{c_i}$	Critical $ S_{21} $ for Configuration- i
S_l	Lower Side Switch
S_u	Upper Side Switch
SS	Series-Series
SP	Series-Parallel
T_s	Switching Period
T_{on}	On Time of The Control MOSFET
T_{TPI}	Temperature of the TPI
T_{PMTPI}	Temperature of PMTPI
T_{CPI}	Temperature of CPI
T_{PMCI}	Temperature of PMCI
$T_{Big-CPI}$	Temperature of Big-CPI
TDK	TDK Corporation
TH_{PM}	Thickness of PM
TPI	Toroid Power Inductor
T_x	Transmitter
VNA	Vector Network Analyzer
VRM	Voltage Regulation Module

V_{driver}	Driver Voltage
V_{in}	Input Voltage
V_o	Output Voltage
V_{o_WPT}	Output for Wireless Power Transfer
V_{o_wired}	Output for Wired Power Conversion
V_e	Effective Volume
V_{MOS}	Voltage Drop Across the MOSFET
V_{PM}	Volume of PM
V_s	Voltage Source
w_{PM}	Width of PM
WPT	Wireless Power Transfer
Z_{AC}	AC Impedance
Z_{DC}	DC Impedance
Z_{coil}	Impedance of Coil
Z_{loop_i}	Impedance of i th Loop
Z_{in}	Input Impedance
α	Coupling Factor
Φ	Magnetic Flux
Φ_{Ni}	Winding Flux

Φ_{PM}	PM flux
ξ_1	MMF of winding1
ξ_2	MMF of winding2
ξ_{pm}	MMF of the PM
η	Efficiency/Transmission Efficiency
η_i	Transmission Efficiency for Configuration- <i>i</i>
η_{TPI}	Efficiency of Buck Converter with the TPI
η_{PMTPI}	Efficiency of Buck Converter with the PMTPI
η_{big}	Efficiency of Buck Converter with the Big-core TPI
$\eta_{critical}$	Critical Transmission Efficiency
λ	Flux Linkage
μ_{eff}, μ_e	Effective Permeability
μ	Permeability
μ_o	Vacuum Permeability
μ_r	Relative Permeability
Δi	Peak-to-Peak Ripple of the Inductor Current
ρ_{PM}	Resistivity of the PM
ω_o	Angular Resonance Frequency

ACKNOWLEDGMENTS

The author would first like to thank his advisor Dr. Jaber Abu Qahouq for his care, support and guidance during this research. Dr. Abu Qahouq's hard working, passion, professionalism and patience have been encouraging and inspiring the author throughout his work.

The author is grateful to his committee members Dr. Tim A. Haskew, Dr. Jeff Jackson, Dr. Shuhui Li and Dr. Bharat Balasubramanian for their valuable time, advice and support.

From Spring 2012 to Fall 2016, the author received significant help, guidance, advice, support, care and encouragement from his teammates. They are Wangxin Huang, Yuan Cao, Lin Zhang, Zhiyong Xia, Yuncong Jiang and Prasad Arikatla. The author deeply appreciate for all their help.

During this journey, the author received kind help from many professors, staff members, graduate students and undergraduate students from ECE department and throughout the entire UA. He also received "feel at home" help from ever kind friends from this beautiful town, Tuscaloosa. Without their help, the author would not have finished this work on time.

Last but not the least, the author is grateful to his family, whose unconditional love and support encouraged him from deepest heart, which enabled him to accomplish this work.

CONTENTS

ABSTRACT.....	ii
LIST OF ABBREVIATIONS AND SYMBOLS	iv
ACKNOWLEDGMENTS	xiii
LIST OF TABLES.....	xix
LIST OF FIGURES	xx
CHAPTER 1 INTRODUCTION	1
1.1 A Brief Overview.....	1
1.2 Power Inductors.....	2
A. Power Inductor Applications.....	2
B. Power Inductors for Switching Power Converters.....	4
C. Coupled Power Inductors for Switching Power Converters	7
1.3 Wireless Power Transfer systems	9
A. Early Work on WPT.....	9
B. Advances in WPT.....	11
1.4 Other Power Magnetics Components and Systems.....	15
A. Power Transformers.....	15
B. Electric Machines.....	16
1.5 Dissertation Outline.....	17

CHAPTER 2 HIGH CURRENT POWER INDUCTOR WITH NdFeB MAGNET FOR DC-DC POWER CONVERTERS	21
2.1 Introduction	21
2.2 Operation Principle of The PMTPI	23
2.3 Design and Characterization of Fabricated Magnet for PMTPI	26
2.4 Illustration of Saturation Current Doubling	30
2.5 Proof of Concept Experimental Prototype Results	34
A. Fabricated Power Inductors.....	37
B. Saturation Current Doubling of The PMTPI.....	39
C. Thermal Characteristics.....	43
D. Power Inductor Losses	44
E. Total Power Converter Efficiency.....	47
2.6 Summary	48
CHAPTER 3 PERMANENT MAGNET COUPLED POWER INDUCTOR FOR MULTI-PHASE DC-DC POWER CONVERTERS	49
3.1 Introduction	49
3.2 Concepts and Theoretical Analysis	55
A. Structure and Operation Principle of PMCI.....	55
B. Magnetic Circuit Model Analysis	59
C. Permanent Magnet Design for PMCI.....	63
D. Design procedures of PMCI.....	66
3.3 3-D Physical Model Simulation of PMCI	67

3.4	Proof of Concept Experimental Prototype Results	72
A.	Inductance and Saturation Current Measurements.....	75
B.	Thermal Characteristics And Power Inductor Losses	77
C.	Total Power Converter Efficiency	80
3.5	Summary	81
CHAPTER 4 TWO-COIL RECONFIGURABLE WPT SYSTEM		83
4.1	Introduction	83
4.2	Range and Misalignment Tolerance Comparisons between Two-coil and Four-coil Wireless Power Transfer Systems	85
A.	Circuit Model Extraction and Analysis of Four-coil and Two-coil MRC-WPT Systems	85
B.	ANSYS®/HFSS® 3-D Physical Modeling and Simulation Results.....	92
4.3	Two-coil Reconfigurable WPT System	98
4.4	Proof of Concept Experimental Results	101
A.	Perfectly aligned system.....	107
B.	Laterally misaligned system.....	108
4.5	Summary	109
CHAPTER 5 FOUR-COIL RECONFIGURABLE WPT SYSTEM.....		110
5.1	Introduction	110
5.2	Reconfigurable MRC-WPT System.....	112
A.	R-MRC-WPT System	112
B.	Circuit Model Analysis	114

C.	Analytical Model Analysis.....	118
5.3	Proof of Concept Experimental Prototype Results	122
A.	System Descriptions.....	122
B.	DIS Variation	125
C.	R-MRC-WPT System with Lateral Misalignment.....	131
5.4	Additional Comments	134
A.	The Use of Ferrite with the R-MRC-WPT System.....	134
B.	Use of Litz Wire with the R-MRC-WPT System	137
5.5	Summary	137
CHAPTER 6 WIRELESS POWER TRANSFER USING INDUCTOR CURRENT SWITCHING RIPPLE OF POWER CONVERTER.....		139
6.1	Introduction	139
6.2	Power Converter-WPT System and Analysis	141
A.	Buck-WPT System.....	141
B.	Maximum Power Transfer	145
6.3	Proof of Concept Experimental Results.....	147
6.4	Summary	152
CHAPTER 7 CONCLUSIONS AND FUTURE WORK.....		153
7.1.	Summary of Conclusions.....	153
A.	High Current Power Inductor with NdFeB Magnet for Power Converters.....	154
B.	Permanent Magnet Coupled Power Inductor for Multi-Phase DC-DC Power Converters	155

C. Two-Coil Reconfigurable WPT System	156
D. Four-Coil Reconfigurable WPT System	157
E. Wireless power transfer using inductor current switching ripple of power converter.	157
7.2. Possible Future Research Directions	158
A. Power Inductors.....	158
B. Wireless Power Transfer and Harvesting Systems	159
REFERENCES	160
Chapter 1.....	160
Chapter 2.....	170
Chapter 3.....	171
Chapter 4.....	173
Chapter 5.....	174
Chapter 6.....	176
Appendix I	177
Appendix II.....	179
Appendix III.....	180

LIST OF TABLES

2.1. The TPI and PMTPI Design Specifications	33
2.2. Comparisons of fabricated power inductors.....	35
2.3. Saturation current of fabricated power inductors	39
3.1. The Characteristics of The PM.....	65
3.2. Dimensions of PMCI core.....	67
3.3. Comparisons of Fabricated Power Inductors	71
4.1. Circuit model parameters	89
4.2. Comparison between four-coil and two-coil WPT systems.....	92
4.3. Physical model parameters for MRC-WPT system	95
4.4. Comparison between critical values obtained from physical model simulations and circuit model prediction	94
4.5. Parameter specifications.....	101
4.6. Capacitance values in different configurations	102
5.1. Design example parameter values.....	116
5.2. Parameter specifications of the R-MRC-WPT system.....	125
5.3. Properties of ferrite material used in R-MRC-WPT system	134
6.1. Parameter specifications of the Buck-WPT system.....	147
6.2. Δi_r under various WPT load conditions when $D = 0.5$	149

LIST OF FIGURES

1.1.	Illustration of the family of power magnetics	1
1.2.	Illustration of motherboard with voltage regulators (VRs) and PIs highlighted.....	2
1.3.	Automotive subsystems where power inductors are used.....	3
1.4.	(a) Discrete and (b) integrated EMI filter.....	3
1.5.	a) The simplified block diagram of the distributed battery energy storage system architecture [A30] and (b) simplified main power stage schematic of DC-DC boost power converter used in each BPU	6
1.6.	Main power stage illustrative schematics of the two-phase buck power converter (a) using two separate PIs and (b) with the CPI	8
1.7.	Tesla’s early works on WPT: (a) a two-coil configuration and (b) a four-coil configuration	10
1.8.	Midrange WPT system configurations: (a) two-coil system and (b) four-coil system	12
2.1.	(a-1) Top view of the TPI diagram, (a-2) Top view of the PMTPI diagram, and simplified equivalent magnetic circuit models of (b-1) the TPI and (b-2) the PMTPI.....	24
2.2.	Measured hysteresis loop of the fabricated NdFeB-N35EH magnet	28
2.3.	3-D physical model and design parameters of the PMTPI.....	30
2.4.	B field of the (a) TPI and (b) PMTPI when the DC current increases from 0 to 16A (fixed scaling).....	31
2.5.	Demagnetizing field of the PM when the input DC current of PMTPI is 20A (a) 3-D view (b) and (c) cross-section views (auto scaling)	32
2.6.	(a) Illustrative schematics of the buck power converter with the PMTPI and (b) PWM waveforms and waveform measured at phase node	36
2.7.	Fabricated (a) power inductor cores and (b) power inductors	36
2.8.	Measured current waveforms of the TPI, the PMTPI and the Big-core TPI when power inductor DC input current values are 7A (a-1 to a-3) and 14A (b-1 to b-3)	38
2.9.	Inductance values as a function of power inductor current for the Air-core TPI, the TPI, the PMTPI and the Big-core TPI.....	38

2.10. (a) Temperature distribution images of TPI and PMTPI when power inductor current is 7A and 14A and (b) temperature as a function of inductor current	40
2.11. Power inductor losses as a function of current.....	42
2.12. Buck converter efficiencies (considering driver losses) as a function of load current.....	46
3.1. Coupled inductor and its operation in two-phase boost converter	51
3.2. Schematic diagram of core structure and DC flux lines in (a) CPI and (b) PMCI core (front view).....	57
3.3. Operation range of (a) CPI and (b) PMCI core on BH curve	57
3.4. Magnetic circuit models of the PMCI: (a) complex model and (b) simplified model.....	59
3.5. Transformed magnetic circuit model of (a) CPI and (b) PMCI	62
3.6. Magnetic hysteresis loop of the PM	64
3.7. Design procedures of PMCI.....	66
3.8. 3-D physical model and design parameters of the PMCI.....	67
3.9. FEA simulation results	69
3.10. Dimension specifications for (a) power inductor cores and (b) power inductors	71
3.11. Sample experimentally measured waveforms for phase node voltages and inductor currents (DC coupled) which are same for both the CPI and the PMCI.....	73
3.12. Measured current waveforms for CPI and PMCI when power inductor current values are 10 A/phase and 20 A/phase (AC coupled).....	74
3.13. Inductance values as a function of per phase power inductor current	75
3.14. (a) Temperature distribution images and (b) temperature as a function of per phase inductor current.	77
3.15. Power inductor DC losses as a function of per phase inductor current.....	78
3.16. Two-Phase boost converter efficiencies (considering driver losses) as a function of load current.....	80
4.1. MRC-WPT system with spiral structures: (a) two-coil system and (b) four-coil system.....	84
4.2. (a) Physical model of the open-ended Tx/Rx coil, (b) circuit model of the open-ended Tx/Rx coil and (c) circuit model for the two-coil MRC-WPT system.....	87

4.3.	(a) Physical model of the drive-loop/load-loop and Tx/Rx coil, (b) circuit model of the drive-loop/load-loop and Tx/Rx coil, (c) circuit model of the four-coil MRC-WPT system	88
4.4.	k_{TR} as a function of DIS between Tx and Rx	89
4.5.	Parameter specifications of MRC-WPT system.....	92
4.6.	Selected plots for frequency responses of (a) two-coil system, (b) four-coil system, and (c) efficiency as a function of DIS when MIS=0	95
4.7.	Selected plots for frequency responses of (a) two-coil system, (b) four-coil system, and (c) efficiency as a function of MIS when DIS=150mm	96
4.8.	Two-coil reconfigurable WPT system: (a) both Tx side and Rx side are reconfigurable, (b) only Tx side is reconfigurable	98
4.9.	Illustrative efficiency curves for N configurations, (b) efficiency curve for reconfigurable WPT system	100
4.10.	Experimental testing setup for two-coil reconfigurable WPT system, (b) design specifications	102
4.11.	Frequency responses in selected DIS values of (a) config-1, (b) config-2 and (c) config-3	103
4.12.	(a) Efficiency curves for three configurations, (b) efficiency comparison of reconfigurable and conventional WPT system in perfectly aligned case.....	104
4.13.	Frequency responses in selected MIS values of (a) config-1, (b) config-2 and (c) config-3 when DIS=5cm	105
4.14.	(a) Efficiency curves for three configurations, (b) efficiency comparison of reconfigurable and conventional WPT system in laterally misaligned case.....	106
5.1.	(a) Physical model and (b) the simplified circuit model of the R-MRC-WPT system (i=1, 2, ..., n).....	111
5.2.	A 3-D view of $ S_{21} $ as functions of frequency and k_{TR}	117
5.3.	k_{lc_i} as a function of r_i	120
5.4.	(a) Proof of concept prototype of R-MRC-WPT system and (b) parameter specifications.....	124
5.5.	Circuit diagram of four-coil MRC-WPT system using capacitor tuning (Cap-Tuning system)	124
5.6.	$ S_{21} $ as a function of frequency at (a) DIS = 30cm and (b) DIS = 60cm.....	126

5.7.	Transmission efficiency as a function of DIS when Tx and Rx are perfectly aligned (a) transmission efficiency under different configurations and (b) transmission efficiency curves for C-MRC-WPT, R-MRC-WPT and Cap-tuning systems	127
5.8.	Transmission efficiency as a function of lateral misalignment (MIS) when DIS=40cm (a) transmission efficiency under different configurations and (b) transmission efficiency curves for C-MRC-WPT, R-MRC-WPT and Cap-tuning systems	128
5.9.	Transmission efficiency as a function of lateral misalignment (MIS) when DIS=50cm (a) transmission efficiency under different configurations and (b) transmission efficiency curves for C-MRC-WPT, R-MRC-WPT and Cap-tuning systems	129
5.10.	(a) 3-D model of R-MRC-WPT system with ferrite structure on Tx side and Rx side, (b) 3-D view of ferrite structure and (c) cross section view of Tx side structure	133
5.11.	Comparison between transmission efficiency values for the R-MRC-WPT system with and without ferrite structure for (a) different DIS and (b) different MIS (with DIS = 40cm) conditions	135
5.12.	Comparison between transmission efficiency values for the Config-5 (a) without ferrite structure at DIS=40cm, (b) with ferrite structure when DIS = 40cm and (c) under different DIS conditions	136
6.1.	(a) Circuit diagrams of Buck-WPT system, (b) equivalent circuit when looking into ports of L1, (c) diagram of operation waveforms for Buck-WPT system, (d) wired output operating alone, (e) diagram of operation waveforms when wired output operating alone, (f) WPT output operating alone and (g) diagram of operation waveforms when WPT output operating alone	140
6.2.	(a) Equivalent circuit for the WPT power path and (b) illustration of first harmonic approximation of VL when D = 0.5	145
6.3.	The prototype of the Buck-WPT system: (a) a demo for powering the 2A constant current load at Vo_wired and lighting a light bulb at Vo_WPT and (b) more detailed view of the Buck-WPT system	147
6.4.	Power delivered through WPT output When D = 0.5	148
6.5.	Δi_r as a function of D when $R_{opt} = 2.9 \Omega$	148
6.6.	Waveforms of the Buck-WPT system when $R = 2.9 \Omega$. i_r is AC coupled and i_2 is DC coupled	150
6.7.	P_{o_WPT} as a function of I_o at various WPT load values when $V_{o_wired} = 2.5V$	150

6.8. Total Efficiency of the Buck-WPT system (a) for full I_o range and (b) a zoomed in view when $I_o \leq 1A$	151
A.1. General two-port network	177
A.2. Equivalent circuit model of directly coupled inductors that are connected in series	179
A.3. Equivalent circuit model of a coupled inductor	180

CHAPTER 1

INTRODUCTION

1.1 A Brief Overview

The main members of power magnetic devices and systems, family are illustrated in Fig. 1.1, which include power inductors (PI), power transformers, electric machines and inductive wireless power transfer (WPT) coils/systems. Power magnetic devices and systems have been widely used in electric/electronic devices and systems, power transmission systems and energy conversion systems all over the world [A1-A118]. The dissertation focuses on PIs and WPT systems.

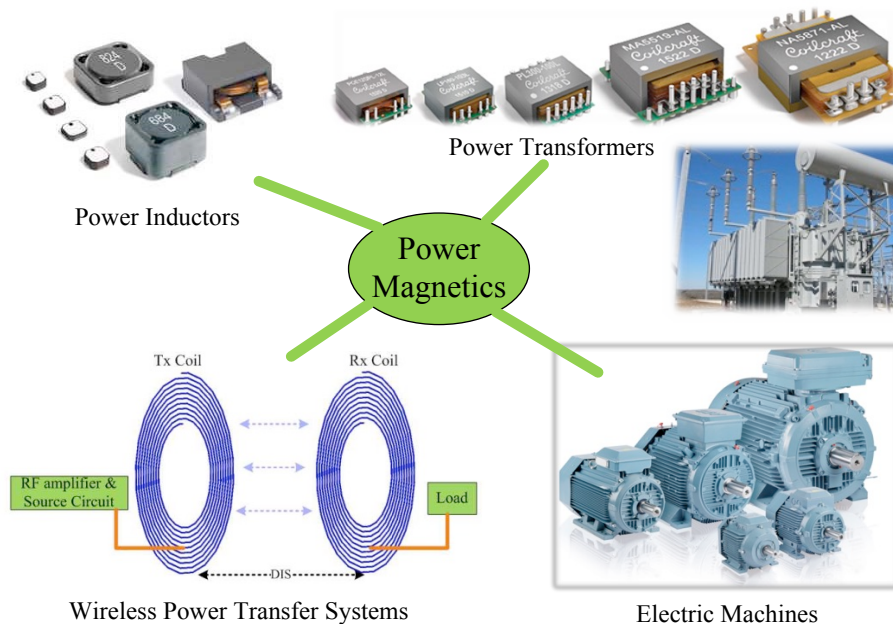


Figure 1.1: Illustration of the family of power magnetics [A1]

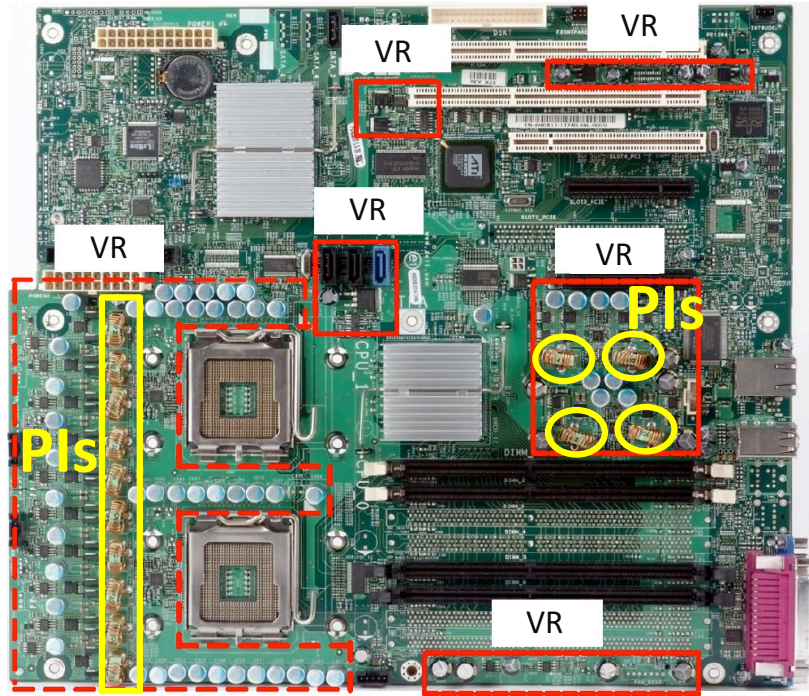


Figure. 1.2: Illustration of motherboard with voltage regulators (VRs) and PIs highlighted [A2]

1.2 Power Inductors

A. Power Inductor Applications

As a passive energy storage element, a PI stores energy in its magnetic field and it resists the change of current passing through its winding. Various types of PIs have a wide range of applications ranging from wearable devices and consumer electronics to automotive electronics and electric vehicle (EV) applications, among others [A1-A65].

Take computer/server mother board as an example, as illustrated in Fig. 1.2. Study in [A2] shows that currently 30% of area of motherboard is occupied by voltage regulators. Among all voltage regulators, PIs account for a large portion (e.g. 30 - 50%) in both size and weight. This means size and weight reduction in each PI will significantly contribute to the size and weight reduction in the whole mother board.

Take the automotive system as another example, many different types of power inductors have been used in a variety of subsystems, as illustrated in Fig. 1.3 [A1], where up to 21 subsystems need one or more PIs. Among various types of PIs that have been used, common mode chokes and differential mode chokes used for filtering electromagnetic interference (EMI) are normally AC inductors, and PIs used in switching power converters are normally DC inductors. [A1-A65].

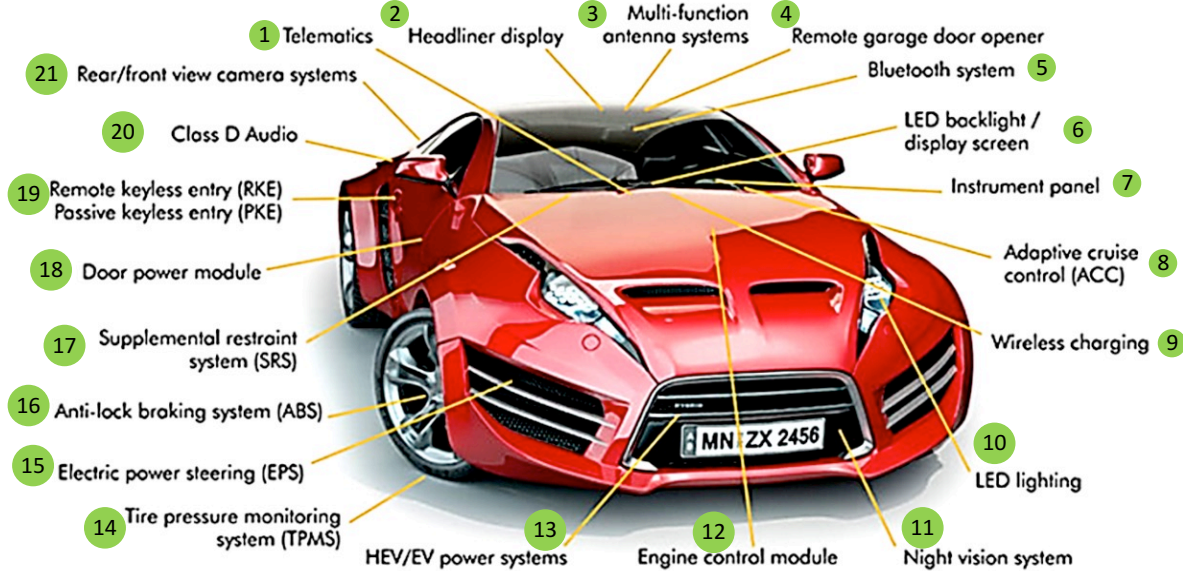


Figure 1.3: Automotive subsystems where power inductors are used [A1]

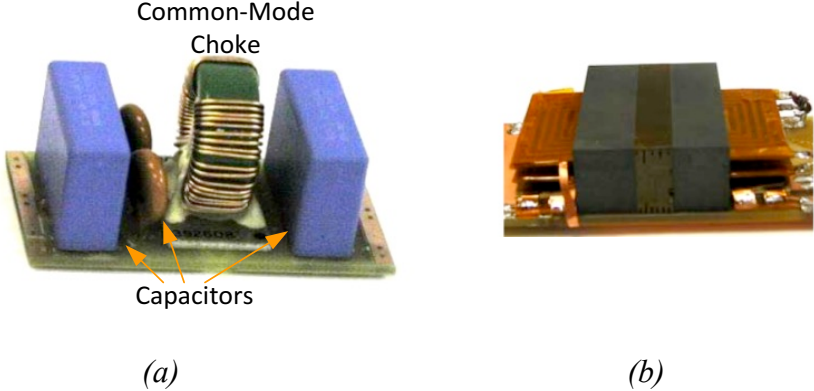


Figure 1.4: (a) Discrete and (b) integrated EMI filter [A3-A5]

A common-mode choke is used for prevention of electromagnetic interference (EMI) from power supply lines in order to prevent malfunctioning of electronic equipment. Common-mode choke passes differential currents while blocking common-mode currents [A3-A5]. A differential mode inductor passes common-mode currents while attenuating differential mode currents. An EMI filter, as an important part for power supply systems to attenuate switching noise and meet EMI standards, normally includes one or more common-mode choke, and/or a couple of differential mode chokes, and several capacitors [A3-A5]. An EMI filter with discrete components is shown in Fig. 1.4(a), where the common-mode choke and capacitors are big in size. By using the planar electromagnetic integration technologies and structural winding capacitance cancellation method, the integrated EMI filter as shown in Fig. 1.4(b) achieved much smaller volume and profile and much better characteristics over a wide frequency range compared to the discrete EMI filter [A3-A5].

PIs for switching power converters is one of two main focuses of this dissertation work.

B. Power Inductors for Switching Power Converters

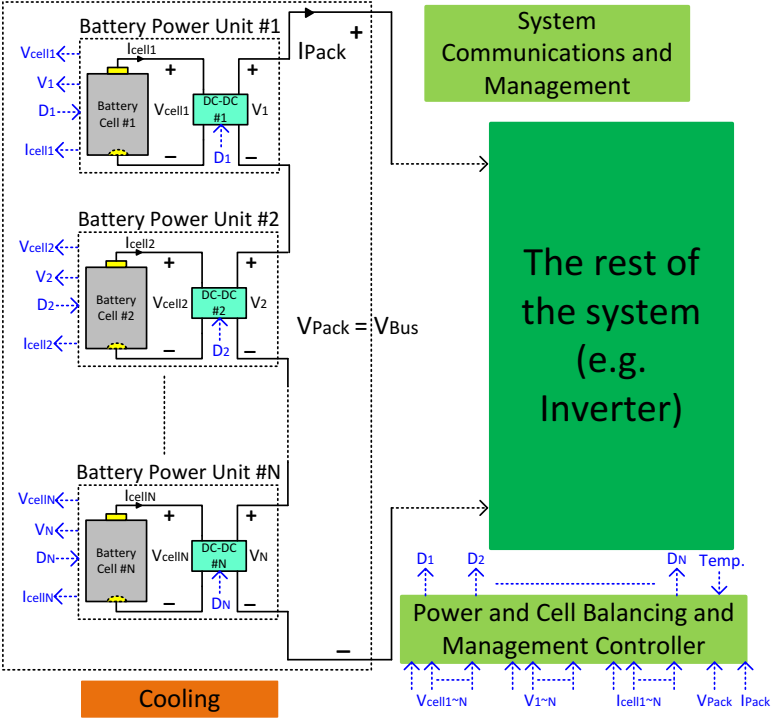
Switching power converters are indispensable parts in electrical platforms and systems such as computing platforms, communication and mobile systems, medical systems, electric vehicles' electronics, military systems, energy harvesting systems, aerospace systems, and almost all peripherals and devices [A6-A65]. The performance of power devices such as power inductors and power FETs (Field Effect Transistors) is critical in switching power converters such as buck converter, boost converter and buck-boost converter [A28-A43].

A power inductor is usually made up of one or more conductor windings (e.g. copper) and a magnetic core that can be of different shapes and dimensions. There are many standard core shapes available in the market, such as EI core, EE core, planar ER core, PQ core and toroid

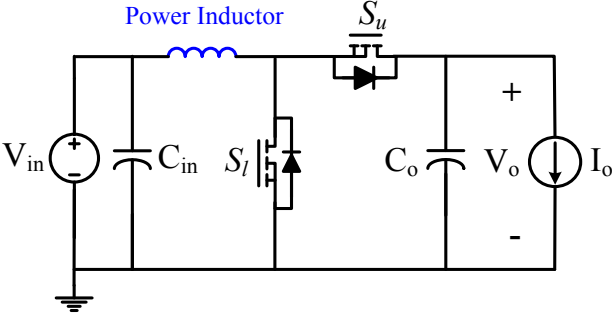
core, among others [A1, A44]. The magnetic core provides shielding for magnetic fluxes and increases the inductance density of the power inductor. However, it limits the maximum DC current of that the power inductor is able to handle and introduces core power loss. The maximum DC current which a power inductor with magnetic core is able to handle, also known as the saturation current, is limited by the saturation magnetization of the magnetic core material. The core loss of a power inductor includes eddy current loss (which is mainly determined by resistivity of core material) and hysteresis loss (which is mainly determined by the coercivity of the magnetic material). In order to increase the inductance density, increase the saturation current and reduce the core loss of a power inductor, magnetic materials with larger permeability, higher saturation magnetization, larger resistivity and smaller coercivity (such as ferrite materials) are desired [A45-A48]. Research work and technological advances over the past few decades have resulted in size and weight reduction of other parts in power electronic circuits, such as power switches and capacitors in addition to controllers, at a much faster rate compared to power inductors [A6-A36, A49-A52].

Power inductor with larger inductance value and higher power density usually has larger size and requires larger magnetic core. The bulky magnetic core and thick copper winding contribute to increase in volume and weight for power inductors. The power inductor is usually the largest and the heaviest component in a switching power converter [A37-A43]. Therefore, it is important to investigate and develop methods to further increase the inductance density and power density of power inductors (i.e. reduce the size of the power inductor without reducing inductance value and saturation current value, or increase the saturation current value for the same size and inductance value). This supports the size reduction of power converters through power inductor miniaturization. For this purpose, different methods, such as the utilization of

new magnetic materials as power inductor cores and designing new power inductor structures, have been presented in the literature [A45-A48, A53-A54].



(a)



(b)

Figure 1.5: (a) The simplified block diagram of the distributed battery energy storage system architecture [A30] and (b) simplified main power stage schematic of DC-DC boost power converter used in each BPU

In many battery powered systems such as mobile phones, tablets, laptops and EVs/HEVs, among others, smaller power converters size and weight are critical to meet size and weight requirements. In a system where multiple battery cells are needed, the battery pack voltage can be regulated by a high power large power converter with large power inductor or when the distributed battery energy storage system presented in [A30] is used there will be the need for several power converters with several power inductors. This is because in the distributed battery energy storage system, rather than connecting battery cells in series to form a battery string and regulating the voltage of the battery string through a high power DC-DC power converter, battery cells are decoupled from one another by connecting each cell with a lower power boost power converter as illustrated in Fig. 1.5(a) [A30]. Each battery power unit (BPU) consists of one battery cell and one boost power converter. Fig. 1.5(b) shows the schematic of boost power converter used in BPU, which include input and output capacitors C_{in} and C_o , control and synchronous power MOSFETs S_u and S_l and a power inductor. A small size and weight reduction in each boost power inductor will contribute to the size and weight reduction in the whole battery pack.

Therefore, it is important to investigate and develop methods to further increase the inductance density and power density of power inductors (reduced size and weight) with high power efficiency, which is an objective in this dissertation work.

C. Coupled Power Inductors for Switching Power Converters

Coupled power inductor (CPI) has several applications, and one of them is in multi-phase power converters [A2, A55-A65]. Fig. 1.6(b) illustrates the application of the CPI in a two-phase buck power converter. Instead of using two separate PIs for two phases as illustrated in Fig. 1.6(a), only one CPI is needed, which helps to reduce the total volume occupied by power

inductors on the power converter board and therefore results in higher power density. The volume reduction of the CPI is because 1) two separate inductors are integrated into one structure, and 2) the inverse coupling results in flux cancellation, which increases the saturation current of the CPI or equivalently reduces volume. Another advantage of the CPI used in DC-DC power converters is the ability to obtain smaller equivalent transient inductance (advantageous for lower output voltage dynamic deviation under transients) with a larger equivalent steady-state inductance (advantageous for smaller steady-state output voltage ripple and higher power efficiency) [A62-A65].

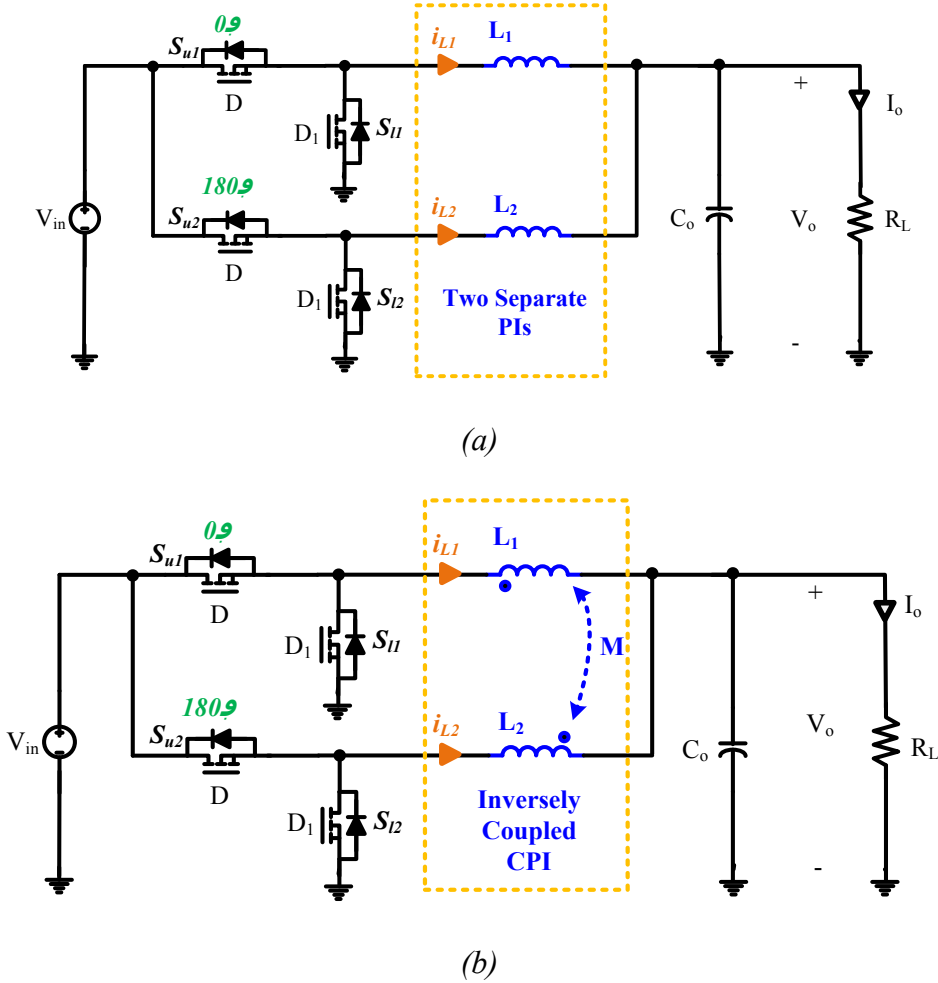


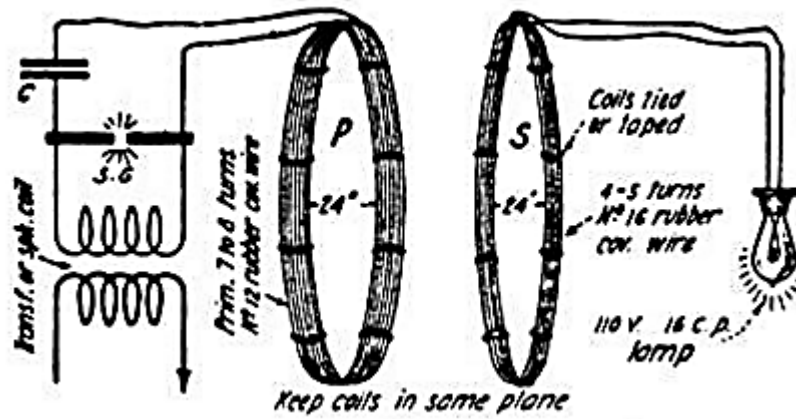
Figure 1.6: Main power stage illustrative schematics of the two-phase buck power converter (a) using two separate PIs and (b) with the CPI

In order to increase the power density of the multi-phase power converters further, it is important to investigate and develop methods to further increase the inductance density and power density of CPIs with high power efficiency, which is an objective in this dissertation work.

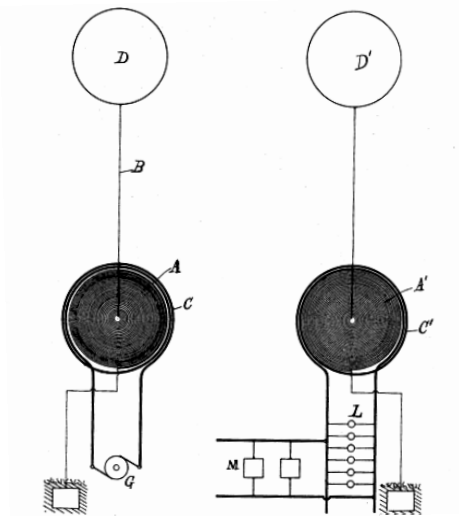
1.3 Wireless Power Transfer systems

A. Early Work on WPT

The early research and development work on WPT dates back to early 20th century [A66-A68]. At that time, Nikola Tesla even attempted to intercontinentally transmit power wirelessly before wired grid transmission [A67]. Fig. 1.7 illustrates two of the early WPT systems suggested by Tesla. Fig. 1.7(a) illustrates an application of Tesla's WPT system for powering a lamp, which include a transmitter (Tx) coil and a receiver (Rx) coil, which is a two-coil configuration [A68-A70]. Fig. 1.7(b) shows that the transmitter side has a driving loop C coupled to a transmitter coil (Tx) A, which significantly steps up the voltage for an elevated terminal D. Similarly, the receiver side has a load loop C' coupled to the receiver coil (Rx) A' which is connected to an elevated terminal D'. It is a four-coil configuration. Through electrical oscillation, a current is discharged through the air between D and D' by conduction [A66, A69]. However, due to the undeveloped power electronic techniques, the efficiencies of the WPT systems were too low at that time to be practical and applicable for a long period of time.



(a) [A68]



(b) [A66]

Figure 1.7: Tesla's early works on WPT: (a) a two-coil configuration and (b) a four-coil configuration

The past decade witnessed the reemerge of the WPT due to the fast development of power electronics and related applications. As a reemerging technology, WPT has several promising and potential applications such as consumer electronics, medical implants and electric vehicle (EV) charging, among others [A69-A73]. Next part discusses more details about the

WPT applications and research advances in recent years. WPT systems and magnetics are one of two main focus area in this dissertation work.

B. Advances in WPT

Electromagnetic based WPT includes radiative (far-field) and non-radiative (near-field) methods. Some radiative WPT systems utilize microwave or laser beam to transfer power for directive long distance but with very limited efficiency [A74-A75]. Non-radiative WPT systems can be categorized into short-range and midrange WPT systems depending on the transmission distance (DIS). Short-range coupling refers to a transmission distance less than or equal to the dimension or diameter of the Tx structure and midrange usually refers to a distance of several times the dimension or diameter of the Tx structure [A69].

B.1 Short-Range WPT Systems

Inductive WPT (IPT) can be used to transfer significant amount of power within a short distance, which is usually less than one coil diameter [A73, A76-A83]. IPT system usually employs a two-coil system, which includes a Tx coil and a Rx coil. This usually aims to maximize total system energy efficiency (which is referred to as maximum energy efficiency principle in [A70]). Short range IPT system usually employs ferrite structures in Tx and Rx to achieve stronger magnetic coupling. It is able to transmit large amount of power with high total system energy efficiency that can go above 90% especially at very short distances [A73, A76-A83]. Example applications for short-range WPT systems are illustrated in Fig. 1.8, which shows that transmission distances of the short-range WPT systems are very limited.

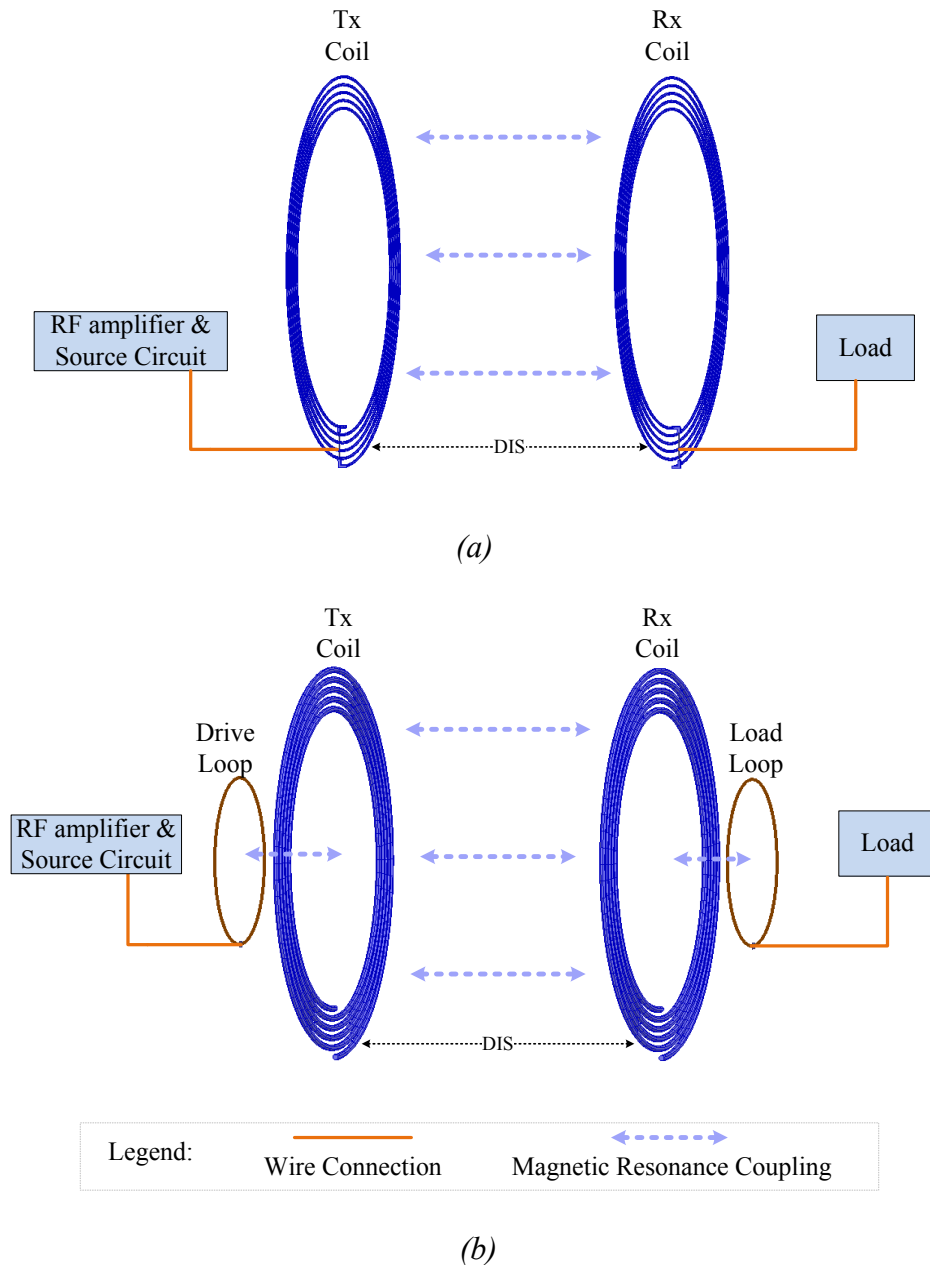


Figure 1.8: Midrange WPT system configurations: (a) two-coil system and (b) four-coil system

B.2 Mid-Range WPT systems

Magnetic resonance coupled (MRC) WPT is suitable for mid-range low power applications such as consumer electronics charging where the transmission distance might be longer than one Tx coil diameter [A84-A101]. Magnetic resonance coupling, as a special form of

inductive coupling, utilizes magnetically coupled resonators (Tx coil and Rx coil) to transfer power wirelessly [A84-A101]. MRC-WPT also has advantages in tolerating larger angular and lateral misalignments [A85-A90]. In the mid-range WPT applications, if system energy efficiency is not the major concern, maximum power transfer principle can be adopted in order to maximize the power delivered to the load and extend the transmission distance at the expense of the system energy efficiency [A84-A91]. Reference [A70] discussed the difference between the maximum power transfer principle and the maximum system energy efficiency principle and how they are related to WPT systems. Two-coil WPT systems and four-coil WPT systems, as illustrated in Fig. 1.8, are commonly used in MRC-WPT systems. For both two-coil and four-coil WPT systems, higher quality factors for both Tx and Rx and stronger magnetic coupling between Tx and Rx are desired in order to maintain higher transmission efficiencies within longer transmission distances [A84-A91, A102].

A two-coil MRC-WPT system improves transmission efficiency and/or transmission distance further by optimizing the series and parallel (shunt) capacitances in the Tx and Rx coils. Various WPT circuit topologies with different resonant types such as Series-Series (SS), Series-Parallel (SP), Parallel-Series (PS), Parallel-Parallel (PP) have been discussed in the literature [A73], [A103]. Some literature such as reference [A103] concluded that the use of series-shunt mixed-resonant coupling for two-coil WPT system allows better flexibility for optimizing the transmission efficiency at different distances.

A four-coil MRC-WPT system, which includes a drive loop, a Tx coil, a Rx coil and a load loop, have been attracting great interests since being further explored in [A84], which shows a four-coil system with 60 cm diameter for Tx and Rx that can transmit 40W over a distance of 2 m (~ 3.33 times of coil diameter). For this later system, the Tx coil to Rx coil transmission

efficiency is 40% and the total system energy efficiency is 15%. In four-coil systems, the Tx and Rx are usually open ended self-resonating coils that are not directly connected to the source and load [A84-A92], and they are inductively coupled to a drive-loop and a load-loop that are connected to source and load respectively. This is unlike the case for two-coil systems where Tx and Rx are directly connected to source and load circuit. Therefore, when both Tx and Rx coils operate at resonance and both of them have the same resonance frequency, higher quality factor can be obtained for Tx and Rx in a four-coil system compared to a two-coil system as explained in [A90-A91]. Meanwhile, the additional two loop-to-coil coupling factors (drive loop to Tx coupling factor and Rx to load loop coupling factor) in the four-coil system provide higher degree of freedom for design optimization to achieve impedance matching, when compared to the two-coil system, in order to extend the transmission distance [A70, A104].

In a four-coil MRC-WPT system, as long as the coupling factor between Tx and Rx (k_{TR}) exceeds a threshold value (k_c), i.e. Rx is within the over coupled region, frequency splitting can exist and nearly constant maximum transmission efficiency can be maintained [A85-A90]. In [A85], a frequency tuning technique is demonstrated to compensate for the efficiency variation (resulted from frequency splitting) when the transmission distance and/or Tx to Rx orientation are varied. By doing so, maximum transmission efficiencies are adaptively tracked. Similar frequency tuning technique is used in [A86-A90] to maintain a high efficiency region for a laterally misaligned MRC-WPT system with various vertical distances between Tx and Rx.

Combination of the frequency tuning and other techniques can further optimize transmission efficiency and/or extend transmission distance. Frequency tuning is combined with a variable coupling technique in [A105], which varies the loop-to-coil coupling factors (drive loop to Tx coil coupling factor and Rx coil to load loop coupling factor) by varying loop-coil

distances (distance between the drive loop and Tx coil and distance between load loop and Rx coil). This technique improves transmission efficiencies within a distance of 100cm compared with fixed coupling system. Similarly, [A106] varies the loop-coil coupling factor by rotating the drive loop and load loop around the axis of the Tx and Rx. This results in improving transmission efficiencies and reducing cross coupling factors (drive loop to load loop coupling factor, drive loop to Rx coupling factor and Tx to load loop coupling factor). However, both techniques (which are referred to as the mechanical tuning methods in the rest of this dissertation) require mechanical movement of the drive loop and load loop, which increases the system volume and complexity.

For the midrange WPT systems, it is important to investigate and develop methods to further extend the transmission range under various distance and misalignment conditions for both two-coil and four-coil system, which are objectives in this dissertation work.

1.4 Other Power Magnetics Components and Systems

A. Power Transformers

A transformer is an electrical device that transfers electrical energy between two or more circuits through electromagnetic induction. Since the invention of the first constant potential transformer in 1885, transformers have become essential for the transmission, distribution, and utilization of AC electrical energy [A107]. Almost all of the world's utility AC electrical power passes through a series of transformers before it reaches the consumer. In power systems, the functionality of transformers can be summarized as: 1) delivering energy from primary side to the secondary side, 2) voltage step-up or step-down and 3) providing electrical isolation between the primary side to secondary side [A108-A117].

In the power grid, a step-up transformer steps up the voltage after generator for efficient, long-distance transmission of electricity. Step-down transformers step voltages down to the levels used by customers. These types of high voltage high power transformers, working at very low frequency (50 Hz/60 Hz), require large step up/down ratios and are very large in size [A108-A111].

High frequency transformers have been widely used in the isolated DC-DC power converters such as flyback converter, forward converter, full bridge converter, half bridge converter, and LLC resonant converters, among others [A112-A117]. These isolated DC-DC power converters using high frequency transformers have been widely used in the applications such as power adapters and supplies for consumer electronics, power supplies for telecommunication systems and data center servers, and on-board battery chargers for EVs, among others [A112-A117]. High frequency transformers work at much higher frequencies (normally larger than 20 kHz) than the bulky power transformers used in power distribution systems (50 Hz/60 Hz), and therefore, have much smaller size. Though the further improvement of the power density and efficiency of power transformers are very important topics, they are not the focus of this dissertation work.

B. Electric Machines

Electric machines, including electric generator and electric motor, convert mechanical power into electrical power and vice versa. Example electric machine applications include power generations, wind turbines, manufacturing productions, electric locomotives, EVs, robots, air conditioners and fans, among others [A118]. Study in [A118] shows that the primary supply of world's electrical energy is generated in three phase synchronous generators using machines with power ratings up to 1500 MW or more and electric motors consume approximately 60% of all

electricity produced. Even though there are many interesting research topics for electric machines such as improvements of power density, energy conversion efficiency, motor drive and control quality, among others, these are not the focus of this dissertation work.

1.5 Dissertation Outline

Next chapter presents the concept, design and experimental evaluation of a high current PI with NdFeB permanent magnet (PMPI). By adding a small piece of fabricated NdFeB magnet (magnet volume is $\sim 0.36\%$ of the PMPI ferrite core volume) in the air gap of the PI, the saturation current of the PMPI is doubled with the same size and inductance value. The desired dimensions of the PM are theoretically calculated before fabrication and then the fabricated PM is characterized. The PMPI is experimentally evaluated in a DC-DC buck power converter. Results show that compared to a PI with the same size and inductance without the PM, the saturation current of the PMPI is doubled. Compared to another PI with a larger size needed to double the saturation current, the ferrite core weight of the PMPI is reduced to 53.6% and the core volume is reduced to 59.2%. Experimental results also show that the addition of the NdFeB-N35EH PM does not introduce additional power losses and increase of temperature for the PMPI and does not affect the power converter efficiency.

Chapter 3 presents a two-phase Coupled power inductor (CPI) design that utilizes a PM in order to achieve almost doubled saturation current with the same size compared to the CPI and more than 76.3% core size reduction compared to the single-phase non-coupled PIs. CPI can achieve size reduction compared with single phase PI because of the magnetic flux cancellation effect. Utilizing CPI in a multi-phase DC-DC power converter yields the benefit of smaller equivalent transient inductance (advantageous for lower output voltage dynamic deviation under transients) with a larger equivalent steady-state inductance (advantageous for smaller steady-

state output voltage ripple and higher power efficiency). The presented permanent magnet coupled power inductor (PMCI) circuit model and required PM dimensions are derived and used as a design guide. The 3-D physical model of the PMCI is developed by using ANSYS®/Maxwell® software package to “visualize” the saturation current doubling. The fabricated PMCI is tested in a two-phase DC-DC boost power converter experimental hardware prototype. Results show that compared to a conventional CPI design with the same size, weight and inductance, the fabricated PMCI almost doubles the saturation current. Compared to another CPI with a larger size but with even a smaller saturation current, the core volume of the PMCI is reduced to 51.9% and the core weight is reduced to 51.2%. Experimental results also show that the addition of the PM does not cause significant additional power losses and temperature rises for the PMCI, and does not affect the multi-phase power converter efficiency.

Chapter 4 first compares two-coil and four-coil configurations for midrange magnetic resonance coupled wireless power transfer (MRC-WPT) systems, then presents a two-coil reconfigurable WPT system topology in order to optimize transmission efficiency under different transmission distance (DIS) and lateral misalignment (MIS) conditions. In the first part, physical model simulation results show that the four-coil system achieves longer transmission distance and larger misalignment tolerance with relatively lower efficiency at close distance compared to the two-coil system. In the second part, the two-coil reconfigurable WPT system includes one Tx side and one Rx side but it could switch between different circuit configurations (which are made up of different values of series and shunt capacitors) at Tx side and/or Rx side. Design guidelines of the two-coil reconfigurable WPT system are devised based on an equivalent circuit model. Proof of concept prototype results show that when the system is perfectly aligned, the

reconfigurable system improves the transmission efficiency by up to 20%. When system is laterally misaligned, the transmission efficiency is improved by up to 19%.

Chapter 5 presents a method for four-coil reconfigurable magnetic resonance coupled wireless power transfer (R-MRC-WPT) system in order to achieve higher transmission efficiency under various DIS and/or MIS conditions. Higher efficiency, longer transmission distance and larger misalignment tolerance can be achieved with the presented R-MRC-WPT system when compared to the conventional four-coil MRC-WPT (C-MRC-WPT) system. The reconfigurability in the R-MRC-WPT system is achieved by adaptively switching between different sizes of drive loops and load loops. All drive loops are in the same plane and all load loops are also in the same plane, this method does not require mechanical movements of the drive loop and load loop and does not result in system volume increase. Theoretical basis of the method for the R-MRC-WPT system is derived based on a circuit model and an analytical model. Results from a proof of concept experimental prototype show that the transmission efficiency of the R-MRC-WPT system is higher than the transmission efficiency of the C-MRC-WPT system and the capacitor tuning system for all DIS and MIS values.

Chapter 6 presents a method to achieve wired power conversion and wireless power transfer (WPT) using a hybrid “Power Converter-WPT system”. By achieving WPT using AC switching ripple of power converter, the system eliminates the need for a transmitter stage of conventional WPT system, which could be beneficial for system size and cost reduction. Using Buck-WPT system (achieves step down DC-DC power conversion and WPT at the same time) as an example, this chapter derives the system operation principle and maximum power transfer conditions for WPT. Experimental results verify the developed method and theoretical derivations.

The last chapter summarizes this work and provides conclusions before discussing some possible future research directions related to the dissertation work.

CHAPTER 2

HIGH CURRENT POWER INDUCTOR WITH NdFeB MAGNET FOR DC-DC POWER CONVERTERS

2.1 Introduction

One of the methods used to increase the saturation current (or effectively reduce the size and weight) of the power inductor utilizes one or more permanent magnet(s) (PM) to partially cancel the magnetic fluxes generated by the power inductor winding [B1-B7]. Recently, this method was studied by using ANSYS®/Maxwell® 3-D physical model simulations in [B2-B5] and showed potential for different power inductor designs and applications.

In this chapter, a power inductor with NdFeB-N35EH magnet (PMPI) is developed, fabricated and experimentally evaluated in a 5V/2V DC-DC buck power converter. The dimensions of the required NdFeB magnet for the PMPI are theoretically devised and the fabricated magnet is characterized. 3-D physical model simulation results are used to visualize the saturation current doubling of the PMPI. Experimental results validate the saturation current doubling and other performance metrics of the PMPI. The experimental evaluation, which compares the PMPI to conventional designs, includes verification of operation, power loss and efficiencies evaluation, size and volume comparisons, inductance values comparisons and thermal characteristics evaluation.

While the idea of using permanent magnet to increase saturation current of power inductor has been previously discussed [B1-B7], the following summarizes the main contribution of chapter: (1) This chapter develops in detail the theoretical and practical guidelines to achieve the doubling of saturation current for a toroid power inductor with a piece of permanent magnet

(PMTPI). (2) Based on the equivalent energy stored in a gapped toroid core and energy supplied by the permanent magnet, this chapter devises the theoretical guidelines to determine the characteristics and dimensions that the permanent magnet needs to have in order to achieve doubling of saturation current. (3) Based on theoretical calculations of the equivalent stored energy, the desired PM is fabricated and its hysteresis loop is experimentally measured. (4) Circuit model is devised in this manuscript and is used to analyze and simulate the PMTPI in order to achieve doubling of saturation current. (5) The chapter evaluates the PMTPI in an actual experimental DC-DC power converter and demonstrate the ability of the PMTPI to have twice the saturation current of a TPI with the same size, same inductance density and same efficiency (in other words without tradeoff or drawback). (6) This chapter verifies the theoretical guidelines and assumptions by using several methods including (a) Experimental measurement of efficiency and inductance from an experimental power converter, (b) thermal rise measurements, and (c) ANSYS®/Maxwell® 3-D physical model simulations.

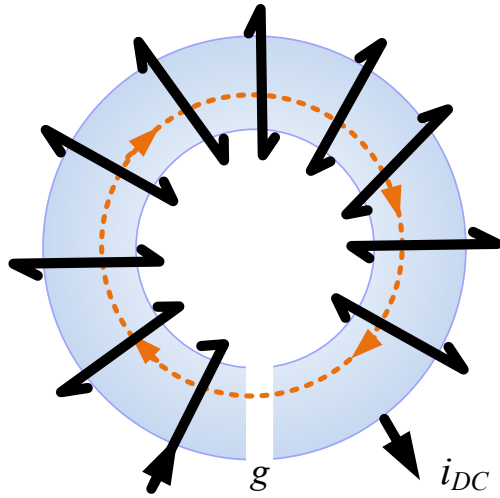
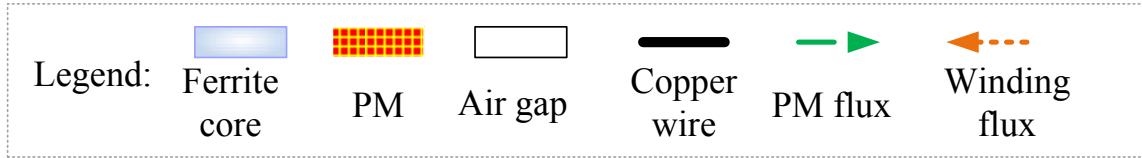
In most power converter designs and in power device development, there is a tradeoff between size and power efficiency. In many design examples, a designer might be able to improve efficiency while increasing size or able to reduce size while decreasing efficiency. Power inductor design is an example device which encounters tradeoff between size, efficiency, inductance density, and saturation current. Therefore, this chapter considers all of these metrics when evaluating the PMTPI and comparing it to other power inductors.

Next section presents the operation principle of the PMTPI based on equivalent magnetic circuit analysis. Section 2.3 presents the dimensions' design and the characterization results of the fabricated NdFeB-N35EH magnet used in the PMTPI. Section 2.4 illustrates the saturation current doubling of the PMTPI by using ANSYS®/Maxwell® 3-D physical model simulation

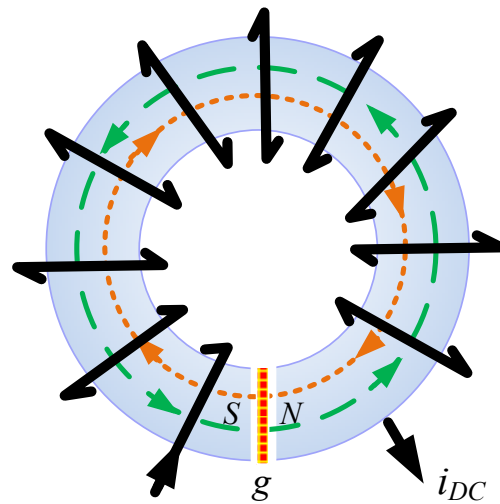
results. Section 2.5 presents the experimental testing results and performance evaluations for the PMTPI. Section 2.6 gives a summary for this chapter.

2.2 Operation Principle of The PMTPI

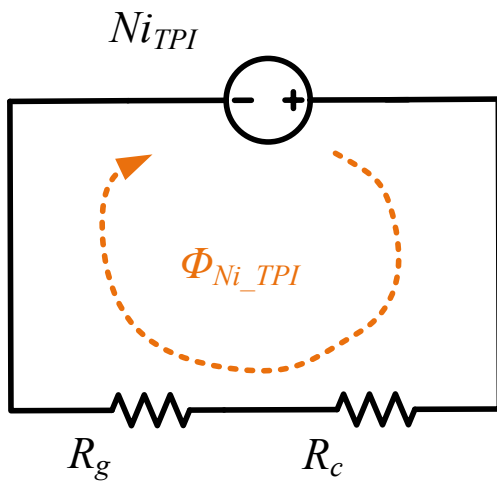
A PMTPI utilizes a PM in its structure in order to partially cancel the flux in the toroid magnetic core generated by the passing current through the windings so that a higher saturation current could be obtained [B2]. In order to increase the saturation current to its maximum possible value while maintaining proper operation with high efficiency/low power loss, the PM characteristics (in addition to the core and windings) have to be carefully designed, as explained in the next section of the chapter. The top views of a TPI and a PMTPI diagrams are illustrated in Fig. 2.1(a). The TPI and the PMTPI have the same ferrite core size, same core gap size, and same number of winding turns (10 turns in this design example). In both the TPI and PMTPI structures, a copper winding is wrapped around the toroid ferrite core. The DC input current direction of winding is shown in Fig. 2.1(a). The flux path generated by winding is represented by the dotted arrowed (orange) line. In PMTPI, a small piece of PM is placed in the ferrite core gap. The north and south poles of the PM are shown in Fig. 2.1(a-2). The flux generated by the PM is in the opposite direction to the flux generated by the current carrying windings. Therefore, the winding fluxes could partially be canceled by the PM fluxes. This flux cancellation effect helps in increasing the saturation current of the PMTPI.



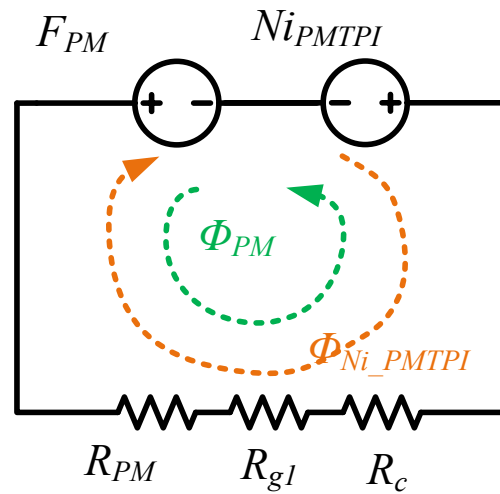
(a-1) TPI



(a-2) PMTPI



(b-1) TPI



(b-2) PMTPI

Figure 2.1: (a-1) Top view of the TPI diagram, (a-2) Top view of the PMTPI diagram, and simplified equivalent magnetic circuit models of (b-1) the TPI and (b-2) the PMTPI

Simplified equivalent magnetic circuit models (without considering the leakage flux and fringing effect) of the TPI and the PMTPI are shown in Fig. 2.1(b). N is number of winding turns, i is current that flows through the winding, F_{PM} is the magnetomotive force (MMF) of the PM, Φ_{Ni} is the winding flux, Φ_{PM} is the PM flux, R_c is the reluctance of the ferrite core, R_g is the reluctance of air gap of the TPI, R_{g1} is the reluctance of air gap of the PMTPI, and R_{PM} is the reluctance of the PM. The magnetic reluctance can be calculated from (2.1) [B8].

$$R = \frac{l_m}{\mu_o \cdot \mu_r \cdot A_c} \quad (2.1)$$

Where μ_o is vacuum permeability, μ_r is relative permeability, l_m is the length of magnetic path and A_c is the cross section area of the power inductor core. By using Kirchhoff's Voltage Law (KVL), (2.2-a) and (2.2-b) can be derived from circuit models shown in Fig. 2.1(b).

$$Ni_{TPI} = \Phi_{Ni_TPI} \cdot (R_c + R_g) \quad (2.2-a)$$

$$Ni_{PMTPI} - F_{PM} = (\Phi_{Ni_PMTPI} - \Phi_{PM}) \cdot (R_c + R_{g1} + R_{PM}) \quad (2.2-b)$$

For the TPI and the PMTPI, the differences between R_c , R_g , R_{g1} , and R_{PM} values are determined by μ_r of the material according to (2.1). μ_r of air is ~ 1 , μ_r of 3C20 ferrite (which is used in fabricated TPI and PMTPI in this chapter) is ~ 5500 [B9], μ_r of NdFeB magnet (which is used in PMTPI) is ~ 1.05 [B10]. Accordingly, $R_{g1} + R_{PM} \approx R_g > R_c$. Thus, (2.2) can be rewritten as (2.3).

$$Ni_{TPI} = \Phi_{Ni_TPI} \cdot (R_c + R_g) \quad (2.3-a)$$

$$Ni_{PMTPI} - F_{PM} = (\Phi_{Ni_PMTPI} - \Phi_{PM}) \cdot (R_c + R_g) \quad (2.3-b)$$

For the power inductor with cross section area of ferrite core A_c , the total flux in the ferrite core is $\Phi = B \cdot A_c$, where B is the flux density in the ferrite core. Saturation current of the

TPI and the PMTPI are derived as in (2.4), where B_{sat} is the saturation flux density of the power inductor core material.

$$I_{sat_TPI} = B_{sat} \cdot A_c \cdot (R_c + R_g) / N \quad (2.4-a)$$

$$I_{sat_PMTPI} = (B_{sat} \cdot A_c \cdot (R_c + R_g) + F_{PM}) / N \quad (2.4-b)$$

For the PMTPI, F_{PM} of the PM has to satisfy $0 < F_{PM} \leq N \cdot I_{sat_TPI}$ to ensure the ferrite core is not saturated by the PM itself (i.e. ferrite core should not be saturated when winding current is zero). When $F_{PM} = N \cdot I_{sat_TPI}$, (2.4) can be rewritten as (2.5). It shows that the saturation current of the PMTPI is twice as large as the saturation current of the TPI (with same winding and same ferrite core). Inductance is defined as $L = \lambda / i = N^2 / R$, where λ is flux linkage [B8]. Thus, when both the TPI and the PMTPI are not saturated, i.e. when $I_{TPI} < I_{sat_TPI}$ and $I_{PMTPI} < I_{sat_PMTPI}$, the inductance values of the TPI and the PMTPI are given by equation (2.6). This equation shows that the TPI and the PMTPI have the same inductance value.

$$I_{sat_PMTPI} = 2 \cdot B_{sat} \cdot A_c \cdot (R_c + R_g) / N = 2 \cdot I_{sat_TPI} \quad (2.5)$$

$$L_{PMTPI} = L_{TPI} = N^2 / (R_c + R_g) \quad (2.6)$$

It can be concluded from the discussion presented in this section that when a piece of properly designed and fabricated PM is placed in the air gap of a TPI (in order to obtain a PMTPI), the saturation current could be doubled and the inductance value remains the same as long as the ferrite core is not saturated.

2.3 Design and Characterization of Fabricated Magnet for PMTPI

PM material type and dimensions have to be carefully selected and designed in order to be able to double the saturation current of the PMTPI without affecting or reducing the inductance value, and in order to avoid core saturation. The PM has to have high enough intrinsic

coercivity (H_{ci}) to make sure the PM is not irreversibly demagnetized by magnetic field generated by maximum winding current. Among commonly used PMs, which include Alnico5, hard ferrite, SmCo and NdFeB magnets [B10], Alnico5 and hard ferrite have relatively small H_{ci} and are easy to be demagnetized in strong reverse field. Thus Alnico5 and hard ferrite are not suitable for designing the PMTPI in this chapter because of the desired high current capability that are given later in this chapter. Both the NdFeB and SmCo magnets are good candidates and can be used for the PMTPI example design presented in this chapter because both of them provide large maximum energy product $(BH)_{max}$ and high H_{ci} . In this work, the NdFeB magnet is selected because 1) it has lower resistivity than the SmCo magnet [B10, B12] which allows for lower eddy current loss of PM [B13] and therefore higher efficiency, and 2) it has larger $(BH)_{max}$ than the SmCo magnet [B10, B12] which allows for smaller size based on (2.9) shown next in this chapter.

NdFeB-N35EH (with thickness of 0.3mm) is fabricated using sintering process [B14] and is characterized by using Physical Property Measurement System (PPMS) DynaCool. Its characterized hysteresis loop at 300 K ($\approx 26.8^\circ\text{C}$) is shown in Fig. 2.2. Both the intrinsic curve and the normal curve are shown. The intrinsic curve represents the intrinsic magnetization ($4\pi M$, in Gaussian unit) as a function of magnetic field (H). The normal curve represents the flux density (B) as a function of H field. The relationship between B and H is $B=\mu\cdot H=\mu_o\cdot\mu_r\cdot H$ and the relationship between B and $4\pi M$ is $B=H+4\pi M$ (in Gaussian units) [B11].

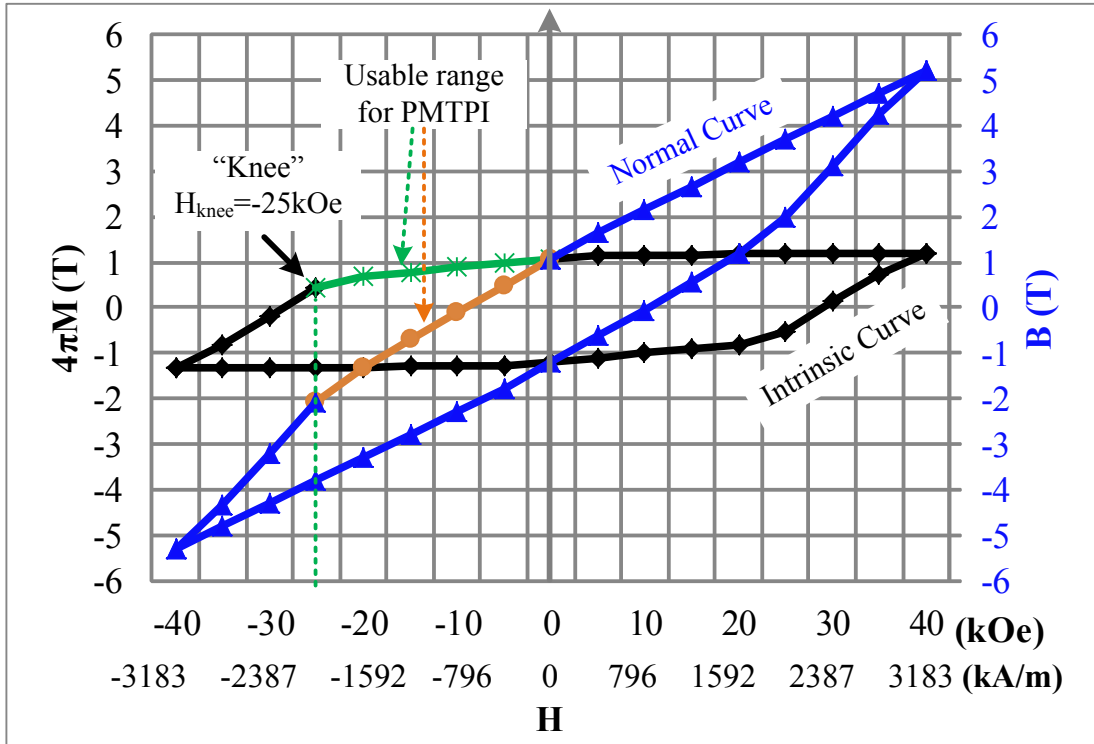


Figure 2.2: Measured hysteresis loop of the fabricated NdFeB-N35EH magnet

It can be obtained from Fig. 2.2 that H_{ci} of the fabricated NdFeB-N35EH magnet is 2244.8kA/m, coercivity $H_c = 718$ kA/m, residual flux density $B_r=1.06$ T and maximum energy product $(BH)_{max}=188$ kJ/m³. For PM materials, when a sufficient reverse H field is applied to the PM and if the PM's operation point is driven to the left part of the "knee" point (nonlinear part of the intrinsic curve), the PM material would start to be irreversibly demagnetized [B11]. At the "knee" point in Fig. 2.2, the magnetic field of NdFeB-N35EH is $H_{knee}=-25$ kOe (or -1989kA/m). This means that as long as the reverse H field (resulted from the current carrying winding of the inductor) is less than 1989 kA/m, the fabricated NdFeB-N35EH magnet will not be irreversibly demagnetized. Therefore, the usable range (also referred to as the linear range) of the NdFeB-

N35EH magnet for PMTPI on the intrinsic curve and normal curve are determined as $H_{knee} \leq H \leq 0$ and are marked in Fig. 2.2.

Next, how to theoretically calculate the required dimensions of NdFeB magnet for the PMTPI is discussed and related equations are devised. The maximum magnetic energy stored in the TPI/PMTPI core (E_{core}) is determined by (2.7) [B8].

$$E_{core} = \frac{1}{2 \cdot \mu_{eff}} \cdot A_{eff} \cdot l_{eff} \cdot B_{sat}^2 \quad (2.7)$$

Where, μ_{eff} , A_{eff} , l_{eff} are the effective permeability, effective cross section area and effective flux path length of gapped ferrite core, respectively. Maximum magnetic energy produced by a PM in the external space (E_{PM}) is determined by (2.8) [B11].

$$E_{PM} = \frac{(BH)_{max}}{2} \cdot l_{PM} \cdot w_{PM} \cdot TH_{PM} \quad (2.8)$$

Where l_{PM} , w_{PM} and TH_{PM} represent length, width and thickness of the PM, respectively. To ensure the ferrite core is not saturated by PM itself, the relationship $E_{core} \geq E_{PM}$ has to be satisfied. As a result, the PM dimensions for the PMTPI (when $E_{core} = E_{PM}$) are derived based on (2.9).

$$l_{PM} \cdot w_{PM} \cdot TH_{PM} = \frac{A_{eff} \cdot l_{eff} \cdot |B_{sat}|^2}{\mu_{eff} \cdot (BH)_{max}} \quad (2.9)$$

Based on the power inductor requirements and specifications given in the next section, the ferrite core are with $\mu_{eff} = 74 \cdot \mu_0$, $A_{eff} = 18.7 \text{mm}^2$, $l_{eff} = 42 \text{mm}$ and B_{sat} at third quadrant is 0.255T [B9]. The NdFeB-N35EH magnet used in PMTPI experiment (refer to Fig. 2.3) are with $l_{PM} = 4 \text{mm}$, $TH_{PM} = 0.3 \text{mm}$ and $(BH)_{max} = 188 \text{kJ/m}^3$. From (2.9), the width of PM can be calculated as $w_{PM} \approx 2.4 \text{mm}$. These calculated dimensions are used in the 3-D physical model simulations and for the fabrication of the PMTPI.

2.4 Illustration of Saturation Current Doubling

The objective of this section is to introduce the power inductors design specifications and visually illustrate different points of operation through 3-D physical model simulation results (before presenting the experimental results in the following section). The 3-D diagram of the TPI and PMTPI designs is shown in Fig. 2.3 and the corresponding design parameter values are listed in Table 2.1. Both the TPI core and the PMTPI core use ferrite material 3C20 ($\mu_r=5500$, B_{sat} in the first quadrant is 0.35T at 25°C and resistivity is 5Ωm at 25°C) [B9]. Two parallel solid magnetic copper wires with the size of AWG16 are used for power inductor windings. The TPI and the PMTPI each has 10 turns of winding.

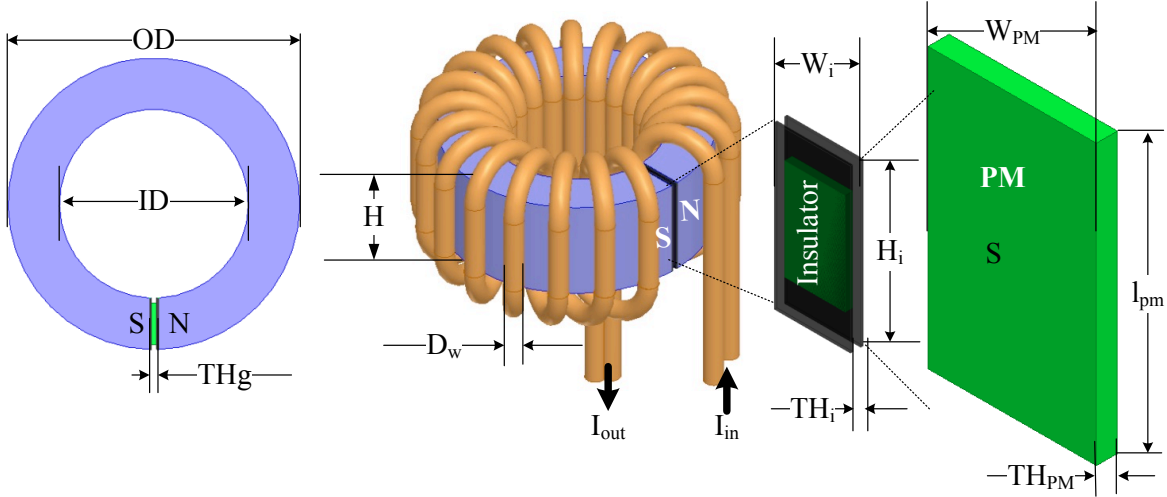
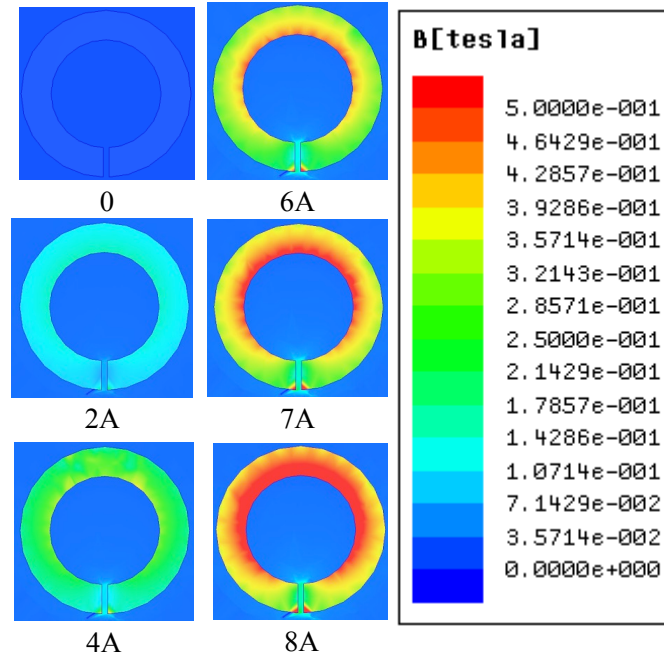
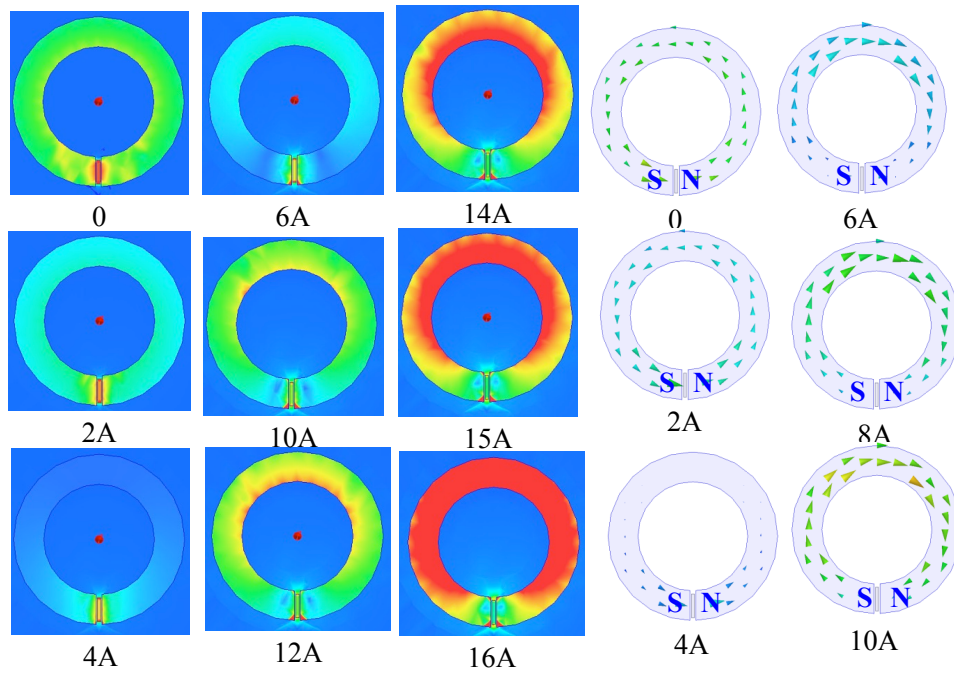


Figure 2.3: 3-D physical model and design parameters of the PMTPI



(a)



(b)

Figure 2.4: *B* field of the (a) TPI and (b) PMTPI when the DC current increases from 0 to 16A (fixed scaling)

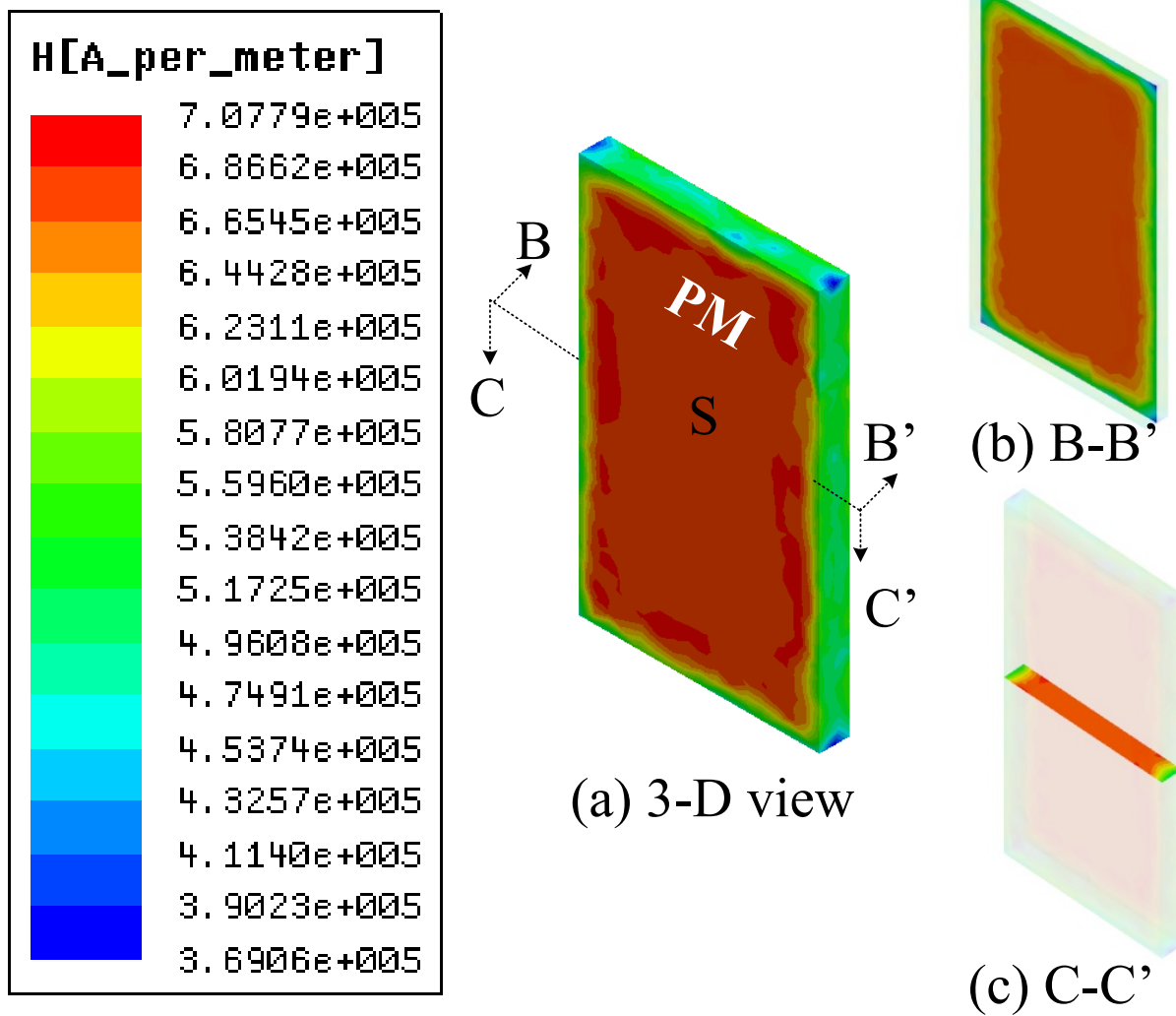


Figure 2.5: Demagnetizing field of the PM when the input DC current of PMTPI is 20A (a) 3-D view (b) and (c) cross-section views (auto scaling)

Table 2.1 The TPI and PMTPI Design Specifications

Parameter	Value	Units	Description
OD	17	mm	Outer diameter of core
ID	11	mm	Inner diameter of core
H	6.4	mm	Height of core
THg	0.6	mm	Length of gap
THpm	0.3	mm	Thickness of PM
Wpm	2.4	mm	Width of PM
Hpm	4	mm	Length of PM
Hi	6.4	mm	Height of insulator
Wi	(OD-ID)/2	mm	Width of insulator
THi	THg-TH _{PM}	mm	Thickness of insulator
N	10	–	Number of winding turns
Dw	1.29	mm	Diameter of copper wire
Tcore	3C20	–	Material type of core
Tpm	NdFeB-N35EH	–	Material type of PM

Fig. 2.4(a) shows the B field of the TPI when the DC input current increases from 0 to 8A. It can be observed that the magnitude of B increases with the increase of the DC input current and the TPI core is partially saturated ($B_{sat}=0.35T$) when the DC input current is 7A, i.e. $I_{sat_TPI}=7A$. Fig. 2.4(b) shows the net B field and B vector of the PMTPI core when the DC input current increases from zero to 16A. It can be observed that when the input current is 0, the ferrite core is not saturated by PM itself. When the input DC current increases from 0 to 16A, the net B value first decreases to zero at 5A and the PMTPI core is partially saturated at 14A. When the DC input current is 5A, the fluxes of winding and PM have the same values but in opposite directions, which makes the net flux inside of the PMTPI ferrite core equals to zero. The B vector directions (directions of arrows shown in Fig. 2.4(b)) change to the opposite direction when the DC input current increases from smaller than 5A to larger than 5A. These simulation results show that saturation current of the PMTPI is twice as large as the saturation current of the TPI, i.e. $I_{sat_PMTPI}=14A=2 \cdot I_{sat_TPI}$, which is consistent with the derivation in (2.5).

As described in section 2.3, demagnetization of NdFeB-N35EH PM occurs when a reverse H field larger than $|H_{knee}|$ (1989kA/m at 26.8 °C) is applied to the PM. The PMTPI design has to ensure that the PM is never demagnetized under the maximum input current and maximum temperature. Fig. 2.5 shows the H field distribution of the PM when the DC input current is 20A. It can be observed from Fig. 2.5(a-c) that the maximum H value is 707.79kA/m (which is much smaller than $H_{knee} = 1989$ kA/m). At 100 °C, H_{knee} is calculated based on the temperature coefficient of NdFeB-N35EH [B10] as 1305 kA/m, which is also larger than the applied field of 707.79kA/m at 20A. This indicates that the PM used in the PMTPI design will not be demagnetized when the input current is as high as 20A and the temperature is up to 100 °C. The highest hypothetical temperature the fabricated NdFeB-N35EH is able to work without starting to be at risk of demagnetization is calculated as 164 °C.

2.5 Proof of Concept Experimental Prototype Results

The PMTPI and the TPI with the specifications as in Fig. 2.3 and table 2.1 are fabricated. An air-core TPI (with the same size as PMTPI, to be referred to as Air-core TPI) and a bigger core TPI (with larger ferrite core but with the same inductance and saturation current of the PMTPI, to be referred to as Big-core TPI) are also fabricated for comparison purposes. A DC-DC power converter (as illustrated in Fig. 2.6(a)) with example specifications is also designed and fabricated in order to test and evaluate the PMTPI in an example experimental setup. The fabricated buck power converter has input voltage (V_{in}) of 5V and output voltage (V_o) of 2V (can be adjusted to suite different applications, including those which require output voltages between 0.8V and 3.3V, such as non-isolated bus converters, digital signal processors, memory chips, computer peripherals, and networking equipment [B15-B18]). Other specifications are switching frequency of 300 kHz, input capacitor (C_{in}) and output capacitor (C_o) of 470 μ F and 681 μ F,

respectively. In Fig. 2.6(a), S_u represents the upper power MOSFET (control switch) and S_l represents the lower power MOSFET (synchronous switch). I_o is load current (which is equal to the power inductor DC current). The Air-core TPI, the TPI, the PMTPI and the Big-core TPI are characterized and evaluated as a part of fabricated buck power converter. Fig. 2.6(b) shows the PWM waveforms for upper and lower side power MOSFETs and the waveform measured at the phase node (switching node).

Table 2.2: Comparisons of fabricated power inductors

	Air-core TPI	TPI	PMTPI	Big-core TPI
Core volume(mm ³)	-	787	787	1330
Core weight(g)	-	3.7	3.7	6.9
Total inductor volume (mm ³)	4250	4250	4250	6736
Footprint size(cm ²)	4.01	4.01	4.01	5.39
NdFeB-N35EH PM size (mm ³)	-	-	4×2.4×0.3 =2.88	-
PM weight(g)	-	-	0.0216	-
Winding length(cm)	37	37	37	39
Inductance(μH)	0.26	6.8	6.8	6.7
Saturation current (A)*	-	7	14	13
DCR (mΩ)@ 25 °C	2.5	2.5	2.5	2.6
Inductance density (μH/cm ²)	0.065	1.7	1.7	1.2
Current density (A/cm ²)	-	1.75	3.49	2.41

(*) Saturation current is defined as the DC current with 10% inductance drop

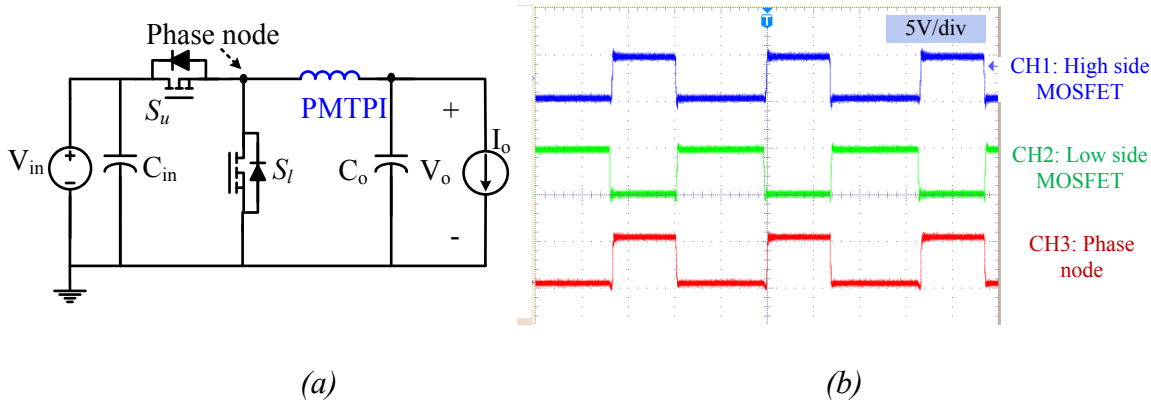
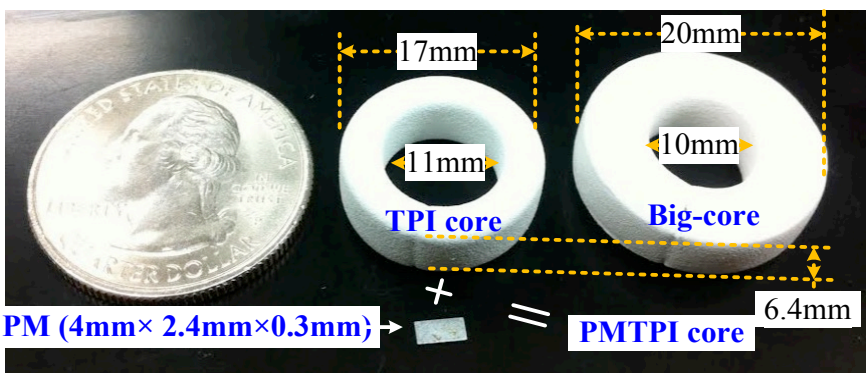
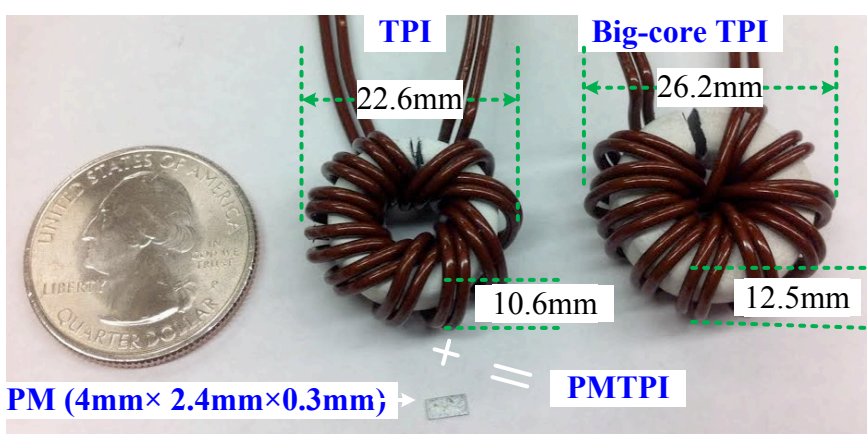


Figure 2.6: (a) Illustrative schematics of the buck power converter with the PMTPI and (b) PWM waveforms and waveform measured at phase node



(a)



(b)

Figure 2.7: Fabricated (a) power inductor cores and (b) power inductors

A. Fabricated Power Inductors

Three of the four fabricated power inductors, the Air-core TPI, the TPI and the PMTPI have the same size. Air-core TPI has a plastic toroid core (non-magnetic core, which has the same permeability as air). The Big-core TPI has a bigger ferrite core and as a result longer winding wires. Fig. 2.7(a) shows the fabricated TPI ferrite core, the Big-TPI ferrite core and the NdFeB-N35EH magnet piece used in PMTPI. Fig. 2.7(b) shows the fabricated TPI and Big-core TPI. The PMTPI is fabricated by simply inserting the PM in the gap of the TPI. This PM magnet has the design specifications as calculated in Section 2.3. The size of the ferrite cores, PM and power inductors are marked on the pictures of Fig. 2.7(b). All of the fabricated inductors have 10 turns of copper winding. Two branches of copper wires are connected in parallel in order to increase the current carrying capability of the power inductor's windings. Some of the most important parameters and measured experimental results for the four fabricated power inductors are summarized in table 2.2 for comparison.

It can be observed from table 2.2 that the sizes and inductance values of the PMTPI and the TPI are the same ($\sim 6.8\mu\text{H}$), but the PMTPI has double of the saturation current compared to the TPI with the same size (14A compared to 7A). The PMTPI has slightly larger inductance ($\sim 6.8\mu\text{H}$) and slightly higher saturation current (14A) compared to Big-core TPI ($\sim 6.7\mu\text{H}$ and 13A), but with 40.8% smaller core size and 46.4% lighter core weight. The volume of the PM (2.88mm^3) is 0.36% of the volume of the PMTPI core (787mm^3). The weight of the PM (21.6mg) is 0.58% of the weight of the PMTPI core. This means that the total weight increase of the PMTPI resulted from the addition of NdFeB-N35EH magnet is negligible. Additional performance evaluation details and comparisons are presented in the following sub-sections.

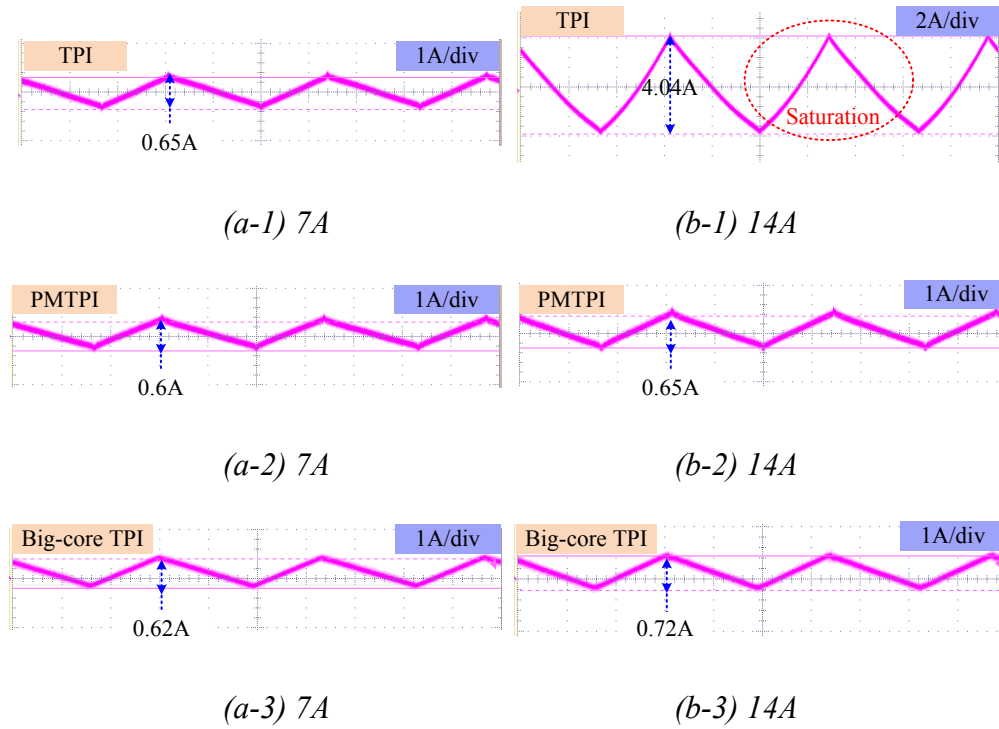


Figure 2.8: Measured current waveforms of the TPI, the PMTPI and the Big-core TPI when power inductor DC input current values are 7A (a-1 to a-3) and 14A (b-1 to b-3)

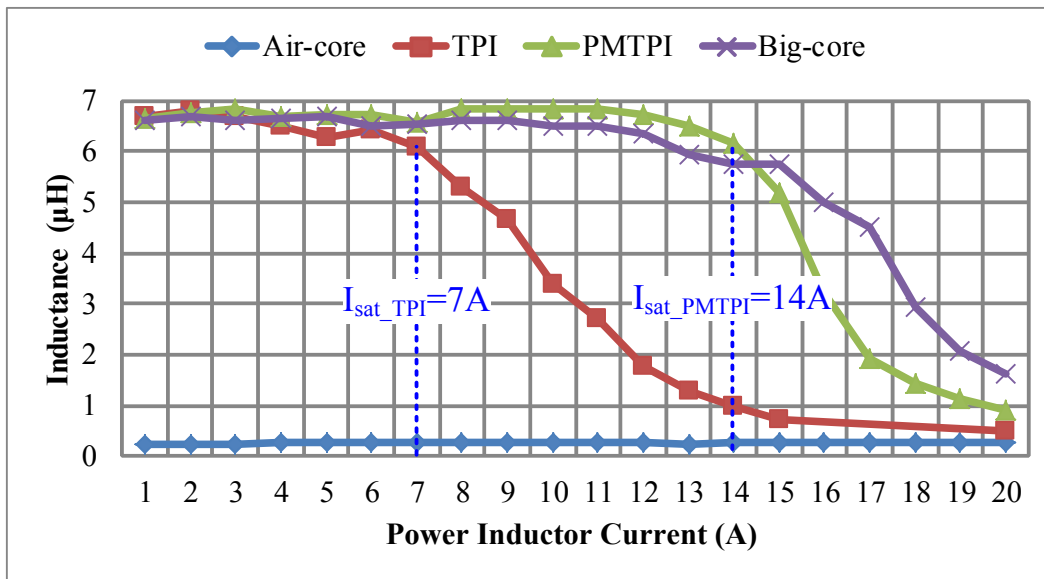


Figure 2.9: Inductance values as a function of power inductor current for the Air-core TPI, the TPI, the PMTPI and the Big-core TPI

Table 2.3: Saturation current of fabricated power inductors

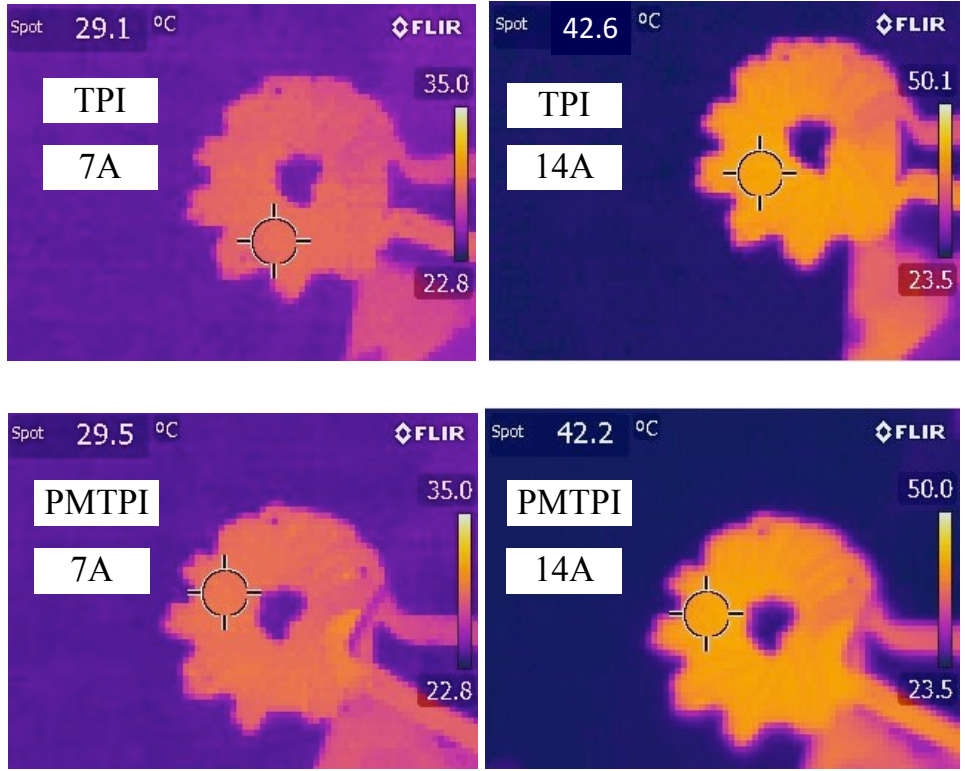
		Air-core TPI	TPI	PMTPI	Big-core TPI
L_{\max} (μH)		0.26	6.8	6.8	6.7
I_{sat} (A)	10% L drop	-	~7	~14	~13
	20% L drop	-	~8	~14.8	~15
	30% L drop	-	~9	~15.5	~17

B. Saturation Current Doubling of The PMTPI

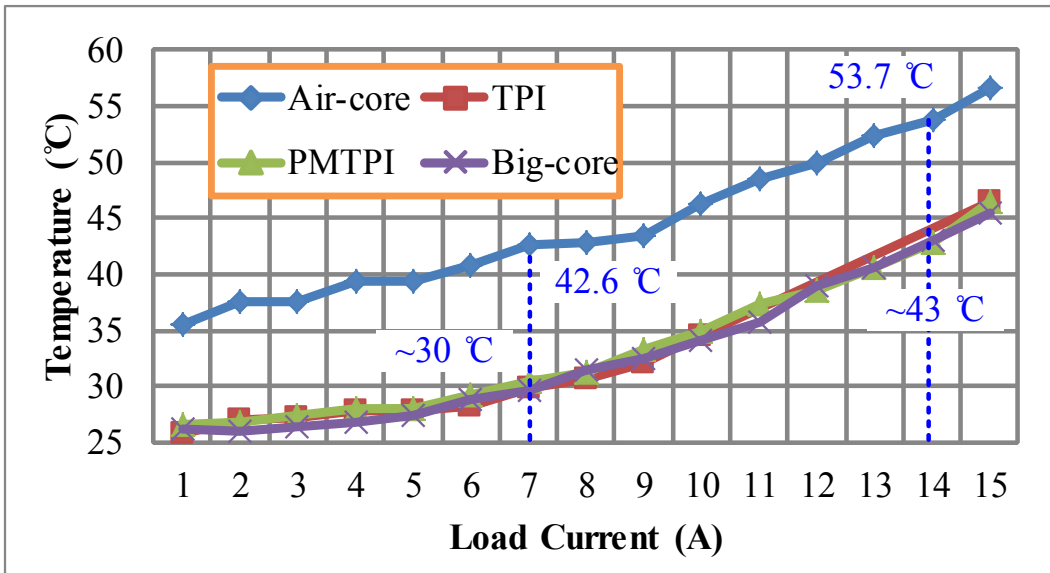
The saturation current values for each of the power inductors are experimentally determined by measuring the drop in the inductance values while increasing the inductor DC current. In other words, the current at which the inductor starts to saturate is detected when the inductance value starts to decrease. The inductor current waveforms are measured and recorded at different current values and then used to calculate the inductance values using (2.10) [B8].

$$L = \frac{(V_{in} - V_{MOS} - V_o)T_{on}}{\Delta i} \quad (2.10)$$

Where, T_{on} is the on time of the upper power MOSFET, V_{MOS} is the voltage drop across the upper power MOSFET and Δi is the peak-to-peak ripple of the inductor current. The measured power inductor current waveform samples are shown in Fig. 2.8. It can be observed that when $I_o=7\text{A}$, Δi of the TPI is the largest (0.65A) and Δi of the PMTPI is the smallest (0.6A), which indicates that the TPI has started to saturate because its inductance value has started to become smaller. When $I_o=14\text{A}$, Δi of the TPI is 4.04A, and the current waveform becomes nonlinear (as in Fig. 2.8(b-1)), which indicates that the current of the TPI is well beyond the saturation current value. On the other hand, Δi of the PMTPI has the smallest value (0.65A), which indicates that addition of PM has prevented the saturation of the PMTPI at higher current values up to 14A.

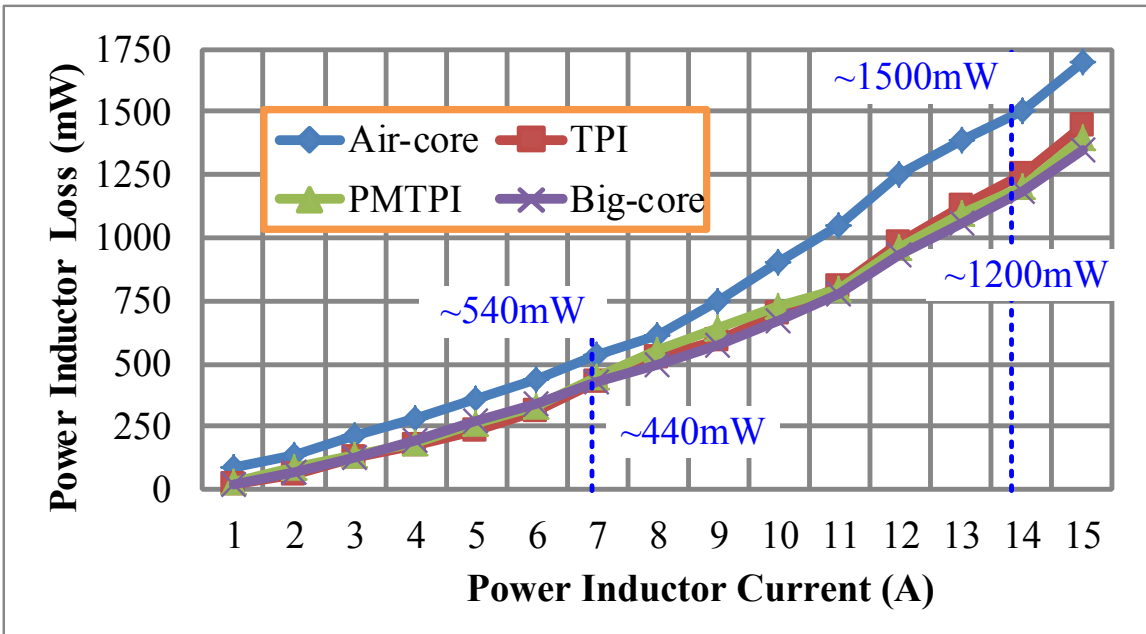


(a) Temperature distribution images

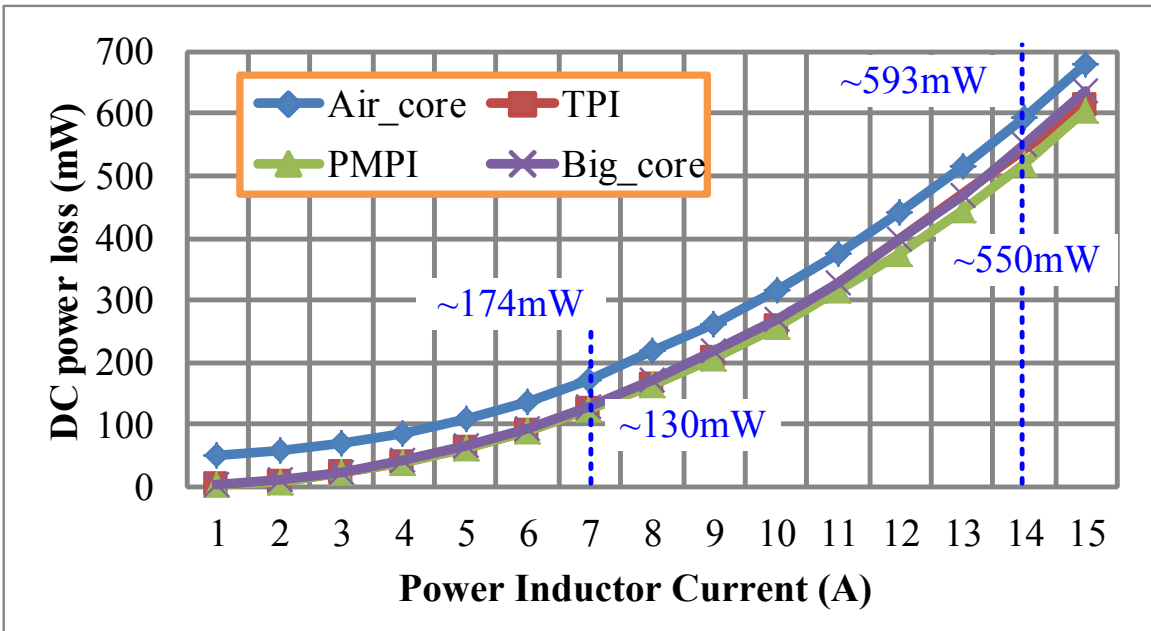


(b) Temperature rise

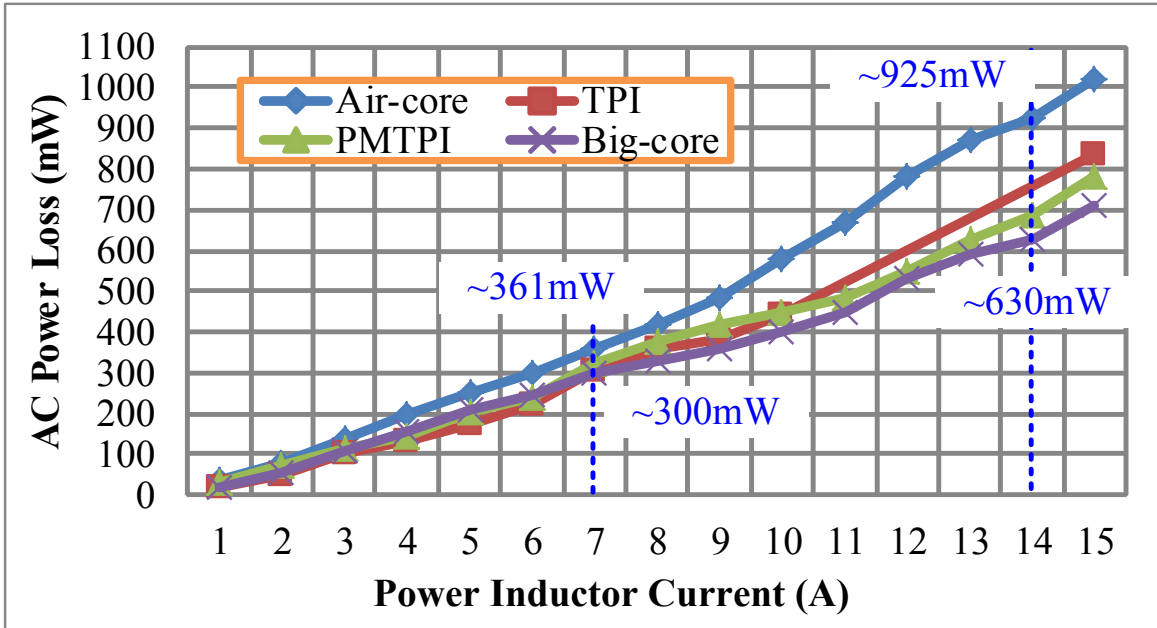
Figure 2.10: (a) Temperature distribution images of TPI and PMTPI when power inductor current is 7A and 14A and (b) temperature as a function of inductor current



(a) Total power inductor losses



(b) Power inductor DC losses



(c) Power inductor AC losses

Figure 2.11: Power inductor losses as a function of current

The inductance values at different power inductor current values (from 1A to 20A) are calculated from the experimentally measured waveforms and are plotted as shown in Fig. 2.9. It can be observed that the Air-core TPI has a constant but the smallest inductance value ($0.26\mu\text{H}$). It is not saturated when the current increases because it does not have a magnetic core. The inductance value of the TPI is nearly constant at $\sim 6.8\mu\text{H}$ when $I_o < 7\text{A}$, i.e. when the current is below the saturation value. The PMTPI's inductance value is nearly constant at $\sim 6.8\mu\text{H}$ when $I_o < 14\text{A}$, i.e. when the current is below the saturation value. This agrees with (2.5) and (2.6) which are derived in Section 2.2. The Big-core TPI's inductance value is nearly constant at $\sim 6.7\mu\text{H}$ when $I_o < 13\text{A}$. The maximum inductance value (L_{max}), the saturation current value (I_{sat}), and the current value at which the inductance drops with a given percentage of L_{max} for each of

the four power inductors are summarized in table 2.3. It can be observed that the TPI, the PMTPI and the Big-core TPI have similar L_{\max} values ($\sim 6.8\mu\text{H}$).

C. Thermal Characteristics

Temperatures of the power inductors at different current values are measured using FLIR T-62101 thermal imaging camera. Sample temperature distribution images of the TPI and PMTPI at selected current values (7A and 14A) are shown in Fig. 2.10(a). Based on the temperature measurement results for the Air-core TPI, the TPI, the PMTPI and the Big-core TPI at various current values (from 1A to 15A), curves for the temperature rise as a function of current are plotted as shown in Fig. 2.10(b). It can be observed that the temperature increases with the increase of current for all power inductors, as expected. The Air-core TPI has the highest temperature at every current value from 1A to 15A. This is because the small inductance value of Air-core TPI ($0.26\mu\text{H}$) leads to large inductor current ripple ($\Delta i \approx 15\text{A}$), which results in higher copper (conduction) power loss. The TPI, the PMTPI and the Big-core TPI have similar temperature rise values. When I_o is less than 11A, the temperature of PMTPI (T_{PMTPI}) is slightly higher than temperature of the TPI (T_{TPI}). For example, when $I_o=7\text{A}$, $T_{\text{PMTPI}}=29.5^\circ\text{C}$ and $T_{\text{TPI}}=29.1^\circ\text{C}$. This is because the NdFeB-N35EH magnet has small resistivity ($\rho_{\text{PM}}=180\mu\Omega\cdot\text{cm}$) and its eddy current loss contributes to the temperature rise of PMTPI. When I_o is larger than 11A, the T_{PMTPI} is slightly smaller than T_{TPI} . For example, when $I_o=14\text{A}$, $T_{\text{PMTPI}}=42.2^\circ\text{C}$ and $T_{\text{TPI}}=42.6^\circ\text{C}$. This is because the saturation of TPI core contributes to larger inductor current ripple and higher power losses. It can be concluded from the results in this sub-section that the addition of NdFeB-N35EH magnet in the PMTPI does not have significant effect on temperature rise.

D. Power Inductor Losses

Power losses in the four different power inductors are measured. The total power inductor losses (P_t) are determined by averaging the instantaneous power dissipation of the inductor over one switching period (T_s). P_t of the Air-core TPI, the TPI, the PMTPI and the Big-core TPI are measured by using Tektronix DPO7104 Digital Phosphor Oscilloscope at various current values ranging from 1A to 15A and are plotted in Fig. 2.11(a). Similar with the trend of the temperature rise, P_t of all power inductors increase when current increases. The Air-core TPI has the highest total loss at every different load current ranging from 1A to 15A. The TPI, the PMTPI and the Big-core TPI have similar P_t at the different current values. When I_o is less than 11A, P_t of PMTPI (P_{t_PMTPI}) is slightly larger than P_t of TPI (P_{t_TPI}). For example, when $I_o=7A$, $P_{t_PMTPI}=450mW$ and $P_{t_TPI}=430mW$. When I_o is larger than 11A, P_{t_PMTPI} is slightly smaller than P_{t_TPI} . For example, when $I_o=14A$, $P_{t_PMTPI}=1200mW$ and $P_{t_TPI}=1250mW$). The variation trends of P_t for all of the four power inductors match the variation trends of the temperature rise discussed in previous sub-section, which is expected.

P_t for each of the four power inductors is composed of DC power losses (P_{DC}) and AC power losses (P_{AC}). DC winding resistance (DCR) of the four fabricated power inductors at 25 °C are measured and are listed in table 2.2. The temperature (T) dependent DCR value is determined from the equation $DCR = DCR_o \cdot (1 + \alpha \cdot (T - T_o))$ [B7], where DCR_o is the DCR at temperature T_o . α is the temperature coefficient of the resistance and for copper (used as power inductor windings) is equal to $3.93 \times 10^{-3}/^{\circ}C$ [B7]. P_{DC} values for the Air-core TPI, the TPI, the PMTPI and the Big-core TPI are calculated from (2.11) [B8] and plotted in Fig. 2.11(b).

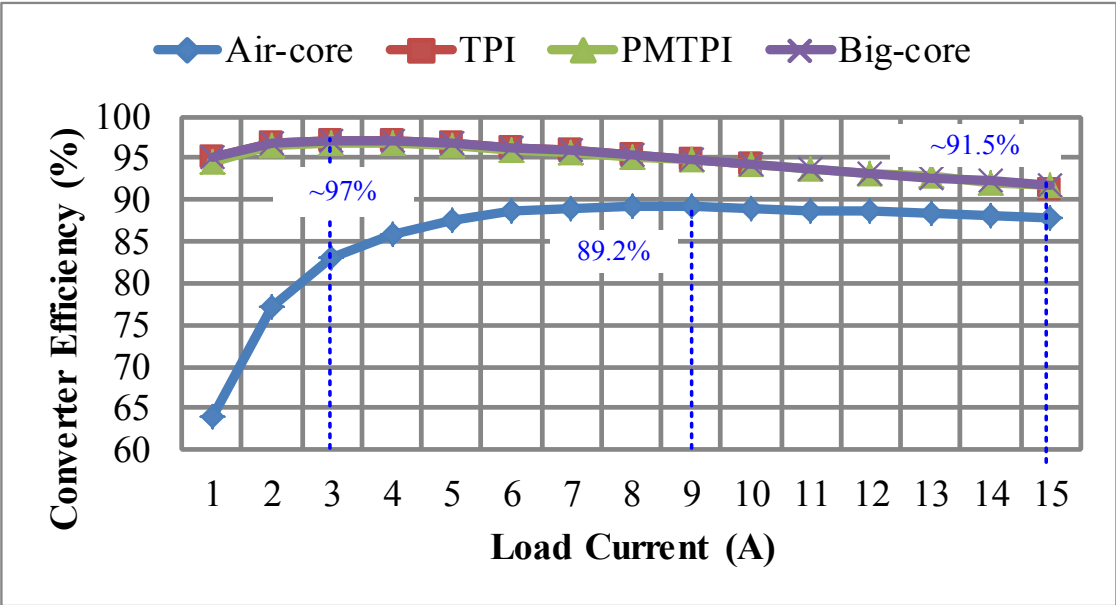
$$P_{DC} = I_{rms}^2 \cdot DCR = (I_o^2 + \frac{\Delta i^2}{12}) \cdot (DCR_o \cdot (1 + \alpha \cdot (T - T_o))) \quad (2.11)$$

Where, I_{rms} is the measured RMS (Root-Mean-Square) value of power inductor current. It can be observed from Fig. 2.11(b) that P_{DC} values of all of the four power inductors increase with the increase of load current. The Air-core TPI has the highest P_{DC} at all current values because it has the largest Δi (~15A) which contributes to larger I_{rms} values at every I_o . Among the other three power inductors with ferrite cores, The Big-core TPI has the largest P_{DC} because it has the longest winding (refer to Table 2.2). The TPI and the PMTPI have similar P_{DC} values because their winding lengths are the same, which is also supported by the fact that they have the same temperature rise.

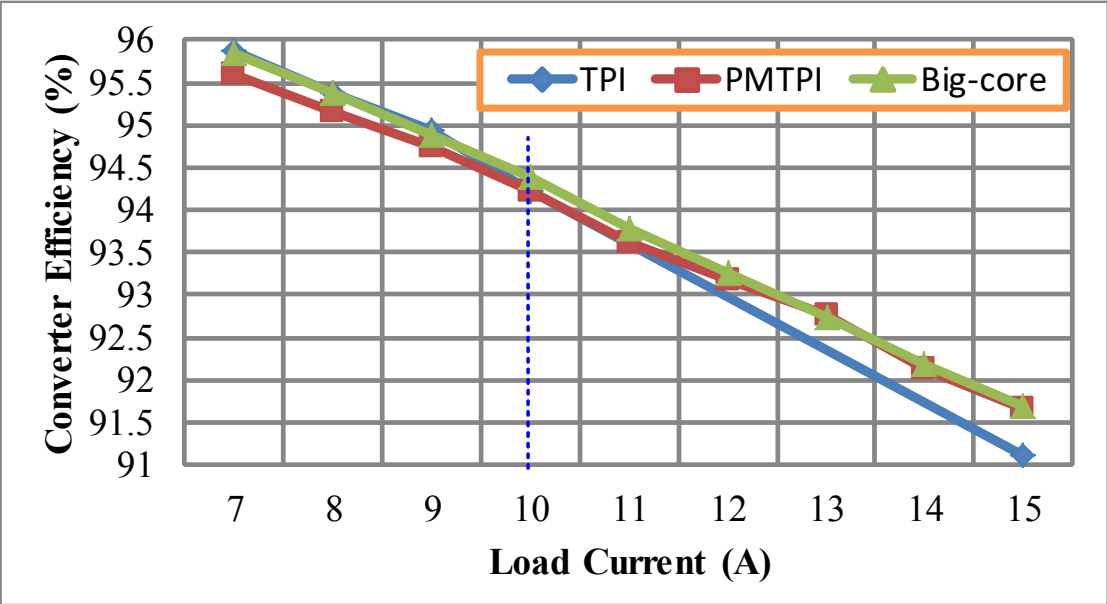
P_{AC} is determined from equation $P_{AC}=P_i-P_{DC}$. P_{AC} is composed of winding AC power loss and core loss. P_{AC} for each of the four power inductors as a function of current is plotted in Fig. 2.11(c). It can be observed that P_{AC} for all of the power inductors increases with the increase of current. The Air-core TPI has the highest P_{AC} due to its largest Δi (~15A). Among the three power inductors with ferrite cores, the Big-core TPI has the smallest P_{AC} due to its largest core size (refer to Table 2.2). The TPI and the PMTPI have the same P_{AC} when $I_o < 11A$. When $I_o \geq 11A$, P_{AC} of the TPI is larger than P_{AC} of the PMTPI because the TPI's core has been saturated. It can be concluded from this sub-section that the addition of the NdFeB-N35EH magnet does not have significant effect on the power losses.

In general, for any gapped power inductor (with or without permanent magnet), the “leakage loss” in the air gap increases as the switching frequency increases [B13, B19-B20]. As the switching frequency increases, the winding proximity effect loss caused by fringing flux in the vicinity of the air gap increases [B19-B20]. The eddy current loss of the permanent magnet piece [B13] might also increase. However, this loss is usually very small compared to the other power losses including the core loss. When designing a power inductor for higher switching

frequency, reducing this loss needs to be taken into consideration while optimizing the overall design.



(a) $0 \leq I_o \leq 15A$



(b) $7A \leq I_o \leq 15A$

Figure 2.12: Buck converter efficiencies (considering driver losses) as a function of load current

E. Total Power Converter Efficiency

The power efficiency (η) of the buck power converter with each of the four power inductors is evaluated in this sub-section. η is determined from (2.12) and is plotted as a function of load current as shown in Fig. 2.12. Both the power stage losses and the driver loss (P_{driver}) are included in the efficiency calculations.

$$\eta = \frac{P_{out}}{P_{in} + P_{driver}} = \frac{V_o \cdot I_o}{V_{in} \cdot I_{in} + V_{driver} \cdot I_{driver}} \quad (2.12)$$

Where, V_{driver} and I_{driver} are voltage and current supplied to driver IC, respectively. It can be observed from Fig. 2.12(a) that the buck power converter with the Air-core TPI (η_{air}) has the lowest efficiency and the buck converters with the rest of the three power inductors have almost the same efficiency. The value of η_{air} peaks at 89.2% when $I_o=9A$ and the efficiencies of buck converter with the TPI (η_{TPI}), with the PMTPI (η_{PMTPI}) and with the Big-core TPI (η_{big}) peak at ~97% when $I_o=3A$. It should be noted that because the switching frequency value and inductance value used are same when experimentally evaluating each of the ferrite power inductors, the switching and conduction losses in the switches of the buck converter are almost the same when the efficiency curves of Fig. 2.12 are recorded.

A zoomed in view of the efficiency curves when $7A \leq I_o \leq 15A$ are shown in Fig. 2.12(b). It is shown that when $I_o < 10A$, η_{TPI} has the largest value but only 0.3% higher than the η_{PMTPI} (e.g. when $I_o=7A$, $\eta_{TPI}=95.87\%$, $\eta_{PMTPI}=95.60\%$ and $\eta_{big}=95.85\%$). When $I_o > 10A$, η_{big} and η_{PMTPI} have almost the same value and both of them are larger than η_{TPI} (e.g. when $I_o=15A$, $\eta_{TPI}=91.11\%$, $\eta_{PMTPI}=91.66\%$ and $\eta_{big}=91.70\%$).

The experimentally measured temperature rise results shown in Fig. 2.10 provide additional support in addition to the experimentally measured efficiency. This is because it can be concluded that since the temperature rise values of the PMTPI are the same as for the other

ferrite power inductors used for comparison, the PMTPI does not have larger total power loss. Therefore, it can be concluded that the PMTPI is able to double the saturation current (from 7A to 14A) while maintaining the same inductance value and the same size without negatively impacting the power converter efficiency.

2.6 Summary

This chapter presents the concept, design and experimental evaluation of a high current PI with NdFeB permanent magnet. Experimental results show that the PMTPI has twice the saturation current with the same size and the same inductance compared with the TPI. On the other hand, compared to the Big-core TPI design without a PM which has larger size in order to obtain the same saturation current and inductance value as the PMTPI design, the PMTPI's core weight is less by 46.4% and its core size is less by 40.8%. The addition of the fabricated NdFeB-N35EH magnet in the core gap of the PMTPI does not increase its total size and the increase in weight is negligible (only 0.58%). Moreover, the PM does not cause significant additional temperature rise and does not affect the efficiency of the power converter.

For different applications such as those with higher power and/or higher frequency, the design methodology and guidelines presented in this manuscript still apply. If higher saturation current is desired, the size and $(BH)_{\max}$ of the PM might increase accordingly and lamination of PM might be required to reduce its eddy current loss.

CHAPTER 3

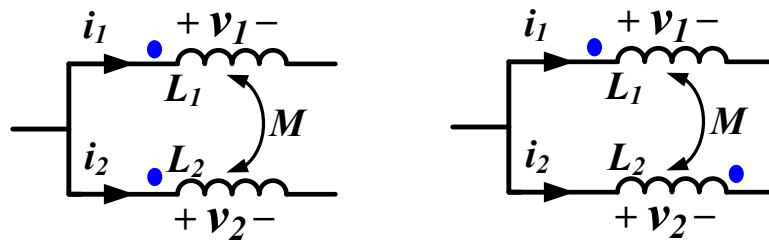
PERMANENT MAGNET COUPLED POWER INDUCTOR FOR MULTI-PHASE DC-DC POWER CONVERTERS

3.1 Introduction

The concept of the permanent magnet power inductor (PMPI) not only doubles the saturation current for a single phase PI, but also reduces its volume and weight significantly as discussed in chapter 2. However, the structure realization and performance of coupled power inductor (CPI) with PM (PMCI) have not been investigated in the literature before, which is a main objective of this chapter.

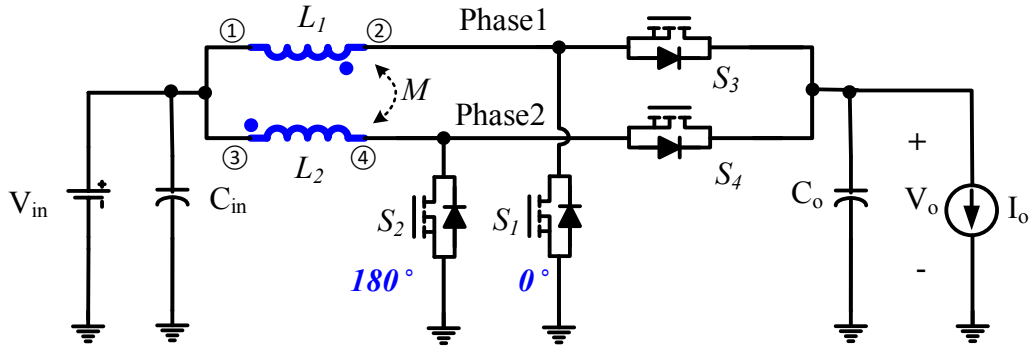
$$\begin{cases} v_1 = L_1 \frac{di_1}{dt} + M \frac{di_2}{dt} \\ v_2 = M \frac{di_1}{dt} + L_2 \frac{di_2}{dt} \end{cases} \quad (3.1.1)$$

$$\alpha = \frac{M}{L_s} \quad (3.1.2)$$

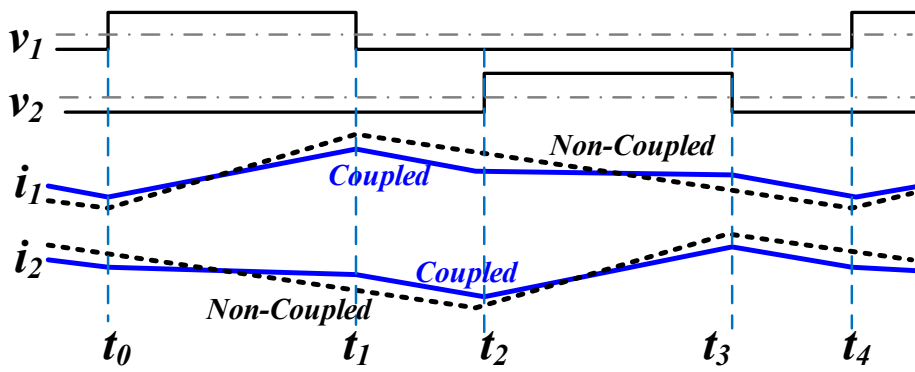


(a) direct coupling

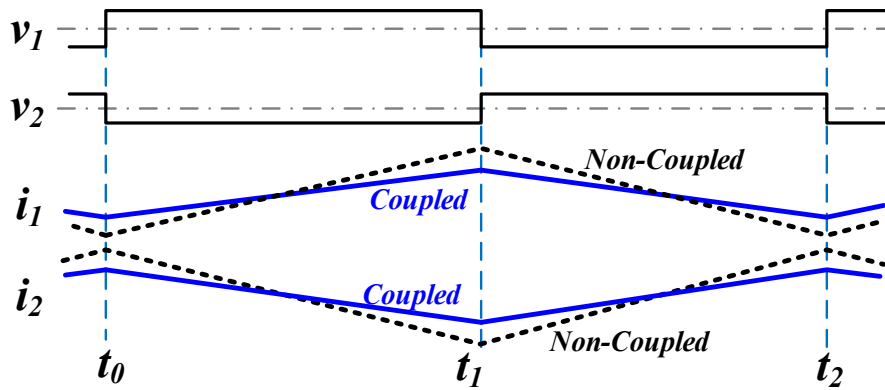
(b) inverse coupling



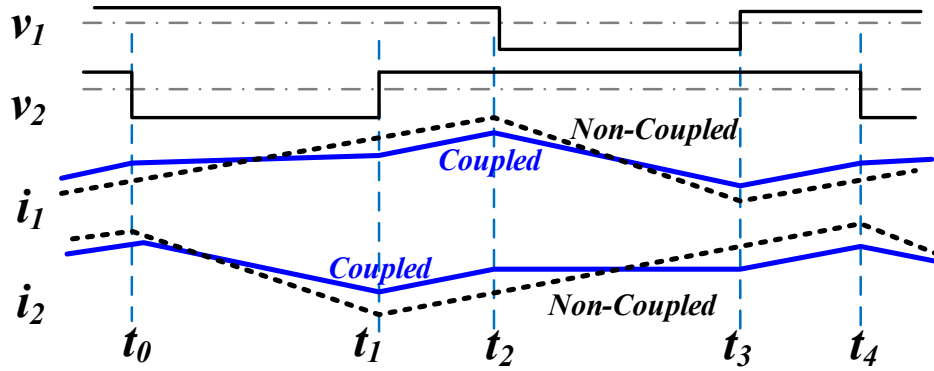
(c) schematic of a boost converter using inversely coupled CPI



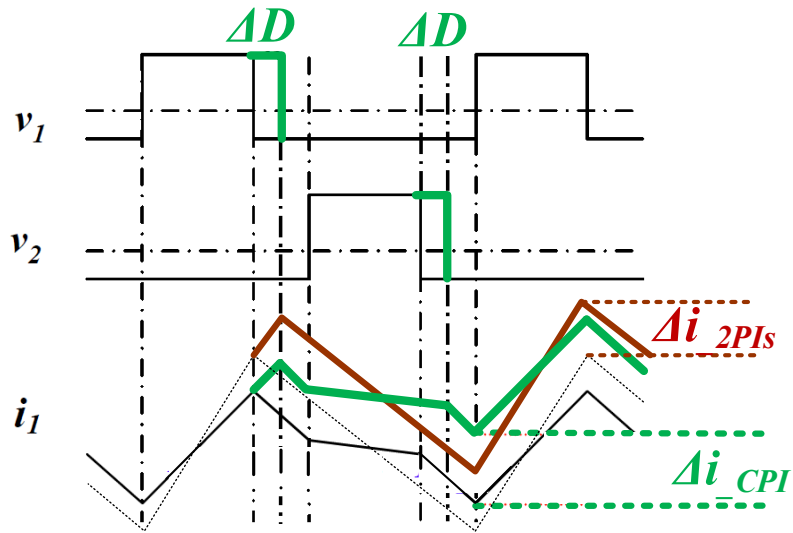
(d) $D < 0.5$



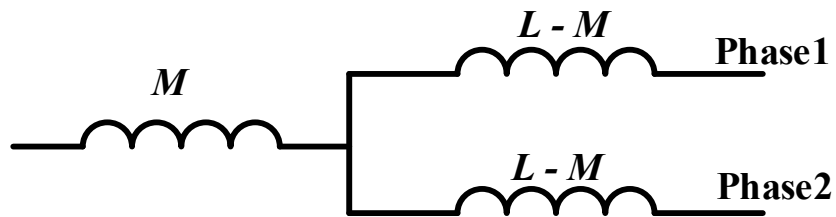
(e) $D = 0.5$



(f) $D > 0.5$



(g) transient operation



(h) equivalent circuit of transient inductance

Figure. 3.1: Coupled inductor and its operation in two-phase boost converter.

In a two-phase CPI, the two coupling types are illustrated in Fig. 3.1(a)-(b), where $L_l = L_2 = L_s$ is self-inductance and M is mutual inductance. Both types can be described by (1-1), where v_1 and v_2 are the voltages applied to the two corresponding windings of the CPI as shown in Fig. 3.1 (a-b). Coupling factor α is determined by (1-2). Both M and α are positive for the direct coupling and negative for the inverse coupling. Inversely coupled CPI is used in multi-phase power converters [C1-C9]. Fig. 3.1(c) illustrates the utilization of the CPI in a two-phase boost power converter. Instead of using two separate PIs for two phases, only one CPI with two coupled windings is needed, which helps to reduce the total volume occupied by power inductors and therefore results in a power converter with higher power density. The volume reduction of the CPI is because 1) two separate inductors are integrated into one core structure which reduces footprint, and 2) the inverse coupling results in flux cancellation, which increases the saturation current of the CPI or equivalently reduces volume.

In order to review the advantage of using the CPI in a multi-phase DC-DC power converter, the operation of the example boost converter using CPI is briefly summarized next in this section. Note that detailed operations for both multi-phase buck converter and boost converter using coupled inductor have been extensively presented in the literature [C1-C9]. Fig. 3.1(d)-(f) show the steady state operation waveforms of the DC-DC power converter with a CPI when the duty cycle $D < 0.5$, $D = 0.5$ and $D > 0.5$. Control signal of S_1 and S_2 are 180° out of phase. S_1 and S_3 are turned on and off complementary, and S_2 and S_4 are turned on and off complementary as well. Consider the case when $D < 0.5$ as an example, during the time interval $t_0 \sim t_1$, S_1 is turned on and S_2 is turned off, and the inductor current i_1 of Phase 1 rises (inductor is charged) and inductor current i_2 of Phase 2 decreases (inductor is discharged), but slopes of i_1 and i_2 are smaller while using CPI compared to the non-coupled case because of the effect of the

inverse coupling. During the time interval $t_1 \sim t_2$, both S_1 and S_2 are turned off, and the slopes of the two inductor currents in the two phases are the same when using CPI and when using two separate PIs that are not coupled. During the time interval $t_2 \sim t_3$, S_1 is turned off and S_2 is turned on, i_1 decreases and i_2 rises, but slopes of i_1 and i_2 are smaller when using CPI compared to the non-coupled case because of the inverse coupling. During the time interval $t_3 \sim t_4$, both S_1 and S_2 are turned off again and the slope of inductor currents are the same again. In a complete switching cycle, the peak-to-peak value of the inductor current ripple is smaller when using a CPI than when using two separate PIs because of inverse coupling. This is the case when $D < 0.5$, $D = 0.5$ and $D > 0.5$, i.e. the current ripple can be smaller under different duty cycle value. The amount of decrease in the steady state inductor current ripple is dependent on both the duty cycle value and the coupling factor value [C1-C9]. The equivalent steady state inductance (L_{SS}) of a CPI is the inductance measured between the two terminals (① and ②) for L_1 , (③ and ④) for L_2 as illustrated in Fig. 3.1(c) for each phase of CPI, which can also be determined by (2-1), where T_{on} is the on time of the control MOSFET, i.e. S_1 and S_2 in Fig. 3.1(c), and Δi is the peak-to-peak ripple of the inductor current for each phase. The smaller steady state inductor current ripple values of the two-phase boost converter while using CPI, as illustrated in Fig. 3.1(d)-(f), show that using CPI results in larger equivalent steady state inductance than using non-coupled inductors. This is advantageous for smaller steady-state inductor current ripple and higher power efficiency. Note that the average inductor currents, or DC component, of i_1 and i_2 are tuned by a closed-loop controller to be equal, as illustrated in Fig. 3.1(d)-(f) in order to equally distribute the thermal stress between two phases.

$$L_{SS} = \frac{V_{in} T_{on}}{\Delta i} \quad (3.2.1)$$

$$L_{tr} = (1 + \alpha)L_S \quad (3.2.2)$$

Fig. 3.1(g) illustrates an example case during transient operation where duty cycle is perturbed by the amount ΔD by the closed-loop controller that regulates the output voltage and maintains equal current distribution between the phases. The resulted amount of change in the average inductor current is determined by an equivalent inductance, which is referred to as equivalent transient inductance (L_{tr}). Fig. 3.1(h) illustrates the equivalent circuit of the transient inductance of a CPI, from which the per-phase L_{tr} is derived in (3.2.2) [C3]. The amount of the change in inductor current when using a CPI (Δi_{CPI} in Fig. 3.1(g)) is larger than it is when using two separate PIs (Δi_{2PIs} in Fig. 3.1(g)). This is because the CPI has a transient inductance value that is smaller than the steady-state inductance value (for a PI with no coupling, the steady-state inductance and the transient inductance are equal). This implies that using a CPI allows for achieving faster dynamic/transient response compared to when using two non-coupled PIs, which is an advantage. To summarize, because an inversely coupled CPI can be designed with the same or larger steady-state inductance compared to two non-coupled PIs while maintaining smaller transient inductance, a power converter can potentially achieve higher efficiency and/or improved transient response. Note that during a design process and optimization of a switching power converter, the designer faces a tradeoff when selecting the inductance value of the power inductor. Larger inductance supports higher efficiency while smaller inductance supports faster transient/dynamic response to load variations while achieving smaller size.

This chapter presents and investigates a structure for permanent magnet coupled power inductor (PMCI), which utilizes a PM to either double the saturation current or equivalently reduces the size and weight of the CPI (or a mix of both). . A PMCI with NdFeB-N35EH PM is developed, fabricated and experimentally evaluated in a 4V/8V DC-DC boost power converter.

Operation principle and magnetic circuit model of the PMCI, and the dimensions of the required PM are theoretically devised and used as design guidelines. 3-D physical model simulation results are used to “visualize” the saturation current doubling of the PMCI. Experimental results validate the developed method. This chapter considers all of design metrics for power inductors including tradeoffs between size, efficiency, inductance density, and saturation current when evaluating the PMCI and comparing it to other power inductors.

The method of inductor core biasing using an extra winding with controllable current, as presented in [C10], can control the inductance values of the inductor under different operation states and achieve saturation current increase. However, the needed extra winding, power source/circuit, and fast controller to adjust the biasing leads to added size, weight, and power losses. On the other hand, The PMCI is able to double the saturation current or equivalently reduce the inductor size significantly without size increase and with negligible weight increase and power loss increase because of the PM. While the extra winding based inductor core biasing requires a high speed controller which controls the injected DC flux for the inductor instantaneously when load varies or during fast load transient (which increases its design complexity), the PMCI does not require control. The PMCI maintains all the advantages of using an inversely coupled power inductor (CPI) in a two-phase DC-DC power converter including high steady-state inductance to transient inductance ratio for higher power efficiency and reduced transient inductance to improve the transient performance while achieving smaller size and weight or higher saturation current.

3.2 Concepts and Theoretical Analysis

A. Structure and Operation Principle of PMCI

Fig. 3.2(a) illustrates the front view diagram of the conventional CPI with EE core

structure. There are three gaps in each inductor, i.e. central gap g_c , left side gap g_1 and right side gap g_2 . Using airgaps in a CPI core helps to 1) increase the saturation current as it is the case in single phase power inductors, and 2) tune the coupling factor between the two phases because coupling factor is dependent on the dimensions of airgaps in the central leg and the side legs. A larger central leg airgap and smaller side leg airgaps lead to a larger coupling factor magnitude, and vice versa. The per-phase input currents I_{DC1} and I_{DC2} and their directions are marked in Fig. 3.2(a) (shown on each of the side legs of the core). The fluxes generated by winding1 and winding2 are represented by the dashed arrowed green line and dotted arrowed orange line, respectively. Fig. 3.2(a) shows that the fluxes of winding1 and winding2 partially cancel with each other in two side legs, resulting in inverse coupling between two phases of a CPI and contributes to the size reduction of the CPI. Fig. 3.2(a) also shows that part of fluxes of winding1 and winding2 superimpose in the central core leg, leading to the saturation of the CPI core when per phase winding current reaches to a certain level, which is referred to as saturation current. If a DC magnetic flux source is added in the central leg of the CPI such that winding fluxes can be partially/fully canceled, then the saturation current of the CPI can be increased. A piece of PM is able to provide the required DC magnetic flux source.

By placing a small piece of PM in the central gap of the CPI, a PMCI is obtained as illustrated in Fig. 3.2(b). The PM needs to have properties as will be described in Section 3.2.C. The dash-dotted arrowed white line denotes the flux path generated by the PM. The PM needs to be placed in the correct polarities such that its flux loops and winding flux loops are in opposite directions. As a result, the winding fluxes and the PM flux partially or completely cancel out, resulting in a significant increase in the saturation current compared to the CPI. When the PMCI is well designed, its saturation current can potentially be doubled compared to a conventional

CPI. Due to the PM flux cancellation effect in addition to the windings' flux cancellations, PMCI can achieve more size reduction compared with CPI.

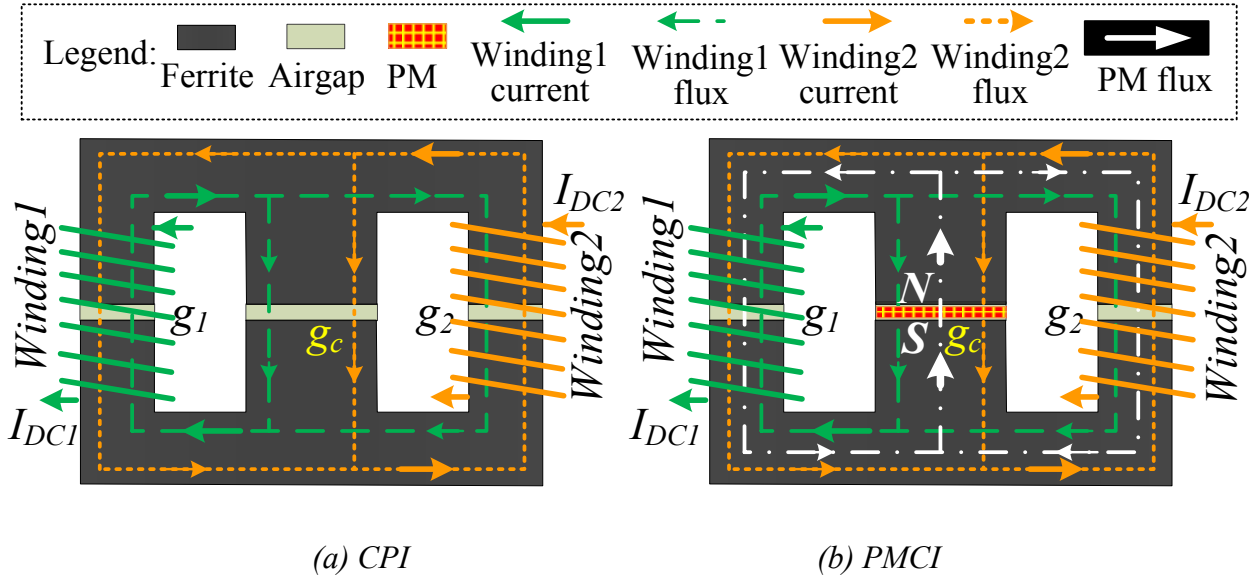


Figure. 3.2: Schematic diagram of core structure and DC flux lines in (a) CPI and (b) PMCI core (front view).

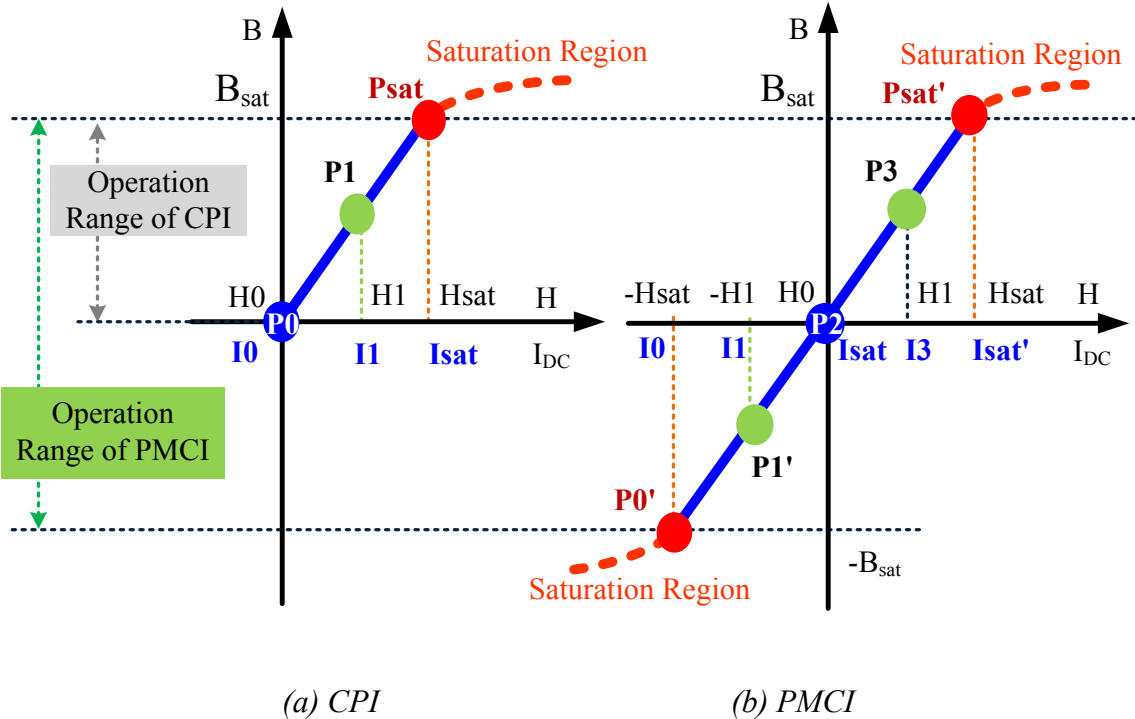
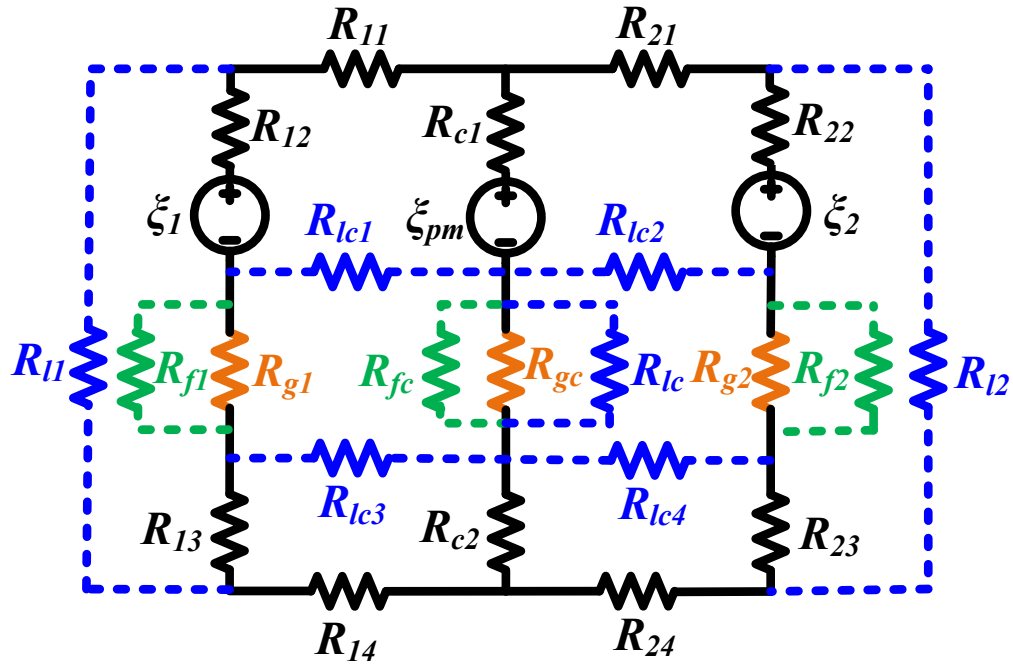
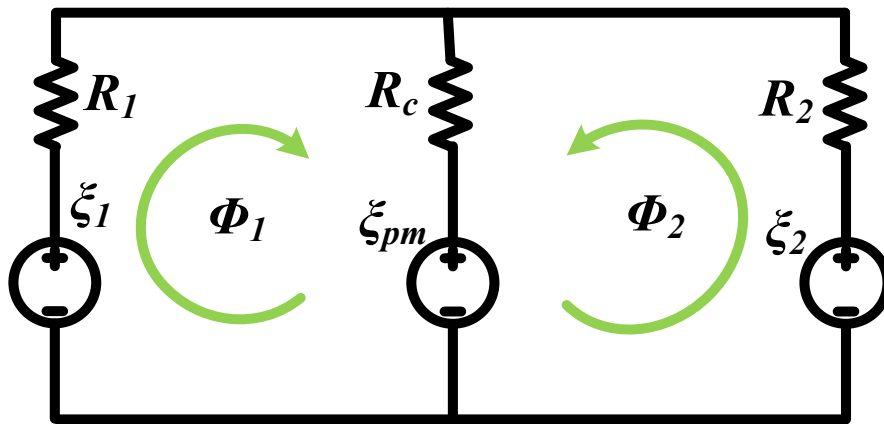


Figure. 3.3: Operation range of (a) CPI and (b) PMCI core on BH curve

Fig. 3.3 illustrates the operation range of CPI core and PMCI core on their BH curves, where hysteresis characteristics for the magnetic core material are neglected in this principle analysis. Same core material is used in the CPI and the PMCI for fair comparison. It is known that the magnetic flux density $B = \mu \cdot H$, where μ is magnetic permeability of the material and H is the applied magnetic field. H is directly proportional to the per phase winding current. B_{sat} is the saturation flux density of the magnetic core material, H_{sat} is the corresponding magnetic field and I_{sat} is the corresponding saturation current. In Fig. 3.3, a series of points including P0, P1, Psat, P0' , P1' , P2, P3 and Psat' denote the operation points of the CPI and the PMCI for different I_{DC} values including I_0, I_1, I_{sat}, I_3 and I_{sat}' . When $I_{DC} = I_0 = 0$, CPI core operates at P0 with zero flux density while PMCI core operating at P0' with flux density value of $-B_{sat}$ because the PM flux exists. This means that the PMCI core is pre-biased by using the PM to its $-B_{sat}$ point when the input current is zero. When $I_{DC} = I_{sat}$, CPI core operates at Psat and starts to saturate while PMCI core operating at P2 with zero net flux density. The zero net flux density is resulted from the flux cancellation between the winding fluxes and the PM flux because they are in opposite directions as illustrated in Fig 3.2(b). When $I_{DC} = I_{sat}' = 2 \times I_{sat}$, CPI core is deeply/highly saturated while PMCI core is just starting to saturate. It can be observed from Fig. 3.3 that the operation range of the CPI core is limited in the first quadrant on the BH curve, while the PMCI core extends its operation range into the third quadrant because of the PM flux cancellation effect. As a result, the PMCI core has twice the operation range compared with the CPI core. This results in the effect of saturation current doubling, i.e. $I_{sat_PMCI} = 2 \times I_{sat_CPI}$, which is further analyzed in the next part of this section based on the magnetic circuit model and is verified by using ANSYS®/Maxwell® 3D physical model simulation results as shown in section 3.3 and the experimental results presented in section 3.4.



(a)



(b)

Figure 3.4: Magnetic circuit models of the PMCI: (a) complex model and (b) simplified model.

B. Magnetic Circuit Model Analysis

The magnetic circuit model for the presented PMCI illustrated in Fig. 3.2(b) is shown in Fig. 3.4. In the complex model shown in Fig. 3.4(a), R_{11} , R_{12} , R_{13} , R_{14} , R_{21} , R_{22} , R_{23} , R_{24} , R_{c1} and R_{c2} are reluctances of magnetic core legs. R_{l1} , R_{l2} , R_{lc} , R_{lc1} , R_{lc2} , R_{lc3} and R_{lc4} are leakage

reluctances. R_{g1} , R_{g2} and R_{gc} are reluctances of air gaps. R_{f1} , R_{f2} and R_{fc} are fringe reluctances of three gaps. Calculations of fringe reluctances and leakage reluctances of the power inductors are discussed in [C6]. Fig. 3.4(a) can be simplified as shown in Fig. 3.4(b). $\zeta_1 = N_1 I_1$ and $\zeta_2 = N_2 I_2$ are magnetomotive force (MMF) of winding1 and winding2, respectively. Φ is the magnetic flux and N is the number of winding turns. ζ_{pm} is the MMF of the PM. R_{lc1} , R_{lc2} , R_{lc3} and R_{lc4} are much larger than the other reluctance values and can be treated as if they each is equal to infinity. The rest of the reluctances are grouped into R_1 , R_2 , and R_c as given by (3.3.1).

$$\begin{cases} R_1 = R_{11} + (R_{12} + R_{13} + (R_{g1} \parallel R_{f1})) \parallel R_{l1} + R_{14} \\ R_2 = R_{21} + (R_{22} + R_{23} + (R_{g2} \parallel R_{f2})) \parallel R_{l2} + R_{24} \\ R_c = R_{c1} + R_{c2} + (R_{gc} \parallel R_{fc} \parallel R_{lc}) \end{cases} \quad (3.3.1)$$

Reluctance values are determined by (3.3.2), where l_e and A_e are the effective length and effective cross section area of the magnetic flux path, respectively. $\mu_e = \mu_r \mu_o$ is the effective permeability, μ_r is relative permeability and μ_o is the vacuum permeability.

$$R = \frac{l_e}{\mu_e A_e} = \frac{l_e}{\mu_r \mu_o A_e} \quad (3.3.2)$$

Inductance can be calculated from $L = \lambda/i = N^2/R$, where λ is flux linkage [C11]. Self-inductance (L_s) for each phase is determined next. When winding1 exists alone, i.e. ζ_{pm} and ζ_2 are shorted, the equivalent reluctance R_{eq1} is calculated as given by (3.4.1). When winding2 exists alone, i.e. ζ_{pm} and ζ_1 are shorted, the equivalent reluctance R_{eq2} is calculated as given by (3.4.2).

$$R_{eq1} = (R_1 + R_c \parallel R_2) = \frac{R_1(R_c + R_2) + R_c R_2}{R_c + R_2} \quad (3.4.1)$$

$$R_{eq2} = (R_2 + R_c \parallel R_1) = \frac{R_2(R_c + R_1) + R_c R_1}{R_c + R_1} \quad (3.4.2)$$

Symmetrical structure for CPI is widely used in multi-phase power converters [C1-C9] and thus is further discussed in this chapter. In a symmetrical structure, $N_1 = N_2 = N$ and $R_1 = R_2 = R$. Accordingly, R_{eq1} and R_{eq2} are simplified as given by (3.5).

$$R_{eq} = R_{eq1} = R_{eq2} = \frac{R(2R_c + R)}{R_c + R} \quad (3.5)$$

Self-inductances for phase1 and phase2 can then be determined from (3.6). When compared to the CPI, the side leg reluctances R_1 and R_2 of the PMCI remain unchanged. However, R_{gc} is affected by the PM. The permeability of the PM material (the relative permeability of NdFeB magnet is ~ 1.05) is only slightly higher than the permeability of the air. This means that the R_c value of the CPI and the R_c value of the PMCI are almost the same, but R_c is slightly higher for the PMCI because of the PM. As a result, the self-inductance values of the CPI and the PMCI are almost equal but the PMCI has slightly larger inductance as a result of placing the PM in the central leg gap of the PMCI core.

$$L_S = L_{S1} = L_{S2} = \frac{N^2}{R_{eq}} = \frac{N^2(R_c + R)}{R(2R_c + R)} \quad (3.6)$$

Mutual inductance can be calculated from (3.7) [C11].

$$M = M_{12} = \frac{N_1 \Phi_{12}}{I_2} = \frac{N_2 \Phi_{21}}{I_1} = M_{21} \quad (3.7)$$

Where Φ_{12} is the magnetic flux generated by I_2 that passes through winding1, and Φ_{21} is the magnetic flux generated by I_1 that passes through winding2. From Fig. 3.4(b), Φ_{12} and Φ_{21} are derived as given by (3.8).

$$\Phi_{12} = \Phi_{21} = \frac{NI}{R_{eq}} \frac{R_c}{R + R_c} = NI \frac{R_c}{R(2R_c + R)} \quad (3.8)$$

Based on (3.7) and (3.8), mutual inductance is derived as in (3.9). The negative sign in

(3.9) comes from the inverse coupling between phase1 and phase2.

$$M = M_{12} = M_{21} = -\frac{N^2 R_c}{R(2R_c + R)} \quad (3.9)$$

The coupling factor (α) of the PMCI is derived as in (3.10).

$$\alpha = \frac{M}{L_s} = -\frac{R_c}{R_c + R} \quad (3.10)$$

It can be observed from (3.9) and (3.10) that the mutual inductance and coupling factor values of CPI and PMCI are also the same. In order to derive the saturation current of CPI and PMCI, Fig. 3.4(b) is transformed into Fig. 3.5. By using Kirchhoff's Voltage Law (KVL), (3.11) can be derived from circuit models shown in Fig. 3.5.

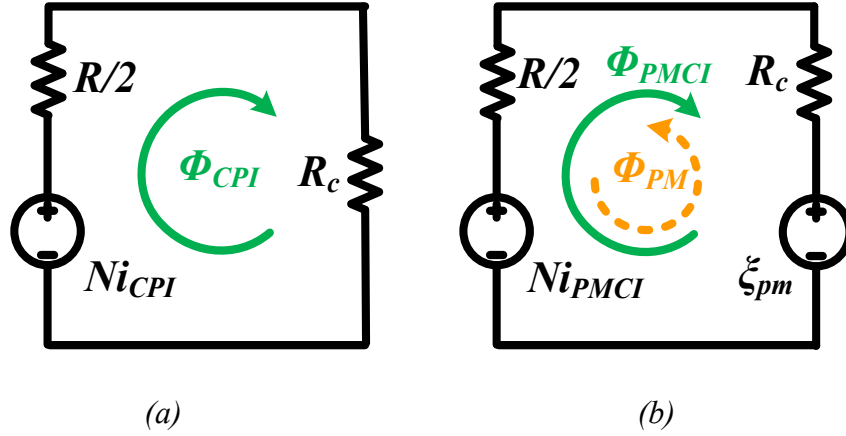


Figure 3.5: Transformed magnetic circuit model of (a) CPI and (b) PMCI.

$$Ni_{CPI} = \Phi_{CPI} \left(R_c + \frac{R}{2} \right) \quad (3.11.1)$$

$$Ni_{PMCI} - \xi_{pm} = (\Phi_{PMCI} - \Phi_{PM}) \left(R_c + \frac{R}{2} \right) \quad (3.11.2)$$

For the CPI and PMCI cores with effective cross section area of A_e , the total flux in the ferrite core is $\Phi = B \cdot A_e$, where B is the flux density in the magnetic core. Per phase saturation

current of the CPI and PMCI are derived as in (3.12), where B_{sat} is the saturation flux density of the power inductor core material.

$$I_{sat_CPI} = \frac{B_{sat} A_e (R_c + \frac{R}{2})}{N} \quad (3.12.1)$$

$$I_{sat_PMCI} = \frac{B_{sat} A_e (R_c + \frac{R}{2}) + \xi_{pm}}{N} \quad (3.12.2)$$

In the PMCI design, ξ_{pm} has to satisfy $0 < \xi_{pm} \leq N \cdot I_{sat_CPI}$ to ensure the magnetic core is not saturated by the PM itself when winding current is zero. When $\xi_{pm} = N \cdot I_{sat_CPI}$, (3.12.2) can be rewritten as (3.13), which shows that the per phase saturation current of the PMCI can be twice as large as the saturation current of the CPI with same windings and same magnetic core (indicating the same inductance, same size and same weight).

$$I_{sat_PMCI} = \frac{B_{sat} A_e (R_c + \frac{R}{2})}{N} + I_{sat_CPI} = 2 \cdot I_{sat_CPI} \quad (3.13)$$

C. Permanent Magnet Design for PMCI

In the PMCI design, PM design is a critical step in order to achieve the saturation current doubling without reducing the inductance value. The PM used in the PMCI should have a BH characteristic with a wide hysteresis loop as shown in Fig. 3.6. The intrinsic curve represents the intrinsic magnetization $4\pi M$ (in Gaussian units) as a function of applied magnetic field (H). The normal curve represents B as a function of H . $B = \mu \cdot H = \mu_o \cdot \mu_r \cdot H$ and $B = H + 4\pi M$ (in Gaussian units) [C12]. B_r is the residual flux density, H_c is coercivity (the reverse field which will reduce B to zero) and H_{ci} is intrinsic coercivity (the reverse field required to reduce $4\pi M$ to zero). For PM materials, demagnetization occurs when a sufficient reverse H field is applied across the PM. When the operation point of the PM is driven to the left part (nonlinear part) of the “knee” point

on BH curve as shown in Fig. 3.6, the PM material will start to be irreversibly demagnetized. To avoid such demagnetization under any operation condition of PMCI, PM materials with sufficiently high H_{ci} and H_{knee} values are needed. Usable/safe operation range of the PM for the PMCI design is marked on both the normal curve and intrinsic curve.

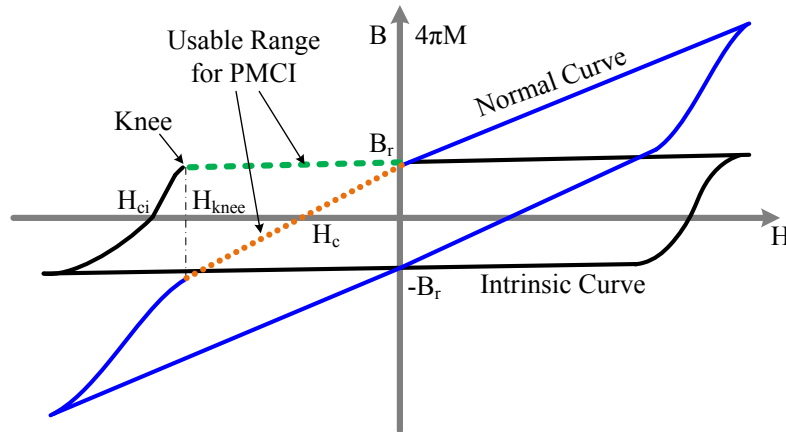


Figure 3.6: Magnetic hysteresis loop of the PM

Similar with PM dimension design for the single phase permanent magnet power inductor as detailed in Chapter 2, dimensions of PM to be used for PMCI design can be determined based on the equivalent energy stored in the magnetic core and energy “supplied” by the PM. Maximum magnetic energy produced by a PM in the external space (E_{PM}) is determined by (3.14) [C12].

$$E_{PM} = \frac{(BH)_{\max}}{2} V_{PM} \quad (3.14)$$

Where $(BH)_{\max}$ and V_{PM} represents maximum energy product and volume of the PM, respectively. The maximum magnetic energy stored in the CPI/PMCI core (E_{core}) is determined by (3.15) [C11].

$$E_{core} = \frac{B_{sat}^2}{2\mu_e} V_e \quad (3.15)$$

Where, μ_e and V_e are the effective permeability and effective volume of gapped magnetic core for each phase, respectively. To ensure the ferrite core is not saturated by the PM itself, the relationship $E_{PM} \leq E_{core}$ has to be satisfied. Let $E_{core} = E_{PM}$, then the volume of PM is derived as in (3.16) and the dimensions of the PM can be determined accordingly. When $E_{PM} = E_{core}$, maximum amount of flux cancellation can be achieved and saturation current can theoretically be doubled without saturating the inductor core by the PM itself. When $E_{PM} < E_{core}$, flux cancellation effect still exist but the potential of the PM in increasing the saturation current of the power inductor is not maximized. In other words, if $E_{PM} < E_{core}$, the saturation current increase would be less than double.

$$V_{PM} = \frac{B_{sat}^2 V_e}{\mu_{eff} \cdot (BH)_{max}} \quad (3.16)$$

Equation (3.16) shows that a higher $(BH)_{max}$ results in lower volume of PM, which contributes to smaller weight and lower cost. Based on requirements for high H_{ci} , H_{knee} and large $(BH)_{max}$ values, NdFeB magnet is used in this work. The main characteristics of fabricated NdFeB-N35EH magnet at 300 K ($\approx 26.8^\circ\text{C}$) are listed in Table 3.1.

Table 3.1. The Characteristics of The PM

Parameter	Value	Parameter	Value
PM type	NdFeB-N35EH	H_{knee}	1989 kA/m
$(BH)_{max}$	188 kJ/m ³	B_r	1.06 T
H_c	574.8 kA/m	Mass density	7.5 g/cm ³
H_{ci}	2244.8 kA/m	Resistivity ρ_{PM}	180 $\mu\Omega\cdot\text{cm}$

D. Design procedures of PMCI

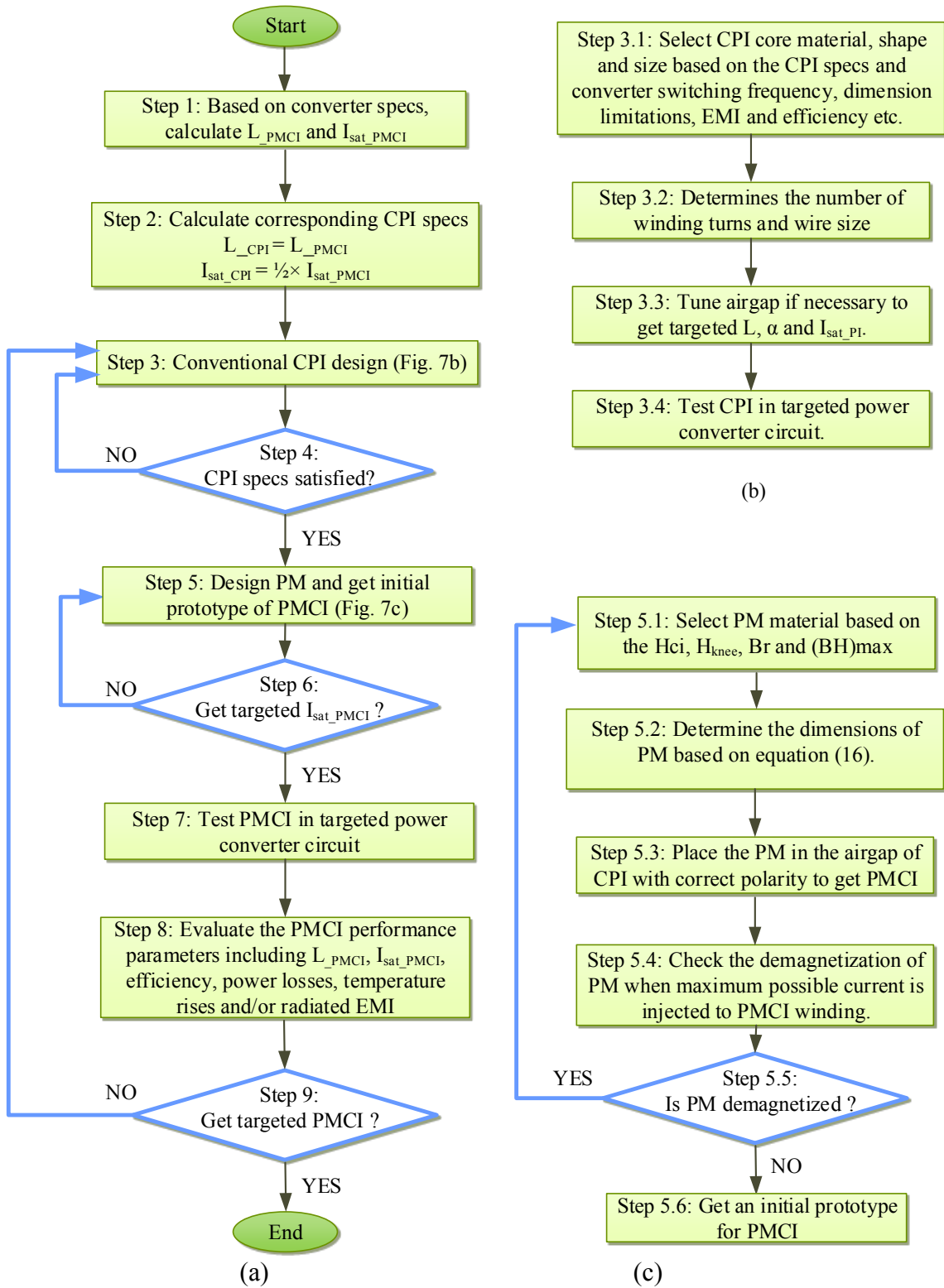


Figure 3.7: Design procedures of PMCI.

Fig. 3.7(a) illustrates the design procedures for PMCI. Sub-steps for CPI design and PMCI design are illustrated in Fig. 3.7(b) and Fig. 3.7(c), respectively. Note that both CPI design process and PMCI design process are multi-step iterative design processes, as it is the case for single-phase power inductor design [C11].

Table 3.2. Dimensions of PMCI Core

Parameter	Value	Parameter	Value
he	8.2 mm	hw	5.7 mm
wi	11.3 mm	wo	16 mm
wc	4.7 mm	tc	4.7mm
$g1=g2=gc$	0.34 mm	PM	4mm×4mm×0.3mm

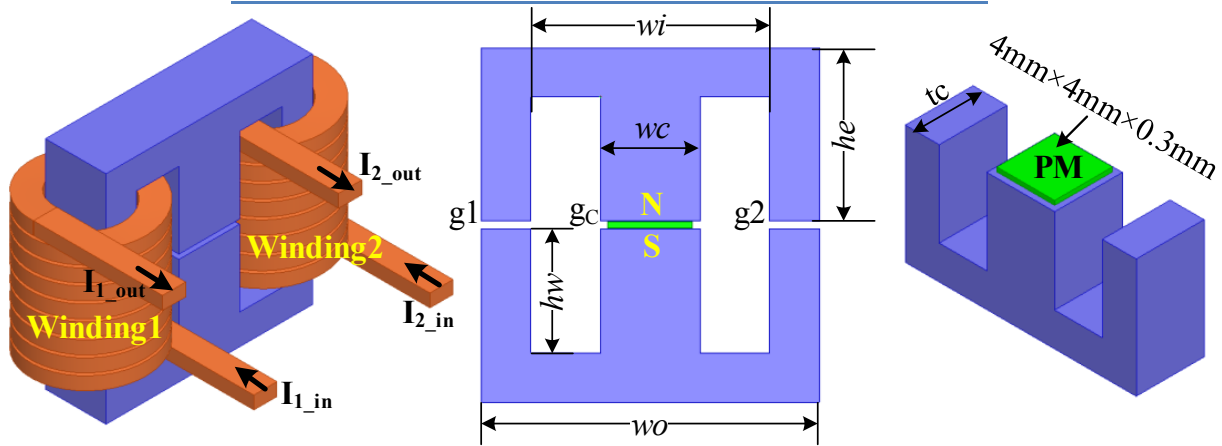
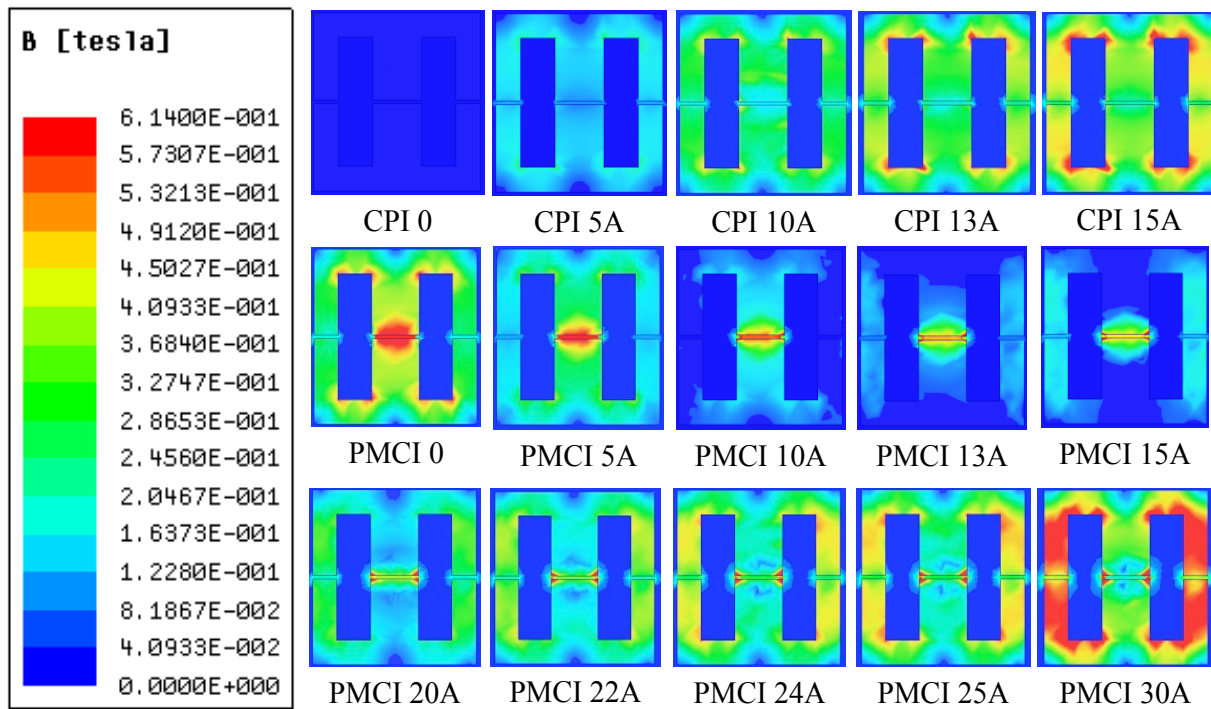


Figure 3.8: 3-D physical model and design parameters of the PMCI

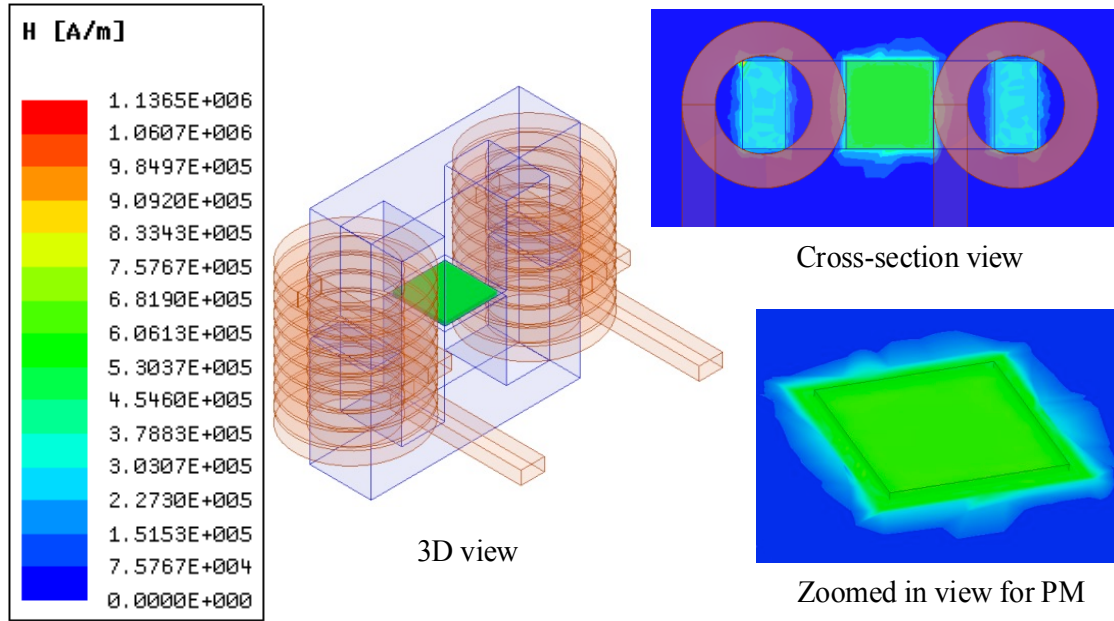
3.3 3-D Physical Model Simulation of PMCI

The 3-D physical model developed in ANSYS®/Maxwell® for the PMCI design is shown in Fig. 3.8 and core dimensions are listed in table 3.2. The CPI and PMCI use the same EE shaped ferrite core E 16/8/5 (EF 16) [C13] from TDK and the ferrite material is N87 (B_{sat} is ~ 0.45 T at 25 °C, resistivity is 10 Ωm and density is ~ 4850 kg/m³) [C14]. Both winding1 and

winding2 have 8.5 turns of copper wire. The core shape, size and windings are predetermined based on an example boost converter application which will be presented in the next section. Based on the datasheet specifications, effective quantities of the PMCI core are calculated as $\mu_{\text{eff}} = \sim 72.1 \cdot \mu_0$, $A_{\text{eff}} = 10 \text{ mm}^2$ and $l_{\text{eff}} = 40.7 \text{ mm}$. The required V_{PM} of NdFeB-N35EH magnet are calculated from (3.16) as $V_{\text{PM}} = 4.83 \text{ mm}^3$. The thickness of the fabricated NdFeB-N35EH magnet is 0.3 mm, then the length and width of the PM can be calculated as $\sim 4 \text{ mm}$.



(a) *B field of CPI and PMCI under various DC current/phase (fixed scaling)*



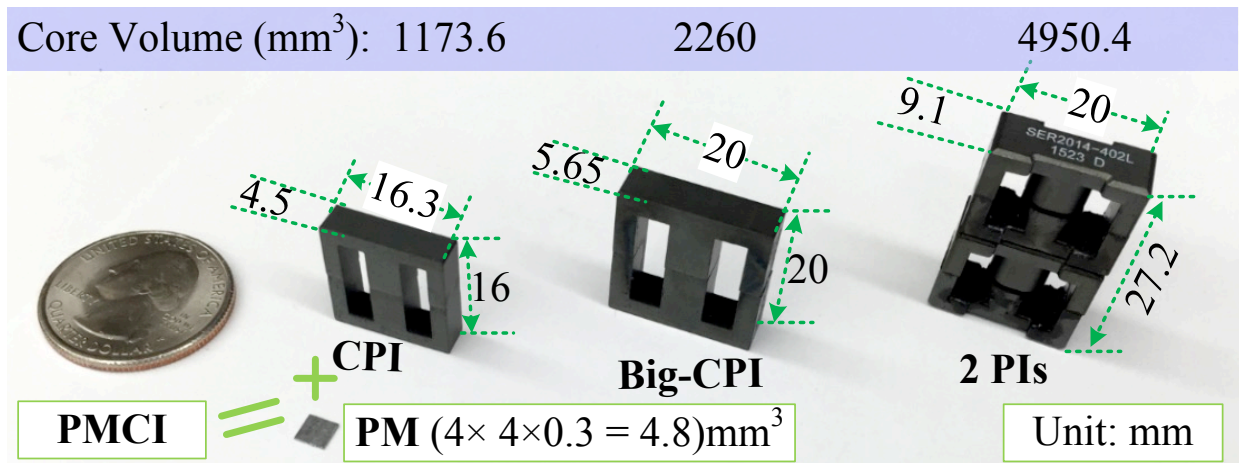
(b) H field of the PM when DC current of PMCI is 30A/phase (auto scaling)

Figure 3.9: FEA simulation results.

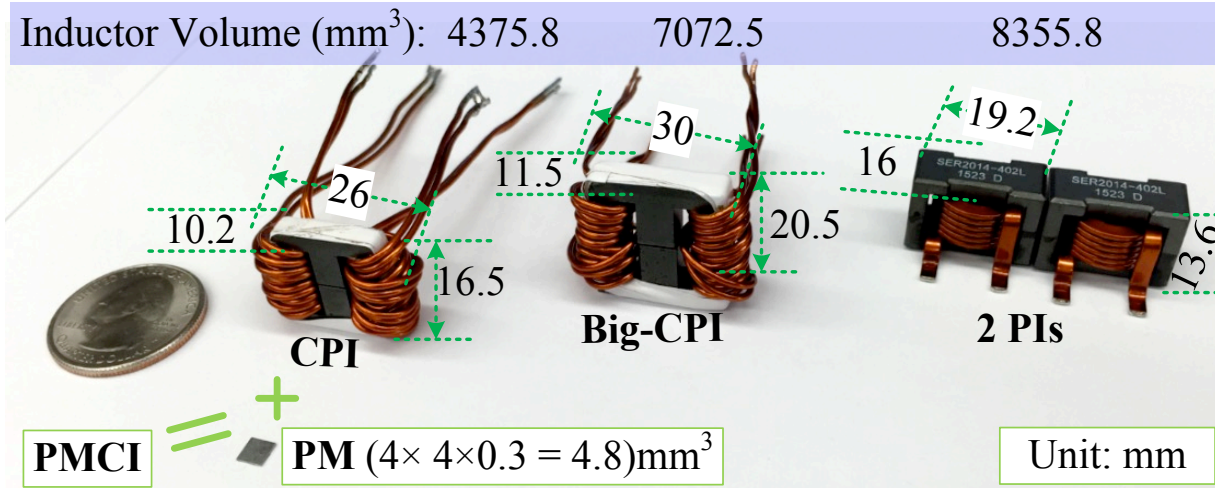
Finite element analysis (FEA) results shown in Fig. 3.9(a) “visualize” the B field distribution of the CPI and PMCI cores when the DC input current increases from 0 to 30 A/phase. For the CPI, the magnitude of B increases with the increase of the DC input current and B values start to approach $B_{\text{sat}} = 0.45$ T when the DC input current is 13 A/phase. Namely, the saturation current of the CPI $I_{\text{sat_CPI}} = 13$ A/phase. For the PMCI, when the input current is 0, the ferrite core has significant amount of magnetic fluxes generated by PM but is not saturated by PM itself. When the input current increases from 0 to 30 A/phase, the net B value of PMCI first decreases to a very small value at 13 A/phase then gradually increases. The PMCI core starts to saturate when the input current is ~ 24 A/phase. The reason why the net flux reaches to its minimum at 13 A/phase is that the cancellation effect between the winding fluxes and PM flux as illustrated in part A of section 3.2. Simulation results show that saturation current of the PMCI

(~24 A/phase) is almost twice as large as the saturation current of the CPI (~13 A/phase) which is consistent with the derivation in (3.13).

Demagnetization of the PM is checked when 30 A/phase is applied to the PMCI and resulted H field distribution as illustrated in Fig. 3.9(b). As discussed in part C of section 3.2, PM operates in its safe range as long as the H field magnitude in the PM is less than the value of H_{knee} , which is 1989 kA/m for the NdFeB-N35EH used in PMCI design at 26.8°C. Fig. 3.9(b) shows that the maximum H value of the PM is 1137 kA/m < $H_{knee} = 1989$ kA/m. The H_{knee} value is calculated based on the temperature coefficient of NdFeB-N35EH [C15] as 1375 kA/m when the PM operates at 100°C, which is also larger than 1137 kA/m. This indicates that the PM used in the PMCI design operates in the safe range even when the input current is as high as 30 A/phase and the temperature is up to 100 °C. The highest hypothetical temperature the fabricated NdFeB-N35EH is able to work safely at with 30 A/phase is calculated as 138°C.



(a)



(b)

Figure 3.10: Dimension specifications for (a) power inductor cores and (b) power inductors.

Table 3.3. Comparisons of Fabricated Power Inductors

	CPI	PMCI	Big-CPI	2 Separate PIs
Core volume(mm ³)	1173.6	1173.6	2260	4950.4
Core volume reduction compared to 2 PIs (%)	-	76.3%	54.3%	-
Core weight(g)	3.78	3.816	7.45	14.37
Core weight reduction compared to 2 PIs (%)	-	73.4%	48.2%	-
Total inductor volume (mm ³)	4375.8	4375.8	7072.5	8355.8
Total inductor weight (g)	13.41	13.45	15.761	24.6
PM size (mm ³)	-	4×4×0.3 =4.8	-	-
PM weight(g)	-	0.036	-	-
Self-Inductance L_s (μ H/phase)	3.2	3.3	3.2	4
Coupling factor α	- 0.29	- 0.29	- 0.29	0
DCR(m Ω /phase) @ 25 $^{\circ}$ C	3.14	3.14	2.93	2
Equivalent steady state inductance L_{SS} (μ H/phase)	4.1	4.25	4.1	4.0
Equivalent transient inductance L_{tr} (μ H/phase)	2.3	2.3	2.3	4
Saturation current (A/phase)*	13	24	18	22

(*) Saturation current is defined as the inductor DC current with ~10% inductance drop

3.4 Proof of Concept Experimental Prototype Results

Fabricated inductors and their dimensions are shown in Fig. 3.10. The PMCI is fabricated by inserting the designed PM in the central gap of the CPI. The characteristics of the fabricated NdFeB-N35EH magnet for the PMCI are specified in Table 3.1 and its dimensions are calculated in section 3.3. A CPI that has bigger core but smaller saturation current compared with PMCI, referred to as Big-CPI, is used for size and weight comparison purpose. The side-leg gaps of CPI, PMCI and Big-CPI are filled with insulation tape, which has almost the same permeability value as the air. The central leg gap of CPI and Big-CPI is filled with air, and the central leg gap of the PMCI is filled with NdFeB magnet and air. Note that the value of the relative permeability of NdFeB magnet (~ 1.05) is very close to that of the air (~ 1).

Two parallel solid magnetic copper wires with the size of AWG 18 are used for power inductor windings. Detailed core dimensions and core material used are specified in section 3.3. Two separate PIs (SER2014-402ML) from Coilcraft [C16] are used for size and weight comparison purposes. A two-phase DC-DC boost power converter as illustrated in Fig. 3.1(c) is designed and fabricated in order to test and evaluate the PMCI. The fabricated converter's input voltage $V_{in} = 4$ V, switching frequency is 150 kHz, input capacitor (C_{in}) and output capacitor (C_o) are 120 μ F and 480 μ F, respectively. Fig. 3.11 shows sample waveforms for the two-phase boost converter when input current is 10A. Since the measured waveforms when using the PMCI are experimentally verified to be the same as when using the CPI, only one group of waveforms are presented to avoid repetition of the same waveforms. Fig. 3.11(a) shows the waveforms measured for the phase node voltages and the inductor currents for phase1 (i_1) and phase2 (i_2) of the two-phase boost converter when $D = 0.3, 0.5$ and 0.7 , respectively. Note that the shape and magnitude of inductor current ripples are affected by the duty cycle and they are the same for the

CPI and PMCI as expected. Fig. 3.11(b) shows the sum of two phase inductors $i_1 + i_2$. Note that ripple values of $(i_1 + i_2)$ are affected by duty cycle. Fig. 3.11(c) shows the waveforms of $(i_1 - i_2)$. Note that the DC values of $(i_1 - i_2)$ are zero, because the currents of phase1 and phase2 are equal (balanced). The analysis and discussion in the rest of the chapter are based on the application example when the input voltage $V_{in} = 4\text{ V}$ and the output voltage $V_o = 8\text{ V}$, i.e. $D = 0.5$.

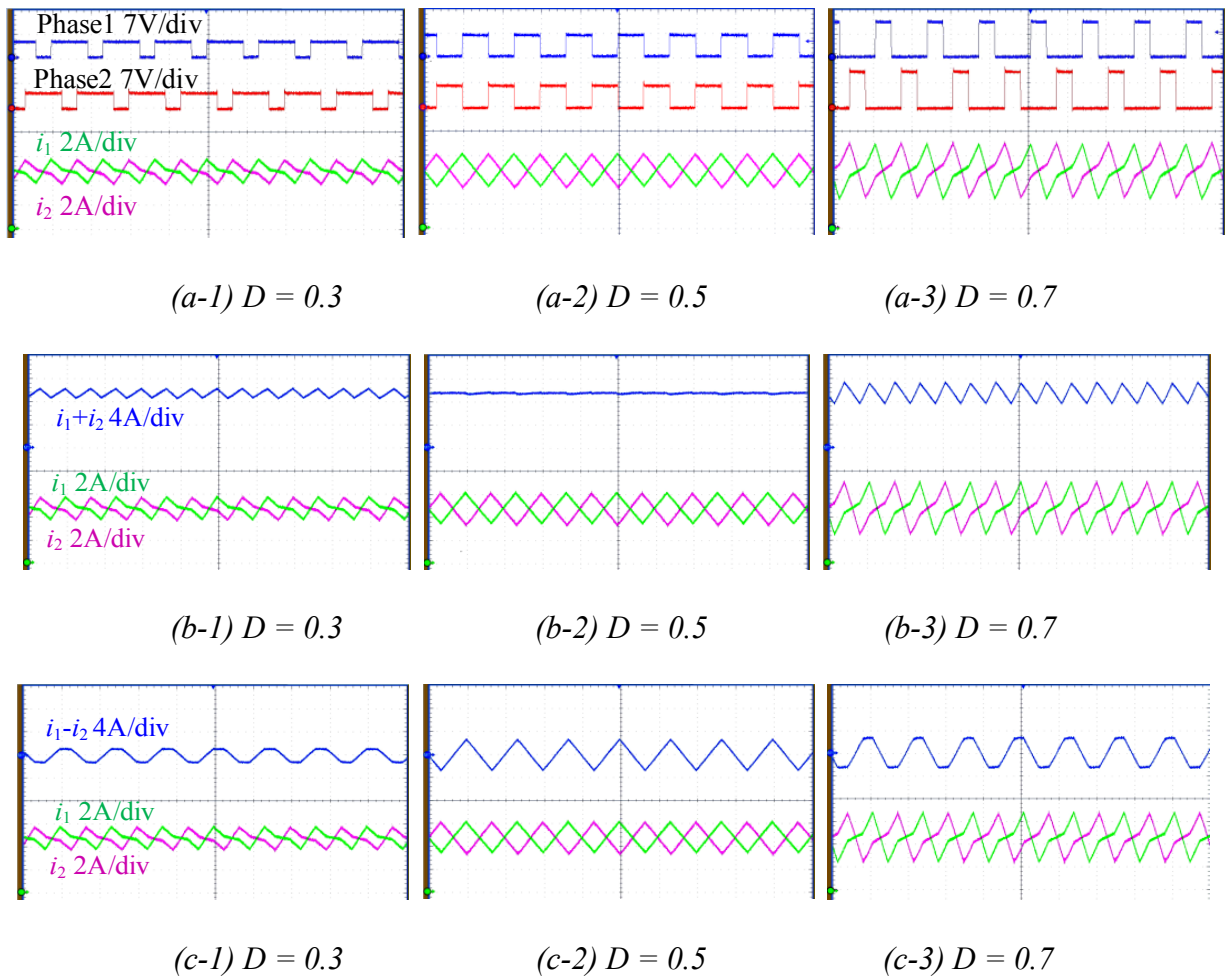


Figure 3.11: Sample experimentally measured waveforms for phase node voltages and inductor currents (DC coupled) which are same for both the CPI and the PMCI.

Some of the most important parameters and measured experimental results for the fabricated power inductors are summarized in table 3.3 for comparison. Results show that the sizes and inductance values of the PMCI and the CPI are the same, but the PMCI has almost double of the saturation current compared to the CPI (24 A/phase compared to 13 A/phase). The PMCI has slightly larger inductance and higher saturation current compared to Big-CPI (18 A/phase), and achieves 48.1% core size reduction and 48.8% core weight reduction. The addition of the PM does not cause any size increase because it is placed in the airgap. The weight of the PM (36 mg) is 0.95% of the weight of the PMCI ferrite core, which means that the total weight increase of the PMCI due to the addition of the NdFeB-N35EH magnet is negligible. Compared to two separate PIs, the PMCI achieves 76.3% core size reduction and 73.4% core weight reduction. Detailed performance evaluations and comparisons are presented in the following sub-sections.

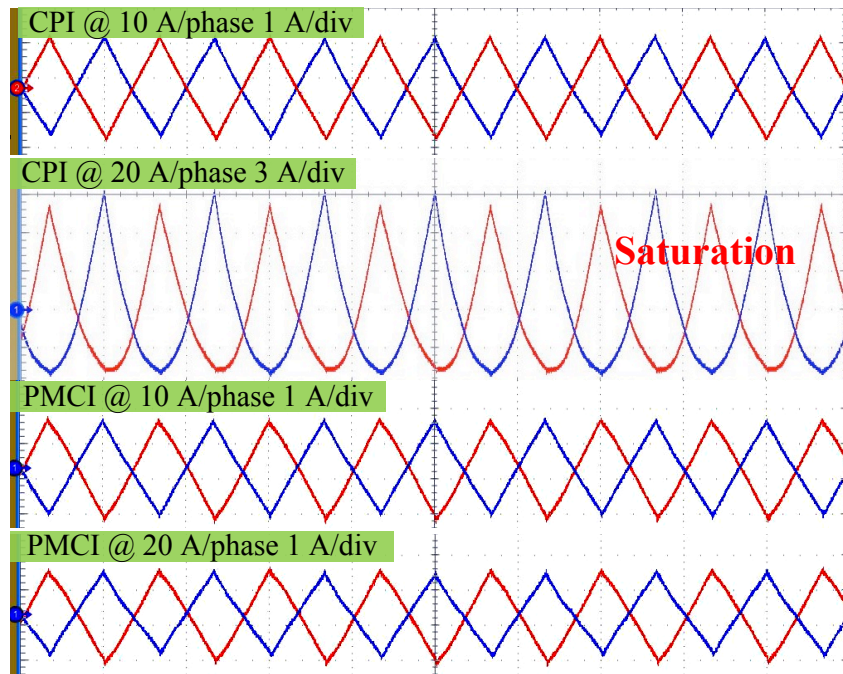


Figure 3.12: Measured current waveforms for CPI and PMCI when power inductor current values are 10 A/phase and 20 A/phase (AC coupled).

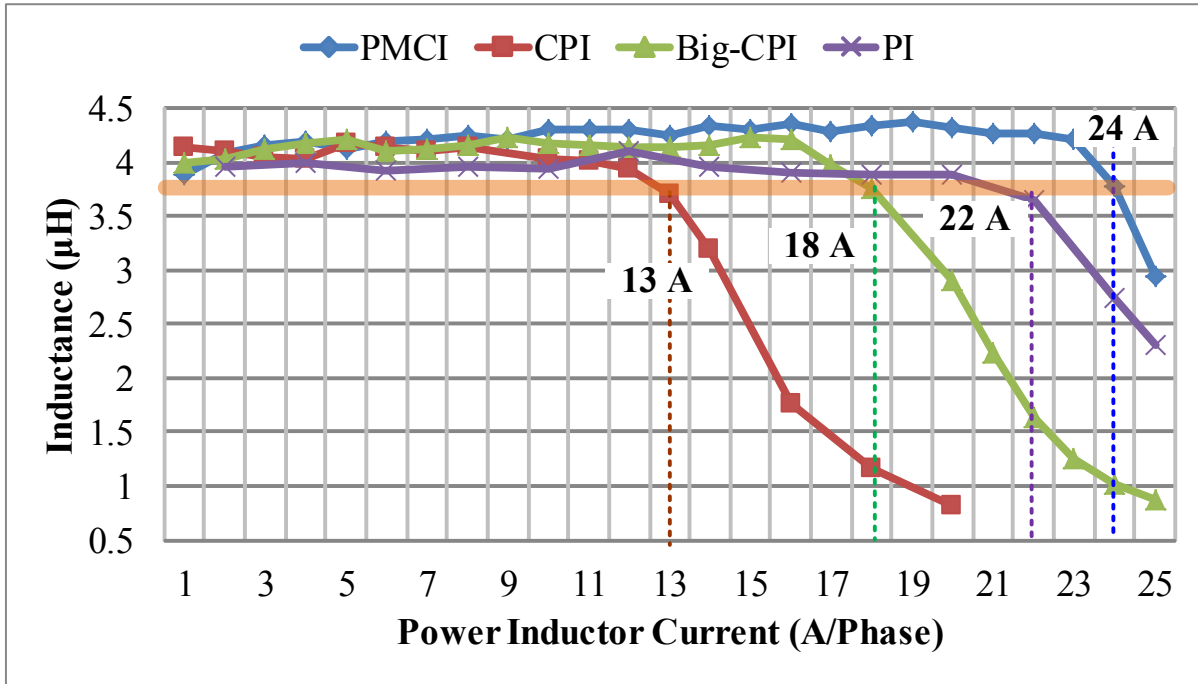


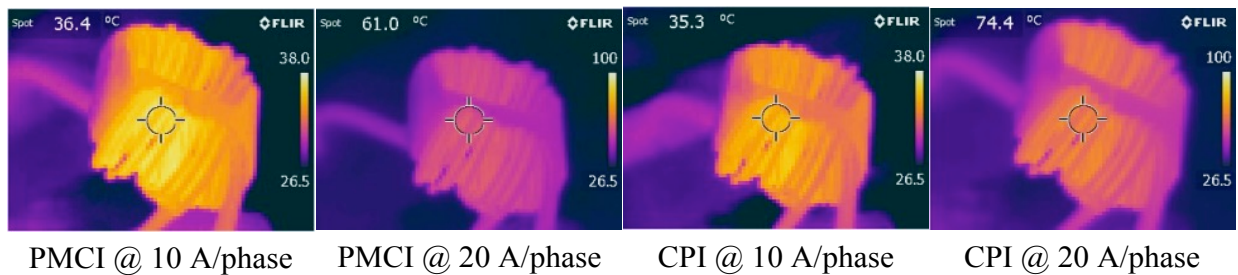
Figure 3.13: Inductance values as a function of per phase power inductor current.

A. Inductance and Saturation Current Measurements

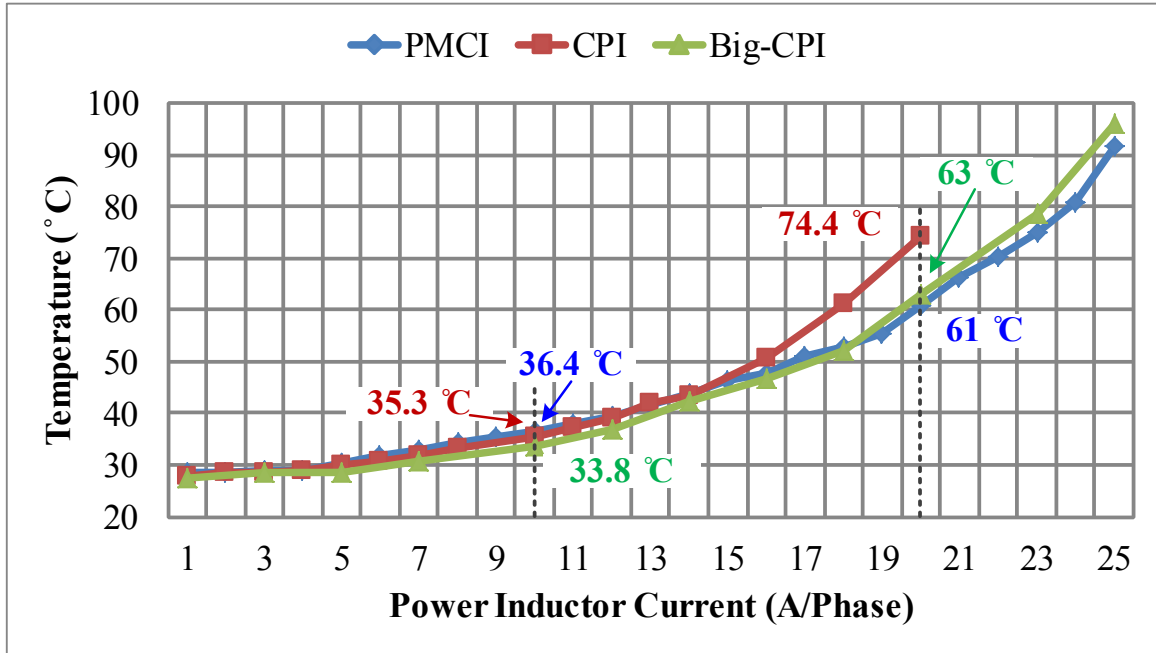
The current value at which the inductor starts to saturate is identified when the inductance value drops by $\sim 10\%$. The per phase equivalent steady state inductance L_{SS} is determined based on (3.2.1). The measured power inductor current waveform samples are shown in Fig. 3.12. The waveform shapes are similar with the case that two separate inductors are used because duty cycle in this example application is 0.5, as illustrated in Fig. 3.1(d)-(f). It can be observed that when inductor is saturated, Δi is larger and the current waveform becomes nonlinear. The inductance values at different power inductor current values (from 1 A to 25 A/phase) are calculated from the experimentally measured waveforms and are plotted in Fig. 3.13. The CPI has nearly constant inductance value of $\sim 4.1 \mu\text{H}/\text{phase}$ when current is less than its saturation current value 13 A/phase. The PMCI has nearly constant inductance value of $\sim 4.25 \mu\text{H}/\text{phase}$

when current is less than its saturation value 24 A/phase. This verifies magnetic circuit model analysis and 3-D physical model simulation results for saturation current doubling. The Big-CPI has nearly constant inductance value of $\sim 4.1 \mu\text{H}/\text{phase}$ before starting to saturate at 18 A/phase. The single phase PI has nearly constant inductance value of $\sim 4.0 \mu\text{H}$ before starting saturation at 22A.

During load transient, voltage overshoot or undershoot are suppressed by controller through varying the duty cycles dynamically. Because test results have shown that steady state operation waveforms are the same in the case of CPI and PMCI with various duty cycles, transient waveforms will also be the same. In other words, equivalent transient inductance will be the same for CPI and PMCI as also supported by (3.2.2). Using (3.2.2), the calculated results are listed in table 3.3. Results show that the CPI, PMCI and Big-CPI have the same L_{tr} value ($\sim 2.9 \mu\text{H}$), which is smaller than the L_{tr} value of the single phase PI ($4 \mu\text{H}$). As a result, a power converter that uses a CPI, PMCI or Big-CPI will have the same transient performance and will be better than when using two separate PIs.



(a)



(b)

Figure 3.14: (a) Temperature distribution images and (b) temperature as a function of per phase inductor current.

B. Thermal Characteristics And Power Inductor Losses

Temperature rise values for the power inductors at different current values are measured using FLIR T-62101 thermal imaging camera. Sample temperature distribution images of the CPI and PMCI are shown in Fig. 3.14(a). Based on the temperature measurement results, curves for the temperature rise as a function of per-phase inductor current are plotted, as shown in Fig. 3.14(b). It can be observed that the temperature increases with the increase of current for all power inductors, as expected. When inductor current is less than the saturation current of CPI (13 A/phase), all three inductors have similar temperature rise values but the temperature of PMCI (T_{PMCI}) is slightly higher than temperatures of the CPI (T_{CPI}) and Big-CPI ($T_{Big-CPI}$). For example, at 10 A/phase, $T_{PMCI} = 36.4^{\circ}\text{C}$, $T_{CPI} = 35.3^{\circ}\text{C}$ and $T_{Big-CPI} = 33.8^{\circ}\text{C}$. This is because eddy current loss of the NdFeB-N35EH magnet contributes to the temperature rise of PMCI due to its

small resistivity ($\rho_{PM} = 180 \mu\Omega \cdot \text{cm}$). Meanwhile, there exists large DC bias in the B field of the PMCI core when inductor current is small because of the PM, as illustrated in Fig. 3.9(a). As a result, the core loss of the PMCI at small inductor current will be slightly increased, which also contributes to higher T_{PMCI} values. When inductor current is larger than 13 A/phase and smaller than the saturation current of the Big-CPI (18 A/phase), the $T_{Big-CPI}$ has the smallest values because of its big size. T_{CPI} is larger than T_{PMCI} because the saturation of CPI core contributes to larger inductor current ripple and higher core and winding losses. When inductor current is larger than 18 A/phase, both T_{CPI} and $T_{Big-CPI}$ have larger values than T_{PMCI} . This is because both CPI and Big-CPI cores are saturated but PM cancels the magnetic flux in PMCI core and helps to reduce the core and winding losses. For example, at 20 A/phase, $T_{PMCI} = 61^\circ\text{C}$, $T_{CPI} = 74.4^\circ\text{C}$ and $T_{Big-CPI} = 63^\circ\text{C}$.

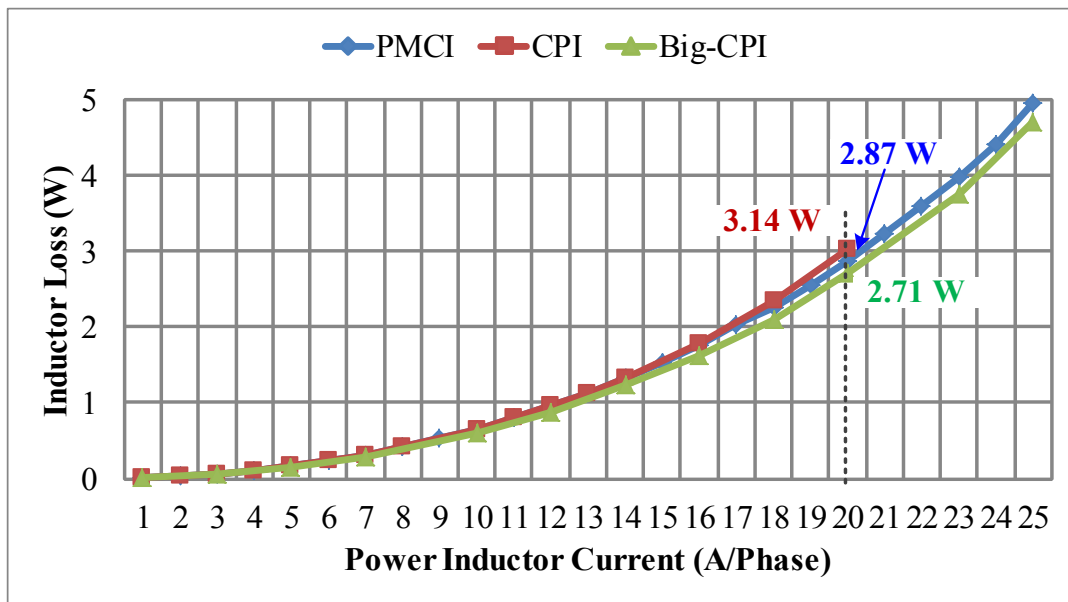


Figure 3.15: Power inductor DC losses as a function of per phase inductor current.

Temperature rise values shown in Fig. 3.14(b) are good indication for total power inductor losses. It is also interesting to know the DC power losses (P_{DC}) of different power inductors. DC winding resistance (DCR) of different power inductors at 25°C are measured and are listed in table 3.3. The temperature (T) dependent DCR per phase can be determined from the equation $DCR=DCR_o \cdot (1+\alpha \cdot (T-T_o))$, where DCR_o is the DCR at temperature T_o , α is the temperature coefficient of the resistance and for copper it is equal to $3.93 \times 10^{-3}/^\circ\text{C}$. P_{DC} values are calculated from (3.17) and plotted in Fig. 3.15.

$$P_{DC} = (I_{rms_1}^2 + I_{rms_2}^2)(DCR_o(1 + \alpha(T - T_o))) \quad (3.17)$$

Where, I_{rms_1} and I_{rms_2} are measured RMS (Root-Mean-Square) values of power inductor current per phase. Fig. 3.15 shows that P_{DC} values of all power inductors increase with the increase of inductor current. The Big-CPI has the smallest P_{DC} because it has the shorter winding and smaller DCR than that of CPI and PMCI. The CPI and the PMCI have similar P_{DC} values before saturation of the CPI. When inductor current is larger than 13 A, namely after saturation of CPI, the PMCI has smaller P_{DC} values, which is also supported by temperature rise values shown in Fig. 3.14.

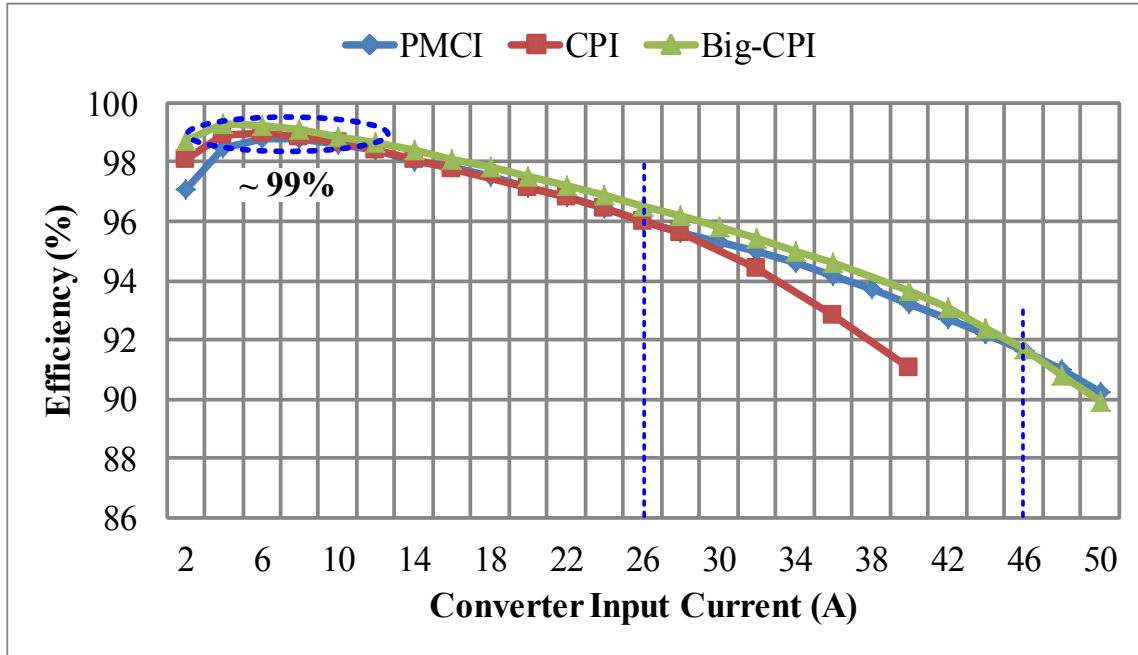


Figure 3.16: Two-Phase boost converter efficiencies (considering driver losses) as a function of load current.

C. Total Power Converter Efficiency

Two-phase boost power converter efficiencies are measured when using PMCI and CPI. Efficiencies are determined by using (3.18) and measured efficiencies are plotted as a function of input current, as shown in Fig. 3.16.

$$\eta = \frac{P_o}{P_{in} + P_{driver}} = \frac{V_o \cdot I_o}{V_{in} \cdot I_{in} + V_{driver} \cdot I_{driver}} \quad (3.18)$$

Where V_{in} is the input voltage measured at two terminals of input capacitor, I_{in} is the input current measured through the constant power source/supply, V_o is the output voltage measured across the two terminals of output capacitor (which is maintained at fixed value by slightly adjusting the duty cycle), and I_o is the output current measured from the DC electronic load used in the experiment. V_{driver} and I_{driver} are voltage and current of the gate drivers, respectively. Note that the converter input current is two times of the per phase power inductor current. Results show that power converter achieves $\sim 99\%$ peak efficiency with all three

coupled power inductors. The power converter with CPI and power converter with PMCI have similar η values before saturation of the CPI. When converter input current is larger than 26 A, namely after saturation of CPI, the converter with PMCI starts to have higher efficiency. During light load conditions, i.e. when the converter input current is smaller than 6 A, the efficiency of the converter with PMCI is less than 1% lower than the efficiency with CPI due to the PM loss and larger PMCI losses because the PM contributes to larger DC bias of the B field, as explained in part B of this section. Power converter with Big-CPI has the highest efficiency when input current is less than 46 A. When input current further increases, Big-CPI is largely saturated and power converter with PMCI starts to have highest efficiency. Efficiency results also agree with temperature rise results shown in Fig. 3.14.

3.5 Summary

The presented PMCI is fabricated based on the guidelines derived from the developed magnetic circuit model and PM characteristics. Experimental results show that the PMCI almost doubles the saturation current compared to the CPI (from 13 A/phase to 24 A/phase) with the same size, weight and the same inductance. PMCI also achieves 48.1% core size reduction and 48.8% core weight reduction compared to the Big-CPI with the same inductance but with a smaller saturation current (~ 18 A/phase). In addition, PMCI achieves $\sim 76.3\%$ core size and $\sim 73.4\%$ core weight reductions compared to two separate single phase PIs with the same steady state inductance and similar saturation current, thanks to the dual flux cancelation effect from the coupling and PM realized by the presented power inductor structure.

It should be noted that the presented PMCI is suitable for unidirectional power converters with unidirectional power flow, and is not suitable or intended for bidirectional power converters with bidirectional power flow. This is because in order for the design to double the saturation

current, the flux density of the PMCI core is designed to be near the saturation flux density value when the current is zero. If the current flows in the opposite/negative direction, it will drive the PMCI core to saturation.

CHAPTER 4

TWO-COIL RECONFIGURABLE WPT SYSTEM

4.1 Introduction

This chapter first compares two-coil and four-coil configurations for midrange magnetic resonance coupled wireless power transfer (MRC-WPT) systems based on the simplified circuit model and 3-D physical model simulations, then presents a two-coil reconfigurable WPT system topology in order to optimize transmission efficiency under different transmission distance (DIS) and lateral misalignment (MIS) conditions. The adaptively reconfigurable WPT system includes only one Tx coil and one Rx coil. Adaptive switches at Tx side and/or Rx side can switch among different circuit configurations (which include different values of series and shunt capacitors) to yield a higher transmission efficiency under various DIS and MIS conditions.

In the next section, physical model simulation results show that the four-coil system achieves longer transmission distance and larger misalignment tolerance with relatively lower efficiency at close distance compared to the two-coil system. Section 4.3 presents the two-coil reconfigurable system. Section 4.4 presents proof of concept experimental results. Section 4.5 gives a summary for this chapter.

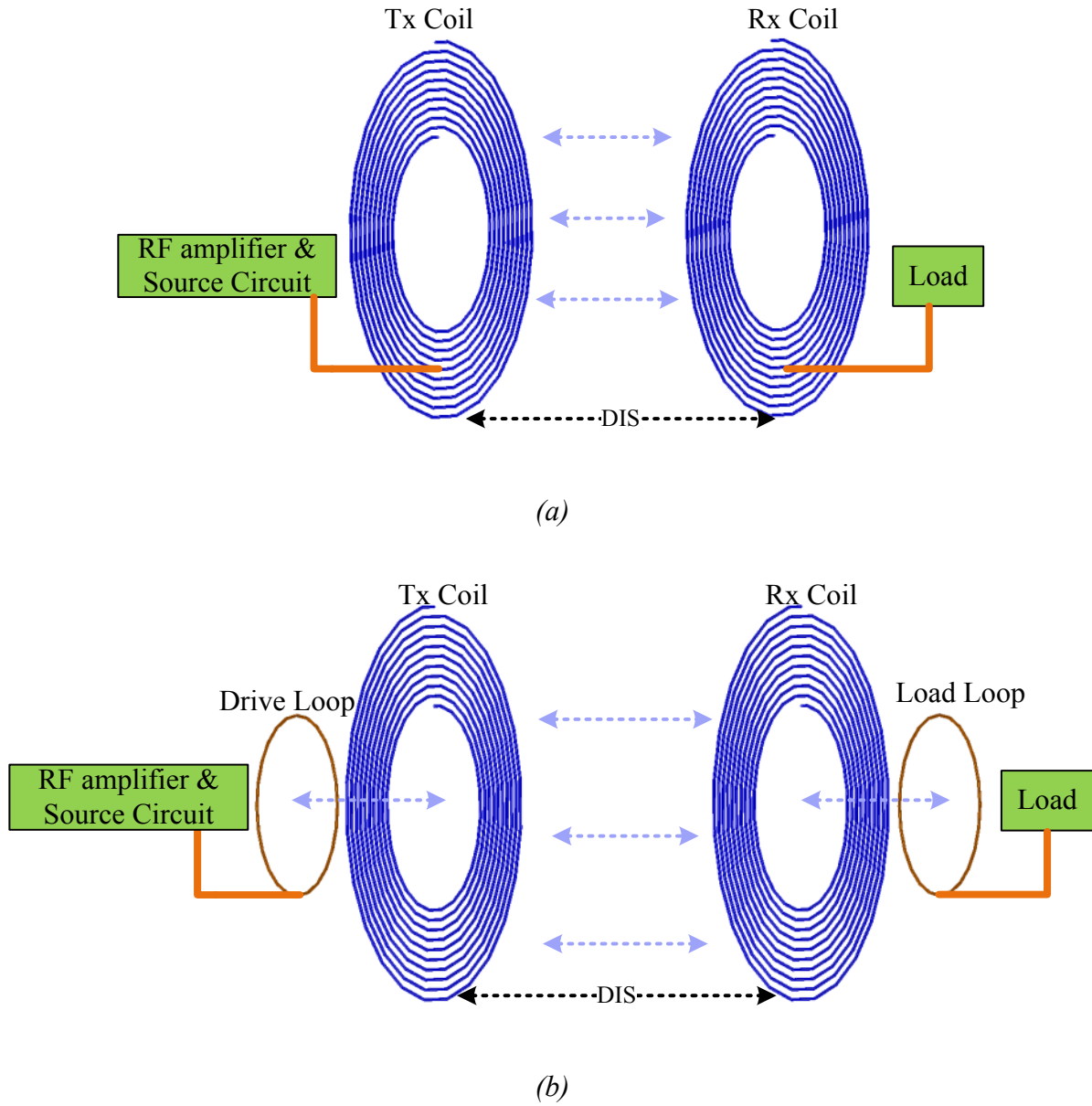


Figure 4.1: MRC-WPT system with spiral structures: (a) two-coil system and (b) four-coil system

4.2 Range and Misalignment Tolerance Comparisons between Two-coil and Four-coil Wireless Power Transfer Systems

Two-coil and four-coil configurations are used in MRC-WPT systems [D1-D13]. As illustrated in Fig. 4.1(a), the two-coil configuration connects the power source and the load to the Tx and the Rx directly. This is unlike the case in the four-coil configurations where Tx and Rx are magnetically coupled to the extra drive loop and load loop that are connected to the power source and the load respectively as illustrated in Fig. 4.1(b). The Tx and the Rx are usually multi-turn spiral shape or helix shape copper coils. The Tx and Rx parameters such as coil diameter, number of turns, wire radius and gap between neighboring turns can vary for different applications based on system requirements. The drive loop and the load loop are usually single copper loop each.

A. Circuit Model Extraction and Analysis of Four-coil and Two-coil MRC-WPT Systems

In this section, a simplified circuit model parameters of the four-coil and the two-coil MRC-WPT systems are first extracted from 3-D physical models then the circuit models are analyzed. No external capacitors are connected to the physical models. That is to say, all capacitances appeared in circuit models are parasitic capacitances of WPT coils. The footnote “₂” in the rest of the chapter is used to differentiate the variables of two-coil systems from the variables of four-coil systems.

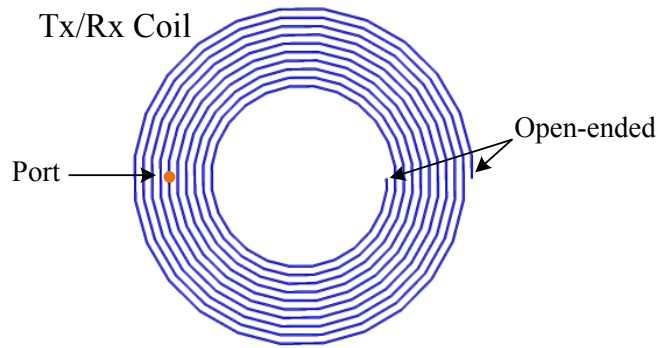
In a two-coil system, when the port is connected to the spiral coil in the way shown in Fig. 4.2(a) and the two ends are open, referring to the open-ended coil, equivalent circuit of coil can then be extracted and is shown in Fig. 4.2(b). In this RLC circuit, L_2 is the self-inductance of the coil, C_2 is the parasitic capacitance of the coil and R_2 is the parasitic resistance of the coil. When a driving source is connected to the port, series resonance occurs when the source frequency

satisfies (4.1). The simplified circuit model of a two-coil MRC-WPT system (Fig. 4.1a) is shown in Fig. 4.2(c). Both the source impedance (R_{s-2}) and load impedance (R_{L-2}) are fixed at 50Ω . k_{TR-2} is the coupling coefficient between the Tx coil and Rx coil, which is calculated from (4.2). In the case of two-coil system, $k_{ij}=k_{TR-2}$, $L_i=L_{T-2}$ is the self-inductance of Tx, $L_j=L_{R-2}$ is the self-inductance of Rx and $M_{ij}=M_{TR}$ is the mutual inductance between Tx and Rx coils.

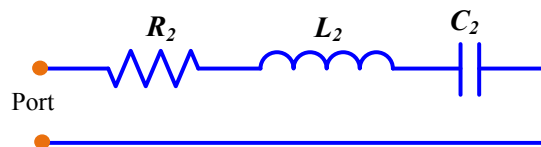
In a four-coil system, the port is connected to the drive/load loop as shown in Fig. 4.3(a) and two ends of Tx/Rx coil are also open. The corresponding equivalent circuit for Fig. 4.3(a) is shown in Fig. 4.3(b). Where the footnote “ l ” represents drive/load loop and the footnote “ $-c$ ” represents Tx/Rx coil. The open-ended coil is modeled as a RLC series resonator. The self-resonance frequency of the coil is also determined by (4.1). The loop is modeled as an inductor L_l in series with a parasitic resistor R_{lp} and without considering the parasitic capacitance because the parasitic capacitance values are negligible. The loop and coil are magnetically coupled with a coupling coefficient of k_{lc} , which is determined by (4.2). The simplified circuit model of the four-coil MRC-WPT system (Fig. 4.1b) is shown in Fig. 4.3(c). Similar to the two-coil system, both the source impedance (R_s) and the load impedance (R_L) are fixed at 50Ω . k_{TR} is the coupling coefficient between the Tx coil and the Rx coil. k_{DT} is the coupling coefficient between the drive loop and Tx coil. k_{RL} is the coupling coefficient between the Rx coil and the load loop. For simplicity, the cross couplings (Drive loop-to-Rx coupling, Drive loop-to-Load loop coupling and Tx-to-Load loop coupling) are ignored because their influences on system transmission efficiency are negligible and only symmetrical systems are analyzed for both two-coil and four-coil systems.

$$f_o = \frac{1}{2\pi\sqrt{LC}} \quad (4.1)$$

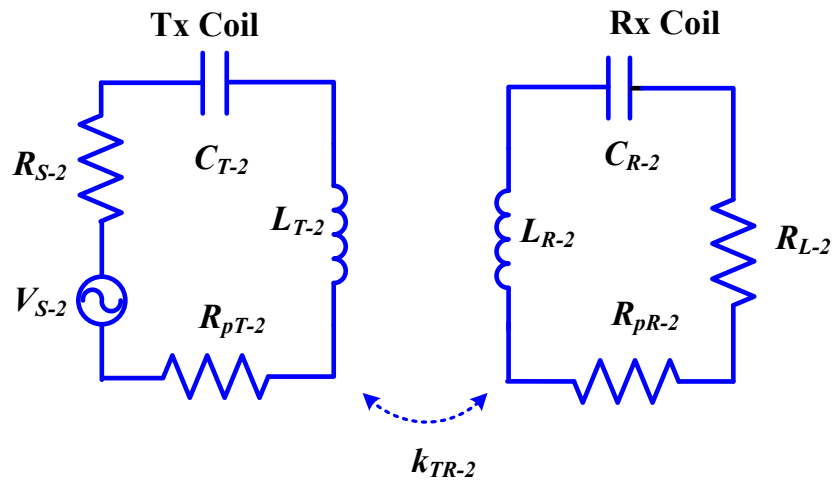
$$k_{ij} = \frac{M_{ij}}{\sqrt{L_i L_j}} \quad (4.2)$$



(a)

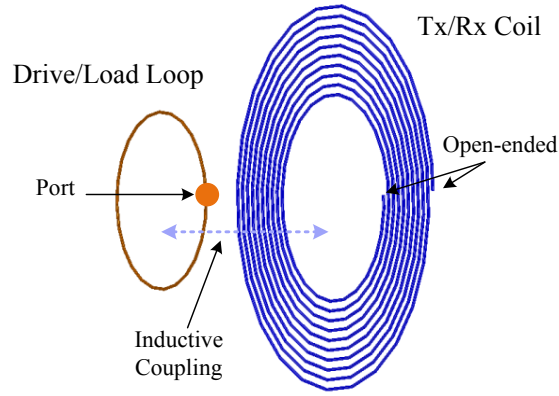


(b)

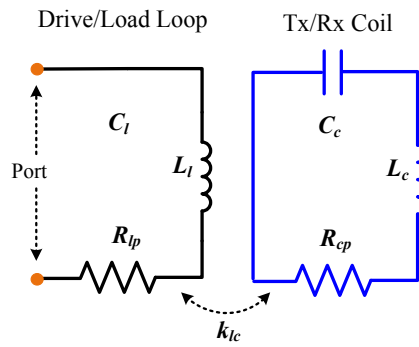


(c)

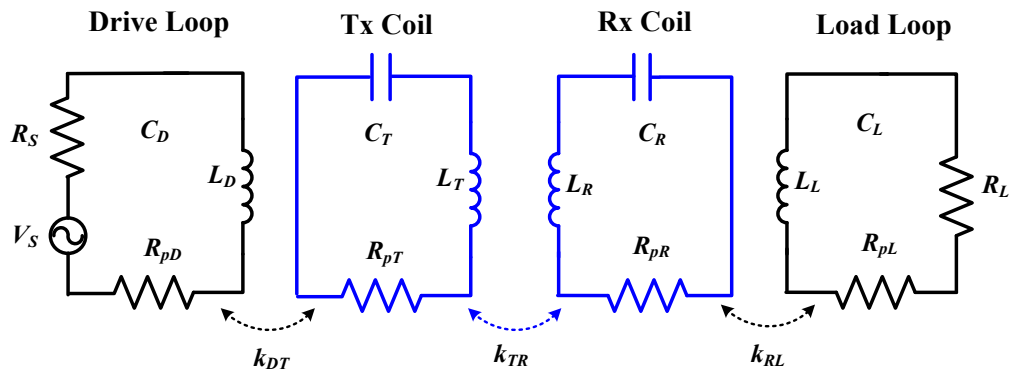
Figure 4.2: (a) Physical model of the open-ended Tx/Rx coil, (b) circuit model of the open-ended Tx/Rx coil and (c) circuit model for the two-coil MRC-WPT system



(a)



(b)



(c)

Figure 4.3: (a) Physical model of the drive-loop/load-loop and Tx/Rx coil, (b) circuit model of the drive-loop/load-loop and Tx/Rx coil, (c) circuit model of the four-coil MRC-WPT system

Table 4.1: Circuit model parameters

Parameters	Values
2-coil f_o of Tx/Rx	10.28 MHz
4-coil f_o of Tx/Rx	10.25MHz
$R_S = R_L = R_o$	50 Ω
$L_T = L_R = L_{coil}$	39.4 μ H
2-coil $C_{T-2} = C_{R-2} = C_{coil-2}$	6.09 pF
4-coil $C_T = C_R = C_{coil}$	6.13 pF
$R_{pT} = R_{pR} = R_{coil}$	1.5 Ω
2-coil Q_{coil-2} (*)	1718
4-coil Q_{coil} (*)	49
$L_D = L_L = L_{loop}$	0.58 μ H
$R_D = R_L = R_{loop}$	0.1 Ω
$k_{DT} = k_{RL} = k_{lc}$	0.15
k_{TR}	Fig. 4.4

*Calculated from (4.3)

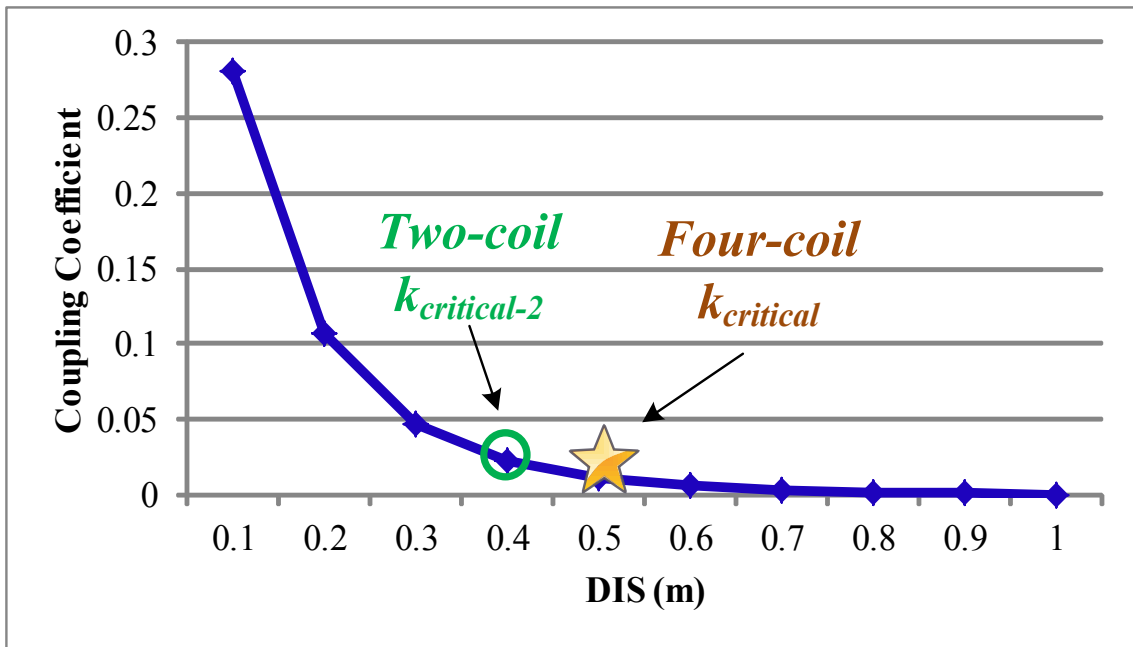


Figure. 4.4: k_{TR} as a function of DIS between Tx and Rx

Circuit model parameters of both two-coil and four-coil systems are shown in Fig. 4.1 (physical model parameters are given in the next section) are extracted from ANSYS® HFSS® and ANSYS® Maxwell® 3-D physical model. Extracted parameters are summarized in Table 4.1, where quality factors are calculated from (4.3). The value of k_{TR} as a function of distance (DIS) is plotted in Fig. 4.4. It can be observed that k_{TR} is inversely proportional to the DIS.

$$Q = \frac{1}{R} \sqrt{\frac{L}{C}} = \frac{1}{\omega_o RC} = \frac{\omega_o L}{R} \quad (4.3)$$

Transmission efficiency (η) of MRC-WPT system can be evaluated by using scattering parameter (S_{21}) as given by (4.4) and (4.5) [D6-D10]. In a MRC-WPT system, critical coupling coefficient (k_{critical}) [D6-D10] represents the smallest k_{TR} value where nearly constant maximum transmission efficiency (η_{critical}) can be maintained. Usually, the smaller the k_{critical} is, the longer DIS the system can achieve. The values of $k_{\text{critical-2}}$ and $\eta_{\text{critical-2}}$ of the two-coil system are derived as in (4.6) and (4.7), respectively [D8-D9]. The values of k_{critical} and η_{critical} of the four-coil system, only for the case when external capacitors are used in the drive loop and load loop, are derived in [D6, D8-D9]. Using similar derivation techniques as those used in [D6, D8-D9], the values of k_{critical} and η_{critical} of four-coil system when no external capacitors are used are derived in this chapter as given by (4.8) and (4.9), respectively. In (4.8) and (4.9), Z_{loop} is the impedance of drive/load loop and is defined as given by (4.10). It can be observed from (4.6) through (4.9) that larger quality factor results in smaller k_{critical} and larger η_{critical} . This means that larger quality factor, as expected, is advantageous in achieving longer transmission distance at higher transmission efficiencies.

Using the extracted circuit model parameters given in Table 4.1 and (4.6) through (4.9), the values of k_{critical} and η_{critical} for both two-coil and four-coil systems are calculated and

summarized in Table 4.2. It can be observed from Table 4.2 that four-coil system has smaller $k_{critical}$ value (0.014) and smaller $\eta_{critical}$ value (92.3%) compared with two-coil system. Therefore, four-coil system is able to transmit for longer DIS but efficiency is $\sim 2\%$ smaller within short distance range. The value of $k_{critical}$ for two-coil system and four-coil system are marked in Fig. 4.4, from which the corresponding transmission distance values ($DIS_{critical}$) are predicted. These predicted values from circuit model analysis are compared with the 3-D physical model simulation results in the next section.

$$S_{21} = 2 \frac{V_L}{V_S} \sqrt{\frac{R_s}{R_L}} \quad (4.4)$$

$$\eta = |S_{21}|^2 \times 100\% \quad (4.5)$$

$$k_{critical-2} = \frac{1}{Q_{coil-2}} \quad (4.6)$$

$$\eta_{critical-2} = |S_{21}|_{critical-2}^2 = \left(\frac{R_{L-2}}{R_{L-2} + R_{coil-2}} \right)^2 \quad (4.7)$$

$$k_{critical} = \frac{1}{Q_{coil}} + k_{lc}^2 \frac{Q_{loop} R_o}{Z_{loop}} \quad (4.8)$$

$$\eta_{critical} = |S_{21}|_{critical}^2 = \left(\frac{k_{lc}^2 Q_{loop} R_o}{k_{critical} Z_{loop}} \right)^2 \quad (4.9)$$

$$Z_{loop} = Z_D = Z_L = R_o + R_{loop} + j\omega L_{loop} \quad (4.10)$$

Table 4.2: Comparison between four-coil and two-coil WPT systems

	Four-coil system	Two-coil system
Q_{coil}	1718	49
$k_{critical}$	0.014	0.02
$ S_{21} _{critical}$	0.96	0.97
$\eta_{critical}$	92.3%	94.1%
$DIS_{critical}$	$\sim 0.4m$	$\sim 0.5m$

B. ANSYS®/HFSS® 3-D Physical Modeling and Simulation Results

In this section, design examples of two-coil and four-coil MRC-WPT systems are compared based on ANSYS® HFSS® 3-D physical model simulations using finite element analysis (FEA) method. FEA methods are widely used for magnetic component simulations [D7-D12]. The physical model parameters are given in Fig. 4.5 and Table 4.3. Two-coil system and four-coil system have the same size of Tx/Rx coils.

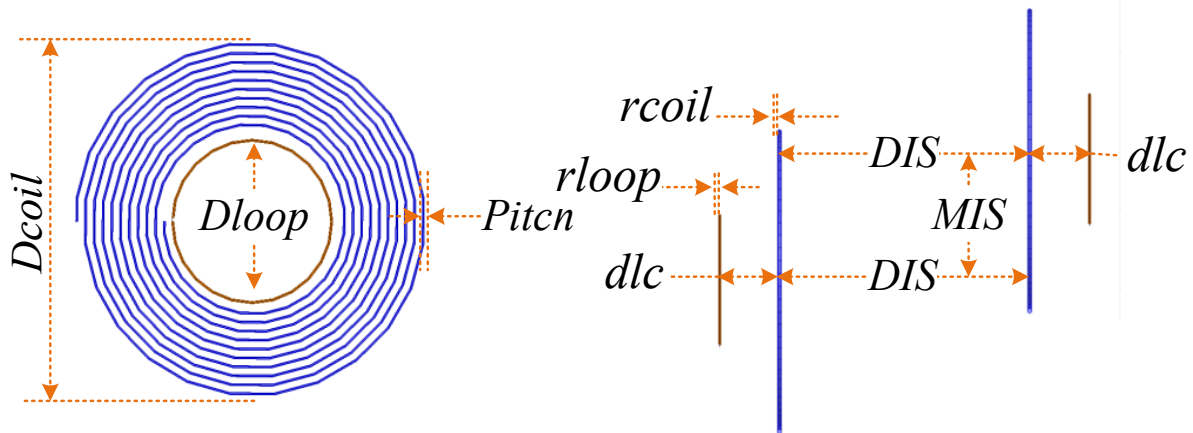


Figure. 4.5: Parameter specifications of MRC-WPT system

Talbe 4.3: Physical model parameters for MRC-WPT system

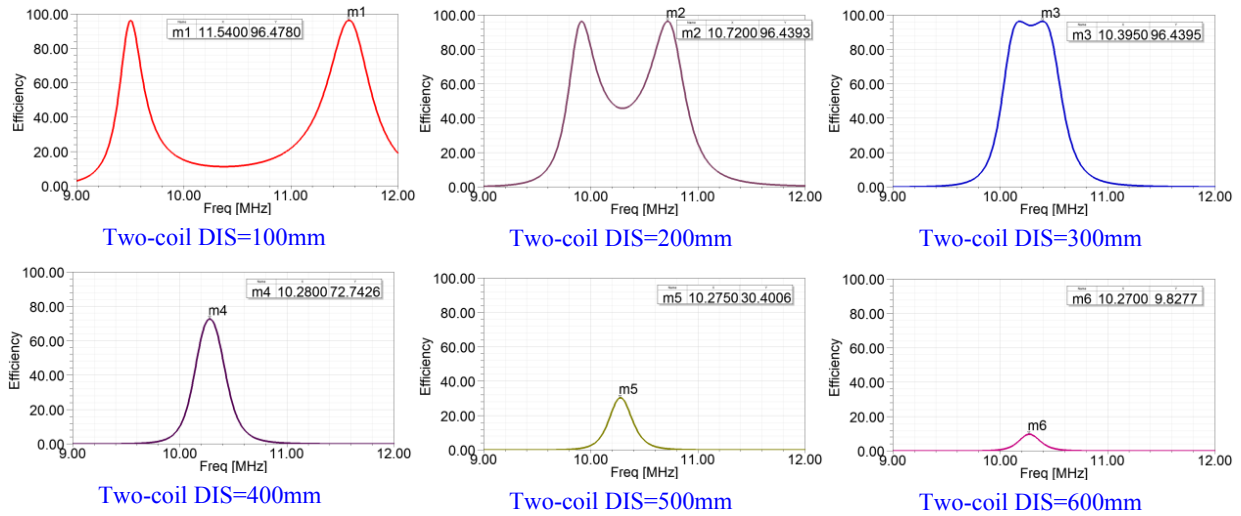
Parameter	Values	Parameter	Values
Coil structure	Spiral	<i>Pitch</i>	10mm
Wire material	copper	<i>rcoil</i>	1.3mm
R_S, R_L	50 Ω	<i>rloop</i>	1.3mm
Coil turns (<i>Ncoil</i>)	10	<i>dlc</i>	70mm
<i>Dcoil</i>	400mm	<i>DIS</i>	0-1000mm
<i>Dloop</i>	180mm	<i>MIS</i>	0-400mm

In perfectly aligned MRC-WPT systems, the lateral misalignment value is $MIS = 0$. Frequency responses of two-coil system and four-coil system at selected distances are illustrated in Fig. 4.6(a) and Fig. 4.6(b) respectively. When the system is positioned in the over-coupled region, where $k_{TR} > k_{critical}$, frequency splitting can be clearly observed. In MRC-WPT systems, nearly constant transmission efficiency can be maintained as long as frequency splitting exists [D6-D9]. When frequency splitting disappears and DIS further increases, efficiency drops rapidly in both two-coil and four-coil systems. The maximum efficiency that the two-coil and four-coil systems are able to maintain when varying DIS from 0 to 1000mm is given in Fig. 4.6(c). It can be observed that in the case of two-coil system, nearly constant maximum efficiency of $\sim 96\%$ is maintained when $DIS \leq 350$ mm. In the case of four-coil system, nearly constant efficiency of $\sim 85\%$ is maintained when $DIS \leq 500$ mm. When $DIS > \sim 370$ mm, efficiency of four-coil system is larger than efficiency of two coil system at every DIS point. For example, when $DIS = 500$ mm, two-coil system achieves efficiency of 30.4 % while four-coil system achieves efficiency as high as 84.2%, which is larger than 2.5 times higher than two-coil system efficiency. Therefore, four-coil system is able to transmit for longer distance (~ 0.5 m) with high efficiency of $\sim 85\%$ but its efficiency at close distance ($DIS < 0.35$ m) is lower than two-coil system efficiency ($\sim 96\%$).

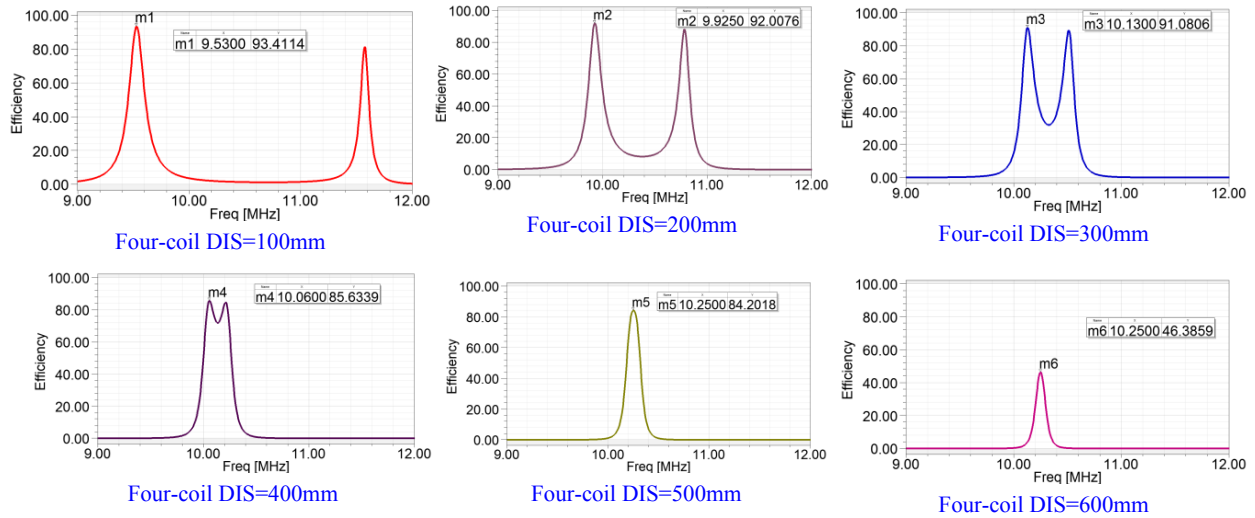
Critical distance and efficiency values obtained from 3-D physical model simulations are compared with circuit model prediction in Table 4.4. The circuit model analysis values closely match with 3D physical model simulation values.

Table 4.4: Comparison between critical values obtained from physical model simulations and circuit model prediction

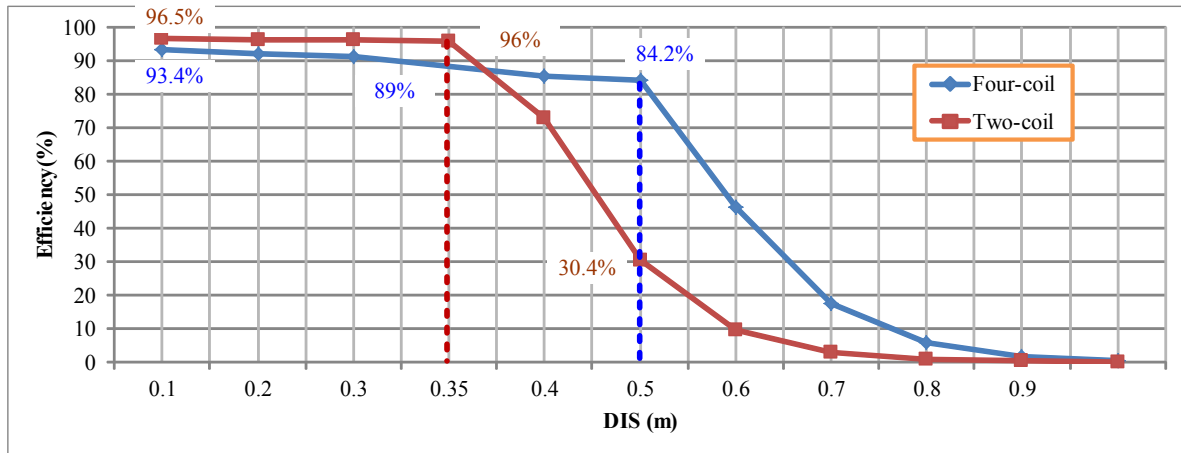
	Circuit Model Prediction	3-D Physical Model Simulation
Two-coil system $\eta_{critical}$	94.1%	~96%
Four-coil system $\eta_{critical}$	92.3%	~90%
Two-coil system $DIS_{critical}$	~0.4m	~ 0.35m
Four-coil system $DIS_{critical}$	~0.5m	~0.5m



(a)

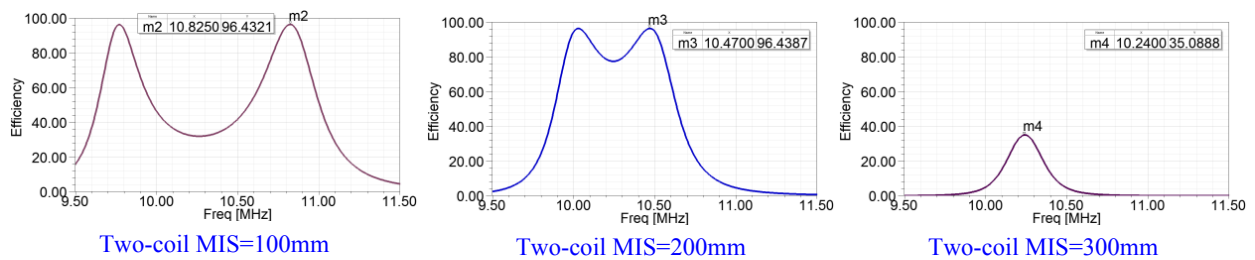


(b)

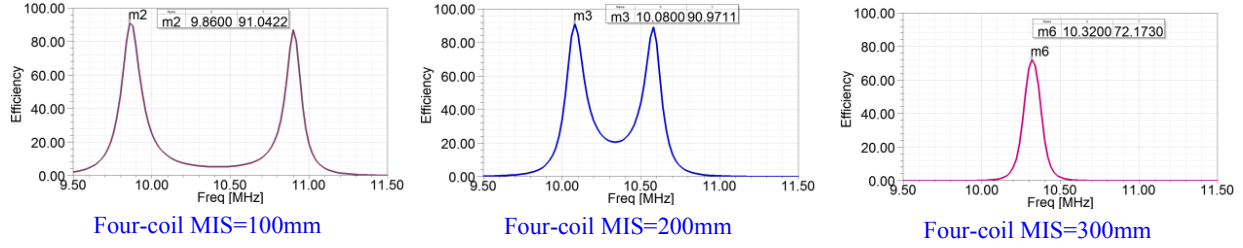


(c)

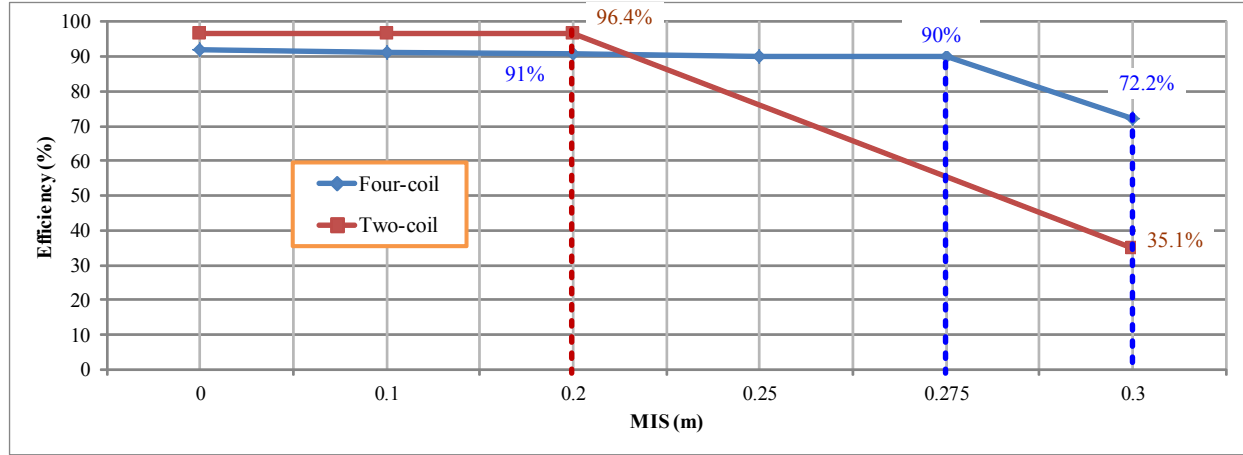
Figure 4.6: Selected plots for frequency responses of (a) two-coil system, (b) four-coil system, and (c) efficiency as a function of DIS when MIS=0



(a)



(b)



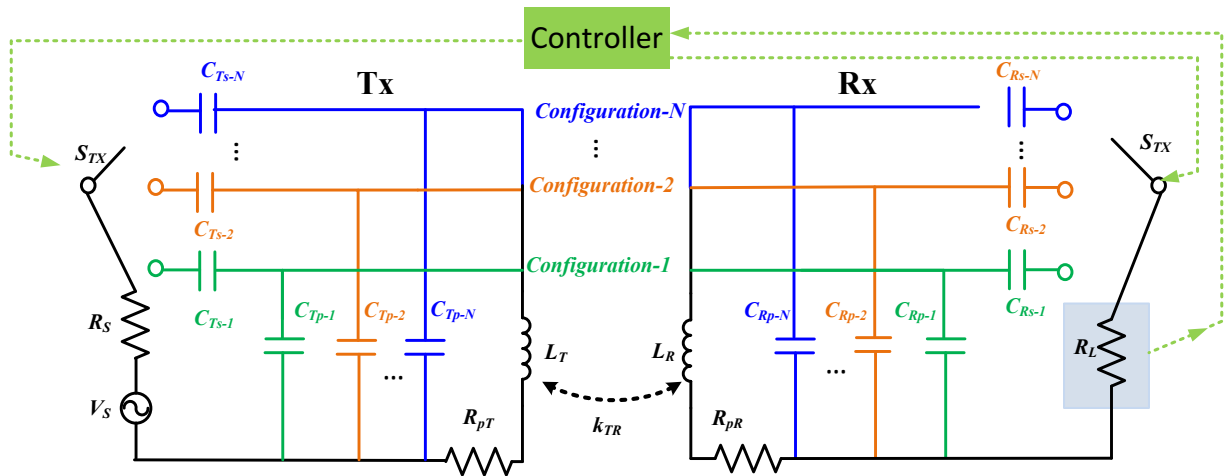
(c)

Figure 4.7: Selected plots for frequency responses of (a) two-coil system, (b) four-coil system, and (c) efficiency as a function of MIS when DIS=150mm

Lateral misalignment is unavoidable in many WPT system applications such as consumer electronics charging [D1]. References [D8, D11-D12] identify high efficiency range for laterally misaligned MRC-WPT systems with different DIS values. Two-coil system and four-coil system are compared in terms of misalignment tolerant capability.

For the simulated laterally misaligned MRC-WPT systems in this chapter, vertical Tx to Rx distance is fixed at DIS = 150 mm. Frequency responses of two-coil system and four-coil system at selected MIS values are illustrated in Fig. 4.7(a) and Fig. 4.7(b), respectively. Frequency splitting is also clearly observed when systems exist in over-coupled region. When frequency

splitting disappears and MIS further increases, efficiency drops rapidly in both two-coil and four-coil systems. The maximum efficiency that the two-coil and four-coil systems are able to maintain when varying the MIS from 0 to 300mm is given in Fig. 4.7(c). It can be observed that in the case of two-coil system, nearly constant maximum efficiency of $\sim 96\%$ is maintained when $MIS \leq 200$ mm, i.e., the high efficiency range is 0.2m. In the case of four-coil system, nearly constant efficiency of $\sim 90\%$ is maintained when $MIS \leq 275$ mm, i.e., the high efficiency range is 0.275m. When $MIS > \sim 210$ mm, efficiency of four-coil system is larger than efficiency of two coil system at every MIS point. For example, when $MIS = 300$ mm, two-coil system achieves efficiency of 35.1 % while four-coil system achieves efficiency as high as 72.2%, which is about two times higher than the two coil system efficiency. It can be concluded that four-coil system has longer high efficiency range than two-coil system when there exists lateral misalignment. In other words, four-coil system has higher misalignment tolerant capability.



(a)

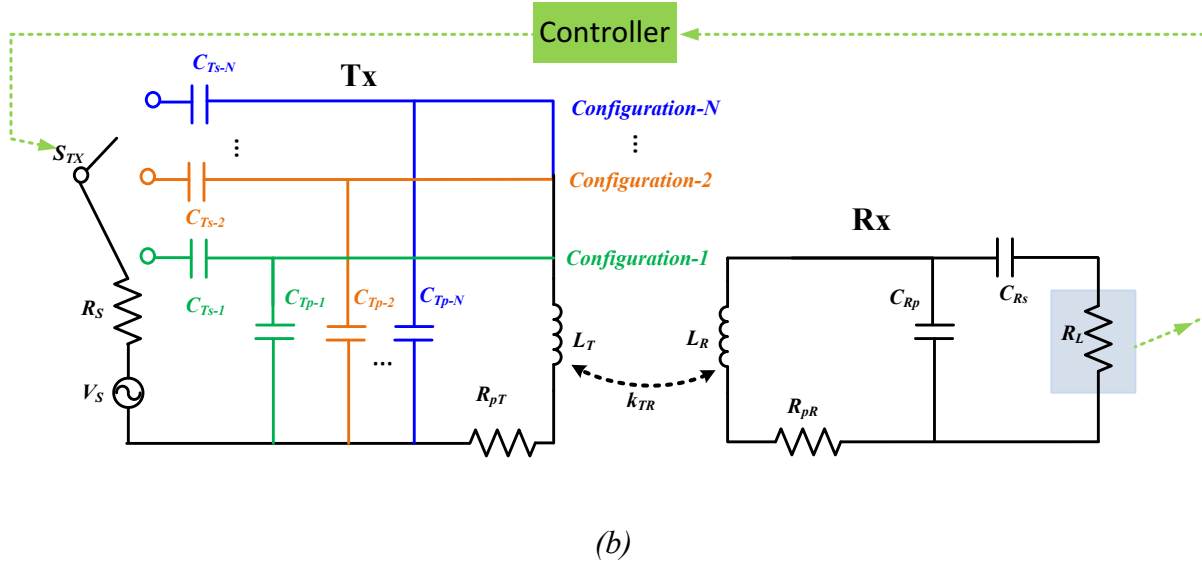


Figure 4.8: Two-coil reconfigurable WPT system: (a) both Tx side and Rx side are reconfigurable, (b) only Tx side is reconfigurable

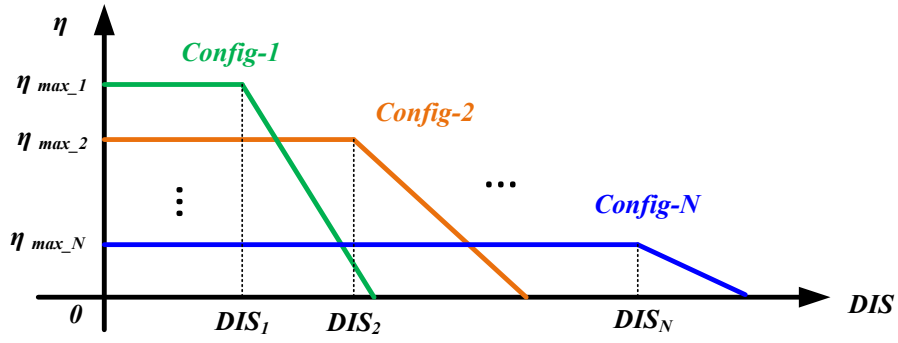
4.3 Two-coil Reconfigurable WPT System

Fig. 4.8(a) illustrates the equivalent circuit model of the two-coil reconfigurable WPT system. In this system, the Tx coil (L_T) and Rx coil (L_R) are coupled with the coupling factor of k_{TR} . There are N numbers of possible configurations in both the Tx and Rx side. Each configuration corresponds to one of the connections made by the switch at Tx side (S_{TX}) and the switch connection at Rx side (S_{RX}). Each configuration has different values of series capacitor and shunt capacitor. E.g. configuration-1 of Tx side has the series capacitor C_{TS-1} and shunt capacitor C_{Tp-1} , configuration-1 of Rx side has the series capacitor C_{RS-1} and shunt capacitor C_{Rp-1} , and so on. Synchronized switches S_{TX} and S_{RX} select one configuration at a time among N different configurations in order to obtain the maximum possible transmission efficiency under different conditions. On and off states of two switches are determined by an adaptive controller

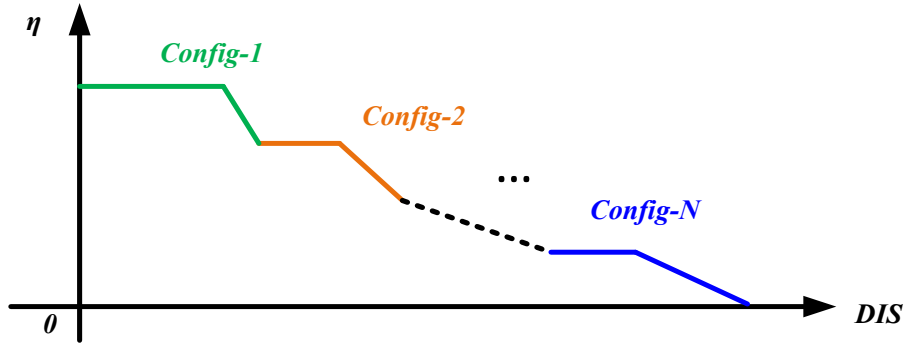
based on the sensed power value at load side (in a way that maximizes the power received at the load side).

In many applications such as consumer electronics charging and medical implantable devices charging, the size of Rx side has critical limitations. Therefore, it is more practical to include N number of adaptive configurations in Tx side while keeping only one configuration in Rx side as shown in Fig. 4.8(b). In this way, the size of Rx side can be significantly reduced.

In a reconfigurable WPT system, it is important to tune the resonance frequency of both Tx side and Rx side to the same value. The resonance frequency is determined by (4.11), where L is the coil inductance, C_s is the series capacitance and C_p is the shunt capacitance. Variations of C_p and/or C_s affect the resonance frequency. In order to obtain the same resonance frequency for all configurations, series capacitances and shunt capacitances need to satisfy (4.12). Since series resonance benefits for achieving relatively higher efficiency within shorter distance while shunt resonance benefits for achieving longer transmission distance with relatively lower efficiency [D14]. Maximum achievable efficiencies of all configurations (η_{max_i} , $i = 1, 2, \dots, N$) can be sorted as (4.13) and transmission distances of all configurations (DIS_i , $i = 1, 2, \dots, N$) while achieving η_{max_i} can be sorted as (4.14). The illustrative diagram of efficiency as a function of DIS for all configurations are shown in Fig. 4.9(a). Efficiency of WPT system at all DIS ranges can be optimized by adaptive configurations as illustrated in Fig. 4.9(b). It can be observed that adaptive reconfigurable WPT system significantly increases transmission efficiency and transmission distance compared with conventional WPT system with only one configuration (e.g. config-2).



(a)



(b)

Figure 4.9: (a) Illustrative efficiency curves for N configurations, (b) efficiency curve for reconfigurable WPT system

$$f_o = \frac{1}{2\pi\sqrt{L(C_p + C_s)}} \quad (4.11)$$

$$C_{s1} > C_{s2} > \dots > C_{sN} \quad (4.12-1)$$

$$C_{p1} < C_{p2} < \dots < C_{pN} \quad (4.12-2)$$

$$\eta_{\max_1} > \eta_{\max_2} > \dots > \eta_{\max_N} \quad (4.13)$$

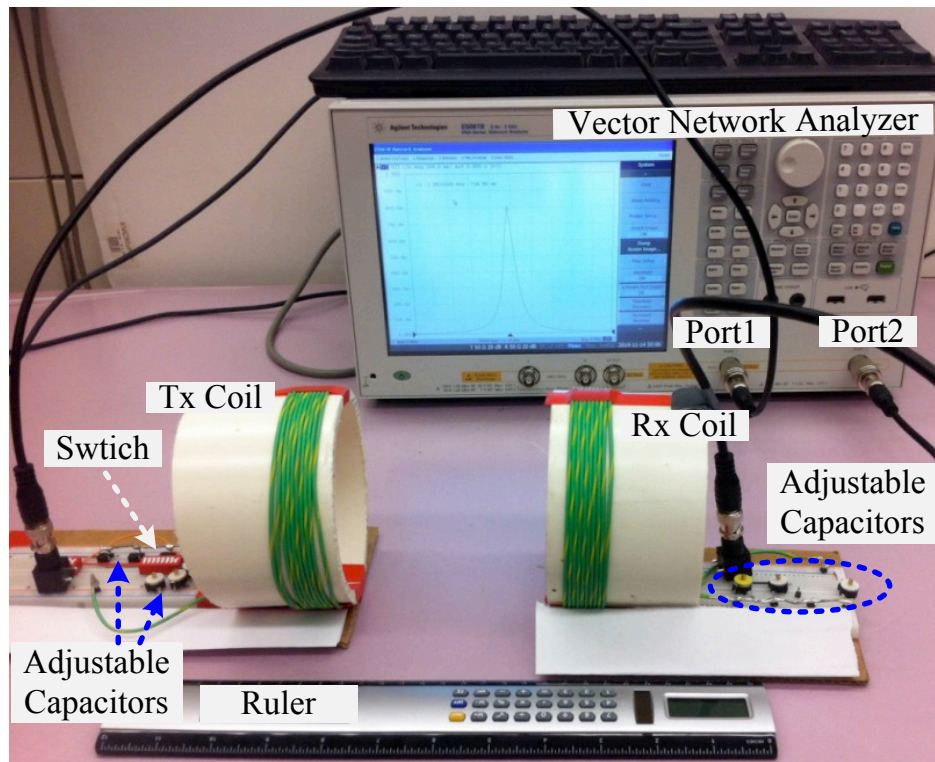
$$DIS_1 < DIS_2 < \dots < DIS_N \quad (4.14)$$

4.4 Proof of Concept Experimental Results

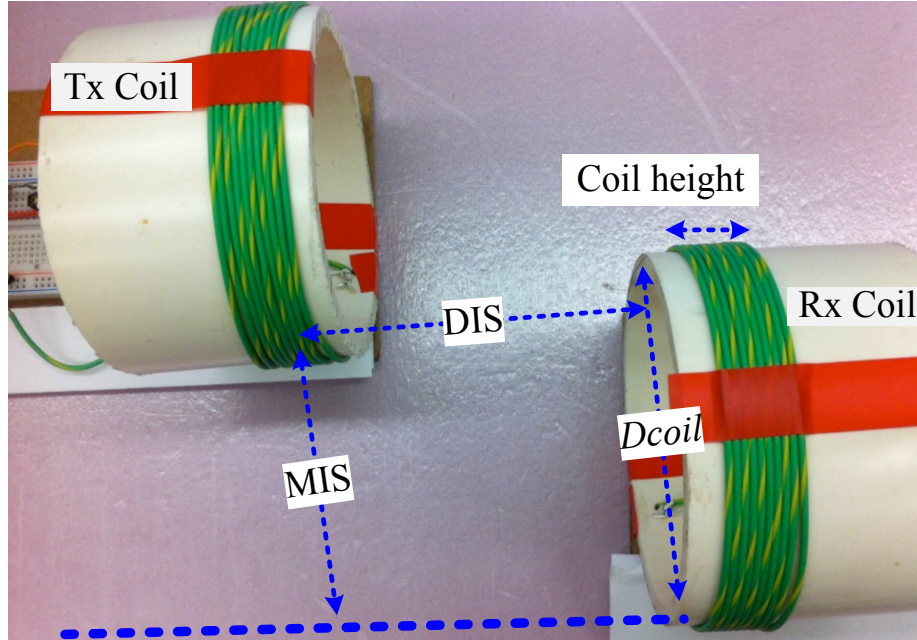
The preliminary proof of concept experimental prototype for the two-coil reconfigurable WPT system with three configurations at Tx side and only one configuration at Rx side is shown in Fig. 4.10(a). Design dimensions and parameters are illustrated in Fig. 4.10(b) and Table 4.5. A Vector network analyzer (VNA) E5061B from Agilent is used to experimentally measure $|S_{21}|$ and transmission efficiency is calculated from (5).

Table 4.5: Parameter specifications

Parameter	Values	Parameter	Values
Coil structure	Helix	Coil height	22mm
Wire material	copper	Rwire	1.1mm
R_S, R_L	50 Ω	Dcoil	11.5cm
Coil turns (Ncoil)	10	DIS	0-20cm
No. of Configurations	3	MIS	0-12cm



(a)



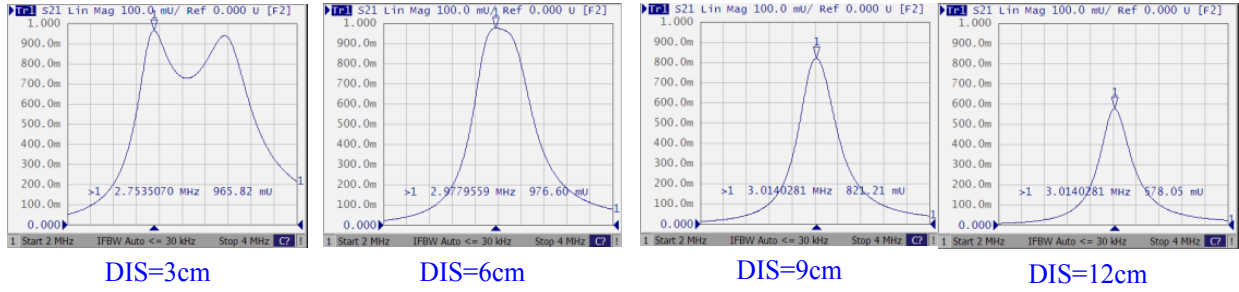
(b)

Figure 4.10: (a) Experimental testing setup for two-coil reconfigurable WPT system, (b) design specifications

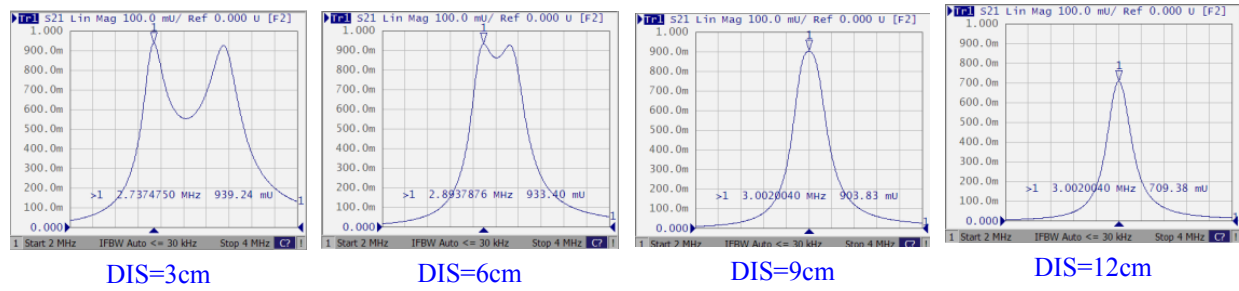
Both Tx side and Rx side circuit is tuned to the resonance frequency of 3MHz. Capacitance values of three configurations in Tx side and one configuration in Rx side are listed in Table 4.6, which obeys constrains in (4.12). Reconfigurable WPT system is experimentally compared with a conventional WPT system (with config-2 only in Tx side) when system is perfectly aligned (MIS=0) and when system is laterally misaligned at DIS=5cm.

Table 4.6: Capacitance values in different configurations

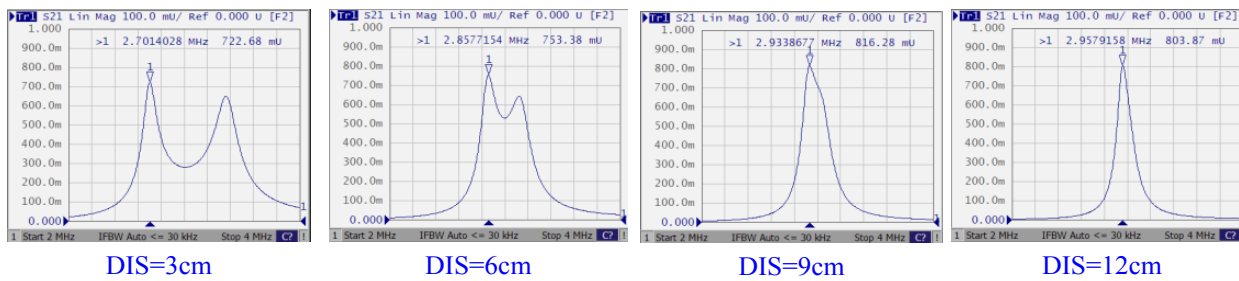
	Configuration	Cs	Cp
Tx side	Config-1	$C_{Ts-1} = 139\text{pF}$	$C_{Tp-1} = 10\text{pF}$
	Config-2	$C_{Ts-2} = 93\text{pF}$	$C_{Tp-2} = 55\text{pF}$
	Config-3	$C_{Ts-3} = 43\text{pF}$	$C_{Tp-3} = 103\text{pF}$
Rx side	–	$C_{Rs} = 120\text{pF}$	$C_{Rp} = 29\text{pF}$



(a) Config-1

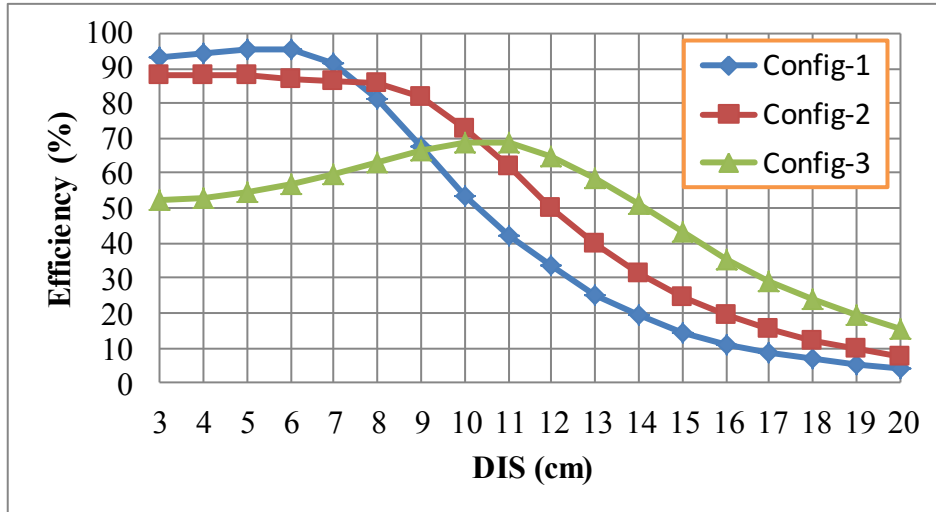


(b) Config-2

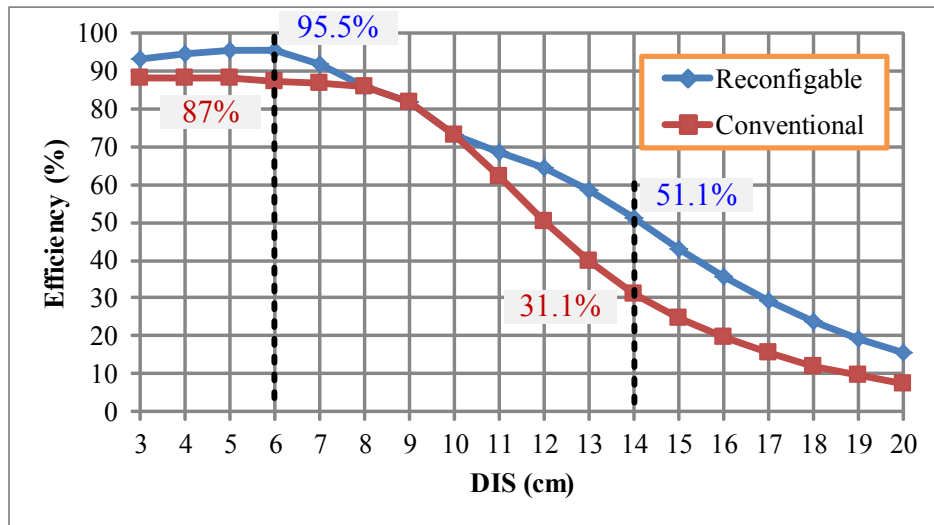


(c) Config-3

Figure 4.11: Frequency responses in selected DIS values of (a) config-1, (b) config-2 and (c) config-3

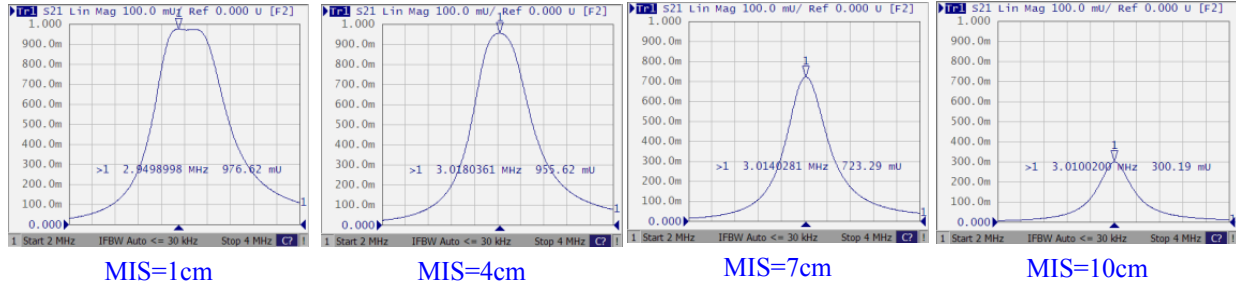


(a)



(b)

Figure 4.12: (a) Efficiency curves for three configurations, (b) efficiency comparison of reconfigurable and conventional WPT system in perfectly aligned case



(a) Config-1

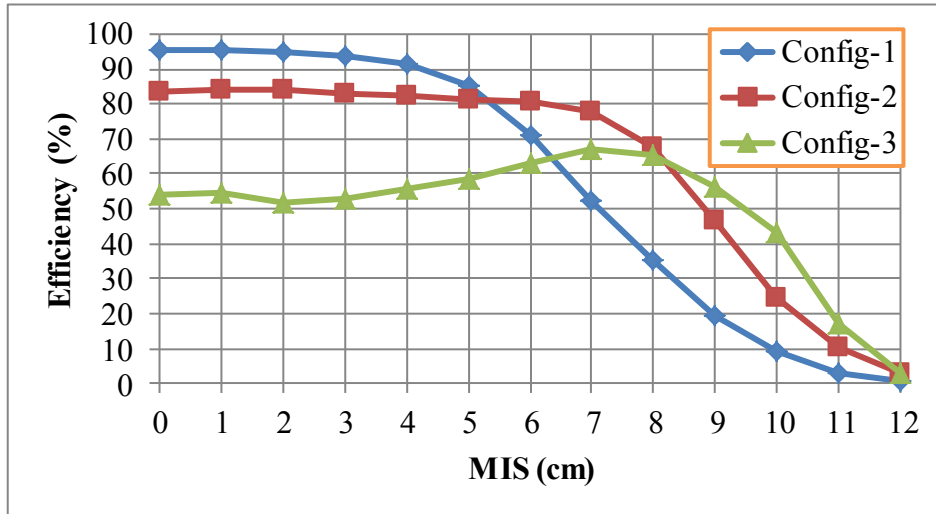


(b) Config-2

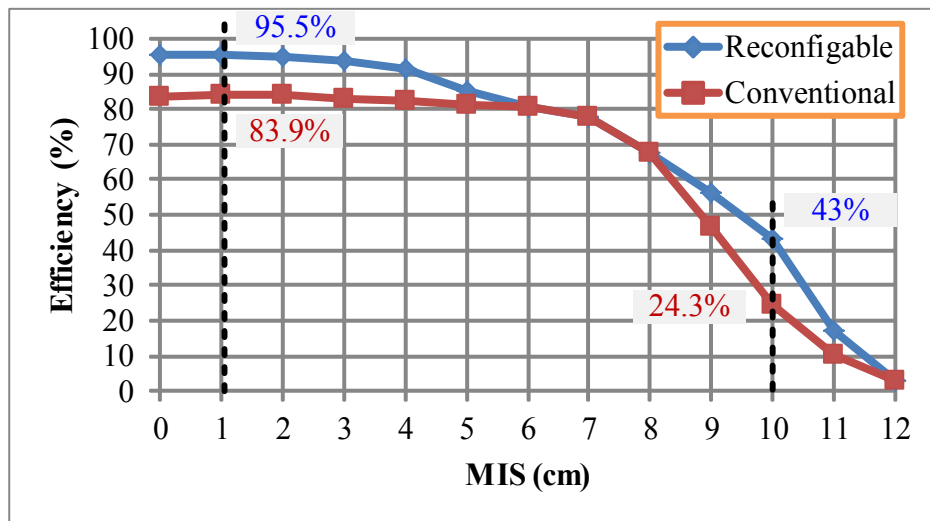


(c) Config-3

Figure 4.13: Frequency responses in selected MIS values of (a) config-1, (b) config-2 and (c) config-3 when DIS=5cm



(a)



(b)

Figure 4.14: (a) Efficiency curves for three configurations, (b) efficiency comparison of reconfigurable and conventional WPT system in laterally misaligned case

A. Perfectly aligned system

In perfectly aligned WPT systems, the lateral misalignment value $MIS=0$. Frequency responses of three different configurations for two-coil system at selected DIS values are illustrated in Fig. 4.11, where x-axis sweeps frequency from 2MHz to 4MHz and y-axis shows the value of $|S_{21}|$. Maximum $|S_{21}|$ value and corresponding frequency are marked on each figure, from which maximum achievable efficiency could be calculated from (4.5). E.g. reading Fig. 4.11(a) at $DIS=3\text{cm}$ finds that maximum $|S_{21}|$ value of 965mU ($=0.965$) is obtained when frequency is 2.75MHz. Therefore, maximum achievable efficiency can be calculated as $0.965^2 \approx 93.1\%$. When the system lies in the over-coupled region, frequency splitting could be clearly observed. In MRC-WPT systems, nearly constant transmission efficiency can be maintained as long as frequency splitting exists [D6-D12]. When frequency splitting disappears and the DIS further increases, efficiency drops down rapidly. The maximum achievable efficiencies that the three configurations of two-coil system are able to maintain when varying the DIS from 0 to 20cm are given in Fig. 4.12(a). These curves have similar shape with the theoretical illustrative curves shown in Fig. 4.9(a). It can be observed that config-1 yields the highest efficiency ($\sim 95\%$) for the short distance range of 0-7cm. Config-2 yields the highest efficiency ($\sim 80\%$) for the medium distance range of 8cm-10cm. Config-3 yields the highest efficiency ($\sim 60\%$) for the relatively longer distance range up to 14cm. It can also be observed that the more configurations are used in the system, the further the transmission efficiency can be optimized within all DIS ranges. Fig. 4.12(b) shows the comparison of the efficiency as a function of DIS between adaptively reconfigurable WPT system and the conventional WPT system. Results show that the reconfigurable system improves the transmission efficiency by up to 8.5% when $DIS=6\text{cm}$ and improves the transmission efficiency by up to 20% when

DIS=14cm. Meanwhile, the reconfigurable WPT system extends the range of over 50% efficiency from 12cm to 14cm, which extends the transmission distance by 16.7%.

B. Laterally misaligned system

Lateral misalignment is unavoidable in many WPT application systems such as consumer electronics charging [D10-D12]. The reconfigurable WPT system with lateral misalignment when DIS=5cm is evaluated. Frequency responses of three different configurations for two-coil system at selected MIS values are illustrated in Fig. 4.13. Frequency splitting could also be clearly observed when the system lies in the over-coupled region. The maximum achievable efficiencies that the three configurations are able to maintain when varying the DIS from 0 to 12cm are given in Fig. 4.14(a). It can be observed that config-1 yields the highest efficiency (~90%) for the short misalignment range of 0-5cm. Config-2 yields the highest efficiency (~75%) for the medium misalignment range of 5cm-8cm. Config-3 yields the highest efficiency (~50%) for the relatively longer misalignment range up to 10cm. Similar to the aligned case, the more configurations are used in the system, the further the transmission efficiency can be optimized within all MIS ranges. Fig. 4.14(b) shows the comparison of the efficiency as a function of MIS between adaptively reconfigurable WPT system and the conventional two-coil WPT. Results show that the reconfigurable system improves the transmission efficiency by up to 11.6% when MIS=1cm and improves the transmission efficiency by up to ~19% when MIS=10cm. Meanwhile, the reconfigurable WPT system extends the range of over 45% efficiency from ~9cm to ~10cm, which extends the misalignment range by 11.1%.

4.5 Summary

1) MRC-WPT system achieves nearly constant transmission efficiency as long as the frequency splitting exists. Both circuit model analysis and 3-D physical model simulation results show that four-coil system is able to efficiently transmit power for longer distance but achieves relatively lower efficiency when the distance is short when compared to the two-coil system. In laterally misaligned case, four-coil system achieves longer high efficiency range and shows higher misalignment tolerant capability compared with two-coil system.

2) The developed two-coil adaptive reconfigurable WPT system tracks the optimum transmission efficiency at different transmission distance ranges and different misalignment ranges by adaptively reconfiguring the circuits at Tx side and/or at Rx side. The reconfigurable WPT system includes only one Tx coil, one Rx coil, one or two synchronized switches, multiple capacitors and the adaptive controller which tracks the power received at the load side. Preliminary proof of concept experimental prototype with three different possible adaptive configurations at Tx side and one configuration at Rx side is designed and evaluated. Results show that the reconfigurable system improves the transmission efficiency by up to 20% in the perfectly aligned case and by up to 19% in laterally misaligned case. The more configurations are used in the adaptively reconfigurable WPT system, the further the transmission efficiency can be optimized for different distance and misalignment ranges.

CHAPTER 5

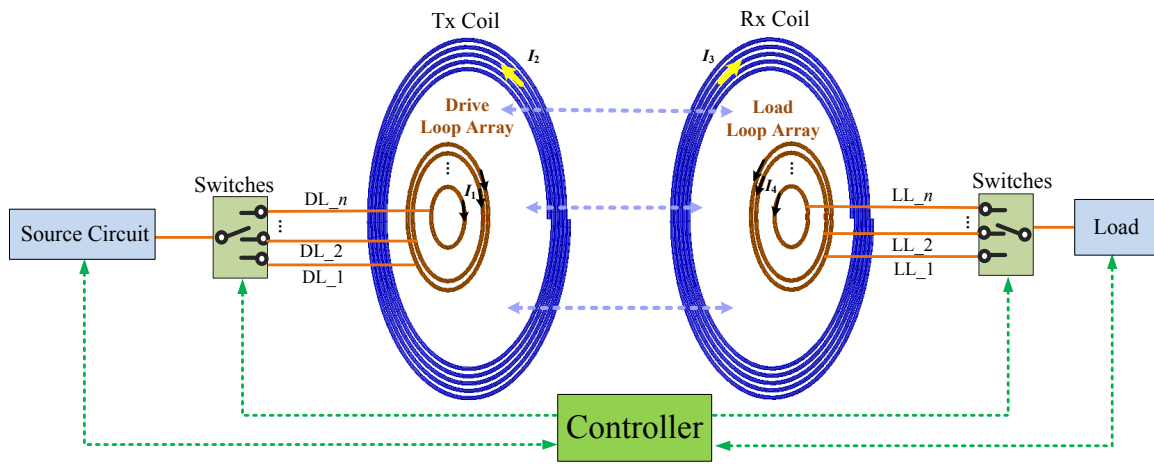
FOUR-COIL RECONFIGURABLE WPT SYSTEM

5.1 Introduction

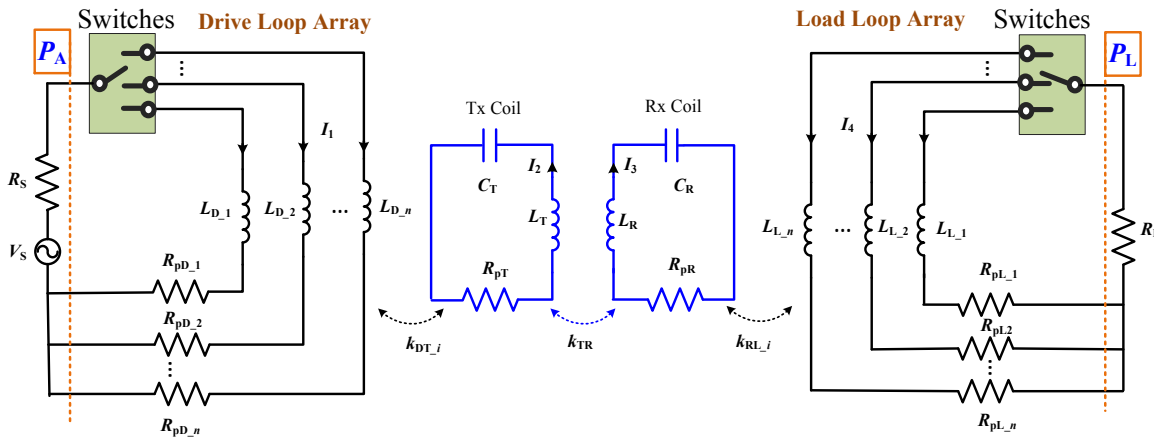
This chapter presents a method for a reconfigurable magnetic resonance coupled WPT (R-MRC-WPT) system in order to obtain maximum achievable transmission efficiency under various transmission distance (DIS) and/or misalignment (MIS) conditions. Higher efficiency, longer transmission distance and larger misalignment tolerance can be achieved with the presented R-MRC-WPT system when compared to the conventional four-coil MRC-WPT (C-MRC-WPT) system. The re-configurability in the R-MRC-WPT system is achieved by adaptively switching between different sizes of drive loops and load loops. Since all drive loops are in the same plane and all load loops are also in the same plane, this method does not require mechanical movements of the drive loop and load loop and does not result in system volume increase. The presented R-MRC-WPT system includes an array of drive loops, one Tx coil, one Rx coil, and an array of load loops. It adaptively switches between different system's configurations and tune the frequency of operation in order to obtain the maximum transmission efficiencies under various DIS and MIS conditions. The R-MRC-WPT is different from adding external tuning circuits such as capacitors and/or inductors to a C-MRC-WPT system with fixed size of drive/load loop. This is because external tuning circuits can only move the system operating point back to the impedance matching point to achieve the maximum possible efficiency at a given DIS (or set of conditions) for the fixed design structure, while switching between different loops reconfigures the system such that

it switches between different designs or operating/efficiency curves that are more optimized for different DIS and MIS conditions.

Next Section presents the R-MRC-WPT system and derives its theoretical basis based on an in depth analysis of a circuit model and an analytical model. Proof of concept experimental prototype results are presented in Section 5.3. Section 5.4 discusses the uses of ferrite and litz wire in R-MRC-WPT system and a summary is given in Section 5.5.



(a)



(b)

Figure 5.1: (a) Physical model and (b) the simplified circuit model of the R-MRC-WPT system ($i=1, 2, \dots, n$)

5.2 Reconfigurable MRC-WPT System

A. R-MRC-WPT System

Fig. 5.1(a) illustrates the physical model of the R-MRC-WPT system. The system includes an array of drive loops with n separate single loops (from DL_1 to DL_ n) placed in the same plane, a Tx coil, a Rx coil and an array of load loops with n separate single loops (from LL_1 to LL_ n) placed in the same plane. There is a switch array attached to the drive-loop array and another switch array attached to the load-loop array. A controller obtains information from load side and source side to decide which drive loop and load loop should be turned on (or connected) under a given operating condition such as a DIS and/or a MIS condition. The decision making is based on the calculation of transmission efficiency, which is defined as the load power (P_L) divided by the maximum available power at drive-loop (P_A), i.e. P_L/P_A . P_L and P_A are marked on Fig. 5.1(b). Note that transmission efficiency is different from the total system energy efficiency as clarified in [E1]. Therefore, the transmission efficiency for the four-coil system in this chapter is the drive loop to load loop efficiency. When switching between different loops using the switch-array, a switch must be turned on in order to keep at least one loop connected before another switch is turned off in order to avoid sudden interruption of current and power flow through the WPT system.

This chapter focuses on the symmetrical system analysis, i.e. DL_ i ($i=1,2,\dots,n$) at Tx side and LL_ i ($i=1,2,\dots,n$) at Rx side are turned on and off simultaneously such that the radii of the drive and load loops are equal for each configuration. The configuration of R-MRC-WPT system when DL_ i and LL_ i are turned on is referred to as Configuration- i . Tx and Rx are magnetically coupled to the DL_ i and LL_ i , respectively. DL_ i and LL_ i are connected to the power source

and the load respectively. Tx and Rx are symmetrical self-resonators (no external capacitors are connected to them) and they are linked through magnetically coupled resonances.

The adaptive reconfiguration for the MRC-WPT system is realized by switching between different loops such that higher efficiency can be obtained for various transmission ranges and misalignment conditions (which is explained in detail next). No mechanical movements are required in the R-MRC-WPT system. Since all drive loops are in the same plane and all load loops are in the same plane, the R-MRC-WPT system does not result in volume increased when compared to the C-MRC-WPT system. Therefore, the R-MRC-WPT system does not suffer from the disadvantages of mechanically tuned WPT systems as explained in part B of section 1.4, where mechanical movement is required and volume is increased.

Fig. 5.1(b) shows the simplified lumped element circuit model for the system illustrated in Fig. 5.1(a), where the capacitors shown with Tx and Rx coils represent the lumped model of the parasitic capacitances in the self-resonating Tx and Rx spiral coils. DL_{*i*} is modeled as an inductor L_{D_i} with a series parasitic resistor R_{pD_i} . DL_{*i*} is connected to an AC voltage source V_s (with a source resistance R_s) from one side and is inductively coupled to Tx with a coupling factor of k_{DT_i} from the other side. The coupling factor is defined in (5.1), where M_{xy} is the mutual inductance, and L_x and L_y are self-inductances. Tx and Rx are modeled as two separate series LCR resonators. Rx is coupled with Tx by a coupling factor of k_{TR} , which is inversely proportional to DIS^3 [E2-E4]. The self-resonance frequencies of two resonators are determined by (5.2) and the angular resonance frequency is defined as $\omega_o=2\pi f_o$. Similar with DL_{*i*}, LL_{*i*} is modeled as an inductor L_{L_i} with a series parasitic resistor R_{pL_i} . LL_{*i*} is connected to load R_L from one side and is inductively coupled to Rx through a coupling factor of k_{RL_i} from the other

side. No external capacitors are connected to drive and load loops and parasitic capacitances of drive and load loops are negligible.

$$k_{xy} = \frac{M_{xy}}{\sqrt{L_x L_y}} \quad (5.1)$$

$$f_o = \frac{1}{2\pi\sqrt{LC}} \quad (5.2)$$

B. Circuit Model Analysis

In this subsection, some important equations for R-MRC-WPT system are derived based on the simplified circuit model shown in Fig. 5.1(b). To simplify analysis, all cross couplings are ignored, only symmetrical system is analyzed, and only one DL_{*i*} and one LL_{*i*} are turned on in each configuration (configuration-*i*). Based on this, all circuit model parameters can be simplified as in (5.3). The impedance of each loop could then be expressed as in (5.4), where, Z_{D_{*i*}} and Z_{L_{*i*}} are the impedances of DL_{*i*} and LL_{*i*}, respectively. These two impedances are equal in the symmetrical case and are renamed as Z_{loop_{*i*}} = Z_{D_{*i*}} = Z_{L_{*i*}}. Z_T and Z_R are the impedances of Tx and Rx, respectively. These two impedances are also equal in the symmetrical case and are renamed as Z_{coil} = Z_T = Z_R. The current in each loop could be determined as given by (5.5) by using Kirchhoff's Voltage Law (KVL). The voltage ratio V_L/V_S as a function of ω and k_{TR} can then be solved for as given by (5.6), where $\omega = 2\pi f$.

$$\left\{ \begin{array}{l} R_{pD_i} = R_{pL_i} = R_{loop_i}, L_{D_i} = L_{L_i} = L_{loop_i} \\ R_{pT} = R_{pR} = R_{coil}, L_T = L_R = L_{coil}, C_T = C_R = C_{coil} \\ R_S = R_L = R_o \\ k_{DT_i} = k_{RL_i} = k_{lc_i}, M_{DT_i} = M_{RL_i} = M_{lc_i} \end{array} \right. \quad (i = 1, 2, \dots, n) \quad (5.3)$$

$$\begin{cases} Z_{\text{loop}_i} = Z_{D_i} = Z_{L_i} = R_o + R_{\text{loop}_i} + j\omega L_{\text{loop}_i} \\ Z_{\text{coil}} = Z_T = Z_R = R_{\text{coil}} + j\omega L_{\text{coil}} + \frac{1}{j\omega C_{\text{coil}}} \end{cases} \quad (i=1,2,\dots,n) \quad (5.4)$$

$$\begin{bmatrix} Z_{D_i} & j\omega M_{\text{lc}_i} & 0 & 0 \\ j\omega M_{\text{lc}_i} & Z_T & -j\omega M_{\text{TR}} & 0 \\ 0 & -j\omega M_{\text{TR}} & Z_R & j\omega M_{\text{lc}_i} \\ 0 & 0 & j\omega M_{\text{lc}_i} & Z_{L_i} \end{bmatrix} \begin{bmatrix} I_1 \\ I_2 \\ I_3 \\ I_4 \end{bmatrix} = \begin{bmatrix} V_S \\ 0 \\ 0 \\ 0 \end{bmatrix} \quad (i=1,2,\dots,n) \quad (5.5)$$

$$\frac{V_L}{V_S}(\omega, k_{\text{TR}}) = \frac{j\omega^3 k_{\text{TR}} k_{\text{lc}_i}^2 L_{\text{coil}}^2 L_{\text{loop}_i} R_L}{(\omega^2 k_{\text{lc}_i}^2 L_{\text{coil}} L_{\text{loop}_i} + Z_{\text{coil}} Z_{\text{loop}_i})^2 + \omega^2 k_{\text{TR}}^2 (L_{\text{coil}} Z_{\text{loop}_i})^2} \quad (i=1,2,\dots,n) \quad (5.6)$$

The voltage ratio in (5.6) can directly be used to calculate the equivalent S_{21} scattering parameter (5.7), which then can be used in (5.8) to evaluate the transmission efficiency (η) for MRC-WPT system when source and load impedances are equal [E1, E3-E8]. Mathematical proofs for (5.7) and (5.8) are provided in appendix I. The series quality factor of the Tx and Rx coils is defined by (5.9). The quality factor of drive/load loop at the self-resonance frequency of Tx/Rx is defined in (5.10).

$$S_{21} = 2 \frac{V_L}{V_S} \quad (5.7)$$

$$\eta = |S_{21}|^2 \times 100\% \quad (5.8)$$

$$Q_{\text{coil}} = \frac{1}{R_{\text{coil}}} \sqrt{\frac{L_{\text{coil}}}{C_{\text{coil}}}} = \frac{1}{\omega_o R_{\text{coil}} C_{\text{coil}}} = \frac{\omega_o L_{\text{coil}}}{R_{\text{coil}}} \quad (5.9)$$

$$Q_{\text{loop}_i} \Big|_{\omega=\omega_o} = \frac{\omega_o L_{\text{loop}_i}}{R_o + R_{\text{loop}_i}} \quad (i=1,2,\dots,n) \quad (5.10)$$

Using the same derivation techniques as in [E3-E5], for configuration- i , the critical coupling factor (k_{c_i}), critical $|S_{21}|$ ($|S_{21}|_{c_i}$) and transmission efficiency (η_i) can be derived as given by (5.11), (5.12-1) and (5.12-2), respectively. Note that k_{c_i} is the smallest Tx to Rx coupling factor (k_{TR}) within which the system is able to maintain nearly constant η_i when configuration- i is selected. In other words, as long as $k_{TR} \geq k_{c_i}$, nearly constant η_i can be maintained in the corresponding transmission distance DIS_i . When $k_{TR} > k_{c_i}$, the system operates in the over coupled region and there exists frequency splitting. When $k_{TR} = k_{c_i}$, the system operates at the critical coupling point, at which the two resonance frequencies merge into one. When $k_{TR} < k_{c_i}$, the system operates in the under coupled region where there is no frequency splitting anymore. In the under coupled region, the η_i quickly decreases as Rx moves away from Tx. Therefore, a smaller k_{c_i} (which corresponds to a longer DIS_i) and a larger $|S_{21}|_{c_i}$ (which corresponds to a higher η_i) are desired in order to extend transmission distance with higher transmission efficiencies.

$$k_{c_i} = \frac{1}{Q_{coil}} + k_{lc_i}^2 \frac{Q_{loop_i} R_o}{Z_{loop_i}} = \frac{1}{Q_{coil}} + k_{lc_i}^2 \frac{\omega}{\frac{R_o}{L_{loop_i}} + j\omega} \quad (i=1,2,\dots,n) \quad (5.11)$$

$$|S_{21}|_{c_i} = \frac{k_{lc_i}^2 Q_{coil} Q_{loop_i} R_o^2}{k_{lc_i}^2 Q_{coil} Q_{loop_i} R_o Z_{loop_i} + Z_{loop_i}^2} = \frac{k_{lc_i}^2 Q_{loop_i} R_o}{k_{c_i} Z_{loop_i}} \quad (i=1,2,\dots,n) \quad (5.12-1)$$

$$\eta_i = |S_{21}|_{c_i}^2 = \left(\frac{k_{lc_i}^2 Q_{coil} Q_{loop_i} R_o^2}{k_{lc_i}^2 Q_{coil} Q_{loop_i} R_o Z_{loop_i} + Z_{loop_i}^2} \right)^2 = \left(\frac{k_{lc_i}^2 Q_{loop_i} R_o}{k_{c_i} Z_{loop_i}} \right)^2 \quad (i=1,2,\dots,n) \quad (5.12-2)$$

$$\eta_i = |S_{21}|_{c_i}^2 = \left(\frac{Q_{coil} R_o^2}{Q_{coil} R_o Z_{loop_i} + \frac{Z_{loop_i}^2}{Q_{loop_i} k_{lc_i}^2}} \right)^2 \quad (i=1,2,\dots,n) \quad (5.12-3)$$

Table 5.1. Design example parameter values [E3]

Parameters	Values	Parameters	Values
f_o	10 MHz	$R_{pD} = R_{pL} = R_{loop}$	0.25Ω
$R_S = R_L = R_o$	50Ω	Q_{loop}	1.25
$L_T = L_R = L_{coil}$	$20.0 \mu\text{H}$	$k_{DT} = k_{RL} = k_{lc}$	0.1
$C_T = C_R = C_{coil}$	12.6 pF	k_{TR}	$0 < k_{TR} < 1$
$R_{pT} = R_{pR} = R_{coil}$	1Ω	Frequency sweep	$8 \text{ MHz} \leq f \leq 12 \text{ MHz}$
$L_D = L_L = L_{loop}$	$1.0 \mu\text{H}$	-	-

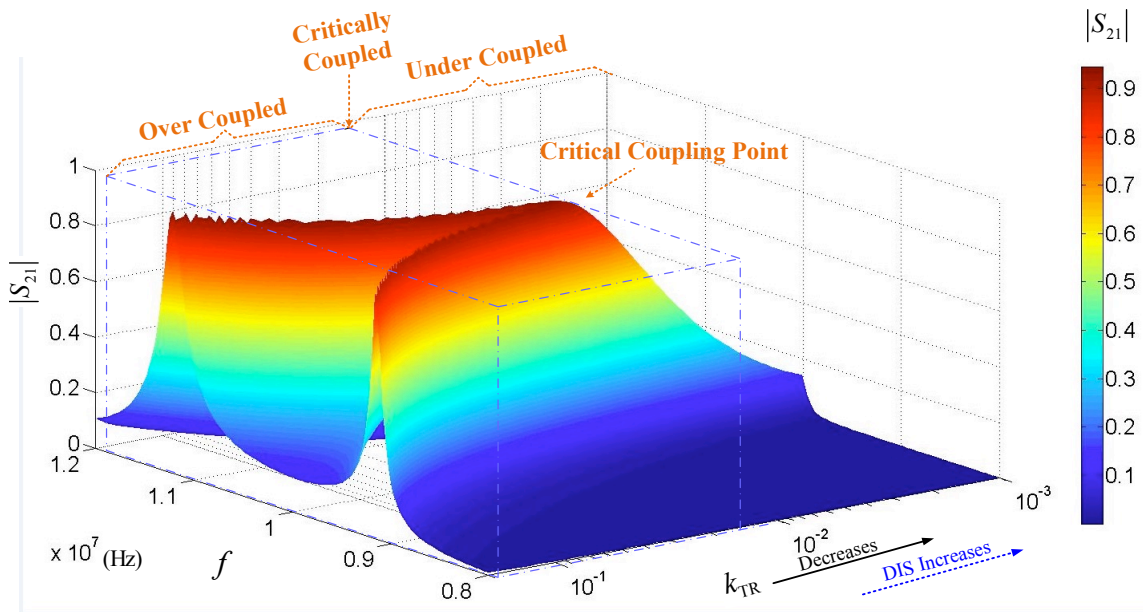


Figure 5.2: A 3-D view of $|S_{21}|$ as functions of frequency and k_{TR}

A 3-D view of $|S_{21}|$ as functions of frequency and k_{TR} is plotted in Fig. 5.2 by using the example parameters shown in Table 5.1, where the x-axis is the frequency, the y-axis is k_{TR} value and z-axis is the value of $|S_{21}|$. As expected, frequency splitting is observed in the over coupled region when $k_{TR} > k_{c_i}$, within which nearly constant $|S_{21}|$ value is maintained. With the decrease

of k_{TR} , the two frequency peaks gradually merge into one at the critical coupling point when $k_{TR} = k_{c_i}$. When k_{TR} decreases further with the increase of DIS, $|S_{21}|$ value decreases quickly.

It can be observed from (5.11) and (5.12-2) that a larger Q_{coil} contributes to both a smaller k_{c_i} and a larger $|S_{21}|_{c_i}$. Based on this, maximizing the value of Q_{coil} can result in increasing the values of DIS_{*i*} and η_{i} . Other factors that affect k_{c_i} and η_{i} include k_{lc_i} , Q_{loop_i} , Z_{loop_i} , and R_o . R_o is fixed at 50Ω in this analysis. Moreover, it can be observed from (5.4) and (5.10) that Z_{loop_i} and Q_{loop_i} are all directly proportional to the L_{loop_i} . In order to clarify the relationship between the physical dimensions of drive/load loop and L_{loop_i} , k_{lc_i} , k_{c_i} , η_{i} , and DIS_{*i*}, analytical model of R-MRC-WPT system is derived and discussed next in the chapter.

C. Analytical Model Analysis

The value of the self-inductance of a single conductor loop is given by (5.13) [E9], where r is the radius of the loop, μ_o is the vacuum permeability, μ_r is the relatively permeability (in the case of air $\mu_r \approx 1$), and d is the diameter of the conductor. It can be observed from (5.13) that the inductance L_{loop_i} of the i^{th} drive/load loop is directly proportional to its radius r_i .

$$L_{loop} = \mu_o \mu_r r \left[\ln\left(\frac{16r}{d}\right) - 2 \right] \quad (5.13)$$

However, the relationship between k_{lc_i} and r_i is not easily observable because when varying r_i , both self-inductance L_{loop_i} and mutual inductance M_{lc_i} change. In order to study how k_{lc_i} varies as a function of r_i , an analytical model of k_{lc_i} as a function of r_i is derived. Mutual inductance of two planar loops is given by (5.14) based on Neumann's equation [E10], where r_1 and r_2 are radii of two different loops respectively, and h is the distance between the two loops.

$$M = \frac{\mu_o \pi r_1^2 r_2^2}{2(r_1^2 + r_2^2 + h^2)^{3/2}} \left(1 + \frac{15}{32} \gamma^2 + \frac{315}{1024} \gamma^4 \right) \quad (5.14-1)$$

$$\gamma = 2r_1 r_2 / (r_1^2 + r_2^2 + h^2) \quad (5.14-2)$$

Multi-turn spiral coil can be modeled as concentric loops and its self-inductance can then be calculated from (5.15), which can be used to calculate the inductance of Tx/Rx coil. In (5.15), n is the number of turns and L_j is the inductance of j^{th} turn in the Tx/Rx coil, which can be calculated from (5.13).

$$L_{\text{coil}} = \sum_{j=1}^n L_j + 2 \times \sum_{a=1}^{n-1} \sum_{b=a+1}^n M_{ab} \quad (5.15)$$

Mutual inductance between two coils can be derived as in (5.16) [E10], where n_1 and n_2 are the number of turns for the two coils, M_{ab} represents the mutual inductance between the a^{th} turn of one coil and the b^{th} turn of the other coil. M_{ab} can be calculated from (5.14).

$$M = \sum_{a=1}^{n_1} \sum_{b=1}^{n_2} M_{ab} \quad (5.16)$$

Based on (5.1) and (5.13)-(5.16), k_{lc_i} can be expressed as in (5.17), where M_{lc_i} is the mutual inductance between i^{th} drive/load loop and Tx/Rx coil, L_{loop_i} is the inductance of i^{th} drive/load loop, n_1 is the number of turns of the drive/load loop (which is equal to 1), and n_2 is the number of turns of Tx/Rx coil.

$$k_{\text{lc}_i} = \frac{M_{\text{lc}_i}}{\sqrt{L_{\text{loop}_i} \times L_{\text{coil}}}} = \frac{\sum_{a=1}^{n_1} \sum_{b=1}^{n_2} M_{ab}}{\sqrt{L_{\text{loop}_i} \times \left(\sum_{b=1}^{n_2} L_b + 2 \times \sum_{a=1}^{n_2-1} \sum_{b=a+1}^{n_2} M_{ab} \right)}} \quad (5.17)$$

From (5.17), k_{lc_i} as a function of r_i can be derived as in (5.18), where r_b is the radius of the b^{th} turn of Tx/Rx coil and d_{lc} is the distance between drive/load loop and Tx/Rx coil.

$k_{lc_i} =$

$$\frac{\sum_{b=1}^{b=n_2} \left[\frac{\mu_0 \pi r_i^2 r_b^2}{2(r_i^2 + r_b^2 + d_{lc}^2)^{3/2}} \left(1 + \frac{15}{32} \gamma_b^2 + \frac{315}{1024} \gamma_b^4 \right) \right]}{\sqrt{\left\{ \mu_0 \mu_r r_i \left[\ln\left(\frac{16r_i}{d}\right) - 2 \right] \right\} \left\{ \sum_{b=1}^{n_2} \mu_0 \mu_r r_b \left[\ln\left(\frac{16r_b}{d}\right) - 2 \right] + 2 \sum_{a=1}^{n_2-1} \sum_{b=a+1}^{n_2} \left[\frac{\mu_0 \pi r_a^2 r_b^2}{2(r_a^2 + r_b^2)^{3/2}} \left(1 + \frac{15}{32} \gamma_{ab}^2 + \frac{315}{1024} \gamma_{ab}^4 \right) \right] \right\}}}$$

(5.18)

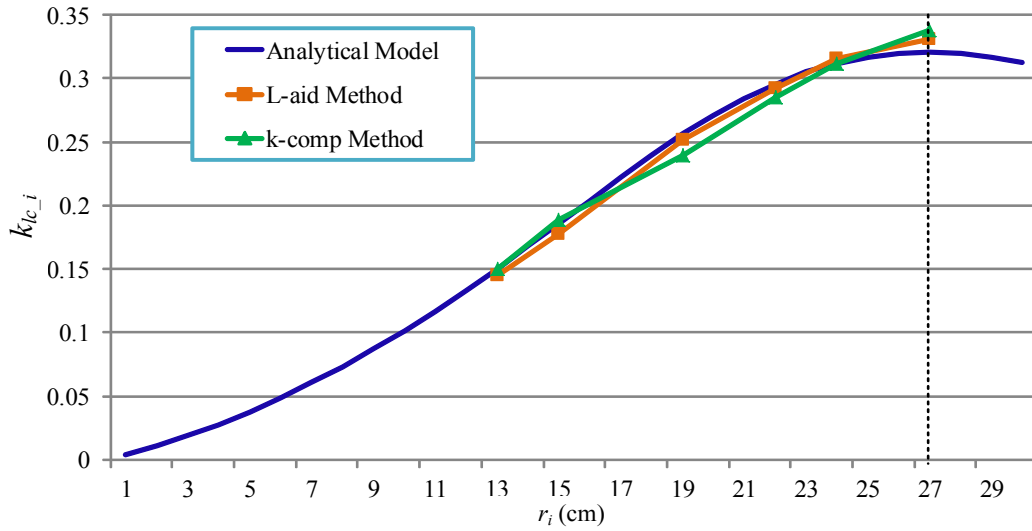


Figure 5.3: k_{lc_i} as a function of r_i

In order to be able to clearly observe the relationship between k_{lc_i} and r_i , k_{lc_i} as a function of r_i is plotted as shown in Fig. 5.3 by using the analytical model in (5.18), where $0 < r_i \leq$ outer radius of Tx/Rx coil (=30 cm) and the other parameters are given in table 5.2. It can be observed from Fig. 5.3 that k_{lc_i} is directly proportional to r_i when $0 < r_i \leq 27$ cm. When $27 \text{cm} < r_i \leq 30$ cm, k_{lc_i} drops slightly. It should be noted that 27cm is equal to $(R_{\text{outer}} + R_{\text{inner}})/2$, where R_{outer} is the outer radius of the spiral coil and R_{inner} is the inner radius of the spiral coil. Therefore, the

maximum theoretical radius of drive/load loop which guarantees that k_{lc_i} is directly proportional to r_i is $r_{\max}=(R_{\text{outer}}+R_{\text{inner}})/2$. This leads to the conclusion that k_{lc_i} is directly proportional to r_i when $0 < r_i \leq r_{\max}$.

In addition to the results obtained from the analytical model, k_{lc_i} as a function of r_i is also measured from the experimental prototype by using the inductance aiding method as given by (5.19) and the k-compensation method as given by (5.20) [E11]. The mathematical proofs for (5.19) and (5.20) are shown in appendix II and III, respectively. All of the inductance values in (5.19) are measured using impedance analysis function of the Vector Network Analyzer (VNA E5061B). When (5.20) is utilized, a SMA 100A signal generator is used to inject a sinusoidal voltage wave into the coil, a Tektronix P5205 differential probe is used to measure the open circuit voltage across the loop array and a Tektronix TCP A300 current probe is used to measure currents. It can be observed that the experimental measurements shown in Fig. 5.3 agree with the results obtained from the analytical model.

$$k_{lc_i} = \frac{L_{\text{aid_}i} - (L_{\text{coil}} + L_{\text{loop_}i})}{2\sqrt{L_{\text{coil}}L_{\text{loop_}i}}} \quad (5.19)$$

$$k_{lc_i} = \sqrt{\left. \frac{V_{2oc} \times I_{2sc}}{V_{1oc} \times I_{1sc}} \right|_i} \quad (5.20)$$

Next, the relationship between k_{lc_i} and transmission efficiency (η_{-i}) is discussed. η_{-i} is derived as in (5.12-2). In order to clearly observe the relationship between k_{lc_i} and η_{-i} , (5.12-2) is rewritten as in (5.12-3), which shows that η_{-i} is directly proportional to k_{lc_i} . Due to the fact that k_{lc_i} is directly proportional to r_i when $0 < r_i \leq r_{\max}$, r_i is directly proportional to η_{-i} .

In order to understand the relationship between k_{lc_i} and DIS_{-i} , it is important to recall the definition of the critical coupling factor k_{l_i} given in Part B of this section (k_{c_i} is the smallest Tx

to Rx coil coupling factor (k_{TR}) within which the system is able to maintain nearly constant η_i when configuration- i is selected). Since k_{TR} is inversely proportional to DIS^3 [E2-E4], a smaller k_{c_i} is desired in order to achieve a longer DIS_i . It can be observed from (5.11) that k_{lc_i} is directly proportional to k_{c_i} , and therefore a smaller k_{lc_i} results in a longer DIS_i . Due to the fact that both k_{lc_i} and L_{loop_i} are directly proportional to r_i , a smaller r_i results in a longer transmission distance DIS_i .

It can be concluded from the analytical model analysis that r_i is directly proportional to η_i but inversely proportional to DIS_i . Therefore, by switching between different configurations, i.e. different sizes of drive/load loops, higher transmission efficiency can be achieved for different ranges of distances.

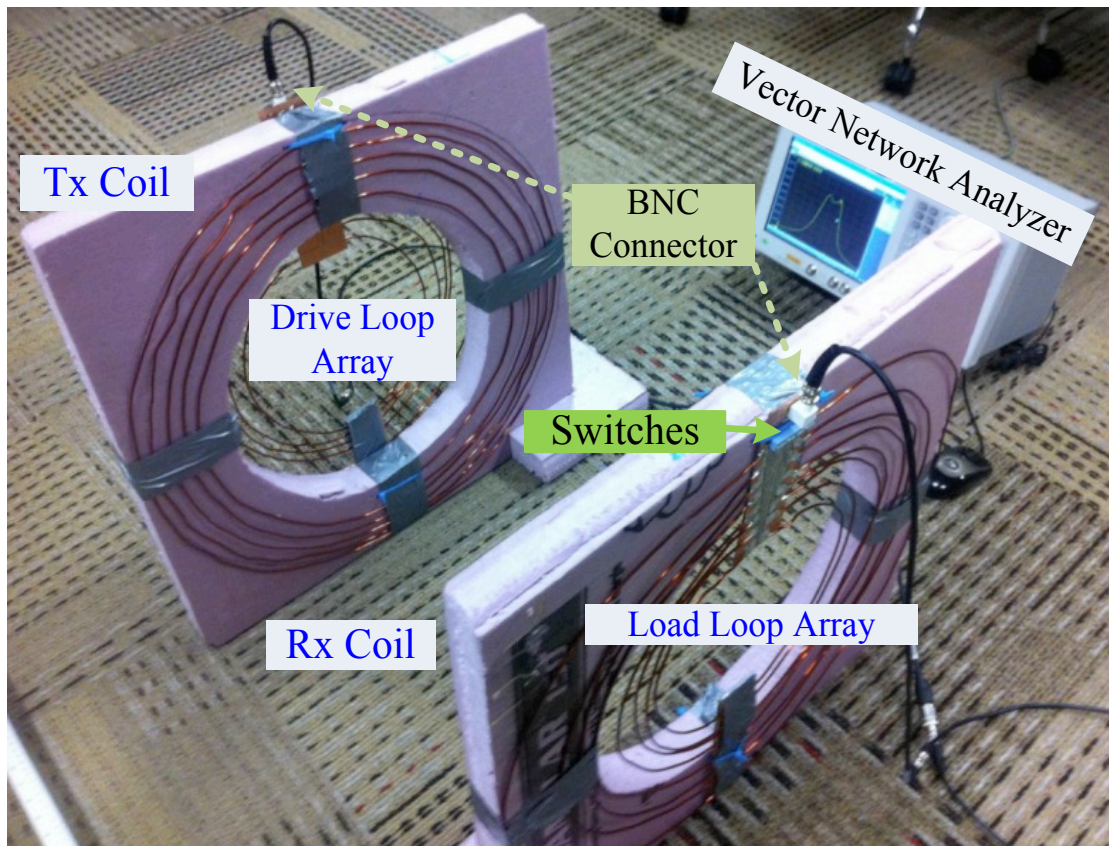
5.3 Proof of Concept Experimental Prototype Results

A. System Descriptions

A proof of concept experimental prototype (photo picture is shown in Fig. 5.4(a)) is developed to study and validate the presented method of the R-MRC-WPT system and to obtain preliminary experimental results. The prototype parameter specifications are shown in Fig. 5.4(b) and Table 5.2. There are six drive loops in the drive loop array and six corresponding load loops in the load loop array. Each drive loop and its corresponding load loop are equal in size and similar in design (symmetrical system). The Drive loop array and the load loop array are connected to two separate switch arrays which are able to turn on one drive loop and a corresponding load loop at the same time. BNC connectors provide interfaces to the external circuits. A Vector Network Analyzer (VNA E5061B) is used for measuring the transmission efficiencies of the R-MRC-WPT system under various distances and misalignment conditions. Configuration- i is abbreviated as Config- i in the rest of this chapter, where $i = 1, 2 \dots 6$. In the

next two subsections, the R-MRC-WPT system performance is evaluated by obtaining experimental measurements and is compared to a C-MRC-WPT system (where there exist only DL₂ and LL₂ in the system) when varying DIS and MIS.

In the next two subsections, the R-MRC-WPT system performance is evaluated by obtaining experimental measurements and is compared to a C-MRC-WPT system (where there exists only DL₂ and LL₂ in the system of Fig. 5.1(a)) and another system using capacitor tuning matrix (where there exists only DL₂ and LL₂ as well), which is abbreviated as Cap-Tuning system (illustrated in Fig. 5.5) in the rest of the chapter.



(a)

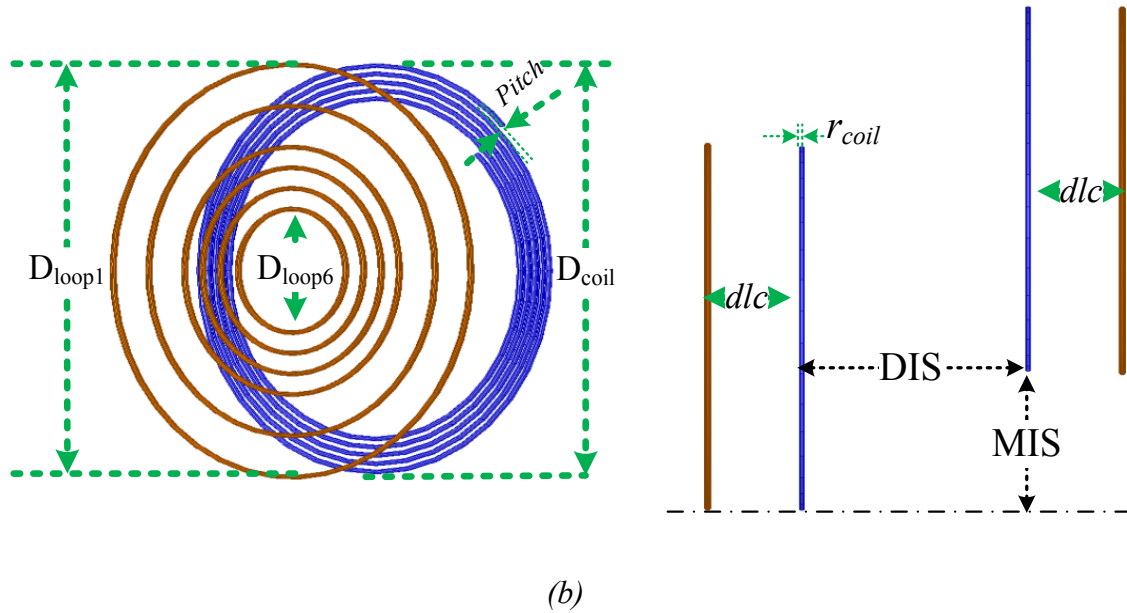


Figure 5.4. (a) Proof of concept prototype of R-MRC-WPT system and (b) parameter specifications

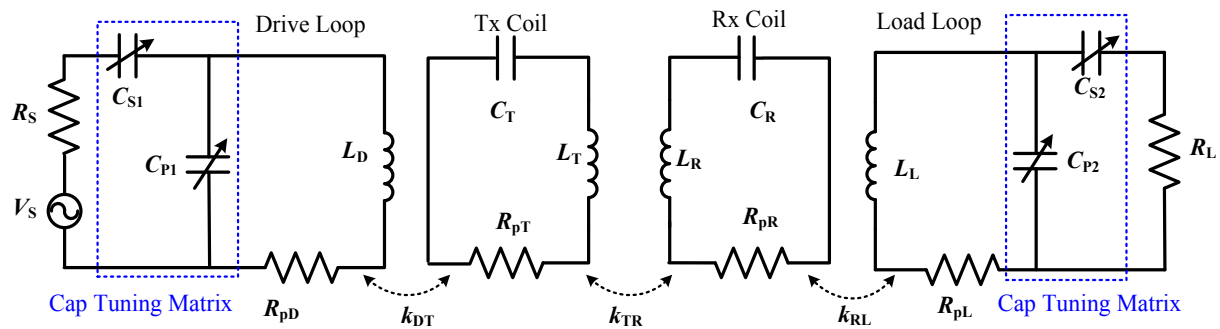


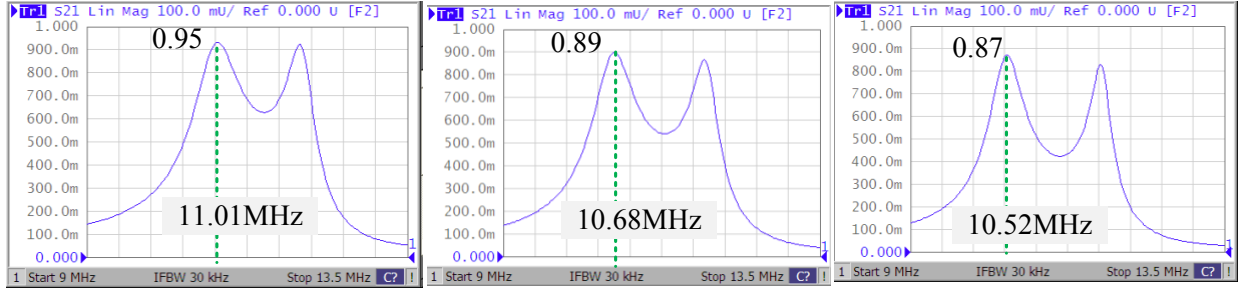
Figure 5.5. Circuit diagram of four-coil MRC-WPT system using capacitor tuning (Cap-Tuning system)

Table 5.2: Parameter specifications of the R-MRC-WPT system

Parameters	Values	Parameters	Values
Coil structure	Spiral	DIS	0-2m
Wire material	Copper	MIS	0-0.6m
R_S, R_L	50 Ω	$DL_1 = 2r_1$	54cm
Coil turns (N_{coil})	5	$DL_2 = 2r_2$	48cm
$D_{coil} = 2R_{outer}$	60cm	$DL_3 = 2r_3$	44cm
Pitch	1.5cm	$DL_4 = 2r_4$	38cm
r_{coil}	1.3mm	$DL_5 = 2r_5$	30cm
r_{loop}	1.3mm	$DL_6 = 2r_6$	26cm
R_{outer}	30cm	R_{inner}	24cm
dlc	5cm	-	-

B. DIS Variation

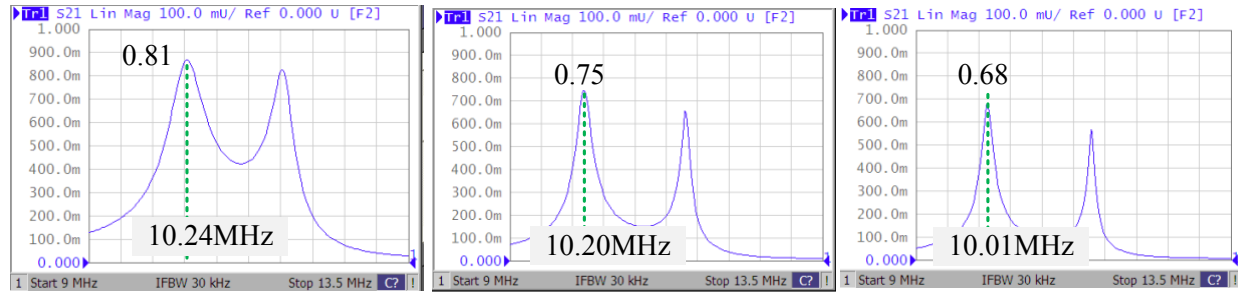
In this subsection, the presented experimental measurements and comparisons are for when MIS = 0 and DIS is changing from 0 to 2m with 10 cm steps. Transmission efficiencies of R-MRC-WPT system when selecting different configurations (from config-1 to config-6) are calculated based on (5.8) from measured data using VNA. Fig. 5.6 shows selected measurement results when DIS = 30cm (Fig. 5.6a) and DIS = 60cm (Fig. 5.6b). It can be observed that when DIS=30cm, frequency splitting exists in all six configurations. The peak value of $|S_{21}|$ decreases gradually from 0.95 to 0.68 as the configuration is changed from config-1 to config-6. Therefore, config-1 has the highest efficiency at DIS=30cm compared to the other configurations. When DIS=60 cm, there is no frequency splitting in config-1, config-2 and config-3 while there exists frequency splitting in the rest of the configurations. The value of $|S_{21}|$ first increases and then decrease when switching from config-1 to config-6. The highest efficiency for DIS=60 cm is obtained when using config-3.



(a-1) DIS = 30cm, Config-1

(a-2) DIS = 30cm, Config-2

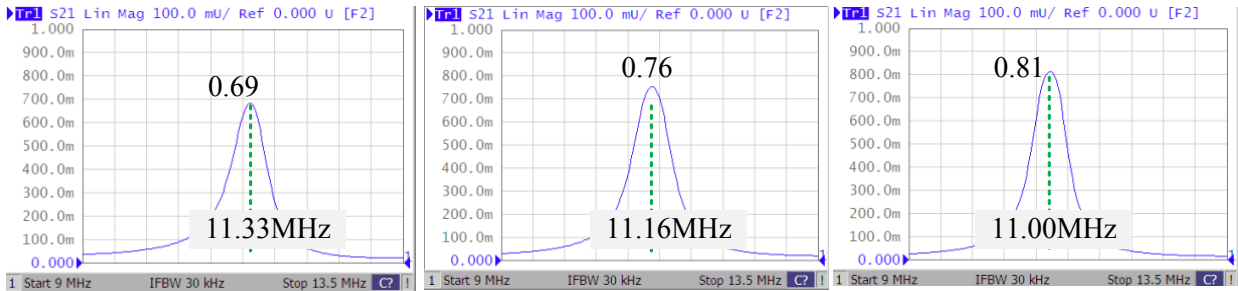
(a-3) DIS = 30cm, Config-3



(a-4) DIS = 30cm, Config-4

(a-5) DIS = 30cm, Config-5

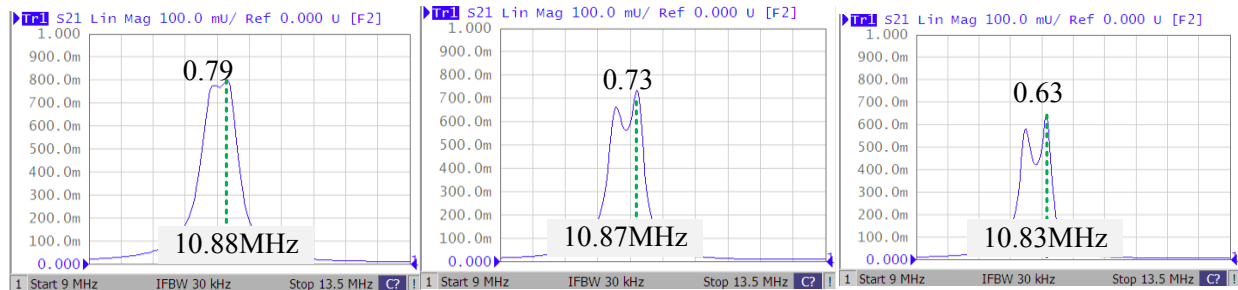
(a-6) DIS = 30cm, Config-6



(b-1) DIS = 60cm, Config-1

(b-2) DIS = 60cm, Config-2

(b-3) DIS = 60cm, Config-3

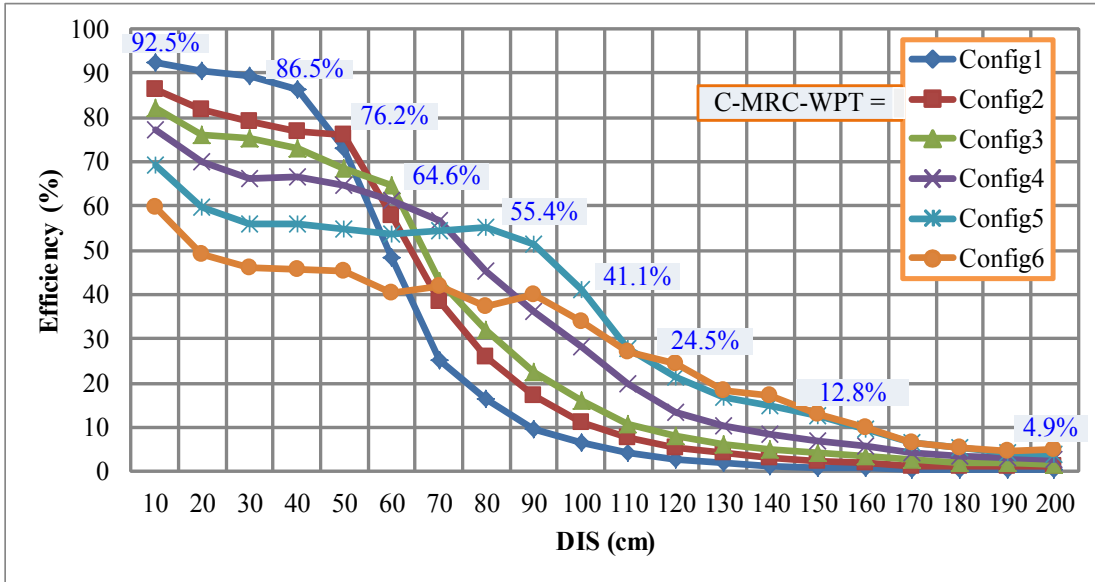


(b-4) DIS = 60cm, Config-4

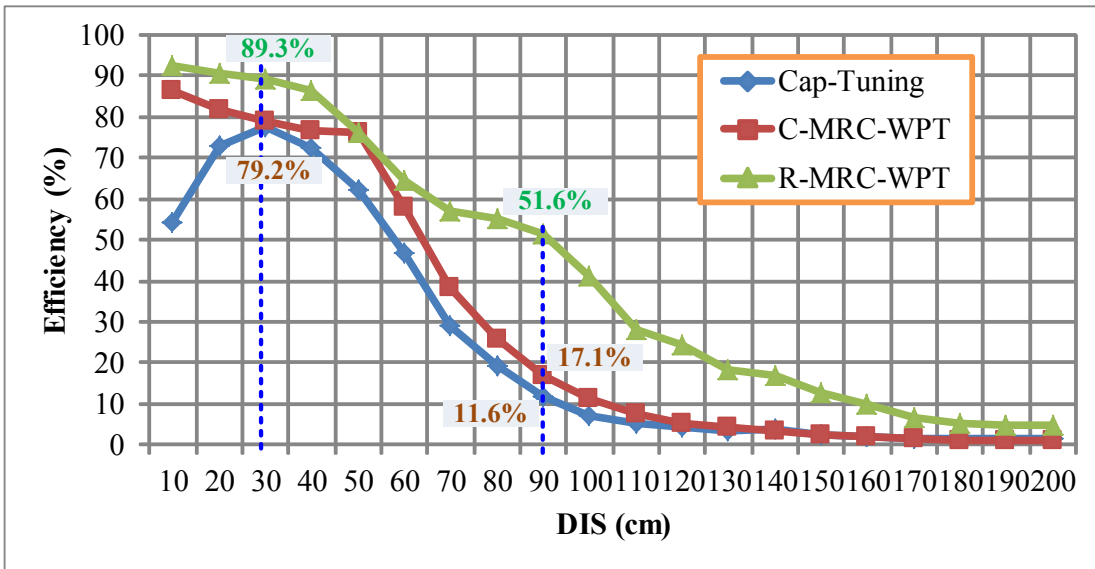
(b-5) DIS = 60cm, Config-5

(b-6) DIS = 60cm, Config-6

Figure 5.6: $|S_{21}|$ as a function of frequency at (a) DIS = 30cm and (b) DIS = 60cm

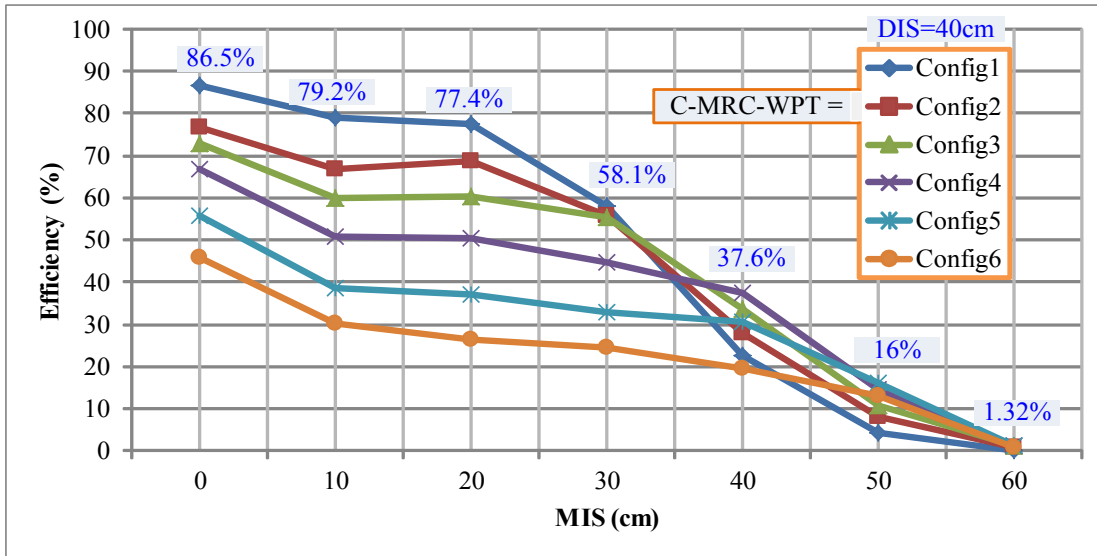


(a)

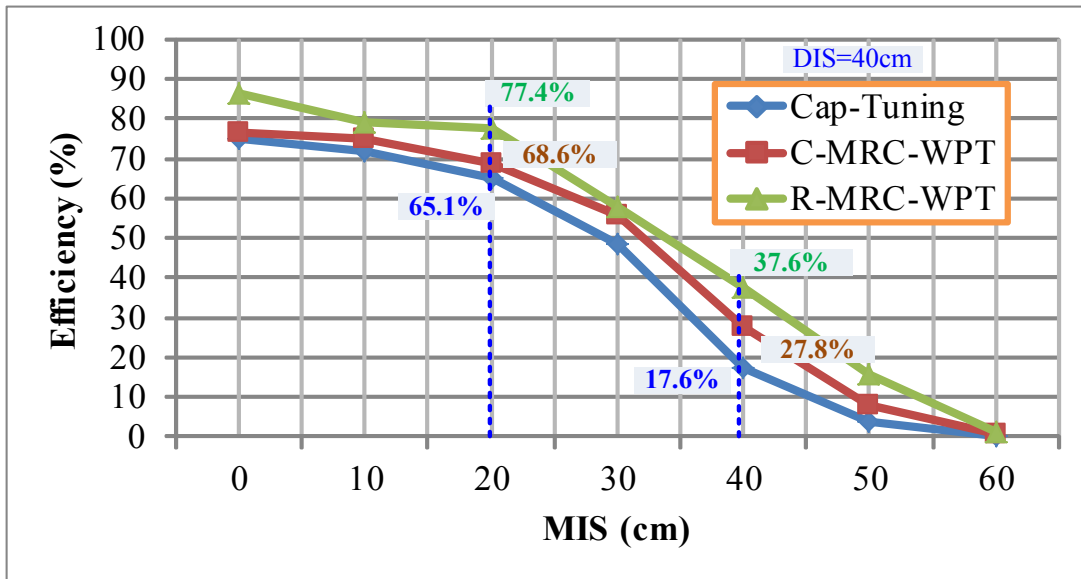


(b)

Figure 5.7: Transmission efficiency as a function of DIS when Tx and Rx are perfectly aligned (a) transmission efficiency under different configurations and (b) transmission efficiency curves for C-MRC-WPT, R-MRC-WPT and Cap-tuning systems

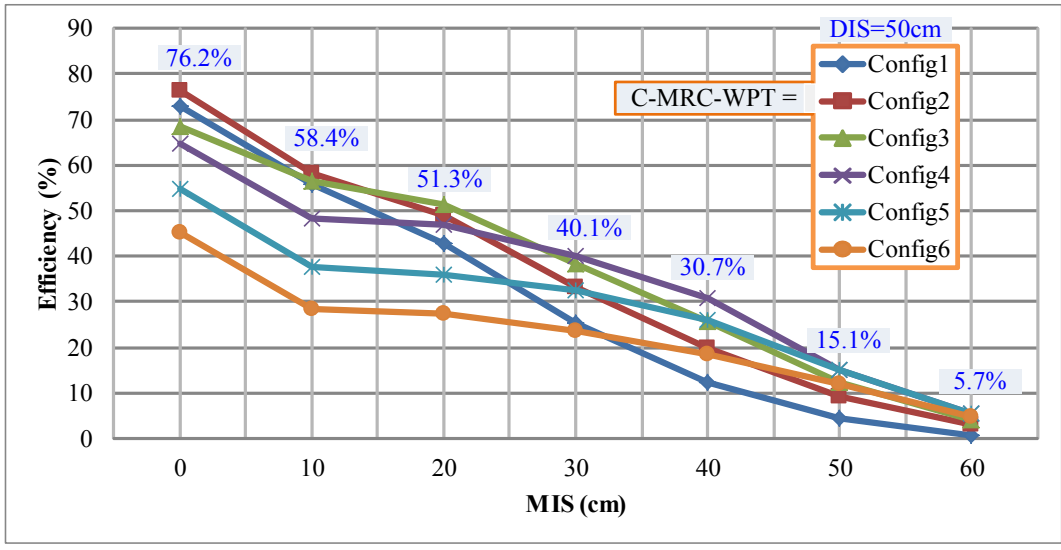


(a)

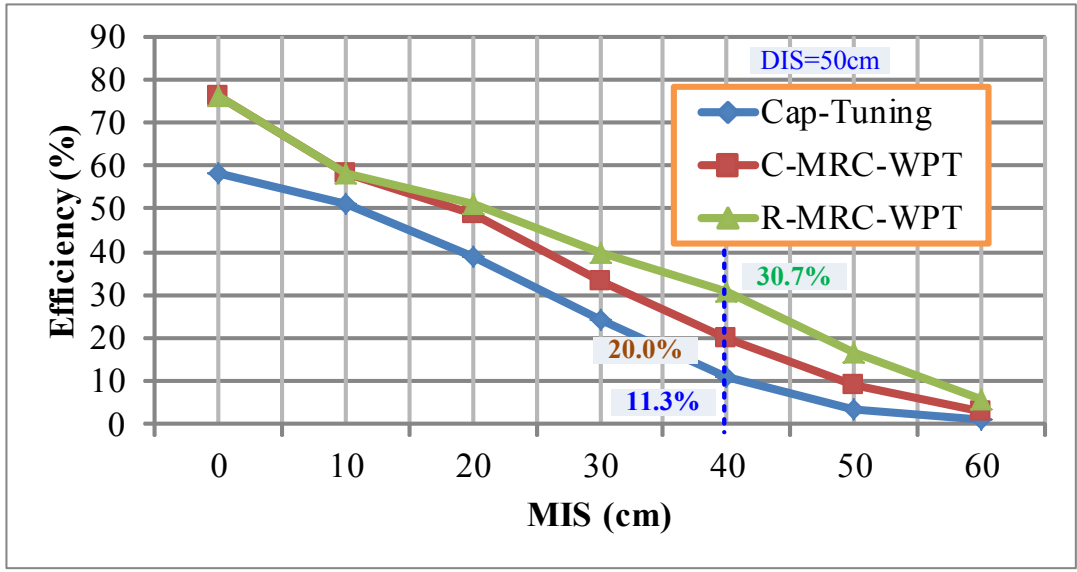


(b)

Figure 5.8: Transmission efficiency as a function of lateral misalignment (MIS) when DIS=40cm (a) transmission efficiency under different configurations and (b) transmission efficiency curves for C-MRC-WPT, R-MRC-WPT and Cap-tuning systems



(a)



(b)

Figure 5.9: Transmission efficiency as a function of lateral misalignment (MIS) when DIS=50cm (a) transmission efficiency under different configurations and (b) transmission efficiency curves for C-MRC-WPT, R-MRC-WPT and Cap-tuning systems

Transmission efficiency as a function of the DIS is plotted in Fig. 5.7. It can be observed from Fig. 5.7(a) that config-1 yields the highest efficiency (~90%) for the short distance range of 0-50 cm. Config-2 yields the highest efficiency (~75%) for the range of 50 cm-55 cm. Config-3 yields the highest efficiency (~65%) for the range of 55 cm-65 cm. Config-4 yields the highest efficiency (~60%) for the range of 65 cm-70 cm. Config-5 yields the highest efficiency for the range of 70cm-110cm. From 70 cm to 90 cm, an efficiency value of ~55% is maintained since config-5 is still in the over coupled region for this distance range. From 90cm to 110cm, efficiency drops from ~55% to ~28% because the system lies in the under coupled region for this distance range. Config-6 yields the highest efficiency for a relatively long distance range of 110 cm-200 cm and efficiency drops from ~28% at 110 cm to ~4.9% at 200 cm. It can be observed that each configuration has highest transmission efficiency for a given distance range and therefore by switching between the different configurations transmission distance can be extended with higher efficiency.

In the R-MRC-WPT system, maximum achievable efficiency at different DIS values can adaptively be tracked while reconfiguring the system such that transmission efficiencies within all DIS ranges are improved. The efficiency curve obtained from the R-MRC-WPT system is compared to the efficiency curves obtained from the C-MRC-WPT system and the Cap-tuning system as shown in Fig. 7b. It can be observed that the transmission efficiency of the R-MRC-WPT system is the highest at every point and the transmission efficiency of Cap-tuning system is the lowest at every point when DIS ranges from 0 to 2m. When compared to the C-MRC-WPT system at DIS = 30 cm, the R-MRC-WPT system improves the efficiency by 10.1%. At DIS = 90 cm, efficiency is improved by 34.5%. If one of the system configurations, for example config-5, is removed from the R-MRC-WPT system, system efficiency in the range of 70 cm<DIS<90

cm would drop from ~55% to ~40%. In other words, the larger the number of configurations used, the higher the transmission efficiency improvement can be obtained for the DIS ranges.

C. R-MRC-WPT System with Lateral Misalignment

In this subsection, the presented experimental measurements and comparisons are for the R-MRC-WPT system when varying MIS values from 0 to 60 cm with 10cm steps at fixed DIS of 40 cm and 50 cm. The transmission efficiency experimental measurement results as a function of the MIS when DIS = 40 cm are plotted in Fig. 5.8(a). It can be observed that config-1 yields the highest efficiency for the MIS range of 0-30 cm. From 0 cm to 20 cm, an efficiency value of ~80% is maintained since config-1 operates in the over coupled region for this MIS range. When Rx position changes from MIS = 20 cm to MIS = 30 cm while using config-1, efficiency drops from 80% to 60%. This indicates that the operation of config-1 moved to the under coupled region when MIS > 20 cm. The results obtained as shown in Fig. 5.8(a) show that config-2 does not yield to a highest efficiency for any MIS range. Config-3 yields the highest efficiency for the MIS range of 30cm-38cm. Config-4 yields the highest efficiency for the range of 38cm-50cm. Config-5 yields the highest efficiency for the range of 50cm-60cm. As it is the case for config-2, config-6 does not yield to a highest efficiency for any MIS range. Each of the other four configurations (config-1, config-3, config-4 and config-5) provides highest transmission efficiency for a given range of MIS.

The resulted transmission efficiency curve of the R-MRC-WPT system is shown in Fig. 5.8(b), and is compared to the efficiency curves of the C-MRC-WPT and the Cap-tuning systems. It can be observed that transmission efficiency of the R-MRC-WPT system is the highest and transmission efficiency of the Cap-tuning system is the lowest. When compared to

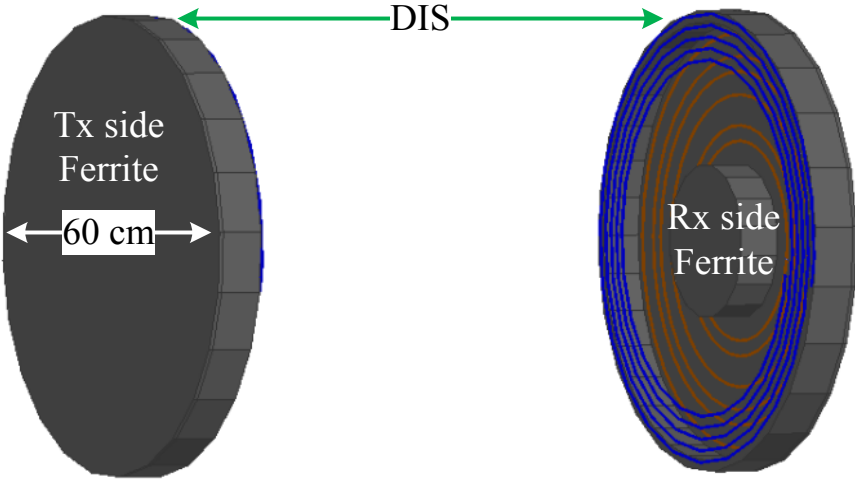
the C-MRC-WPT system at MIS = 20 cm, the R-MRC-WPT system improves the transmission efficiency by 8.8%. At MIS = 40 cm, transmission efficiency is improved by 9.8%.

Experimental measurements and analysis are also performed for the case when varying MIS while fixing DIS at 50 cm. The transmission efficiency as a function of the MIS is plotted in Fig. 5.9(a). It can be observed that config-1 does not yield highest efficiency for any MIS range. This is because when DIS=50cm and MIS=0, config-1 already operates in the under coupled region and its transmission efficiency drops down rapidly when DIS and/or MIS further increases. Config-2 yields the highest efficiency for the MIS range of 0-15cm. Config-3 yields the highest efficiency of ~50% for the MIS range of 15cm-25cm. Config-4 yields the highest efficiency for the MIS range of 30cm-50cm. Config-5 yields the highest efficiency for the range of 50cm-60cm. As it is the case for config-1, config-6 does not yield the highest efficiency for any MIS range. It can be observed that each of the other four configurations (config-2, config-3, config-4 and config-5) can improve the transmission efficiency for a given range of MIS.

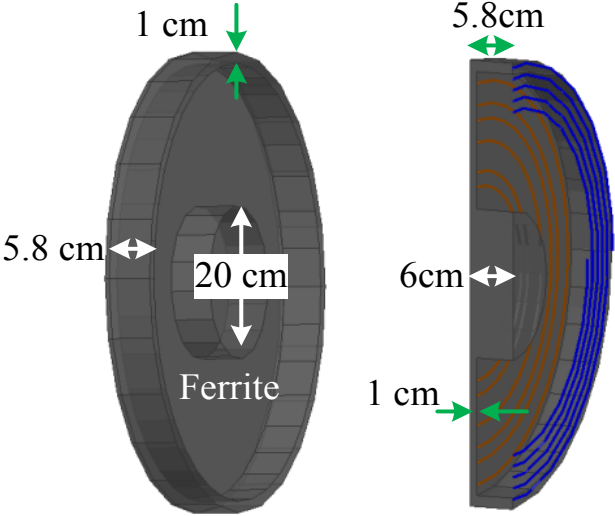
The resulted transmission efficiency curve of the R-MRC-WPT system is compared to the efficiency curves of the C-MRC-WPT and the Cap-tuning systems. It can be observed that transmission efficiency of the R-MRC-WPT system is the highest and transmission efficiency of the Cap-tuning system is the lowest. When compared with C-MRC-WPT system at MIS = 40cm, the R-MRC-WPT system improves the transmission efficiency by 10.7%. Similar to the case when DIS is varied, the larger the number of configurations is, the higher the transmission efficiency improvement can be obtained for the MIS ranges.

From efficiency comparisons above, it can be concluded that the Cap-tuning system can approach the maximum possible efficiency only at a given DIS or MIS value for the fixed design structure, while switching between different loops reconfigures the system such that it switches

between different designs or operating/efficiency curves that are more optimized for different conditions with higher efficiency values.



(a)



(b)

(c)

Figure 5.10: (a) 3-D model of R-MRC-WPT system with ferrite structure on Tx side and Rx side, (b) 3-D view of ferrite structure and (c) cross section view of Tx side structure

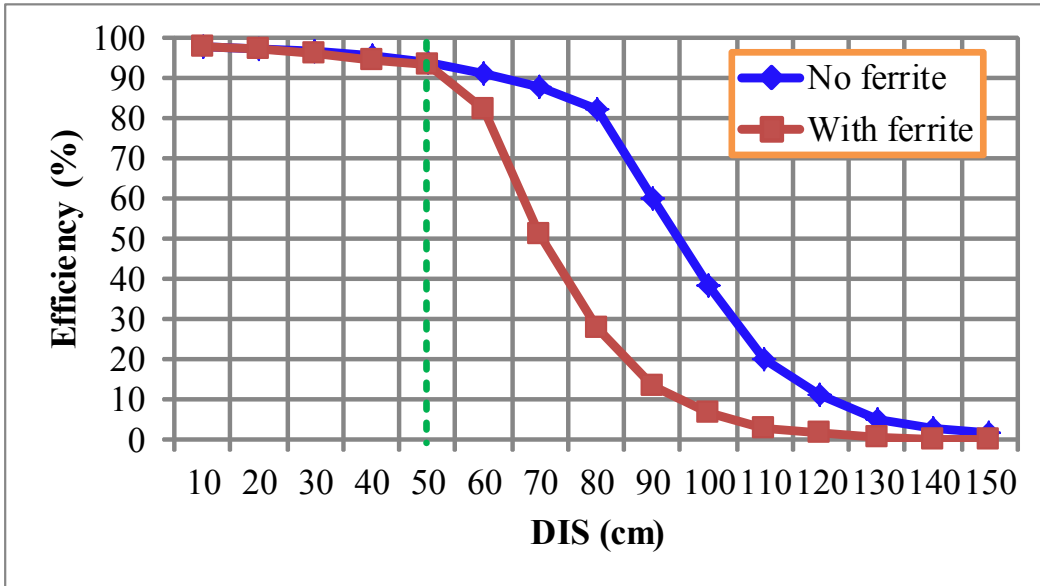
5.4 Additional Comments

A. The Use of Ferrite with the R-MRC-WPT System

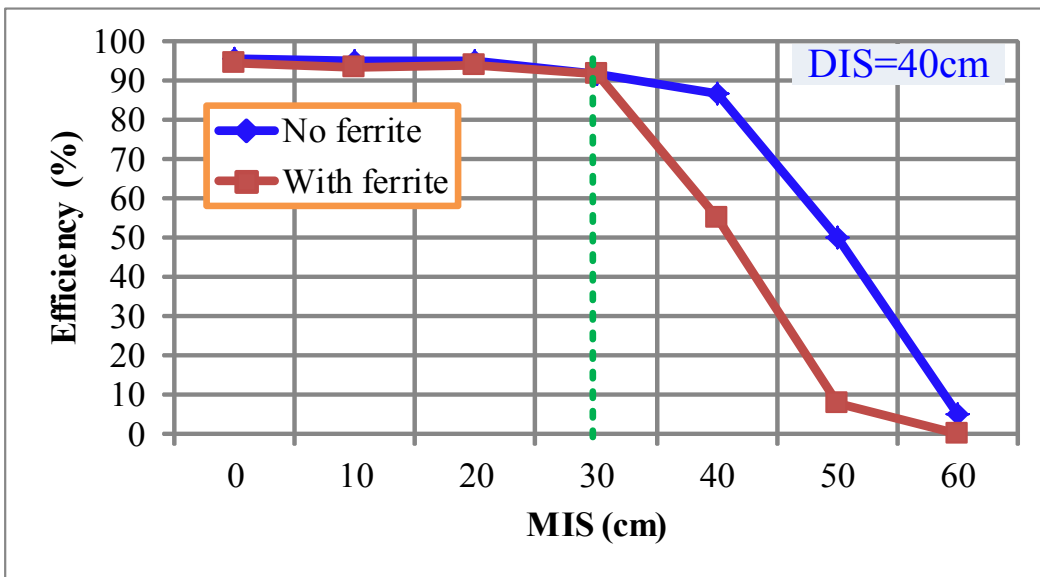
This subsection presents preliminary investigation on the use of the ferrite material in the R-MRC-WPT system by using the ANSYS® HFSS® 3-D physical model simulations. Fig. 5.10 shows the 3-D model of R-MRC-WPT system with ferrite structure used with both the Tx side and the Rx side. The properties of the ferrite material used in the simulation are shown in Table 5.3. Results for transmission efficiency values for the R-MRC-WPT system with and without ferrite material for different DIS and MIS (while DIS = 40cm) conditions are shown in Fig. 5.11 for comparison. It can be observed that the R-MRC-WPT system with and without ferrite has almost the same transmission efficiency for small DIS values (≤ 50 cm) and for small MIS values (≤ 30 cm). When DIS and MIS increase, the R-MRC-WPT system without ferrite has larger transmission efficiency.

Table 5.3: Properties of ferrite material used in R-MRC-WPT system

Property	Value
Material Type	4F1 [E12]
Saturation Flux density	0.32T
Resistivity	$\sim 10^5 \Omega\text{m}$
Magnetic Loss Tangent	0.00035
Relative Permeability	300
Relative Permittivity	15
Mass Density	4600kg/m ³

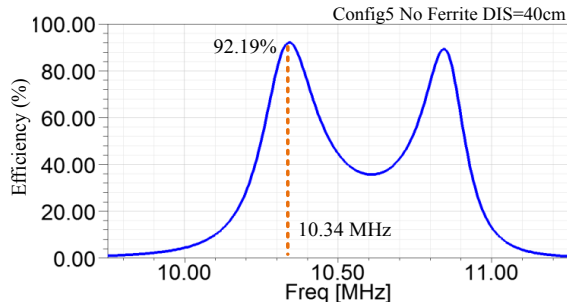


(a)

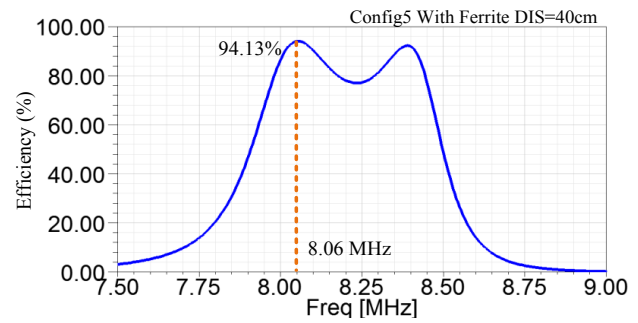


(b)

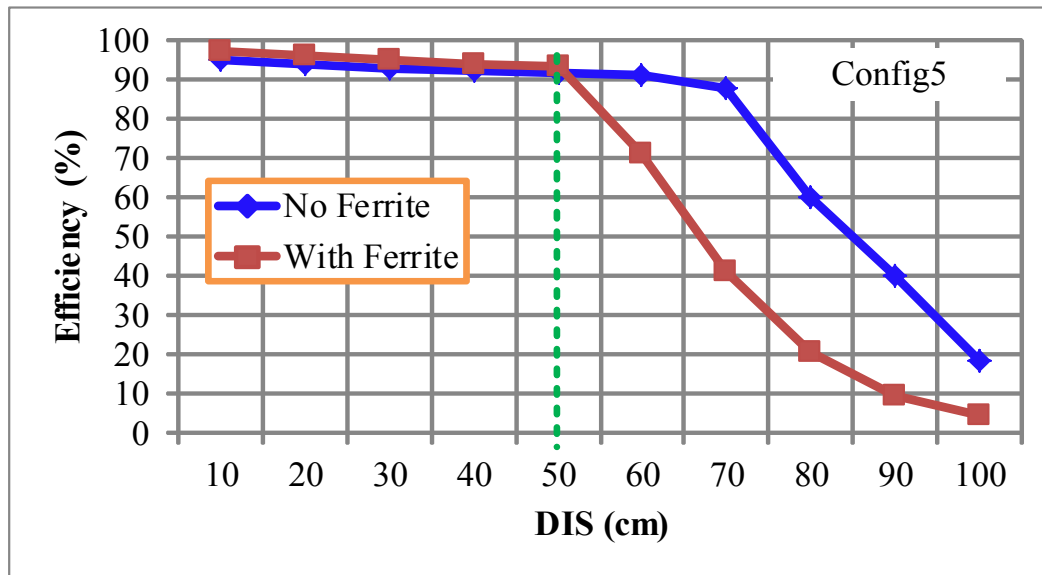
Figure 5.11: Comparison between transmission efficiency values for the R-MRC-WPT system with and without ferrite structure for (a) different DIS and (b) different MIS (with DIS = 40cm) conditions



(a)



(b)



(c)

Figure 5.12: Comparison between transmission efficiency values for the Config-5 (a) without ferrite structure at DIS=40cm, (b) with ferrite structure when DIS = 40cm and (c) under different DIS conditions

However, the results in Fig. 5.11 do not mean the ferrite has no effect on the four-coil MRC-WPT system. For example in Fig. 5.12(a) and Fig. 5.12(b), operation frequency of Config-5 without ferrite (10.34 MHz) is ~ 2.5 MHz higher than that with ferrite (8.06 MHz). This is because ferrite has much higher relative permeability (~ 300 in this design) than air (~ 1) and therefore effective inductance/mutual inductance values of the coils increase and self-resonance

frequency of Tx/Rx coil decreases according to (5.2). Transmission efficiencies with and without ferrite for Config-5 under various DIS conditions are compared in Fig. 5.12(c), which shows that the transmission efficiency with ferrite is slightly higher than that without ferrite at close distance ($DIS \leq 50\text{cm}$). When DIS increases, efficiency of Config-5 without ferrite is higher than that with ferrite. Therefore, it is possible to increase the transmission efficiency of the four-coil MRC-WPT system at shorter distances by adding ferrite structure while decreasing transmission efficiency at longer distances.

The use of ferrite structure might achieve larger transmission efficiency improvement at shorter distances for a two-coil system [E11, E13-E19]. However, in the R-MRC-WPT system, the transmission efficiency has already been improved as a result of reconfiguring the system such that only a smaller improvement can be achieved at shorter distances when using ferrite structure.

B. Use of Litz Wire with the R-MRC-WPT System

Litz wire is designed to reduce the skin effect and proximity effect losses in conductors used at high frequencies. Commercially available Litz wires can operate with frequencies up to 2.8 MHz [E20]. Even though 2.8 MHz is lower than the operation frequency of the R-MRC-WPT system presented in this chapter (which is higher than 10MHz), higher transmission efficiency might be obtained by using Litz wire. This topic is a candidate for future investigation.

5.5 Summary

The chapter presented a method for R-MRC-WPT system that adapts the reconfiguration of four-coil WPT system in order to improve transmission efficiency under various transmission distances and misalignment conditions. The re-configurability of the system is realized by adaptively switching between different sizes of drive loops and load loops, which does not result

in the disadvantages that exist in mechanical tuning method such as volume increase and requirement of mechanical movements. Theoretical basis for the presented method are devised from a circuit model and an analytical model and are validated by using a proof of concept experimental prototype results. Experimental results show that the R-MRC-WPT system has better performances than the C-MRC-WPT system and Cap-Tuning system in terms of transmission efficiency, transmission distance and misalignment tolerance. Analysis also shows that when a larger number of configurations are used in the system, higher efficiency improvement can be achieved under various DIS and/or MIS conditions.

While this work focuses on presenting the R-MRC-WPT system for low-power applications such as consumer electronics, the concept is candidate for higher power levels. However, there might be health and safety concerns above certain power levels especially that the presented system transmits power for distances that are larger than one coil diameter. Future work includes but is not limited to developing and implementing adaptive control algorithms to automatically realize the system re-configurability.

CHAPTER 6

WIRELESS POWER TRANSFER USING INDUCTOR CURRENT SWITCHING RIPPLE OF POWER CONVERTER

6.1 Introduction

A conventional inductive WPT system normally includes a transmitter (Tx) side circuit, a Tx coil, a receiver (Rx) coil, and Rx side electronics/load. The major part of the Tx side circuit is the DC-AC inverter/power amplifier such as full-bridge/half-bridge inverter and class-E power amplifier [F2-F4]. The generated high frequency AC drives the Tx coil to create oscillating magnetic field in the proximity of the Tx coil. Energy is then delivered to Rx coil through this oscillating magnetic field to realize WPT. The Tx side circuitry and Tx coil are essential parts in conventional WPT system but they are bulky in size and weight.

DC-DC power converters have been widely used in many applications such as computing platforms, consumer electronics and renewable energy systems, among others [F5]. DC-DC buck power converter, for example, steps down the DC voltage from one level to another. Inductor current in a buck converter includes DC component (equals to the output current) and AC switching ripple. The AC ripple in the power inductor generates high frequency oscillating magnetic field. This oscillating magnetic field is usually considered a disadvantage and a “trouble maker” in terms of radiated electromagnetic interference (EMI), but its potential for WPT has not been well explored before.

This chapter presents a WPT method that utilizes the inductor’s current AC ripple of a DC-DC power converter by placing a Rx coil to the proximity of the planar power inductor of a

power converter. By doing so, the power converter-WPT system achieves DC-DC power conversion (wired power transfer) and WPT function at the same time, which helps to eliminate the Tx side circuitry and Tx coil of the conventional WPT system and achieves size and cost reduction of the total system. Next section presents the developed method based on an example Buck-WPT system (achieves step down DC-DC power conversion and WPT at the same time) and devises its operation principle and maximum power transfer condition. Section 6.3 presents proof of concept experimental prototype results. Section 6.4 gives the summary for this chapter.

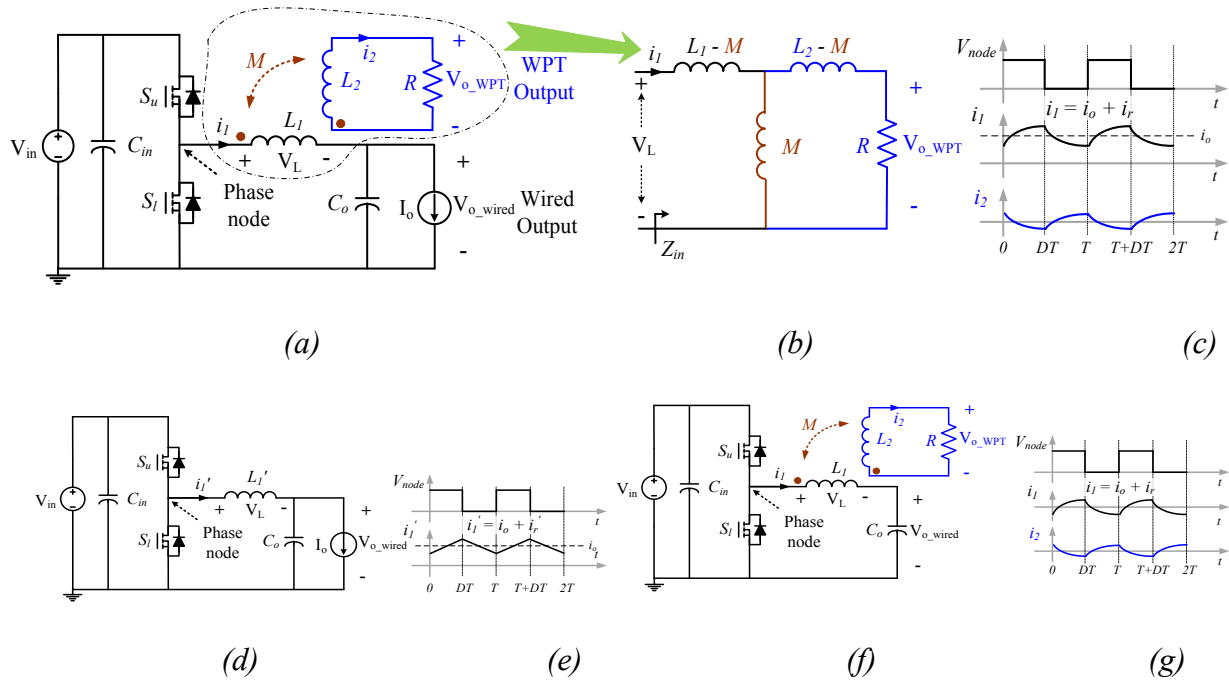


Figure 6.1: (a) Circuit diagrams of Buck-WPT system, (b) equivalent circuit when looking into ports of L_1 , (c) diagram of operation waveforms for Buck-WPT system, (d) wired output operating alone, (e) diagram of operation waveforms when wired output operating alone, (f) WPT output operating alone and (g) diagram of operation waveforms when WPT output operating alone

6.2 Power Converter-WPT System and Analysis

A. Buck-WPT System

Using Buck-WPT system as an example, this section presents the concept and operation principle of Power converter-WPT system that realizes DC-DC power conversion (wired power transfer) and WPT operation at the same time. Fig. 6.1(a) illustrates the circuit diagram of the Buck-WPT system. The system has one input V_{in} and two outputs: one for WPT, which is referred to as V_{o_WPT} , and one for wired power transfer, which is referred to as V_{o_wired} . The current of the inductor $i_l = I_o + i_r$ by superposition consists of the DC current component (I_o) and the AC ripple current component (i_r) as illustrated in Fig. 6.1(c). V_{node} is the voltage at the phase node, which has the same waveform shape as the PWM control signal of high side/control MOSFET S_u . In a Buck-WPT system, V_{o_wired} and V_{o_WPT} can operate simultaneously without interrupting the operation of each other as illustrated in Fig. 6.1(a) and (c), or each of them can operate alone as illustrated in Fig. 6.1(d)-(e) and Fig. 6.1(f)-(g), respectively.

The wired power path has the same operation as the conventional buck converter without WPT and it mainly depends on the DC current value I_o for power delivery and regulation. The power inductor L_1 and output capacitor C_o are used to form the LC low pass filter leading to V_{o_wired} . The WPT power path does not have a stand-alone Tx side driving circuit and Tx coil. Instead, it utilizes the buck converter power stage as the Tx side circuit and uses power inductor L_1 as the Tx coil. The AC component of the inductor current is used to achieve WPT. This is because the AC ripple of the current generates oscillating magnetic field in the proximity of the Tx coil with L_1 , which can be used for inductive WPT to a receiver Rx. When a planar receiver (Rx) coil with L_2 is placed in the proximity of the planar Tx coil, the Tx and Rx coils are coupled through a mutual inductance M . As a result, certain amount of power can be delivered to the

WPT load R . The Buck-WPT system eliminates Tx side circuitry and Tx coil compared with the conventional WPT system, which helps to reduce the size and cost of the total system.

It is important to investigate and show whether or not the operation of the two outputs impact each other. The equivalent circuit when looking into the port of L_1 is extracted as shown in Fig. 6.1(b). It can be seen from Fig. 6.1(b) that for the DC component of the inductor's current I_o , the DC impedance $Z_{in} = Z_{DC} = 0$. This means that even when there exists the WPT output, the DC voltage gain of the buck power path from V_{in} to V_{o_wired} maintains the ideal relationship $V_{o_wired}/V_{in} = D$ (D is the duty cycle) as in conventional buck converter and is not affected by the WPT operation. For the AC ripple component of the inductor's current i_r , the impedance $Z_{in} = Z_{AC}$ is derived as

$$\begin{aligned} Z_{AC} &= j\omega(L_1 - M) + (j\omega M \parallel (j\omega(L_2 - M) + R)) \\ &= \frac{k^2 \omega^2 L_1 L_2 R}{R^2 + \omega^2 L_2^2} + j\omega(L_1 - \frac{\omega^2 k^2 L_1 L_2^2}{R^2 + \omega^2 L_2^2}) \\ &= R_{eq} + j\omega L_{eq} \end{aligned} \quad (6.1)$$

Where $\omega = 2\pi f$ is the angular frequency and k is the coupling factor between L_1 and L_2 , which is defined as

$$k = \frac{M}{\sqrt{L_1 L_2}} \quad (6.2)$$

The equivalent resistance R_{eq} and equivalent inductance L_{eq} obtained in (6.1) determine the inductor's current ripple i_r . Let I_{Lmin} and I_{Lmax} be the minimum and maximum values of inductor's current, respectively. When the switch S_u shown in Fig. 6.1(a) is turned on, (6.3) can be obtained based on Kirchhoff's Voltage Law (KVL)

$$V_{in} - V_{o_wired} = R_{eq} i_L + L_{eq} \frac{di_L}{dt} \quad (6.3)$$

Solving (6.3) yields

$$I_{L\max} = \left(I_{L\min} - \frac{V_{in} - V_{o_wired}}{R_{eq}} \right) e^{-DT/\tau} + \frac{V_{in} - V_{o_wired}}{R_{eq}} \quad (6.4)$$

Where $T = 1/f$ is the switching period and τ is equivalent time constant, which is determined from $\tau = L_{eq}/R_{eq}$. Similarly, when S_u is off, the following equation can be obtained based on KVL

$$-V_{o_wired} = R_{eq}i_L + L_{eq} \frac{di_L}{dt} \quad (6.5)$$

Solving (6.5) yields

$$I_{L\min} = \left(I_{L\max} + \frac{V_{o_wired}}{R_{eq}} \right) e^{-T(1-D)/\tau} - \frac{V_{o_wired}}{R_{eq}} \quad (6.6)$$

From (6.4) and (6.6), the peak to peak value of i_r is obtained as

$$\Delta i_r = I_{L\max} - I_{L\min} = \frac{V_{in} \left(e^{\frac{DT}{\tau}} - 1 \right) \left(e^{\frac{T}{\tau}} - e^{-\frac{DT}{\tau}} \right)}{e^{\frac{DT}{\tau}} \left(e^{\frac{T}{\tau}} - 1 \right) R_{eq}} \quad (6.7)$$

When there is no load on the WPT branch, i.e. $R = \infty$, Z_{AC} becomes

$$Z_{AC} \Big|_{R=\infty} = \left(R_{eq} + j\omega L_{eq} \right) \Big|_{R=\infty} = 0 + j\omega L_1 \quad (6.8)$$

This means that Δi_r , when there is no WPT load, becomes as in (6.9), which is the same as in conventional buck converter.

$$\Delta i_r \Big|_{R=\infty} = \frac{V_{in} (1-D)DT}{L_1} \quad (6.9)$$

When the WPT output is shorted, i.e. $R = 0$, Z_{AC} becomes

$$Z_{AC} \Big|_{R=0} = \left(R_{eq} + j\omega L_{eq} \right) \Big|_{R=0} = 0 + j\omega L_1 (1-k^2) \quad (6.10)$$

This means that Δi_r at $R = 0$ becomes

$$\Delta i_r|_{R=0} = \frac{V_{in}(1-D)DT}{L_1(1-k^2)} \quad (6.11)$$

Where $0 \leq k^2 < 1$, and $0 < L_1(1-k^2) \leq L_1$. This yields $\Delta i_r|_{R=0} \geq \Delta i_r|_{R=\infty}$, which means the inductor ripple Δi_r gets to its largest value when WPT load is shorted. In a practical Buck-WPT system, WPT load has $0 < R \leq \infty$, therefore the boundaries of Δi_r can be expressed as

$$\frac{V_{in}(1-D)DT}{L_1} \leq \Delta i_r < \frac{V_{in}(1-D)DT}{L_1(1-k^2)} \quad (6.12)$$

From the first glance on (6.12), the existence of the WPT branch increases the value of the inductor current ripple because $\Delta i_r \geq \Delta i_r|_{R=\infty}$. But this is true only when inductance L_1 is not affected by the existence of Rx coil for WPT, i.e. when the Rx coil does not have a magnetic core (e.g. ferrite core). In this design example, as it is the case in many tightly coupled WPT systems, Tx coil has a ferrite plate on its back side for shielding purpose and to enhance the mutual coupling between Tx and Rx. This means when the Rx coil with ferrite plate is placed in the proximity of the Tx coil, self-inductance of Tx coil will be increased. i.e. L_1 in Fig. 6.1(a) for Buck-WPT system is greater than L_1' in Fig. 6.1(c) where there is no Rx coil for WPT ($L_1 > L_1'$). The amount of the increase in self-inductance of Tx coil because of the Rx ferrite is determined by several factors such as the geometry and dimensions of the Rx ferrite plate, the distance between Tx coil and Rx coil, and the properties of ferrite material, among others. This means that the existence of the Rx coil with ferrite might finally lead to a smaller Δi_r value at some load conditions because of the increase in the self-inductance of L_1 . Example load condition where the Buck-WPT system gets smaller Δi_r will be discussed in the experimental section. In summary, the existence of the WPT output does not affect the DC voltage gain of the wired output, but it affects the inductor's current ripple. Example design and waveforms will be illustrated in the experiment section.

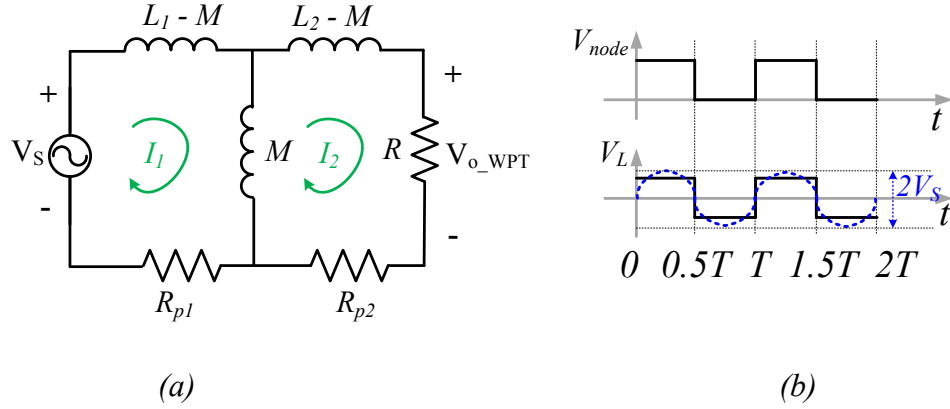


Figure 6.2: (a) Equivalent circuit for the WPT power path and (b) illustration of first harmonic approximation of V_L when $D = 0.5$

B. Maximum Power Transfer

In order to perform analysis to estimate the amount of power delivered to the WPT output, the equivalent circuit of the WPT power path is extracted as in Fig. 6.2(a). For more accurate power estimation, parasitic resistance R_{p1} of L_1 and parasitic resistance R_{p2} of L_2 are included in the model. V_S represents the peak value of sinusoidal approximation of V_L , as illustrated in Fig. 6.2(b) for the case when $D = 0.5$. The following can be obtained from Fig. 6.2 based on mesh analysis

$$\begin{bmatrix} j\omega L_1 + R_{p1} & -j\omega M \\ -j\omega M & j\omega L_2 + R + R_{p2} \end{bmatrix} \begin{bmatrix} I_1 \\ I_2 \end{bmatrix} = \begin{bmatrix} V_S \\ 0 \end{bmatrix} \quad (6.13)$$

The power delivered to the load R can then be calculated as

$$P = I_{2,rms}^2 R = \frac{V_S^2 k^2 \omega^2 L_1 L_2 R}{2(\omega^2 (L_1 (R + R_{p2}) + L_2 R_{p1}))^2 + (R_{p1} (R + R_{p2}) - \omega^2 L_1 L_2 (1 - k^2))^2} \quad (6.14)$$

Solving $dP/dR = 0$ yields the optimum resistance R_{opt} for maximum power transfer

$$R_{opt} = R \Big|_{\frac{dP}{dR}=0} = \sqrt{\frac{k^2 \omega^2 L_1 L_2 (k^2 \omega^2 L_1 L_2 - 2\omega^2 L_1 L_2 + 2R_{p1} R_{p2}) + \omega^4 L_1^2 L_2^2 + \omega^2 L_1^2 R_{p2}^2 + \omega^2 L_2^2 R_{p1}^2 + R_{p1}^2 R_{p2}^2}{\omega^2 L_1^2 + R_{p1}^2}} \quad (6.15)$$

Substituting the value of R_{opt} obtained in (6.15) into (6.14) yields maximum power P_{max} that can be delivered by the WPT branch as in (6.16).

$$P_{max} = P \Big|_{R=R_{opt}} \quad (6.16)$$

When parasitic resistances are neglected, i.e. $R_{p1} = R_{p2} = 0$, optimum resistance R_{opt_0} becomes

$$R_{opt_0} = R_{opt} \Big|_{R_{p1}=R_{p2}=0} = \omega L_2 (1 - k^2) \quad (6.17)$$

The corresponding maximum power P_{max_0} then becomes

$$P_{max_0} = P \Big|_{R=R_{opt_0}} = \frac{k^2 V_S^2}{4\omega L_1 (1 - k^2)} \quad (6.18)$$

Equation (6.18) shows that P_{max_0} is directly proportional to k and V_S , but inversely proportional to L_1 and ω . V_S , L_1 and ω are all related to current ripple value of the buck converter. Larger V_S , smaller L_1 and smaller ω all lead to a larger inductor current ripple, resulting in larger WPT output P_{max_0} . In a buck converter, Δi_r has the largest value when $D = 0.5$, which indicates that P_{max_0} is also maximized at $D = 0.5$ assuming all other design variables are constant. When $D = 0.5$, V_L is a square wave with the peak value of $\pm V_{in}/2$. Based on first harmonic approximation, V_S is denoted as $2V_{in}/\pi$ when $D = 0.5$, as illustrated in Fig. 6.2(b) [F6].

Total efficiency of the Buck-WPT system is evaluated as

$$\eta = \frac{P_{o_Buck} + P_{o_WPT}}{P_{in} + P_{driver}} = \frac{V_o I_o + I_{2,rms}^2 R}{V_{in} I_{in} + V_{driver} I_{driver}} \quad (6.19)$$

Where P_{o_Wired} is the output power from wired output, P_{o_WPT} is the output power from WPT output and $P_{driver} = V_{driver} I_{driver}$ is the power switches' driver power loss.

6.3 Proof of Concept Experimental Results

A proof of concept experimental prototype of Buck-WPT system is developed in order to study and validate the presented method of the Power converter-WPT system and to obtain preliminary experimental results. Photo pictures of the Buck-WPT system are shown in Fig. 6.3 and specifications are detailed in Table 6.1. The prototype in Fig. 6.3(a) shows that the Buck-WPT system achieves wired DC-DC power conversion (5V to 2.5V with $I_o = 2A$) and WPT (illustrated by the lighted incandescent bulb) at the same time. The Buck-WPT system is tested under different load conditions. When $D = 0.5$, V_S is calculated as 3.183 V.

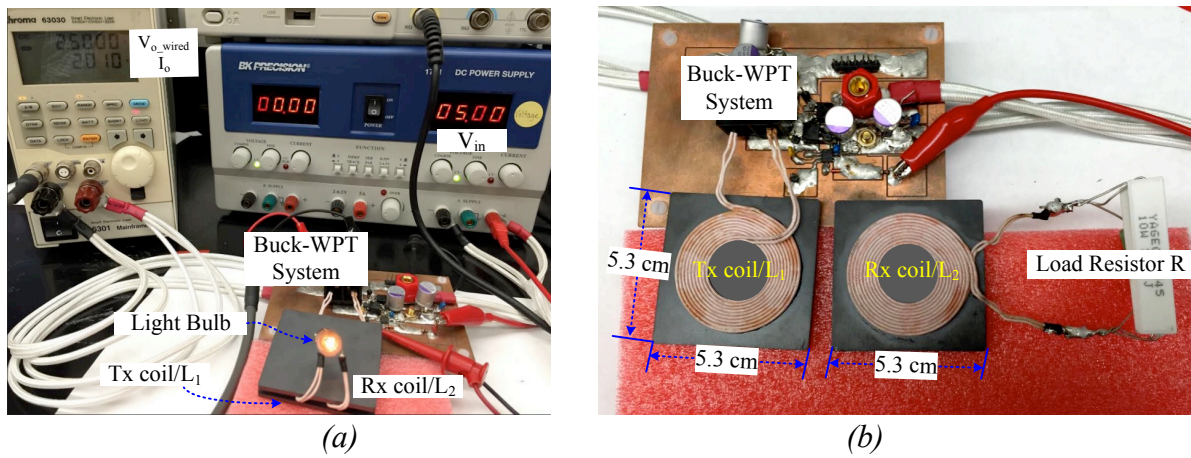


Figure 6.3: The prototype of the Buck-WPT system: (a) a demo for powering the 2A constant current load at V_{o_wired} and lighting a light bulb at V_{o_WPT} and (b) more detailed view of the Buck-WPT system

Table 6.1. Parameter specifications of the Buck-WPT system

Parameters	Values	Parameters	Values
Switching frequency f_s	150 kHz	WPT transmission distance	2 mm
V_{in}	5 V	Tx/Rx ferrite dimensions	5.3cm×5.3cm×0.6cm
V_o	1 V - 3.3 V	R_{p1} @ 150 kHz	0.12 Ω
L_1	2.706 μ H	R_{p2} @ 150 kHz	0.25 Ω
L_2	9.724 μ H	C_{in}	470 μ F
L_1'	1.877 μ H	C_o	1.04 mF
M	4.268 μ H	k	0.832

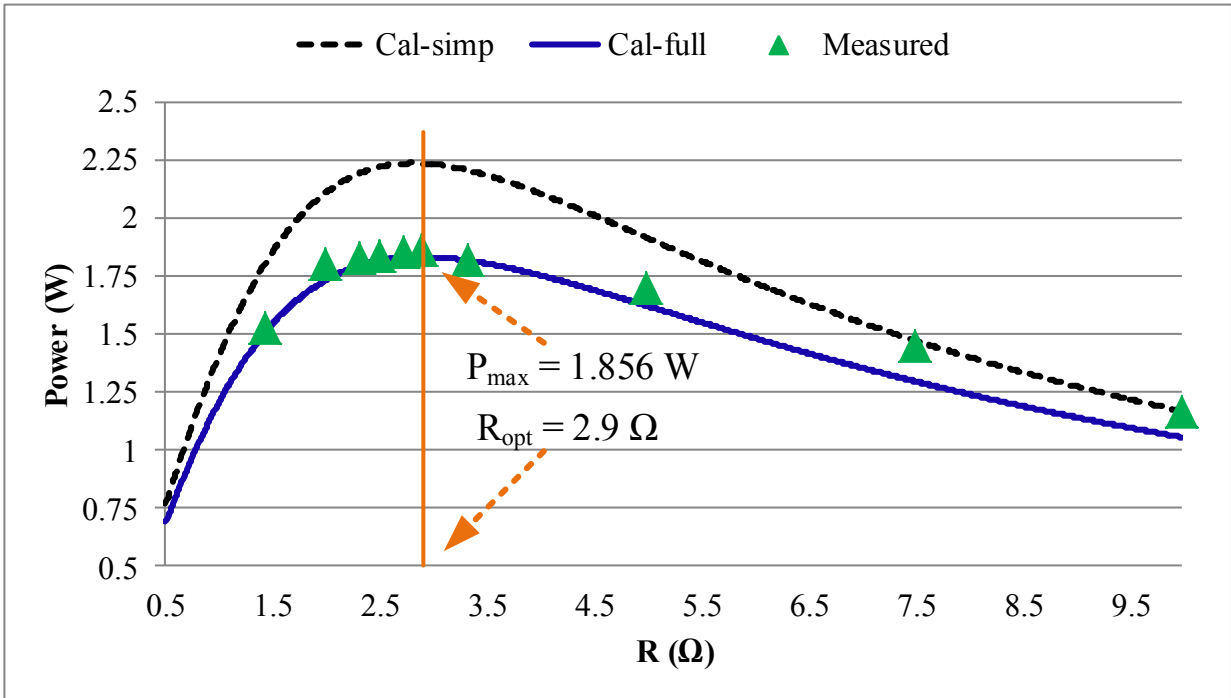


Figure 6.4: Power delivered through WPT output When $D = 0.5$

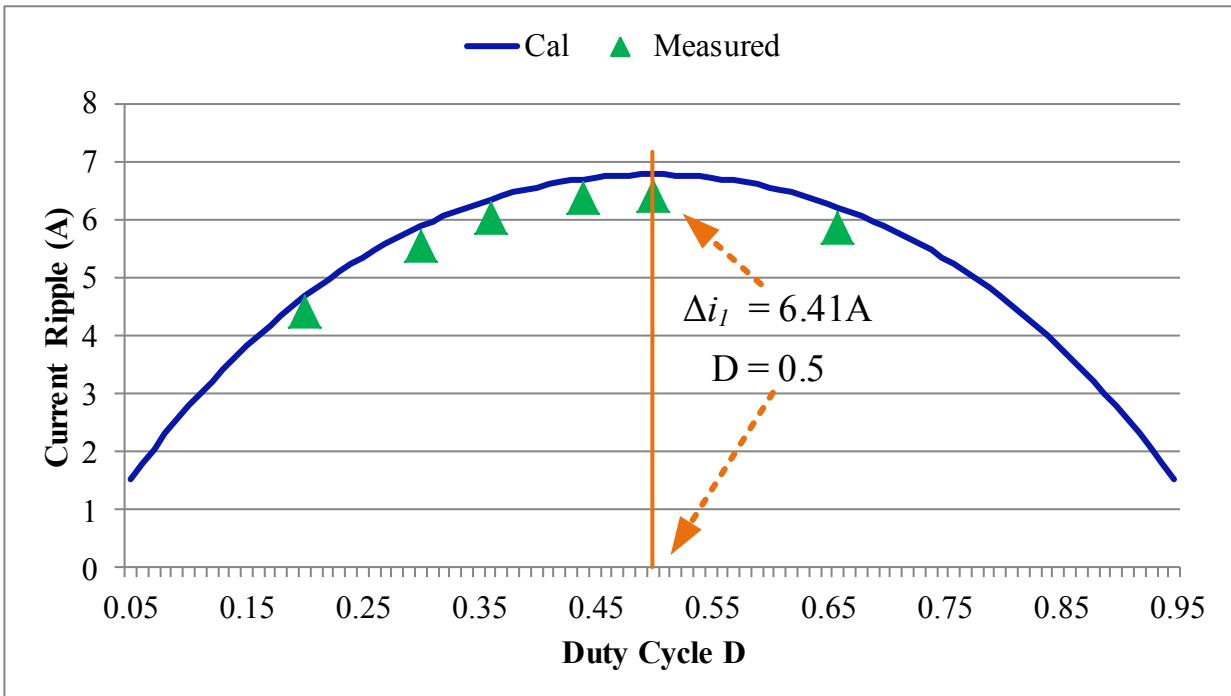


Figure 6.5. Δi_r as a function of D when $R_{opt} = 2.9 \Omega$

Fig. 6.4 shows the values of P_{o_WPT} under various WPT load R values when the wired output has no load ($P_{o_wired} = 0$) and $D = 0.5$. The curve “Cal-simp” is calculated by using the simplified model derived in (6.17) and (6.18). The curve “Cal-full” is calculated by the full model derived in (6.14) - (6.16), which considers parasitic resistances R_{p1} and R_{p2} . As expected, the “Cal-full” curve has a better match with the measured results than the “Cal-simp” curve. Measured maximum value of P_{o_WPT} is $P_{max} = 1.856$ W at $R_{opt} = 2.9 \Omega$ as indicated on Fig. 6.4.

Fig. 6.5 shows a plot for inductor current ripple Δi_r as a function of D at maximum WPT load condition $R_{opt} = 2.9 \Omega$. The “Cal” curve is calculated by (6.7), which matches the measured value within 5.5% error. Fig. 6.6 shows sample waveforms measured from Buck-WPT system with various values of V_{o_wired} at $R_{opt} = 2.9 \Omega$. Waveforms include the phase node voltage, i_r and i_2 . Δi_r and RMS values of i_2 are marked on the figure. When $D = 0.5$, both Δi_r and $I_{2,rms}$ are at their maximum values, and P_{o_WPT} also is at its maximum value since $P_{o_WPT} = I_{2,rms}^2 R$. Table 6.2 shows the measured Δi_r values under various load conditions when $D = 0.5$. The column “Buck” ($\Delta i_r = 4.44$ A) represents the case when WPT branch is removed. In this case, inductance $L_1' = 1.877 \mu\text{H}$ is less than $L_1 = 2.706 \mu\text{H}$ as expected. L_1 is larger because the existence of the ferrite plate for Rx coil increases self-inductance of the Tx coil, as explained in part A of section 6.2. Table 6.2 also shows that when WPT load is less than 10Ω , inductor current ripple values are larger than 4.44A, but when $R = 10 \Omega$, $\Delta i_r = 4.09$ A ($< 4.44\text{A}$). This verifies the discussion in part A of section 6.2 that “the existence of the Rx coil with ferrite might finally lead to a smaller Δi_r value at some load conditions”.

Table 6.2. Δi_r under various WPT load conditions when $D = 0.5$

R (Ω)	Buck	1.43	2	2.5	2.9	3.33	5	7.5	10
Δi_r (A)	4.44	7.88	7.30	6.77	6.40	6.11	5.32	4.48	4.09

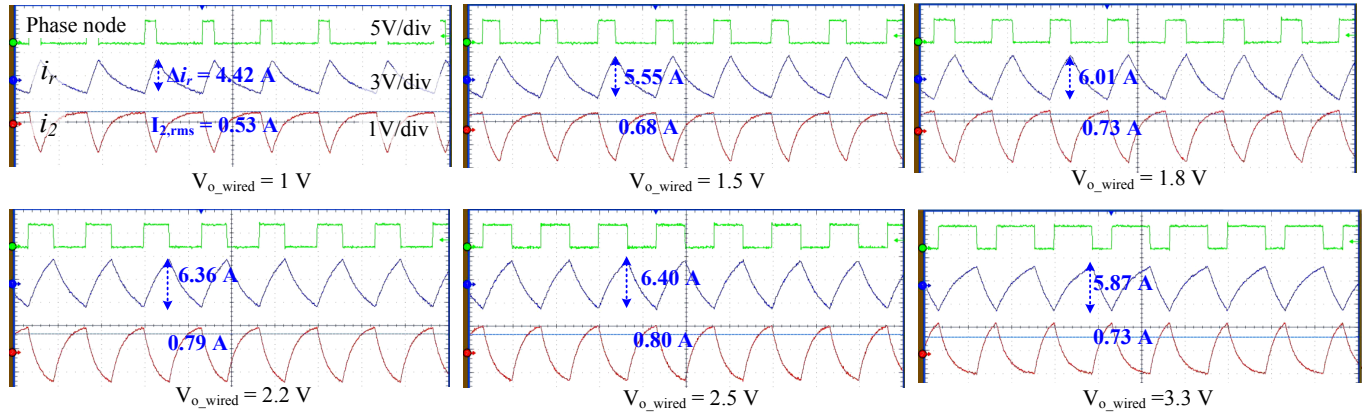


Figure 6.6: Waveforms of the Buck-WPT system when $R = 2.9 \Omega$. i_r is AC coupled and i_2 is DC coupled.

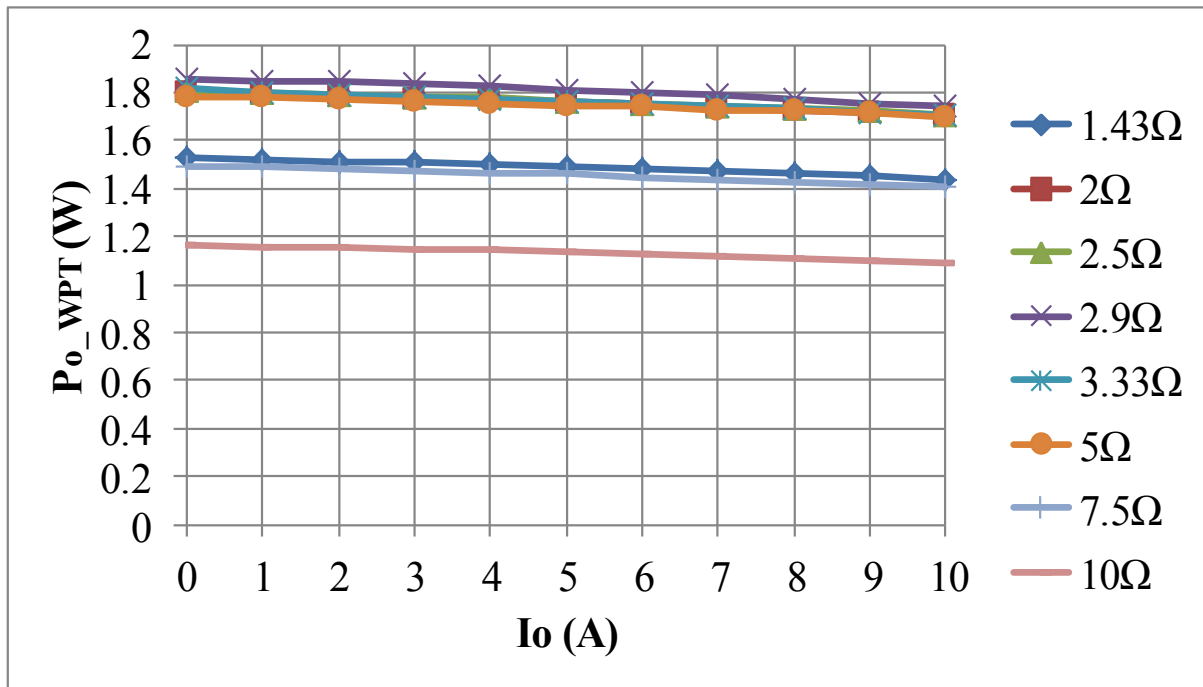
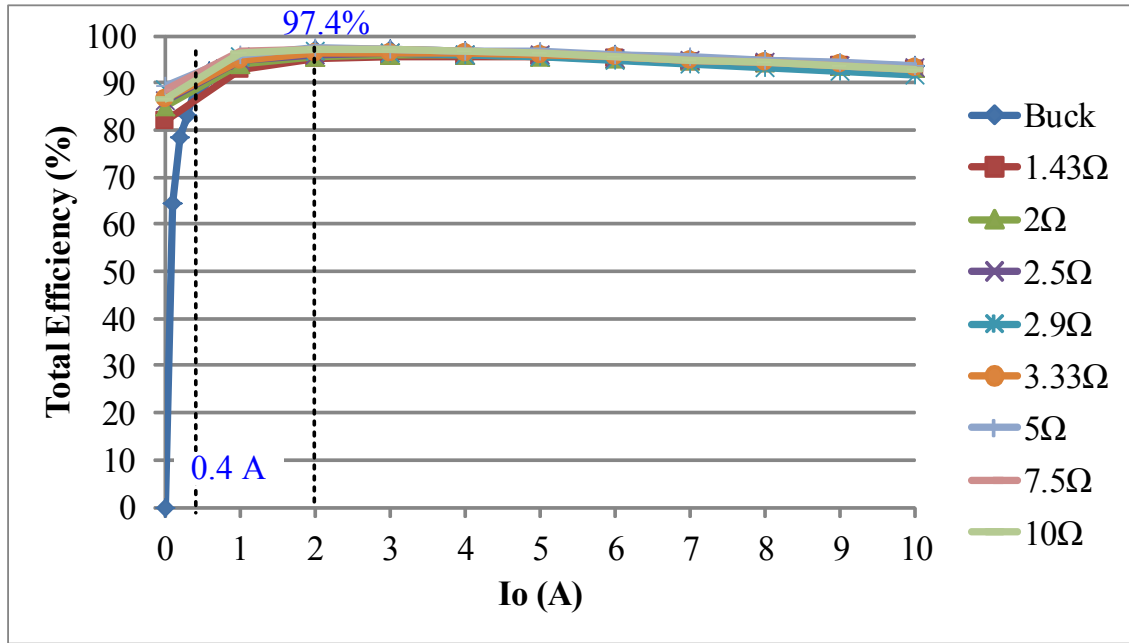
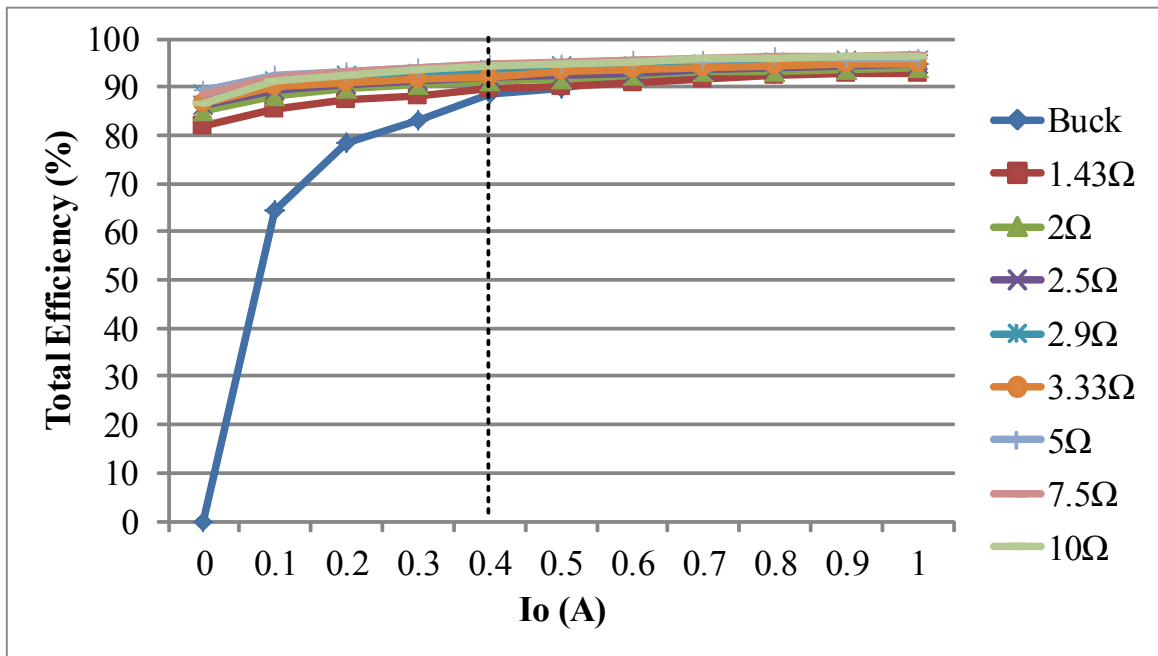


Fig. 6.7. P_{o_WPT} as a function of I_o at various WPT load values when $V_{o_wired} = 2.5V$



(a)



(b)

Figure 6.8: Total Efficiency of the Buck-WPT system (a) for full I_o range and (b) a zoomed in view when $I_o \leq 1A$

P_{o_WPT} values as a function of I_o at various WPT load R values when $V_{o_wired} = 2.5V$ are plotted in Fig. 6.7. It shows that P_{o_WPT} maintains nearly constant within 6.4% variations in full load range of wired output at a given WPT load R value. The small variations of P_{o_WPT} are due to the small variations in D in order to keep $V_{o_wired} = 2.5V$. Fig. 6.8 shows the measured efficiency curves of Buck-WPT system. The curve “Buck” represents the efficiency when buck converter works alone as shown in Fig. 6.1(c). All efficiency curves have very close values when $I_o > 0.4A$. Fig. 6.8(b) shows that when $I_o < 0.4A$, the Buck-WPT system with various WPT load R values achieves much higher efficiency than when there is no WPT output. The achieved efficiency improvement reaches up to ~85% (when I_o approaches to zero). This means that the Buck-WPT system is better than conventional buck converter in terms of light load efficiency when a WPT load exists.

6.4 Summary

This chapter presented a method for Power converter-WPT system that achieves wired power conversion and WPT at the same time. The method eliminates the Tx side circuitry and Tx coil of a conventional WPT system by achieving WPT using inductor current ripple of a DC-DC power converter. As a result, the system size and cost could be reduced. The method is validated by using an example Buck-WPT system. Experimental prototype results verify derived operation principle of Buck-WPT system and maximum power transfer condition for WPT output. Results also show that the Buck-WPT system achieves better light load efficiency compared with conventional buck converter and the achieved light load efficiency improvement reaches up to ~85%.

CHAPTER 7

CONCLUSIONS AND FUTURE WORK

7.1. Summary of Conclusions

Power magnetic devices and systems including power inductors (PI), power transformers, electric machines, and inductively coupled coils such as those used in Wireless Power Transfer (WPT) have been widely used in electric/electronic devices and systems, power transmission systems and energy conversion systems around the world. This dissertation work focuses on PIs and WPT Systems.

Power Inductors are indispensable in many electronic devices and usually they are the bulkiest and/or heaviest component in switching power converters, inverters and filters. Research work and technological advances over the past few decades have resulted in size and weight reduction of other parts in power electronic circuits, such as power switches and capacitors in addition to controllers, at a much faster rate compared to power inductors. Power inductor with larger inductance value and higher power rating usually has larger size and requires larger magnetic core and copper windings. Therefore, the first part of this dissertation work investigates and develops methods to further increase the inductance density and power density of power inductors (i.e. reduce size and weight) with high power efficiency.

On the other hand, Wireless Power Transfer (WPT), has several promising and potential applications such as consumer electronics, medical implants and electric vehicle (EV) charging, among others. During the past decade and currently, there is an increasing interest to develop WPT magnetics and systems with higher efficiency, smaller size and longer transmission

distances under varying conditions to meet several applications' demands. Therefore, the second part of this dissertation work investigates and develops methods to improve WPT systems.

In this dissertation work, several concepts and techniques have been developed in order to (1) further increase the inductance density and power density of power inductors (i.e. reduce size and weight) with high power efficiency and (2) develop WPT magnetics and systems with higher efficiency and longer transmission distances under varying conditions. The contribution of this work is summarized in the following subsections:

A. High Current Power Inductor with NdFeB Magnet for Power Converters

In Chapter 2, a concept is devised and developed which will result in doubling the saturation current of a high current PI with NdFeB permanent magnet (PMPI). By adding a well-designed small piece of fabricated NdFeB magnet (magnet volume is $\sim 0.36\%$ of the PMPI ferrite core volume) in the air gap of the PI, the saturation current of the PMPI is doubled with the same size and inductance value. Magnetic circuit model of PMPI is devised as a design guideline. The desired dimensions of the PM are theoretically calculated before fabrication and then the fabricated PM is characterized. The 3-D physical model of the PMPI is developed by using ANSYS®/Maxwell® software package to illustrate the saturation current doubling. The PMPI is experimentally evaluated in a DC-DC buck power converter. Results show that compared to a PI with the same size and inductance without the PM, the saturation current of the PMPI is doubled. Compared to another PI with a larger size needed to double the saturation current, the ferrite core weight of the PMPI is reduced to 53.6% and the core volume is reduced to 59.2%. Experimental results also show that the addition of the NdFeB-N35EH PM does not introduce additional power losses and increase of temperature for the PMPI and does not affect the power converter efficiency. This work contributes to higher density single-phase power electronic converters with

high efficiency for smaller and efficient devices and equipment, such as power adaptors, mobile electronics devices, renewable energy systems, battery management systems and electric vehicles (EVs), among others.

B. Permanent Magnet Coupled Power Inductor for Multi-Phase DC-DC Power Converters

Chapter 3 presents a two-phase Coupled power inductor (CPI) design that utilizes a PM in order to achieve almost doubled saturation current with the same size compared to the CPI and more than 76% core size reduction compared to the single-phase non-coupled PIs. CPI can achieve size reduction compared with single phase PI because of the magnetic flux cancellation effect. Utilizing CPI in a multi-phase DC-DC power converter yields the benefit of smaller equivalent transient inductance (advantageous for lower output voltage dynamic deviation under transients) with a larger equivalent steady-state inductance (advantageous for smaller steady-state output voltage ripple and higher power efficiency) while increasing saturation current or reducing size. The presented permanent magnet coupled power inductor (PMCI) circuit model and required PM dimensions are derived and used as a design guide. The 3-D physical model of the PMCI is developed by using ANSYS®/Maxwell® software package to “visualize” the saturation current doubling. The fabricated PMCI is tested in a two-phase DC-DC boost power converter experimental hardware prototype. Results show that compared to a conventional CPI design with the same size, weight and inductance, the fabricated PMCI almost doubles the saturation current. Compared to another CPI with a larger size but with even a smaller saturation current, the core volume of the PMCI is reduced to 51.9% and the core weight is reduced to 51.2%. Experimental results also show that the addition of the PM does not cause significant additional power losses and temperature rises for the PMCI, and does not affect the multi-phase power converter efficiency. This work contributes to higher density multi-phase power electronic

converters with high efficiency for smaller and efficient devices and equipment such as consumer electronics, telecommunication systems, data center servers and EVs, among others.

C. Two-Coil Reconfigurable WPT System

Chapter 4 first presents a comparison between two-coil and four-coil WPT configurations for midrange magnetic resonance coupled wireless power transfer (MRC-WPT) systems, then devise a two-coil reconfigurable WPT system topology in order to optimize/maximize transmission efficiency under varying transmission distance (DIS) and lateral misalignment (MIS) conditions. In the first part, physical model simulation results show that the four-coil system achieves longer transmission distance and larger misalignment tolerance with relatively lower efficiency at close distance compared to the two-coil system. In the second part, the two-coil reconfigurable WPT system includes one Tx side and one Rx side and is able to switch between different circuit configurations (which are made up of different values of series and shunt capacitors) at Tx side and/or Rx side. Design guidelines of the two-coil reconfigurable WPT system are devised based on an equivalent circuit model. Proof of concept prototype results show that when the system is perfectly aligned, the reconfigurable system improves the transmission efficiency by up to 20%. When system is laterally misaligned, the transmission efficiency is improved by up to 19%. The main contributions of this work include (1) developing theoretical analysis and simulation models that show the performance differences between the two WPT system types and how the efficiency is impacted by different parameters and (2) devising a two-coil WPT reconfigurable system for highest efficiency for a wider range of distance compared to the conventional system which can achieve highest efficiency for a much narrower distance range. This work contributes to extending the transmission distances and/or efficiency in applications which can benefit from having two-coil WPT systems.

D. Four-Coil Reconfigurable WPT System

Chapter 5 presents a four-coil reconfigurable magnetic resonance coupled wireless power transfer (R-MRC-WPT) system in order to achieve higher transmission efficiency under various DIS and/or MIS conditions. It contributes to higher efficiency, longer transmission distance and larger misalignment tolerance that can be achieved with the presented R-MRC-WPT system when compared to the conventional four-coil MRC-WPT (C-MRC-WPT) system. The reconfigurability in the R-MRC-WPT system is achieved by adaptively switching between different sizes of drive loops and load loops. All drive loops are in the same plane and all load loops are also in the same plane, this method does not require mechanical movements of the drive loop and load loop and does not result in system volume increase. Theoretical basis of the method for the R-MRC-WPT system is derived based on a circuit model and an analytical model. Results from a proof of concept experimental prototype show that the transmission efficiency of the R-MRC-WPT system is higher than the transmission efficiency of the C-MRC-WPT system and the capacitor tuning system for all DIS and MIS values. This work contributes to extending the transmission distances and/or efficiency in applications which can benefit from having four-coil WPT systems.

E. Wireless power transfer using inductor current switching ripple of power converter

Chapter 6 presents a method to achieve wired power conversion and wireless power transfer (WPT) using a hybrid “Power Converter-WPT system”. By achieving WPT using AC switching ripple of power converter, the system eliminates the need for a transmitter stage of a conventional WPT system, which could be beneficial for system size and cost reduction. In addition, it is shown that the hybrid system can achieve higher light load efficiency due to the utilization of part of the switching ripple energy when there exists WPT load. Using Buck-WPT

system (achieves step down DC-DC power conversion and WPT at the same time) as an example, the work derives the system operation principle and maximum power transfer conditions for WPT. Experimental results verify the developed method and theoretical derivations. This work contributes to improving the power density and system efficiency, as well as reducing the cost in applications where both wireless power transfer and wired power conversion are needed.

7.2. Possible Future Research Directions

The following subsections provide a brief outlook on some possible future research directions that are related to the work presented in this dissertation.

A. Power Inductors

Power inductors are still one of the largest and heaviest components in a switching power converter especially when tight regulation for wide load and input range is required and high efficiency is a must. The following are example possible future research topics:

- (1) Investigate alternative and better power inductor geometries that take advantage of the PMPI and PMCI concepts in order to yield additional size/volume reduction and efficiency improvement.
- (2) Continue developing more accurate models which take into consideration the effect of multiple parameters on power losses, efficiency and size performances of the power inductors.
- (3) Investigate on-chip integration configurations and fabrication schemes for the PMPI and PMCI.

- (4) Investigate the use of different soft and hard magnetic materials which can yield PMPI and PMCI with smaller size and higher efficiency at different power levels and various operation conditions.
- (5) Investigate concepts that allow for the use of PMPI and PMCI in power converters with bidirectional power flow.

B. Wireless Power Transfer and Harvesting Systems

The work in this dissertation focused on the configurations and performances of power magnetics part for inductively coupled wireless power transfer systems. The following are example possible future research topics:

- (1) Investigate the development of control algorithms and circuits/embedded systems to realize closed-loop controllers for the presented two-coil reconfigurable WPT system.
- (2) Investigate the development of control algorithms and circuits/embedded systems to realize closed-loop controllers for the presented four-coil reconfigurable WPT system.
- (3) Investigate efficient low-cost power electronic circuits to drive the Tx coils.
- (4) Investigate efficient low-cost power electronic circuits and controllers to achieve voltage/current/power regulation at the Rx side under varying distances, misalignments, and surrounding objects.
- (5) Investigate and develop control methods and/or modified topologies which allow for regulating power converter with dual types of outputs, one wireless and one wired, based on the presented Hybrid Power Converter-WPT system which can yield power regulation system with reduced size and cost.

REFERENCES

Chapter 1

- [A1] Coilcraft, "Automotive Applications for Coilcraft Magnetics," [online]. Available: http://www.coilcraft.com/prod_hitemp.cfm, April, 2016.
- [A2] Q. Li, "Low-Profile Magnetic Integration for High-Frequency Point-of-Load Converter," PhD dissertation, Virginia Polytechnic Institute and State University, 2011.
- [A3] Rengang Chen, J. D. van Wyk, S. Wang; W. G. Odendaal, "Planar electromagnetic integration technologies for integrated EMI filters," 2003 Industry Applications Conference, 38th IAS Annual Meeting, pp. 1582 - 1588, vol. 3, 2003.
- [A4] R. Chen, J. D. van Wyk, S. Wang and W. G. Odendaal, "Application of structural winding capacitance cancellation for integrated EMI filters by embedding conductive layers," 2004 Industry Applications Conference, 39th IAS Annual Meeting, vol 4, pp. 2679 - 2686, 2004.
- [A5] J. D. van Wyk; F. C. Lee, "On a Future for Power Electronics," IEEE Journal of Emerging and Selected Topics in Power Electronics, vol. 1, no. 2, pp. 59 - 72, Feb. 2013.
- [A6] X. Peng, W. Jia, Y. Kaiwei, M. Yu, and F. C. Lee, "Investigation of candidate topologies for 12 V VRM," Seventeenth Annual IEEE Applied Power Electronics Conference and Exposition, vol. 2, pp. 686-692, March 2002.
- [A7] B. Huffman and R. Flatness, "Power Conversion from Milliamps to Amps at Ultra-High Efficiency," Linear Technology Application Note 54, March 1993.
- [A8] Y. Panov and M. Jovanovic, "Design and performance evaluation of low-voltage/high-current dc/dc on-board modules," Annual IEEE Applied Power Electronics Conference and Exposition, vol. 1, pp. 545-552, March 1999.
- [A9] J. Wei and F. Lee, "Two-Stage Voltage Regulator for Laptop Computer CPUs and Corresponding Advanced Control Schemes to Improve Light Load Performance," Applied Power Electronics Conference and Exposition, Nineteenth Annual IEEE , vol. 2, pp. 1294-1300, March 2004.
- [A10] A. Consoli, G. Scarcella, G. Giannetto, and A. Testa, "A multiphase DC/DC converter for automotive dual voltage power systems," IEEE Industrial Application Magazine, vol. 6, pp. 35-42, December 2004.

- [A11] P. Xu, R. Yuan-Chen, M. Ye, and F. C. Lee, "A family of novel interleaved DC/DC converters for low-voltage high-current voltage regulator module applications," In Proceeding IEEE 32nd Annual Power Electronics Specialists Conference, vol. 3, pp. 1507-1511, June 2001.
- [A12] P. Hazucha, G. Schrom, et. al. "A 233-MHz 80%-87% efficient four-phase DC-DC converter utilizing air-core inductors on package," IEEE Journal of Solid-State Circuits, vol. 40, Issue 4, pp. 838-845, April 2005.
- [A13] Yan Dong, Jinghai Zhou, F.C. Lee, Ming Xu, and Shuo Wang, "Twisted Core Coupled Inductors for Microprocessor Voltage Regulators," IEEE Transactions on Power Electronics, vol. 23, no. 5, pp. 2536, September 2008.
- [A14] W. Li, X. Ly, Y. Deng, J. Liu, and X. He, "A Review of Non-Isolated High Step-Up DC-DC Converters in Renewable Energy Applications," IEEE Applied Power Electronics Conference and Exposition, vol. 12, pp. 364-369, February 2009.
- [A15] M. Ferdowsi and K. P. Yalamanchili, "Review of Multiple Input DC-DC Converters for Electric and Hybrid Vehicles," IEEE Vehicle Power and Propulsion Conference, pp. 160-163, September 2005.
- [A16] G. J. Vachtsevanos and K. C. Kalaitzakis, "On the Control and Stability of Grid Connected Photovoltaic Sources," IEEE Transactions on Energy Conversion, vol. EC-2, issue 4, pp. 556-562, December 1987.
- [A17] D.D. Lu and V. G. Agelidis, "Photovoltaic-Battery-Powered DC Bus System for Common Portable Electronic Devices," IEEE Transactions on Power Electronics, vol. 24, Issue 3, pp. 849-855, March 2009.
- [A18] M. Ayres, et. al., "Photovoltaic cell model for the International Space Station," the Twenty-Eighth IEEE Photovoltaic Specialists Conference, pp. 1301-1303, September 2000.
- [A19] O. Garcia, P. Zumel, A. de Castro, and A. Cobos, "Automotive DC-DC bidirectional converter made with many interleaved buck stages," IEEE Transactions on Power Electronics, vol. 21, Issue 3, pp. 578-586, May 2006.
- [A20] K. Siri and K. A. Conner, "Fault-tolerant scaleable solar power bus architectures with maximum power tracking," Sixteenth Annual IEEE Applied Power Electronics Conference and Exposition, vol. 2, pp. 1009-1014, March 2001.
- [A21] J. Abu Qahouq and L. Huang, "A Constant Switching Frequency Coupled-Inductor VR with Improved Light Load Efficiency," IEEE Applied Power Electronics Conference and Exhibition, pp. 844-849, February 2008.
- [A22] J. Abu Qahouq, O. Abdel-Rahman, L. Huang and I. Batarseh, "On Load Adaptive Control of Voltage Regulators for Power Managed Loads: Control Schemes to Improve

- Converter Efficiency and Performance,” IEEE Transactions on Power Electronics, vol. 22, no. 5, September 2007.
- [A23] J. Abu Qahouq, “Control Scheme for Sensor-Less Operation and Detection of CCM and DCM Operation Modes in Synchronous Switching Power Converters,” IEEE Transactions on Power Electronics, vol. 25, no.10, pp. 2489-2495, October 2010.
- [A24] J. Abu Qahouq, “Analysis and Design of N-Phase Current Sharing Auto-Tuning Controller,” IEEE Transactions on Power Electronics, vol. 25, no. 6, pp. 1641 - 1651, June 2010.
- [A25] J. Abu Qahouq, H. Mao, H. Zhou, and I. Batarseh, “Interleaved Current Doublers with Parallel Connected Transformers Scheme,” The IET Journal (formerly IEE) of Power Electronics, vol. 1, no. 1, pp. 27–37, March 2008.
- [A26] J. Abu Qahouq and L. Huang, “Highly Efficient VRM For Wide Load Range with Dynamic Non-Uniform Current Sharing,” IEEE Applied Power Electronics Conference and Exhibition, pp. 543–549, February 2007.
- [A27] Y. Kaiwei, Q. Yang, X. Ming, and F. C. Lee, “A novel winding-coupled buck converter for high frequency, high-step-down DC-DC conversion,” IEEE Transactions on Power Electronics, vol. 20, no. 5, pp. 1017-1024, September 2005.
- [A28] H.N. Nagaraja, D.K. Kasta, A. Petra, "Design Principles of a Symmetrically Coupled Inductor Structure for Multiphase Synchronous Buck Converters," IEEE Trans. Ind. Electron., vol. 58, no. 3, pp. 988-997, Mar. 2011.
- [A29] Jaber A. Abu Qahouq and Vara Prasad Arikatla, "Online closed-loop autotuning digital controller for switching power converters," IEEE Trans. Ind. Electron., vol. 60, no. 5, pp. 1747-1758, May 2013.
- [A30] Wangxin Huang and Jaber A. Abu Qahouq, "Energy Sharing Control Scheme for State-of-Charge Balancing of Distributed Battery Energy Storage System," IEEE Trans. Ind. Electron., vol. 62, no. 5, pp. 2764-2776, May 2015.
- [A31] Z. Gu, D. Zhang and Z. Zhao, "Input Current Ripple Cancellation Technique for Boost Converter Using Tapped Inductor," IEEE Trans. Ind. Electron., vol. 61, no. 10, pp. 5323-5333, Oct. 2014.
- [A32] Y.Hsieh, J.Chen, L.Yang, C.Wu and W.Liu, "High-Conversion-Ratio Bidirectional DC–DC Converter With Coupled Inductor," IEEE Trans. Ind. Electron., vol. 61, no. 1, pp. 210-222, Jan. 2014.
- [A33] X. Liu, J. Xu, Z. Chen and N. Wang, "Single-Inductor Dual-Output Buck-Boost Power Factor Correction Converter," IEEE Trans. Ind. Electron., vol. 62, no. 2, pp. 943-952, Feb. 2015.

- [A34] Wangxin Huang and Jaber A. Abu Qahouq, "An online battery impedance measurement method using DC-DC power converter control," *IEEE Trans. Ind. Electron.*, vol. 61, no. 11, pp. 5987-5995, Nov. 2014.
- [A35] G.D. Capua and N. Femia, "A Critical Investigation of Coupled Inductors SEPIC Design Issues," *IEEE Trans. Ind. Electron.*, vol. 61, no. 6, pp. 2724-2734, June 2014.
- [A36] Y. Tang and S. Xie, "Pulsewidth Modulation of Z-Source Inverters With Minimum Inductor Current Ripple," *IEEE Trans. Ind. Electron.*, vol. 61, no. 1, pp. 98-106, Jan. 2014.
- [A37] Z. Dang, J. Abu Qahouq, "Evaluation of High-Current Toroid Power Inductor with NdFeB Magnet for DC-DC Power Converters," *IEEE Transaction on Industrial Electronics*, vol. 62, no. 11, pp. 6868-6876, Nov. 2015.
- [A38] Z. Dang and J. Abu Qahouq, "Permanent Magnet Power Inductor Circuit and Physical Modeling," *International Review on Modelling and Simulations (I.RE.MO.S.)*, vol. 5, no. 5, pp. 2001-2006, Oct. 2012.
- [A39] Z. Dang and J. Abu Qahouq, "Permanent Magnet Toroid Power Inductor with Increased Saturation Current," *The 2013 IEEE Applied Power Electronics Conference and Exposition, APEC'2013*, pp. 2624-2628, Mar. 2013.
- [A40] Z. Dang and J. Abu Qahouq, "Permanent magnet power inductor with EE core for switching power converters," *The 2015 IEEE Applied Power Electronics Conference and Exposition, APEC'2015*, pp. 1073-1077, Mar. 2015.
- [A41] Z. Dang and J. Abu Qahouq, "On-Chip Three-Phase Coupled Power Inductor for Switching Power Converters," *The 2015 IEEE Applied Power Electronics Conference and Exposition, APEC'2015*, pp. 1045-1050, Mar. 2015.
- [A42] Z. Dang and J. Abu Qahouq, "On-chip coupled power inductor for switching power converters," *The 2014 IEEE Applied Power Electronics Conference and Exposition, APEC'2014*, pp 2854-2859, Mar. 2014.
- [A43] Z. Dang and J. Abu Qahouq, "Modelling and Design Guidelines of High Density Power Inductor for Battery Power Unit," *The 2016 IEEE Applied Power Electronics Conference and Exposition, APEC'2014*, Mar. 2016.
- [A44] Ferroxcube, "Soft Ferrites and Accessories", [Online]. Available: http://www.ferroxcube.com/FerroxcubeCorporateReception/datasheet/FXC_HB2013.pdf.
- [A45] R.A. Salas and J. Pleite, "Equivalent Electrical Model of a Ferrite Core Inductor Excited by a Square Waveform Including Saturation and Power Losses for Circuit Simulation," *IEEE Trans. on magnetics*, vol. 49, no. 7, pp. 4257-4260, July 2013.

- [A46] H. Jia, J. Lu, X. Wang, K. Padmanabhan and Z. J. Shen, "Integration of a Monolithic Buck Converter Power IC and Bondwire Inductors With Ferrite Epoxy Glob Cores," IEEE Trans. on Power Electron., vol. 26, no. 6, pp. 1627-1630, June 2011.
- [A47] M. Perdigao, J. Trovao, J. Alonso and E. Saraiva, "Large-Signal Characterization of Power Inductors in EV Bidirectional DC-DC Converters Focused on Core Size Optimization," IEEE Trans. Ind. Electron., no. 99, pp. 1-11, Feb. 2015.
- [A48] P. Herget, N. Wang, E.J. O'Sullivan, B.C. Webb, L.T. Romankiw, R. Fontana, X. Hu, G. Decad and W.J. Gallagher, "A Study of Current Density Limits Due to Saturation in Thin Film Magnetic Inductors for On-Chip Power Conversion," IEEE Trans. on magnetics, vol. 48, no. 11, pp. 4119-4122, Nov. 2012.
- [A49] B. Zhao, Q. Song, W. Liu, "Experimental Comparison of Isolated Bidirectional DC-DC Converters Based on All-Si and All-SiC Power Devices for Next-generation Power Conversion Application," IEEE Trans. Ind. Electron., vol. 61, no. 3, pp. 1389 - 1393, Mar. 2014.
- [A50] Y. Nakakohara, H. Otake, T. M. Evans, T. Yoshida, M. Tsuruya and K. Nakahara, "Three-Phase LLC Series Resonant DC/DC Converter Using SiC MOSFETs to Realize High-Voltage and High-Frequency Operation," IEEE Trans. Ind. Electron., vol. 63, no. 4, pp. 2103 - 2110, April 2016.
- [A51] O. Khan, W. Xiao and H. H. Zeineldin, "Gallium-Nitride-Based Submodule Integrated Converters for High-Efficiency Distributed Maximum Power Point Tracking PV Applications," IEEE Trans. Ind. Electron., vol. 63, no. 2, pp. 966 - 975, Feb. 2016.
- [A52] J. Shea, "Power System Capacitors - [Book Review]," IEEE Electrical Insulation Magazine, vol. 22, no. 4, pp. 63 - 63, April 2006.
- [A53] T. Sato, K. Watanabe, H. Igarashi, T. Matsuo, T. Mifune, K. Kawano, M. Suzuki, Y. Uehara and A. Furuya, "3-D Optimization of Ferrite Inductor Considering Hysteresis Loss," IEEE Trans. on magnetics, vol. 49, no. 5, pp. 2129-2132, May 2013.
- [A54] T. Modeer, S. Norrga and H. Nee, "High-Voltage Tapped-Inductor Buck Converter Utilizing an Autonomous High-Side Switch," IEEE Trans. Ind. Electron., no. 99, pp. 1-11, Oct. 2014.
- [A55] J. Ewanchuk and J. Salmon, "Three-limb Coupled Inductor Operation for Paralleled Multi-level Three-Phase Voltage Sourced Inverters," IEEE Trans. Ind. Electron., vol. 60, no. 5, pp. 1979-1988, May 2013.
- [A56] M. Mohammadi and H. Farzanehfard "New Family of Zero-Voltage-Transition PWM Bidirectional Converters With Coupled Inductors," IEEE Trans. Ind. Electron., vol. 59, no. 2, pp. 912-919, Feb 2012.

- [A57] H. Wu, K. Sun, L. Chen, L. Zhu and Y. Xing, "High Step-Up/Step-Down Soft-Switching Bidirectional DC-DC Converter with Coupled-Inductor and Voltage Matching Control for Energy Storage Systems," *IEEE Trans. Ind. Electron.*, no. 99, pp. 1-11, Jan. 2016.
- [A58] S. M. Chen, T. J. Liang, L. S. Yang and J. F. Chen, "A Boost Converter With Capacitor Multiplier and Coupled Inductor for AC Module Applications," *IEEE Trans. Ind. Electron.*, vol. 60, no. 4, pp. 1503 - 1511, April 2013.
- [A59] G. Chen, Y. Deng, Y. Tao, X. He, Y. Wang and Y. Hu, "Topology Derivation and Generalized Analysis of Zero-Voltage-Switching Synchronous DC-DC Converters with Coupled Inductors," *IEEE Trans. Ind. Electron.*, no. 99, pp. 1-1, Mar. 2016.
- [A60] G. Spiazzi and S. Buso, "Analysis of the Interleaved Isolated Boost Converter With Coupled Inductors," *IEEE Trans. Ind. Electron.*, vol. 62, no. 7, pp. 4481-4491, July 2015.
- [A61] F. Yang, X. B. Ruan, Y. Yang, Z.H. Ye, "Interleaved Critical Current Mode Boost PFC Converter With Coupled Inductor," *IEEE Trans. Power Electron.*, vol. 26, no. 9, pp. 2404-2413, Sep. 2011.
- [A62] P. L. Wong, P. Xu, B. Yang, and F. C. Lee, "Performance improvements of interleaving VRMs with coupling inductors," *IEEE Trans. Power Electron.*, vol. 16, no. 4, pp. 499-507, Jul. 2001.
- [A63] Q. Li, Y. Dong, F. C. Lee and D. J. Gilham, "High-Density Low-Profile Coupled Inductor Design for Integrated Point-of-Load Converters" *IEEE Trans. Power Electron.*, vol. 28, no. 1, pp. 547 - 554, Jan. 2013.
- [A64] Y. Yang, D. Yan, F.C. Lee, "A new coupled inductors design in 2-phase interleaving VRM," *IEEE 6th International Power Electronics and Motion Control Conference*, pp. 344-350, May 2009.
- [A65] G.Y. Zhu, B. McDonald, K.R. Wang "Modeling and Analysis of Coupled Inductors in Power Converters," *IEEE Trans. Power Electron.*, vol. 26, no. 5, pp. 1355-1363, May 2011.
- [A66] N. Tesla, "System of transmission of electrical energy," U.S. Patent, No. 645576, Mar, 20, 1900.
- [A67] N. Tesla, "Apparatus for Transmitting Electrical Energy," U.S. Patent, 1119732, Patented Dec. 1, 1914.
- [A68] [Online]. Available: <http://www.tfcbooks.com/articles/witricity.htm>, 2013.
- [A69] S. Y. R. Hui, "Magnetic Resonance for Wireless Power Transfer: A Look Back," *IEEE Power Electronics Magazine*, vol. 3, no. 1, pp. 14-31, Jan. 2016.

- [A70] S. Hui, W. Zhong, C. Lee, "A Critical Review of Recent Progress in Mid-Range Wireless Power Transfer," *IEEE Trans. Power Electron.* Vol. 29, no. 9, pp. 4500-4511, Sept. 2014.
- [A71] J. Kim, H. Son, D. Kim, Y. Park, "Optimal design of a wireless power transfer system with multiple self-resonators for an LED TV," *IEEE Trans. Consumer Electron.*, vol. 58, no. 3, pp. 775-780, Aug. 2012.
- [A72] R. Wu, W. Li, H. Luo, J.K.O. Sin, C.C. Yue, "Design and Characterization of Wireless Power Links for Brain-Machine Interface Applications," *IEEE Trans. Power Electron.*, vol.29, no.10, pp. 5462-5471, Oct. 2014.
- [A73] W. Chwei-Sen, O. H. Stielau, and G. A. Covic, "Design considerations for a contactless electric vehicle battery charger," *IEEE Trans. Ind. Electron.*, vol. 52, no. 5, pp. 1308-1314, Oct. 2005.
- [A74] G. A. Landis, "Reevaluating Satellite Solar Power Systems for Earth," *IEEE 4th World Conference on Photovoltaic Energy Conversion*, pp.1939-1942, May 7-12, 2006.
- [A75] A. Sahai, D. Graham, "Optical wireless power transmission at long wavelengths," *International Conference on Space Optical Systems and Applications (ICSOS)*, pp. 164-170, 11-13, May 2011.
- [A76] U. K. Madawala and D. J. Thrimawithana, "A bidirectional inductive power interface for electric vehicles in V2G systems," *IEEE Trans. Ind. Electron.*, vol. 58, no. 10, pp. 4789-4796, Oct. 2011.
- [A77] M. G. Eagen, D. L. O'Sullivan, J. G. Hayes, M. J. Willers, and C. P. Henze, "Power factor corrected single stage inductive charger for electric vehicle batteries," *IEEE Trans. Ind. Electron.*, vol. 54, no. 2, pp. 1217-1226, Apr. 2007.
- [A78] G. A. Covic, J. T. Boys, M. L. G. Kissin, and H. G. Lu, "A three-phase inductive power transfer system for roadway-powered vehicles," *IEEE Trans. Ind. Electron.*, vol. 54, no. 6, pp. 3370-3378, Dec. 2007.
- [A79] M. Budhia, G. A. Covic, and J. T. Boys, "Design and Optimization of Circular Magnetic Structures for Lumped Inductive Power Transfer Systems," *IEEE Trans. Power Electron.*, vol. 26, no.11, pp. 3096-3108, Nov. 2011.
- [A80] O.C. Onar, J.M. Miller, S.L. Campbell, C. Coomer, C. P. White, and L.E. Seiber, "Oak Ridge National Laboratory Wireless Power Transfer Development for Sustainable Campus Initiative," *IEEE Transportation Electrification Conference and Expo (ITEC)*, pp. 1-8, June 2013.
- [A81] J.M. Miller, O.C. Onar, M. Chinthavali, "Primary-Side Power Flow Control of Wireless Power Transfer for Electric Vehicle Charging", *IEEE Journal of Emerging and Selected Topics in Power Electron.*, vol. 3, no. 1, pp. 147-162, Mar. 2015.

- [A82] S.Y. Choi, J. Huh, W.Y. Lee, C.T. Rim, "Asymmetric Coil Sets for Wireless Stationary EV Chargers With Large Lateral Tolerance by Dominant Field Analysis," *IEEE Trans. Power Electron.*, vol.29, no.12, pp. 6406-6420, Dec. 2014.
- [A83] J. Lee, B. Han, "A Bidirectional Wireless Power Transfer EV Charger Using Self-Resonant PWM," *IEEE Trans. Power Electron.*, vol.30, no.4, pp. 1784-1787, April 2015.
- [A84] A. Kurs, A. Karalis, R. Moffatt, J. D. Joannopoulos, P. Fisher, and M. Soljačić, "Wireless power transfer via strongly coupled magnetic resonances," *Science*, vol. 317, no. 5834, pp. 83-86, Jul. 2007.
- [A85] A. P. Sample, D. A. Meyer, and J. R. Smith, "Analysis, experimental results, and range adaptation of magnetically coupled resonators for wireless power transfer," *IEEE Trans. Ind. Electron.*, vol. 58, no. 2, pp. 544-554, Feb. 2011.
- [A86] Z. Dang, Y. Cao and J. Abu Qahouq, "Reconfigurable Magnetic Resonance-Coupled Wireless Power Transfer System," *IEEE Transactions on Power Electronics*, vol. 30, no. 11, pp. 6057-6069, Nov. 2015.
- [A87] Z. Dang and Jaber Abu Qahouq, "Range and Misalignment Tolerance Comparisons between Two-coil and Four-coil Wireless Power Transfer Systems," *The 2015 IEEE Applied Power Electronics Conference and Exposition, APEC'2015*, pp. 1234-1240, Mar. 2015.
- [A88] Z. Dang and Jaber Abu Qahouq, "Elimination Method for the Transmission Efficiency Valley of Death in Laterally Misaligned Wireless Power Transfer Systems," *2015 IEEE Applied Power Electronics Conference and Exposition, APEC'2015*, pp. 1644-1649, Mar. 2015.
- [A89] Z. Dang and J. Abu Qahouq, "Modeling and Investigation of Magnetic Resonance Coupled Wireless Power Transfer System with Lateral Misalignment," *The 2014 IEEE Applied Power Electronics Conference and Exposition, APEC'2014*, pp 1317-1322, Mar. 2014.
- [A90] Z. Dang, "Magnetic Resonance Coupled Wireless Power Transfer Systems," *Master Thesis, The University of Alabama*, Dec. 2013.
- [A91] Z. Dang, J.A. Abu Qahouq, "Modelling and Simulation of Magnetic Resonance Coupled Wireless Power Transfer Systems," *International Review of Modelling and Simulation (I.RE.MO.S)*, vol. 6, no. 5, pp. 1607-1617, Oct. 2013.
- [A92] Y. Zhang, Z. Zhao, K. Chen, "Frequency Decrease Analysis of Resonant Wireless Power Transfer," *IEEE Trans. Power Electron.*, vol.29, no.3, pp. 1058-1063, March 2014.
- [A93] Y. Lim, H. Tang, S. Lim, J. Park, "An Adaptive Impedance-Matching Network Based on a Novel Capacitor Matrix for Wireless Power Transfer," *IEEE Trans. Power Electron.*, vol.29, no.8, pp. 4403-4413, Aug. 2014.

- [A94] W.M. Ng, C. Zhang, D. Lin, S.Y.R. Hui, "Two- and Three-Dimensional Omnidirectional Wireless Power Transfer," *IEEE Trans. Power Electron.*, vol.29, no.9, pp. 4475-4478, Sep. 2014.
- [A95] J. Yin, D. Lin, C. Lee and S.Y.R. Hui, "A Systematic Approach for Load Monitoring and Power Control in Wireless Power Transfer Systems Without Any Direct Output Measurement," *IEEE Trans. Power Electron.*, vol. 30, no. 3, pp. 1657-1667, March 2015.
- [A96] W. Zhong, C. Zhang, X. Liu, S.Y.R. Hui, "A Methodology for Making a Three-Coil Wireless Power Transfer System More Energy Efficient Than a Two-Coil Counterpart for Extended Transfer Distance," *IEEE Trans. Power Electron.*, vol. 30, no. 2, pp. 933-942, Feb. 2015.
- [A97] B.L. Cannon, J.F. Hoburg, D.D. Stancil, S.C. Goldstein, "Magnetic Resonant Coupling As a Potential Means for Wireless Power Transfer to Multiple Small Receivers," *IEEE Trans. Power Electron.*, vol. 24, no. 7, pp. 1819-1825, July 2009.
- [A98] H. Li, J. Li, K. Wang, W. Chen, X. Yang, "Included in Your Digital Subscription A Maximum Efficiency Point Tracking Control Scheme for Wireless Power Transfer Systems Using Magnetic Resonant Coupling," *IEEE Trans. Power Electron.*, no. 99, pp. 1-11, 2014.
- [A99] K. Chen, Z. Zhao, "Analysis of the Double-Layer Printed Spiral Coil for Wireless Power Transfer", *IEEE Journal of Emerging and Selected Topics in Power Electron.*, vol.1, no.2, pp. 114-121, Jun. 2013.
- [A100] C. Zhang, W. Zhong, X. Liu; S.Y.R. Hui, "A Fast Method for Generating Time-Varying Magnetic Field Patterns of Mid-Range Wireless Power Transfer Systems," *IEEE Trans. Power Electron.*, vol.30, no.3, pp. 1513-1520, March 2015.
- [A101] S. Aldhaher, P.C.-K. Luk, J.F. Whidborne, "Electronic Tuning of Misaligned Coils in Wireless Power Transfer Systems," *IEEE Trans. Power Electron.*, vol.29, no.11, pp. 5975-5982, Nov. 2014.
- [A102] M. Zargham, P.G. Gulak "Maximum Achievable Efficiency in Near-Field Coupled Power-Transfer Systems," *IEEE Trans. Biomedical Circuits and Systems*, vol. 6, no.3, pp. 228-245, June 2012.
- [A103] L.H. Chen, S. Liu, Y.C. Zhou, and T.J. Cui, "An Optimizable Circuit Structure for High-Efficiency Wireless Power Transfer," *IEEE Trans. Ind. Electron.*, vol. 60, no. 1, pp. 339-349, Jan. 2013.
- [A104] M. Kiani, M. Ghovanloo, "The circuit theory behind coupled-mode magnetic resonance-based wireless power transmission," *IEEE Trans. Circuit and Systems I: Regular Papers*, vol.59, no. 9 pp. 2065-2074, Sep. 2012.

- [A105] T. P. Duong and J. W. Lee, "Experimental results of high-efficiency resonant coupling wireless power transfer using a variable coupling method," *IEEE Microw. Wireless Components Lett.*, vol. 21, no. 8, pp. 442-444, Aug. 2011.
- [A106] Y. Zhang, Z. Zhao, "Frequency-Splitting Analysis of Four-Coil Resonant Wireless Power Transfer" *IEEE. Trans. Industry App.*, vol. 50, no. 4, pp. 2436-2445, July 2014.
- [A107] F. Bedell, "History of A-C wave Form, Its Determination and Standardization," *Transactions of the American Institute of Electrical Engineers*, vol. 61, no. 12, pp. 864 - 868, Dec. 1942.
- [A108] U.S. Department of Energy, "Benefits of Using Mobile Transformers and Mobile Substations for Rapidly Restoring Electrical Service," a report to the United States Congress pursuant to Section 1816 of the Energy Policy Act of 2005, August 2006. [online]. Available: http://energy.gov/sites/prod/files/oeprod/DocumentsandMedia/MTS_Report_to_Congress_FINAL_73106.pdf
- [A109] U.S. Department of Energy, "LARGE POWER TRANSFORMERS AND THE U.S.ELECTRIC GRID," Infrastructure Security and Energy Restoration Office of Electricity Delivery and Energy Reliability, April 2014.
- [A110] HITACHI, "Generator Step-up Transformers(GSU)," [online]. Available: <http://www.hitachi.com/products/power/TandD/gsu/index.html>
- [A111] United States Department of Labor, "Illustrated Glossary: Substations," [online]. Available: https://www.osha.gov/SLTC/etools/electric_power/illustrated_glossary/substation.html
- [A112] D. Czarkowski, M. K. Kazimierczuk, "Linear circuit models of PWM flyback and buck/boost converters," *IEEE Transactions on Circuits and Systems I: Fundamental Theory and Applications*, vol. 39, no. 8, pp. 688 - 693, Aug. 1992.
- [A113] M. Jinno, P. Y. Chen and K. C. Lin, "An Efficient Active LC Snubber for Forward Converters," *IEEE Transactions on Power Electronics*, vol. 24, no. 6, pp. 1522 - 1531, June 2009.
- [A114] I. S. de Freitas, C. B. Jacobina, E. Cipriano dos Santos Jr., "Single-Phase to Single-Phase Full-Bridge Converter Operating With Reduced AC Power in the DC-Link Capacitor," *IEEE Transactions on Power Electronics*, vol. 25, no. 2, pp. 272 - 279, Feb. 2010.
- [A115] F. Ma, A. Luo, X. Xu, H. Xiao, C. Wu and W. Wang, "A Simplified Power Conditioner Based on Half-Bridge Converter for High-Speed Railway System," *IEEE Transactions on Industrial Electronics*, vol. 60, no. 2, pp. 728 - 738, Feb. 2013.

- [A116] S. Y. Chen, Z. R. Li and C. L. Chen, "Analysis and Design of Single-Stage AC/DC LLC Resonant Converter," IEEE Transactions on Industrial Electronics, vol. 59, no. 3, pp. 1538 - 1544, Mar. 2012.
- [A117] J. Deng, S. Li, S. Hu, C. C. Mi and R. Ma, "Design Methodology of LLC Resonant Converters for Electric Vehicle Battery Chargers," IEEE Transactions on Vehicular Technology, vol. 63, no. 4, pp. 1581 - 1592, April 2014.
- [A118] Woodbank Communications Ltd, "Electrical Machines - Generators (Description and Applications)," [online]. Available: <http://www.mpoweruk.com/generators.htm>

Chapter 2

- [B1] J.T. Ludwing, "Inductor Biased with Permanent Magnets: Part I-Theory and Analysis," Trans. American Institute of Electrical Engineers, PartI: Communication and Electronics, vol. 79, no. 3, pp. 273-278, July 1960.
- [B2] Zhigang Dang and J. A. Qahouq, "Permanent Magnet Toroid Power Inductor with Increased Saturation Current," in Proc. IEEE Appl. Power Electron. Conf., pp 2624-2628, Mar. 2013.
- [B3] Zhigang Dang and J. Abu Qahouq, "Permanent Magnet Power Inductor Circuit and Physical Modeling," International Review on Modelling and Simulations (I.RE.MO.S.), vol. 5, no. 5, pp. 2001-2006, Oct. 2012.
- [B4] Zhigang Dang and J. Abu Qahouq, "Evaluation of Permanent Magnet Power Inductor with EE Core for Switching Power Converters," in Proc. IEEE Appl. Power Electron. Conf., pp. 1073-1077, Mar. 2015.
- [B5] Zhigang Dang and J. Abu Qahouq, "Modelling and Design Guidelines of High Density Power Inductor for Battery Power Unit," in Proc. IEEE Appl. Power Electron. Conf., Mar. 2016.
- [B6] G.M. Shane, S.D. Sudhoff, "Design Paradigm for Permanent-Magnet-Inductor-Based Power Converters," IEEE Trans. Energy Conversion, vol. 28, no. 4, pp. 880-893, Dec, 2013.
- [B7] R. Wrobel, N. McNeill and P.H. Mellor, "Performance Analysis and Thermal Modeling of a High-Energy-Density Prebiased Inductor," IEEE Trans. Ind. Electron., vol. 57, no. 1, pp. 201-208, Jan. 2010.
- [B8] R. W. Erickson, D. Maksimovic. "Fundamentals of Power Electronics", Springer, 2000.
- [B9] FERROXCUBE, "3C20 Material Specification," [Online]. Available: <http://ferrite.ru/uploads/pdf/products/ferroxcube/materials/3c20.pdf>, Feb. 2007.

- [B10] Arnold Magnetices Technologies Corp., "Neodymium-Iron-Boron Magnet Catalogs" [Online]. Available: http://www.arnoldmagnetics.com/Neodymium_Literature.aspx , 2015.
- [B11] B.D. Cullity, C.D. Graham, "Introduction to Magnetic Materials", 2nd edition Wiley-IEEE Press, 2009.
- [B12] Dura Magnetices, Inc., "Available Samarium Cobalt Magnet Grades," [Online]. Available: <http://www.duramag.com/samarium-cobalt-magnets-smco/available-samarium-cobalt-magnet-grades/>, 2015.
- [B13] F. Fiorillo, "Measurement and characterization of magnetic materials," Elsevier Academic Press, ISBN 0-12-257251-3, page. 31, 2004.
- [B14] D. Brown, B. Ma, Z. Chen, "Developments in the processing and properties of NdFeB-type permanent magnets," J. of Magnetism and Magnetic Materials, vol. 248, no. 3, pp. 432-440, Aug. 2002.
- [B15] Texas Instrument, "A 5-V Input, 1.8-V Output, 6-A Synchronous Buck Converter," [Online] Available: <http://www.ti.com/lit/ug/sl00246/sl00246.pdf>, April 2006.
- [B16] T. D. Surd, T. A. Pering, A. J. Stratakos and R. W. Brodersen, "A Dynamic Voltage Scaled Microprocessor System," IEEE Journal of Solid-state Circuits, vol. 35, no. 11, pp. 1571-1580, Nov. 2000.
- [B17] Linear Technology: "LTC3617: ± 6 A Monolithic Synchronous Step-Down Regulator for DDR Termination" [Online] Available: <http://cds.linear.com/docs/en/datasheet/3617fa.pdf>, 2011.
- [B18] Texas Instrument, "TPS 56121: 4.5-V to 14-V Input High-Current Synchronous Buck Converter," [Online] Available: <http://www.ti.com/lit/ds/slusah4b/slusah4b.pdf>, March 2013.
- [B19] J. Fletcher, B. Williams and M. Mahmoud, "Airgap fringing flux reduction in inductors using open-circuit copper screens," IEE Proc. Electr. Power Appl., vol. 152, no. 4, pp. 990-996, July 2005.
- [B20] J. Hu, "Optimization of Shapes for Round Wire, High Frequency Gapped Inductor Windings," IEEE Industry Applications Conference, Thirty-Third IAS Annual Meeting, vol. 2, pp. 907-912, Oct. 1998.

Chapter 3

- [C1] G. Spiazzi and S. Buso, "Analysis of the Interleaved Isolated Boost Converter With Coupled Inductors," IEEE Trans. Ind. Electron., vol. 62, no. 7, pp. 4481-4491, July 2015.

- [C2] F. Yang, X. B. Ruan, Y. Yang, Z.H. Ye, "Interleaved Critical Current Mode Boost PFC Converter With Coupled Inductor," IEEE Trans. Power Electron., vol. 26, no. 9, pp. 2404-2413, Sep. 2011.
- [C3] P. L. Wong, P. Xu, B. Yang, and F. C. Lee, "Performance improvements of interleaving VRMs with coupling inductors," IEEE Trans. Power Electron., vol. 16, no. 4, pp. 499-507, Jul. 2001.
- [C4] Y. Dong, J. Zhou, F. C. Lee, M. Xu and S. Wang, "Twisted Core Coupled Inductors for Microprocessor Voltage Regulators," IEEE Trans. Power Electron., vol. 23, no. 5, pp. 2536 - 2545, May 2008.
- [C5] Q. Li, Y. Dong, F. C. Lee and D. J. Gilham, "High-Density Low-Profile Coupled Inductor Design for Integrated Point-of-Load Converters" IEEE Trans. Power Electron., vol. 28, no. 1, pp. 547 - 554, Jan. 2013.
- [C6] Y. Yang, D. Yan, F.C. Lee, "A new coupled inductors design in 2-phase interleaving VRM," IEEE 6th International Power Electronics and Motion Control Conference, pp. 344-350, May 2009.
- [C7] G.Y. Zhu, B. McDonald, K.R. Wang "Modeling and Analysis of Coupled Inductors in Power Converters," IEEE Trans. Power Electron., vol. 26, no. 5, pp. 1355-1363, May 2011.
- [C8] C. Wang, "Investigation on Interleaved Boost Converters and Applications," PhD dissertation, Virginia Polytechnic Institute and State University, July 2009.
- [C9] M. Phattanasak, W. Kaewmanee and P. Thounthong, "Study of two-phase interleaved boost converter using coupled inductors for a fuel cell," International Conference on Electrical Engineering/Electronics, Computer, Telecommunications and Information Technology (ECTI-CON), pp. 1-6, May 2013.
- [C10] S. Ahsanuzzaman, T. McRae, M. Peretz, A. Prodi, "Low-volume Buck Converter with Adaptive Inductor Core Biasing," IEEE Applied Power Eletroncis Conference and Exposition, pp. 335-339, Mar. 2012.
- [C11] R. W. Erickson, D. Maksimovic. "Fundamentals of Power Electronics", Springer, 2000.
- [C12] B.D. Cullity, C.D. Graham, "Introduction to Magnetic Materials", 2nd edition Wiley-IEEE Press, 2009.
- [C13] EPCOS AG, "E16/8/5 (EF 16)," [Online]. Available: http://en.tdk.eu/inf/80/db/fer_13/e_16_8_5.pdf, 2015.
- [C14] EPCOS AG, "SIFERRIT material N87," [Online]. Available: <http://en.tdk.eu/blob/528882/download/4/pdf-n87.pdf>, Sept. 2006.

- [C15] Tridelta Magnet Systems GmbH, "Sintered NdFeB Magnets,"[Online]. Available: http://www.tridelta.de/viomatrix/imgs/download/sintered__ndfeb_magnets.pdf, 2016.
- [C16] Coilcraft, "SER2000 Series High Current Shielded Power Inductors," [Online]. Available: <http://www.coilcraft.com/ser2000.cfm>, 2016.

Chapter 4

- [D1] S. Y. Hui, "Planar Wireless Charging Technology for Portable Electronic Products and Qi," Proceedings of the IEEE, Vol 101, No. 6, pp. 1290-1301, June 2013.
- [D2] U. K. Madawala and D. J. Thrimawithana, "A bidirectional inductive power interface for electric vehicles in V2G systems," IEEE Trans. Ind. Electron., vol. 58, no. 10, pp. 4789–4796, Oct. 2011.
- [D3] M. Budhia, G. A. Covic, and J. T. Boys, "Design and optimization of magnetic structures for lumped inductive power transfer systems," in Proc. IEEE ECCE, 2009, pp. 2081–2088.
- [D4] S. Hui, W. Zhong, C. Lee, "A Critical Review of Recent Progress in Mid-Range Wireless Power Transfer," IEEE Trans. Power Electron. Vol. 29, No. 9, pp. 4500-4511, Sept. 2014.
- [D5] A. Kurs, A. Karalis, R. Moffatt, J. D. Joannopoulos, P. Fisher, and M. Soljačić, "Wireless power transfer via strongly coupled magnetic resonances," Science, vol. 317, no. 5834, pp. 83–86, Jul. 2007.
- [D6] A. P. Sample, D. A. Meyer, and J. R. Smith, "Analysis, experimental results, and range adaptation of magnetically coupled resonators for wireless power transfer," IEEE Trans. Ind. Electron., vol. 58, no. 2, pp. 544–554, Feb. 2011.
- [D7] Z. Dang, Y. Cao and J. Abu Qahouq, "Reconfigurable Magnetic Resonance-Coupled Wireless Power Transfer System," IEEE Transactions on Power Electronics, vol. 30, no. 11, pp. 6057-6069, Nov. 2015.
- [D8] Z. Dang, "Magnetic Resonance Coupled Wireless Power Transfer Systems," Master Thesis, The University of Alabama, Dec. 2013.
- [D9] Z. Dang, J.A. Abu Qahouq, "Modelling and Simulation of Magnetic Resonance Coupled Wireless Power Transfer Systems," International Review of Modelling and Simulation (I.RE.MO.S), vol. 6, no. 5, pp. 1607-1617, Oct. 2013.
- [D10] Z. Dang and Jaber Abu Qahouq, "Range and Misalignment Tolerance Comparisons between Two-coil and Four-coil Wireless Power Transfer Systems," The 2015 IEEE Applied Power Electronics Conference and Exposition, APEC'2015, pp. 1234-1240, Mar. 2015.

- [D11] Z. Dang and Jaber Abu Qahouq, "Elimination Method for the Transmission Efficiency Valley of Death in Laterally Misaligned Wireless Power Transfer Systems," 2015 IEEE Applied Power Electronics Conference and Exposition, APEC'2015, pp. 1644-1649, Mar. 2015.
- [D12] Z. Dang and J. Abu Qahouq, "Modeling and Investigation of Magnetic Resonance Coupled Wireless Power Transfer System with Lateral Misalignment," The 2014 IEEE Applied Power Electronics Conference and Exposition, APEC'2014, pp 1317-1322, Mar. 2014.
- [D13] Y. Cao, Z. Dang and J. Abu Qahouq, "Dynamic Efficiency Tracking Controller for Reconfigurable Four-coil Wireless Power Transfer System," The 2016 IEEE Applied Power Electronics Conference and Exposition, APEC'2016, Mar. 2016.
- [D14] L.H. Chen, S. Liu, Y.C. Zhou, and T.J. Cui, "An Optimizable Circuit Structure for High-Efficiency Wireless Power Transfer," IEEE Trans. Ind. Electron., vol. 60, no. 1, pp. 339-349, Jan. 2013.

Chapter 5

- [E1] S. Hui, W. Zhong, C. Lee, "A Critical Review of Recent Progress in Mid-Range Wireless Power Transfer," IEEE Trans. Power Electron. Vol. 29, no. 9, pp. 4500-4511, Sept. 2014.
- [E2] A. Kurs, A. Karalis, R. Moffatt, J. D. Joannopoulos, P. Fisher, and M. Soljačić, "Wireless power transfer via strongly coupled magnetic resonances," Science, vol. 317, no. 5834, pp. 83-86, Jul. 2007.
- [E3] A. P. Sample, D. A. Meyer, and J. R. Smith, "Analysis, experimental results, and range adaptation of magnetically coupled resonators for wireless power transfer," IEEE Trans. Ind. Electron., vol. 58, no. 2, pp. 544-554, Feb. 2011.
- [E4] Z. Dang, "Magnetic Resonance Coupled Wireless Power Transfer Systems," Master Thesis, The University of Alabama, Dec. 2013.
- [E5] Z. Dang, J.A. Abu Qahouq, "Modelling and Simulation of Magnetic Resonance Coupled Wireless Power Transfer Systems," International Review of Modelling and Simulation (I.RE.MO.S), vol. 6, no. 5, Oct. 2013.
- [E6] Z. Dang, J. A. Abu Qahouq, "Modeling and Investigation of Magnetic Resonance Coupled Wireless Power Transfer System with Lateral Misalignment," in Proc. IEEE Appl. Power Electron. Conf., pp. 1317-1322, Mar. 2014.
- [E7] Z. Dang and Jaber Abu Qahouq, "Range and Misalignment Tolerance Comparisons between Two-coil and Four-coil Wireless Power Transfer Systems," The 2015 IEEE Applied Power Electronics Conference and Exposition, APEC'2015, pp. 1234-1240, Mar. 2015.

- [E8] Z. Dang and Jaber Abu Qahouq, "Elimination Method for the Transmission Efficiency Valley of Death in Laterally Misaligned Wireless Power Transfer Systems," 2015 IEEE Applied Power Electronics Conference and Exposition, APEC'2015, pp. 1644-1649, Mar. 2015.
- [E9] F. W. Grover, "Inductance Calculations: Working Formulas and Tables," New York: Dover, 1946, pp.134.
- [E10] S. Raju, R. Wu, M. Chan and C. Yue, "Modeling of mutual coupling between planar inductors in wireless power applications," IEEE Trans. Power Electron., vol. 29 no.1 pp. 481-490, Jan. 2014.
- [E11] O.C. Onar, J.M. Miller, S.L. Campbell, C. Coomer, C. P. White, and L.E. Seiber, "Oak Ridge National Laboratory Wireless Power Transfer Development for Sustainable Campus Initiative," IEEE Transportation Electrification Conference and Expo (ITEC), pp. 1-8, June 2013.
- [E12] Ferroxcube, "Soft Ferrite and Accessories Data Handbook 2013," July 2013. [Online]. Available:
http://www.ferroxcube.com/FerroxcubeCorporateReception/datasheet/FXC_HB2013.pdf
- [E13] U. K. Madawala and D. J. Thrimawithana, "A bidirectional inductive power interface for electric vehicles in V2G systems," IEEE Trans. Ind. Electron., vol. 58, no. 10, pp. 4789-4796, Oct. 2011.
- [E14] M. G. Eagen, D. L. O'Sullivan, J. G. Hayes, M. J. Willers, and C. P. Henze, "Power factor corrected single stage inductive charger for electric vehicle batteries," IEEE Trans. Ind. Electron., vol. 54, no. 2, pp. 1217-1226, Apr. 2007.
- [E15] G. A. Covic, J. T. Boys, M. L. G. Kissin, and H. G. Lu, "A three-phase inductive power transfer system for roadway-powered vehicles," IEEE Trans. Ind. Electron., vol. 54, no. 6, pp. 3370-3378, Dec. 2007.
- [E16] M. Budhia, G. A. Covic, and J. T. Boys, "Design and Optimization of Circular Magnetic Structures for Lumped Inductive Power Transfer Systems," IEEE Trans. Power Electron., vol. 26, no.11, pp. 3096-3108, Nov. 2011.
- [E17] J.M. Miller, O.C. Onar, M. Chinthavali, "Primary-Side Power Flow Control of Wireless Power Transfer for Electric Vehicle Charging", IEEE Journal of Emerging and Selected Topics in Power Electron., vol. 3, no. 1, pp. 147-162, Mar. 2015.
- [E18] S.Y. Choi, J. Huh, W.Y. Lee, C.T. Rim, "Asymmetric Coil Sets for Wireless Stationary EV Chargers With Large Lateral Tolerance by Dominant Field Analysis," IEEE Trans. Power Electron., vol.29, no.12, pp. 6406-6420, Dec. 2014.
- [E19] J. Lee, B. Han, "A Bidirectional Wireless Power Transfer EV Charger Using Self-Resonant PWM," IEEE Trans. Power Electron., vol.30, no.4, pp. 1784-1787, April 2015.

- [E20] New England Wire Technologies, [Online]. Available:
<http://www.newenglandwire.com/products/litz-wire-and-formed-cables/round.aspx>
- [E21] J. Hong and M.J. Lancaster, "Microstrip Filters for RF/Microwave Applications," Wiley, July 2001.
- [E22] J.D. Irwin and R.M. Nelms, "Basic Engineering Circuit Analysis, 10th Edition", Wiley, Oct. 2010.

Chapter 6

- [F1] N. Tesla, "System of transmission of electrical energy," U.S. Patent, No. 645576, Mar, 20, 1900.
- [F2] W. Zhong, C. Zhang, X. Liu and S.Y. R. Hui, "A Methodology for Making a Three-Coil Wireless Power Transfer System More Energy Efficient Than a Two-Coil Counterpart for Extended Transfer Distance," IEEE Trans. Power Electron., vol. 30, no. 2, pp. 933-942, Feb. 2015.
- [F3] Q. Li and Y. Liang, "An Inductive Power Transfer System With a High-Q Resonant Tank for Mobile Device Charging," IEEE Trans. Power Electron., vol. 30, no. 11, pp. 6203-6212, Nov. 2015.
- [F4] M. Liu, M. Fu and C. Ma, "Parameter Design for a 6.78-MHz Wireless Power Transfer System Based on Analytical Derivation of Class E Current-Driven Rectifier," IEEE Trans. Power Electronics, vol. 31, no. 6, pp. 4280-4291, June 2016.
- [F5] J.D. van Wyk and F.C. Lee, "On a Future for Power Electronics," IEEE J. of Emerging and Selected Topics in Power Electron., vol.1, no.2, pp. 59-72, June 2013.
- [F6] J. M. Carrasco, E. Galvan, G.E. Valderrama, "R. Ortega and A.M. Stankovic, Analysis and Experimentation of Nonlinear Adaptive Controllers for the Series Resonant Converter," IEEE Trans. Power Electronics, vol. 15, no. 3, pp. 536-544, May, 2000.

Appendix I

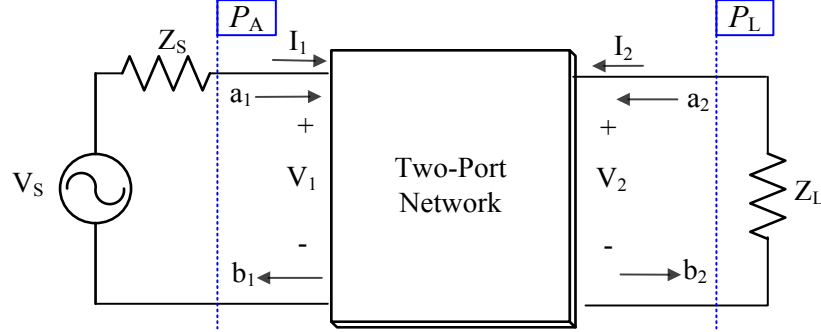


Figure A.1: General two-port network

A general two-port network is shown in Fig. A.1, where a_1 and a_2 are incident waves and b_1 and b_2 are reflected waves. a_1 and b_2 are defined in (A-1) and (A-2), respectively [E21]. In this chapter, $Z_s = Z_L = Z_0 = 50\Omega$.

$$a_1 = \frac{V_1 + I_1 Z_0}{2\sqrt{Z_0}} \quad (\text{A-1})$$

$$b_2 = \frac{V_2 - I_2 Z_0}{2\sqrt{Z_0}} \quad (\text{A-2})$$

From the definition of S_{21} , the following can be obtained:

$$S_{21} = \left. \frac{b_2}{a_1} \right|_{a_2=0} = \frac{\frac{V_2 - I_2 Z_0}{2\sqrt{Z_0}}}{\frac{V_1 + I_1 Z_0}{2\sqrt{Z_0}}} = \frac{V_2 - (-V_2)}{V_S} = \frac{2V_2}{V_S} \quad (\text{A-3})$$

According to the maximum power transfer theorem [E22], the maximum available power (P_A) at port one of the two-port network is given by:

$$P_A = \left(\frac{1}{2}V_S\right)^2 / Z_0 \quad (\text{A-4})$$

Therefore, the transmission efficiency of the two-port network is

$$\eta = \frac{P_L}{P_A} = \frac{V_2^2 / Z_L}{\left(\frac{1}{2}V_S\right)^2 / Z_0} = 4 \frac{V_2^2}{V_S^2} = S_{21}^2 \quad (\text{A-5})$$

Appendix II

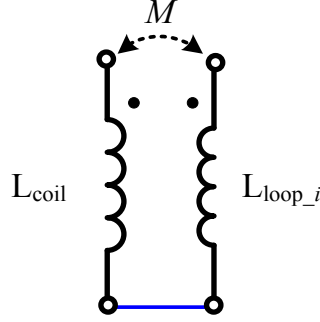


Figure A.2: Equivalent circuit model of directly coupled inductors that are connected in series

When L_{coil} and L_{Loop_i} are connected in series and are directly coupled as shown in Fig. A.2, the equivalent inductance L_{aid_i} is given by (A-6) [E22].

$$L_{aid_i} = L_{coil} + L_{loop_i} + 2M \quad (A-6)$$

Therefore, the mutual inductance between L_{coil} and L_{Loop_i} is given by

$$M = \frac{L_{aid_i} - (L_{coil} + L_{loop_i})}{2} \quad (A-7)$$

Based on (5.1) and (A-7), k_{lc_i} can be calculated as

$$k_{lc_i} = \frac{M_{lc}}{\sqrt{L_{coil}L_{loop_i}}} = \frac{L_{aid_i} - (L_{coil} + L_{loop_i})}{2\sqrt{L_{coil}L_{loop_i}}} \quad (A-8)$$

Appendix III

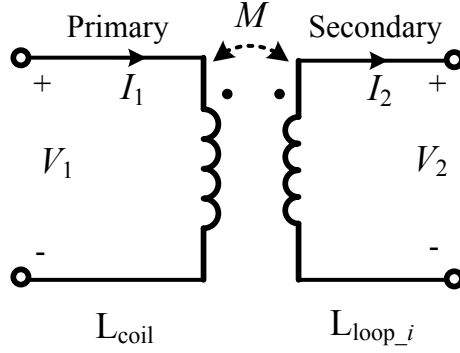


Figure A.3: Equivalent circuit model of a coupled inductor

For Fig. A.3, the following can be derived using circuit analysis [E22]:

$$\begin{cases} v_1(t) = L_{\text{coil}} \frac{di_1}{dt} - M \frac{di_2}{dt} \\ v_2(t) = -M \frac{di_1}{dt} + L_{\text{loop}_i} \frac{di_2}{dt} \end{cases} \quad (\text{A-9})$$

When the secondary side is open circuit, $I_2 = 0$ and (A-9) can be rewritten as

$$\begin{cases} v_{1oc}(t) = L_{\text{coil}} \frac{di_{1oc}}{dt} \\ v_{2oc}(t) = -M \frac{di_{1oc}}{dt} \end{cases} \quad (\text{A-10})$$

When the secondary side is shorted (short circuit), $V_2 = 0$. Therefore,

$$L_{\text{loop}_i} \times I_{2sc} = M \times I_{1sc} \quad (\text{A-11})$$

From (A-10) and (A-11), the following can be obtained:

$$\begin{cases} \left| \frac{V_{2oc}}{V_{1oc}} \right| = \frac{M}{L_{\text{coil}}} \\ \left| \frac{I_{2sc}}{I_{1sc}} \right| = \frac{M}{L_{\text{loop}_i}} \end{cases} \quad (\text{A-12})$$

Thus, using (5.1) and (A-12),

$$k_{lc_i} = \frac{M_{lc}}{\sqrt{L_{\text{coil}}L_{\text{loop}_i}}} = \sqrt{\frac{V_{2oc} \times I_{2sc}}{V_{1oc} \times I_{1sc}} \Big|_i} \quad (\text{A-13})$$